Year : 2024

Quaternary landscape evolution in the Kalahari Basin: The Chobe Enclave (northern Botswana)

Mokatse Thuto

Mokatse Thuto, 2024, Quaternary landscape evolution in the Kalahari Basin: The Chobe Enclave (northern Botswana)

Originally published at : Thesis, University of Lausanne

Posted at the University of Lausanne Open Archive http://serval.unil.ch
Document URN : urn:nbn:ch:serval-BIB_033A70722F6D1

UNIL | Université de Lausanne

Faculté des géosciences et de l'environnement

Institut des dynamiques de la surface terrestre

"Quaternary landscape evolution in the Kalahari Basin: The Chobe Enclave (northern Botswana)".

THESE DE DOCTORAT

Présentée à la

Faculté des géosciences de l'environnement de l'Université de Lausanne

pour l'obtention du grade de

Docteur en sciences de la Terre

Par

Thuto Mokatse

Directeur de thèse
Prof. Eric P. Verrecchia

Jury
Présidente du jury : Prof. Marie-Elodie Perga
Expert externe : Prof. Sebastien Castelltort
Expert interne : Prof. Torsten Vennemann

Lausanne

2024

UNIL | Université de Lausanne
Faculté des géosciences et de l'environnement
bâtiment Géopolis bureau 4631

IMPRIMATUR

Vu le rapport présenté par le jury d'examen, composé de

Présidente de la séance publique :	Mme la Professeure Marie-Elodie Perga
Présidente du colloque :	Mme la Professeure Marie-Elodie Perga
Directeur de thèse :	M. le Professeur Eric Verrecchia
Expert interne :	M. le Professeur Torsten Vennemann
Expert externe :	M. le Professeur Sébastien Casteltort

Le Doyen de la Faculté des géosciences et de l'environnement autorise l'impression de la thèse de

Monsieur Thuto MOKATSE

Titulaire d'un
Master of Science
de Botswana International University of Science and Technology, Botswana

intitulée

QUATERNARY EVOLUTION OF AN AFRICAN HIGH PLATEAU: THE CHOBE ENCLAVE (NORTHERN BOTSWANA)

Lausanne, le 21 février 2024

Pour le Doyen de la Faculté des géosciences et de l'environnement

Professeure Marie-Elodie Perga

QUATERNARY LANDSCAPE EVOLUTION IN THE KALAHARI BASIN: THE CHOBE ENCLAVE (NORTHERN BOTSWANA)

Abstract

The Chobe Enclave is a region within the middle Kalahari Basin of northern Botswana where the imprint of (neo)tectonics is often concealed by sedimentary cover of low-relief environments. These conditions render detailed paleo-environmental reconstructions difficult. A combination of near-surface geophysical surveys, sedimentological analyses, and optically stimulated luminescence (OSL) dating was utilized to investigate relationships between landscape development and tectonic influences. Furthermore, mineralogical and quartz microtextures allowed a comprehensive reconstruction of paleoenvironments during the Late Pleistocene to Holocene to be assessed.

The Chobe Enclave is bounded by fault systems (Chobe and Linyanti faults) integral to the landscape evolution. Prior to the formation of the current Chobe-Linyanti sub-basin, a fluvial/aeolian environment developed over about 200 Ka, which transitioned to a lacustrine/palustrine environment about 80 Ka, where limestones and diatomites formed. Following the later tectonic event at this stage, the results point to a burial of fluvial channels during the Late Pleistocene and syndepositional uplift of the sand ridges revealed by the erosional bounding surfaces. Moreover, the tectonic influence on the landscape was attested by the incision of these sand ridges forming fluvial watergaps. During this phase, with continuous erosion and reworking about 10 Ka, the earlier formed palustrine carbonates were exposed forming an inverted relief.

The hydrochemical changes in lacustrine/palustrine environments during the Late Pleistocene to Holocene were linked to the formation of authigenic sepiolite. The mineralogical relationships between palustrine carbonates and sepiolite indicate a precipitation sequence from an evaporitic system, involving calcite, sepiolite, and amorphous silica. Additionally, quartz grain microtextures from different facies in the Chobe Enclave floodplain were analyzed to reconstruct the sedimentary history. The facies displayed similar granulometric characteristics, pointing to a homogenization of sands from various sources under similar reworking conditions. Quartz microtextures reveal a primary, strong aeolian imprint with alternating fluvial / palustrine / weathering phases, reflecting the complex history of a paleo-alluvial fan influenced by hydrological changes and tectonic influences during the Late Pleistocene.

French version

La Chobe Enclave est une région située dans le bassin du Kalahari central dans le nord du Botswana. L'empreinte des (néo)tectoniques y est souvent dissimulée par une couverture sédimentaire déposée dans des environnements à faible relief, rendant ainsi difficile une analyse détaillée de la reconstruction paléo-environnementale. Une combinaison de levés géophysiques de surface, d'analyses sédimentologiques et de datations par luminescence stimulée optiquement (OSL) a été utilisée pour étudier la relation entre le développement du paysage et les influences tectoniques. De plus, analyses minéralogiques et microtexturales des grains de quartz ont permis une reconstruction complète des paléoenvironnements du Pléistocène tardif à l'Holocène.

La Chobe Enclave est délimitée par des systèmes de failles (failles de la Chobe et de la Linyanti) qui sont essentiels à l'évolution du paysage. Avant la formation du sous-bassin actuel Chobe-Linyanti, un environnement fluvial/éolien (~200 Ka) prospérait, passant à un environnement lacustre/palustre (~80 Ka) où des calcaires et des diatomites se sont formés. À la suite d'événements tectoniques ultérieurs à cette étape, les résultats indiquent un enfouissement des chenaux fluviaux durant le Pléistocène tardif et une remontée syn-sédimentaire des crêtes sableuses révélée par des surfaces de délimitation érosives. De plus, l'influence tectonique sur le paysage a été attestée par l'incision de ces crêtes formant des entailles de surimpositions fluviales. Au cours de cette phase, du fait d'une érosion et de remaniements continus (< ~10 Ka), les carbonates palustres formés antérieurement ont été dégagés, formant ainsi un relief inversé.

Les changements hydrogéochimiques dans les environnements lacustres / palustres du Pléistocène tardif à l'Holocène ont conduit à la formation de sépiolite authigène. Les relations minéralogiques entre les carbonates palustres et la sépiolite indiquent une séquence de précipitation à partir d'un système évaporitique, impliquant la formation successive de calcite secondaire, de sépiolite puis de silice amorphe. De plus, l'analyse microtexturale des grains de quartz provenant des différents faciès de la plaine d'inondation de la Chobe Enclave a permis de reconstruire l'histoire sédimentaire. Les faciès présentent des caractéristiques granulométriques similaires, suggérant une homogénéisation des sables provenant de diverses sources dans des conditions de remaniement similaires. Les microtextures des quartz révèlent une forte empreinte éolienne primaire avec des phases alternées fluviales/palustres/d'altération, reflétant l'histoire complexe d'un paléo-cône alluvial influencé par des changements hydrologiques et des influences tectoniques durant le Pléistocène tardif.

Acknowledgements

First and foremost, I am deeply thankful and forever indebted to my advisor, Prof. Eric Verrecchia, for his guidance, support, and invaluable insights throughout my entire research journey. His mentorship has been instrumental in shaping the direction and quality of this thesis. Special thanks to my co-advisor Prof. Elisha Shemang for his very helpful comments on my research.

I would like to express my sincere gratitude to Dr. James Irving for his training and use of geophysical equipment, data acquisition, as well as his guidance and patience during the processing of the data.

I am indebted to the Earth & Environmental Science Department (EESD) at Botswana International University of Technology (BIUST) for providing the geophysical equipment and the necessary resources used for this project. My heartfelt thanks go to EESD team, Trust Manyiwa and Calistus Ramotoroko for their support in the field during the difficult days of COVID-19 lockdowns and Boniface Kgosidintsi for his continuous support and help during data acquisition and processing.

I would like to thank Dr Christoph Shmidt and Dr. Shlomy Vainer for their support and provision of Optically Stimulated Luminescence (OSL) ages. As well as Dr. Nathalie Diaz for her collaborative spirit and stimulating discussions, Dr. Charlotte Prud'homme, Dr. Shlomy Vainer, Dr. John Van Thuyne for their unwavering support, encouragement, and understanding during the ups and downs of my academic journey. I am grateful to Laetitia Monbaron, Micaela Faria for the help in the laboratory and Dr. Aurelien Ballu for logistics and resources, as well as to Prof. Thierry Adatte, Dr. Hassan Khozyem and Dr. Brahim Bomou at ISTE for their crucial help in mineralogical data acquisitions.

I extend my appreciation to the members of the jury, Prof. Sebastien Castelltort and Prof. Torsten Vennemann for acceptance to evaluate this PhD.

Finally, I want to express my deepest appreciation to my family and friends who always checked on me, offering encouragement during my lowest points throughout my stay in Switzerland.

Table of contents

CHAPTER 1

Introduction

The research centre in the Chobe Enclave, northern Botswana

1.1 Sediments in the Chobe Enclave

The predominant section of the intracratonic middle Kalahari basin in southern Africa, intersected by the southwestward extension of the East African Rift System (EARS), comprises accumulation of aeolian, fluvial, and lacustrine sediments (Grove, 1969; Kinabo et al., 2008; Huntsman-Mapila et al., 2009). The differential deformation of elevated structural axes within the Kalahari basin led to the formation of multiple sub-basins, notably the Makgadikgadi-Okavango-Zambezi basin (MOZB) during the early Pleistocene (Vainer et al., 2021). The region experienced formation of megafans and paleolakes (Shaw et al., 1992; Burrough and Thomas, 2013) during different phases of the Quaternary, with preservation of remnants of waterbodies where the structural depression accommodates an endorheic hydrological system. These depressions contain reworked sediments transported into the basin (Huntsman-Mapila et al., 2005; Vainer et al., 2021; Garzanti et al., 2022). Such features are observed among one of the main structural depressions, i.e. the Chobe-Linyanti basin. forming a local and significant depocenter. Part of this basin, which includes the Chobe Enclave (northern Botswana; Fig. 1; see also Fig. 2.1), serves as an illustrative example for the Pleistocene-Holocene evolution of a semi-desert - deltaic region, offering insights into the complex interplay of geological, climate, and tectonic processes.

Understanding the geological evolution of semi-desert / deltaic regions of the Kalahari Basin is crucial for unravelling the challenges posed by these regions in which the environments changed significantly during the Quaternary. Interactions between Earth surface processes, including neotectonics and particularly in the central southern African plateaus, led to diversified landscapes, encompassing lacustrine / palustrine environments with alluvial fan / deltaic development systems (Kinabo et al., 2007, 2008; Bufford et al., 2012). Nevertheless, the formation and timing of such sedimentary deposits remain poorly understood since the stratigraphy of the Kalahari Basin during the Late Quaternary is spatially extremely variable, resulting in difficult lateral correlations (McCarthy, 2013, and references therein). Even though some studies attempted to link sedimentary processes to regional paleohydrological records (e.g., Shaw, 1988; Shaw et al., 1997, 2003; Ringrose et al., 1999, 2005; Burrough and Thomas, 2009; Diaz et al., 2019), details regarding the influence of tectonics, rivers, and biogeochemical conditions in sediment supply during landscape evolution are still unclear.

Meanwhile, the sedimentology of the Chobe Enclave of northern Botswana emerges as a particularly intriguing aspect, as it unveils a multifaceted landscape. Sediments form both a siliceous environment, mainly made up of quartz grains (reaching 99% in pure sands) in floodplains and dune systems, and “platforms” or “islands”, made of carbonate-rich deposits (limestones). The origin of the carbonate deposits, although they are mentioned, described, and/or sampled in this research, do not constitute the primary emphasis of the work, as they add a layer of complexity to the overall geological framework, which would deserve an entire new study.

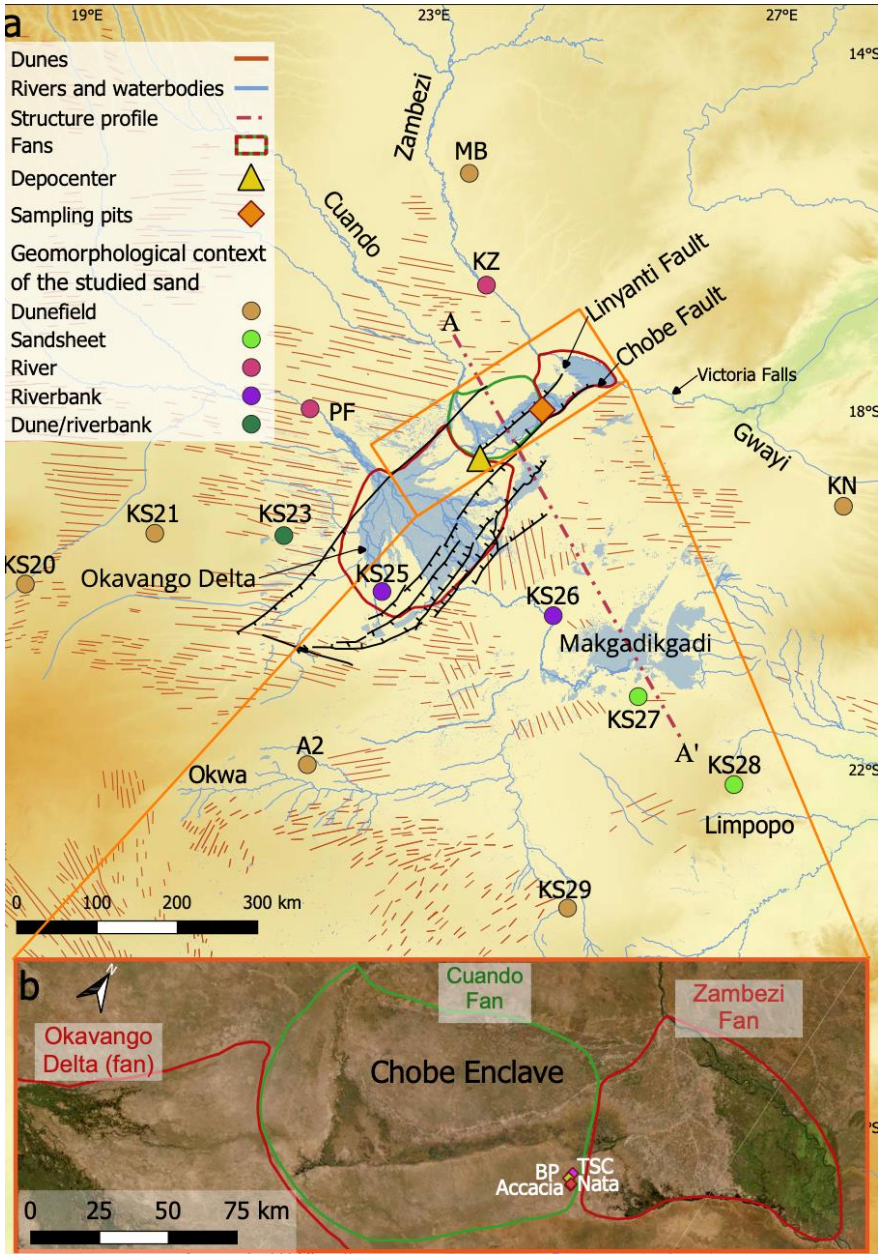

Figure 1.1: (a) Structural elements of southern Africa including the East African Rift Fault System and intracratonic structural axes that have been operated since the Neogene. The shaded area indicates the Okavango Rift Zone. The background is an SRTM 30-sec DEM. (b) Close-up of the Chobe Enclave from Google Earth showing the extensions of fans and the four outcrops studied in this thesis: Baobab Pit (BP), TSC Island, Nata Island (Nata), and Accacia quarry (Accacia). Figure from Vainer et al. (2023, submitted).

1.2 Thesis objectives

This thesis will focus on the sandy floodplains of the Chobe Enclave (northern Botswana) formed by large sandy deposits of varying grain sizes in order to reconstruct the onset of the geomorphological system as well as the dynamic and chemical pathways involved in the sedimentary record. The research is articulated around the following main questions:

1. What is the geometry of floodplain sediments and what does their relationship with landforms mean?

The approach used to answer this question is two-fold, based on geophysical and geomorphological acquisitions of data. Geophysical techniques, i.e. Electrical Resistivity Tomography (ERT) and Ground Penetrating Radar (GPR), were utilized to help map and delineate the lateral distribution of Quaternary deposits along the surface and their vertical thickness variation. In this manner, it was possible to depict lithological and sedimentological variations within the subsurface in order to reconstruct the dynamic system of the floodplain. The geomorphological approach allowed to focus on tectonically influenced landscapes as they can be identified by a series of indicators, from entrenched channels to relief inversions. The relationship between sedimentary deposits and relief inversions provides valuable clues about the dynamic interplay of erosion, deposition, and (neo)tectonic activity. The surface expression of sedimentary bodies emphasizes the role of relief inversions in shaping the landscape.

2. What can we learn from the sediments to reconstruct the paleoenvironmental settings?

This work focused on a better understanding of the depositional environments, within the related tectonic regime, using the common components of the sedimentary deposits from the Chobe Enclave (quartz sands, clay minerals, diatomites, and carbonate layers): their presence and characteristics always provide information about the evolution of the paleoenvironments.

Quartz grains in sediments (from sands to limestones) can indicate the way they were transported and their history through their multiple reworking owing to imprints of microfeatures

at the surface of the grain (Krinsley and Doorkamp, 1973; Mahaney, 2002; Vos et al., 2014). These microtextures are essentially due to the resistance of weathering of the quartz grains.

On another note, the nature and composition of clay minerals indicate the prevailing source and/or biogeochemical conditions at work during deposition. For example, the presence of kaolinite may suggest legacy of a warm and humid climate, whereas smectite may indicate a more seasonally contrasted environment.

On the other hand, occurrences of diatomaceous earth may refer to a shallow and clear water environment in which diatoms can thrive and settle down. Small lakes or ponds would provide such still water environments under neutral to slightly alkaline conditions in which diatomite frustules can be preserved. In addition, carbonates (limestones) in the Chobe Enclave address two main questions: how could such large and thick limestone layers form and what were their calcium sources in such a largely siliceous environment, totally depleted in Ca? Limestones and diatomites are critical to address as changes in abundance and facies of diatomite and carbonate deposits are obviously related to the water sources and fluctuations as well as the water balance in terms of evaporation.

Finally, a particular mineral is also observed in the Chobe Enclave: barite. Its presence is puzzling although the source of sulfate could point to the large presence of evaporites (gypsum) in the Central Kalahari (Makgadikgadi Basin), which could be brought by wind. The problem is that gypsum is only observed as minor traces in the Chobe Enclave and Ba cannot originate from the Makgadikgadi Basin. Consequently, the presence of barite raises the question of a potential occurrence of Ba conventional source, which is hydrothermalism (Hanor, 2000). Indeed, a present-day hot spring can be observed in the most northern part of the Chobe Enclave, near Kasane (Mukwati et al., 2018). The tectonic context of the Chobe Enclave could have provided a favorable environment for discontinuous hydrothermalism, a point that will be discussed in this thesis.

3. What could be the chronology (relative and absolute) of events?

The interpretation of stratigraphic successions and outcrop correlations is often based on a mutli-proxy approach, where various components are considered together to build a comprehensive understanding of paleoenvironmental changes. Relative succession of events and landscapes are

proposed in this manuscript, based on multivariate analyses of various proxies. Additionally, the integration of Optically Stimulated Luminescence (OSL) data from sands of the Chobe Enclave helped to establish an absolute chronological framework for the reconstruction of the paleoenvironments.

1.3 Organization of the manuscript

The manuscript is organized into six chapters:

- **Chapter 1** (this chapter) presents the context and the main research questions addressed in this manuscript.
- **Chapter 2** deals with a state-of-the-art and an overview of the research conducted in the Chobe Enclave. After the general context of the Chobe Enclave, topography and climate are outlined, followed by the context of the Chobe-Linyanti hydrological basin. Then, geological settings and geomorphological features are detailed.
- **Chapter 3** provides the description of deposit geometry and the nature of landforms in the Chobe Enclave. The sand ridges and their margins are investigated using geophysical surveys (ERT and GPR) coupled with sedimentological data and OSL ages.
- **Chapter 4** details the occurrence and significance of an authigenic fibrous clay mineral (sepiolite) and the sub-environments in which they formed, including the potential influence of hydrothermalism in the Chobe Enclave.
- **Chapter 5** presents a not-so-conventional approach of the study of quartz grains, i.e. the quartz microtextural analysis. The various quartz trapped in the various sedimentary facies observed in the Chobe Enclave were analyzed and a chronology of events associated with the facies and their succession in the described logs is proposed based on the observed microfeatures.
- **Chapter 6** includes the final conclusions of the thesis. Moreover, some perspectives and future challenges are also proposed in this final chapter.

Chapters 2, 3, and 4 have been published in peer-reviewed journals (see list below). Chapter 5 is presently under review.

List of published papers:

Mokatse, T., Prud'Homme, C., Vainer, S., Adatte, T., Shemang, E., Verrecchia, E. P. (2023). Sepiolite as a multifactorial indicator of paleoenvironments in the Chobe Enclave (northern Botswana). *Sedimentary Geology*, *454*, 106459.

Mokatse, T., Vainer, S., Irving, J., Schmidt, C., Kgosidintsi, B., Shemang, E., Verrecchia, E. P. (2022). Geometry of sedimentary deposits and evolution of the landforms in the Chobe Enclave, Northern Botswana. *Geomorphology*, *415*, 108406.

Mokatse, T., Diaz, N., Shemang, E., Van Thuyne, J., Vittoz, P., Vennemann, T., Verrecchia, E. P. (2022). Landscapes and Landforms of the Chobe Enclave, Northern Botswana. In *Landscapes and Landforms of Botswana* (pp. 91-116). Cham: Springer International Publishing.

References

Bufford, K.M., Atekwana, E.A., Abdelsalam, M.G., Shemang, E., Atekwana, E.A., Mickus, K., Moidaki, M., Modisi, M.P., Molwalefhe, L., 2012. Geometry and faults tectonic activity of the Okavango Rift Zone, Botswana: Evidence from magnetotelluric and electrical resistivity tomography imaging. Journal of African Earth Sciences, 65, pp.61-71.

Burrough, S.L., Thomas, D.S.G., 2009. Geomorphological contributions to palaeolimnology on the African continent. Geomorphology 103 (3), 285–298.

Burrough, S. L., Thomas, D. S., 2013. Central southern Africa at the time of the African Humid Period: a new analysis of Holocene palaeoenvironmental and palaeoclimate data. Quaternary Science Reviews, 80, 29-46.

Diaz, N., Armitage, S.J., Verrecchia, E.P., Herman, F., 2019. OSL Dating of a carbonate island in the Chobe Enclave, NW Botswana. Quaternary Geochronology 49, 172–76.

Garzanti, E., Pastore, G., Stone, A., Vainer, S., Vermeesch, P., Resentini, A., 2022. Provenance of Kalahari Sand: Paleoweathering and recycling in a linked fluvial-aeolian system. Earth-Science Reviews, 224, 103867.

Grove, A.T., 1969. Landforms and climatic change in the Kalahari and Ngamiland. Geographical Journal 135, 191–212.

Hanor, J.S., 2000. Barite–Celestine Geochemistry and Environments of Formation. Reviews in Mineralogy and Geochemistry, 40, 193-275. DOI: 10.2138/rmg.2000.40.4.

Huntsman-Mapila, P., Kampunzu, A.B., Vink, B., Ringrose, S., 2005. Cryptic indicators of provenance from the geochemistry of the Okavango Delta sediments, Botswana. Sedimentary Geology, 174(1-2), 123-148.

Huntsman-Mapila, P., Tiercelin, J.J., Benoit, M., Ringrose, S., Diskin, S., Cotten, J., Hémond, C., 2009. Sediment geochemistry and tectonic setting: Application of discrimination diagrams to early stages of intracontinental rift evolution, with examples from the Okavango and Southern Tanganyika rift basins. Journal of African Earth Sciences, 53(1-2), 33-44.

Kinabo, B.D., Atekwana, E.A., Hogan, J.P., Modisi, M.P., Wheaton, D.D., Kampunzu, A.B., 2007. Early structural development of the Okavango rift zone, NW Botswana. J. Afr. Earth Sci. 48, 125–136.

Kinabo, B.D., Hogan, J.P., Atekwana, E.A., Abdelsalam, M.G., Modisi, M.P., 2008. Fault growth and propagation during incipient continental rifting: Insights from a combined aeromagnetic and Shuttle Radar Topography Mission digital elevation model investigation of the Okavango Rift Zone, northwest Botswana. Tectonics 27, TC3013Natu.

Krinsley, D., Doornkamp, J., 1973. Atlas of Quartz Sand Surface Textures. Cambridge: Cambridge University Press.

Mahaney, W.C., 2002. Atlas of Sand Grain Surface Textures and Applications. New York: Oxford University Press.

McCarthy, T.S., 2013. The Okavango Delta and its place in the geomorphological evolution of southern Africa. South African Journal of Geology, 116(1), 1-54.

Mukwati, B.T., Tafesse, N.T., Bagai, Z.B., Laletsang, K., 2018. Hydrogeochemistry of the Kasane Hot Spring, Botswana. Univ. J. of Geosci., 6, 5, 131-146. DOI: 10.13189/ujg.2018.060501.

Ringrose, S., Downey, B., Genecke, D., Sefe, F., Vink, B., 1999. Nature of sedimentary deposits in the western Makgadikgadi basin, Botswana. Journal of Arid Environ- ments 43 (4), 375–397.

Ringrose, S., Huntsman-Mapila, P., Kampunzu, A.B., Downey, W., Coetzee, S., Vink, B., Matheson, W., Vanderpost, C., 2005. Sedimentological and geochemical evidence for palaeo-environmental change in the Makgadikgadi subbasin, in relation to the MOZ rift depression, Botswana. Palaeogeography, Palaeoclimatology, Palaeoecology 217 (3–4), 265–287.

Shaw, P.A., 1988. After the flood: the fluvio-lacustrine landforms of Northern Botswana. Earth-Science Reviews 25, 449–456.

Shaw, P.A., Thomas, D.S.G., Nash, D.J., 1992. Late Quaternary fluvial activity in the dry valleys (mekgacha) of the middle and southern Kalahari, southern Africa. Journal of Quaternary Science 7 (4), 273–281.

Shaw, P.A., Stokes, S., Thomas, D.S.G., Davies, F.B.M., Holmgren, K., 1997. Palaeoecology and age of a Quaternary high lake level in the Makgadikgadi basin of the middle Kalahari, Botswana. South African Journal of Science 93 (6), 273–276.

Shaw, P.A., Bateman, M.D., Thomas, D.S.G., Davies, F., 2003. Holocene fluctuations of Lake Ngami, Middle Kalahari: chronology and responses to climatic change. Quaternary International 111 (1), 23–35.

Vainer, S., Matmon, A., Erel, Y., Hidy, A.J., Crouvi, O., De Wit, M., Geller, Y., ASTER Team, 2021. Landscape responses to intraplate deformation in the Kalahari constrained by sediment provenance and chronology in the Okavango Basin. Basin Research, 33(2), 1170-1193.

Vainer, S., Schmidt, C., Garzanti, E., Matmon, A., Ben Dor, Y., Pastore, G., Mokatse, T., Prud'homme, C., Leanni, L., ASTER Team, Verrecchia, E.P. (2023 – submitted) Chronology of sedimentation and landscape evolution in nascent rifting settings in the Okavango Rift Zone, southern Africa. JGR Earth Surface, 35 p.

Vos, K., Vandenberghe, N. & Elsen, J., 2014. Surface textural analysis of quartz grains by scanning electron microscopy (SEM): From sample preparation to environmental interpretation. Earth-Science Reviews, 128, 93–104. Available from: https://doi.org/10.1016/j.earscirev.2013.10.013

CHAPTER 2

Landscapes and Landforms of the Chobe Enclave, Northern Botswana

A deep exposure of a palustrine carbonate overlying the Yellow sands (reworked paleosols) in a quarry section.

2. Landscapes and Landforms of the Chobe Enclave, Northern Botswana

Published as:

Mokatse, T., Diaz, N., Shemang, E., Van Thuyne, J., Vittoz, P., Vennemann, T., Verrecchia, E.P., 2022. Landscapes and landforms of the Chobe Enclave, Northern Botswana, in: Eckardt, F. (Ed.), Landscapes and Landforms of Botswana. Springer-Nature, Dordrecht, 91-116. doi.org/10.1007/978-3-030-86102-5_6.

In this chapter, the personal work entails the writing of section 2.1.1 and 2.2.2 and a contribution of the reading and editing of the whole chapter. Sections 2.1.1 and 2.2.2 reported mainly the details of the Chapter introduction and the geological settings.

Synopsis

In this chapter, the state-of-the-art overview of the PhD topic is outlined. This entails the introduction to the Chobe Enclave area (geology and physical geography) and the main research challenges and questions to be investigated. This chapter paved the way for the conceptualization of the different chapters addressed in this thesis. As the Chobe Enclave is situated in a semi-arid environment of an intra-cratonic basin, more challenges are posed by the tectonic activity associated with the deposits as well as the region evolution during the Late Quaternary. Furthermore, the lack of outcrops in the area adds to the general complexity of rare archives in the region.

Abstract

The northern part of the Chobe Enclave (an administrative district of northern Botswana) is an agricultural area situated between relatively pristine national parks situated in the Middle Kalahari Basin. It belongs to the Linyanti-Chobe structural basin and constitutes a syntectonic depocenter formed within a large structural depression, known as the Okavango Graben, a tectonic structure of a likely trans-tensional nature. The landscape includes fossil landforms, such as sand dunes, pans, sand ridges, and carbonate islands resulting from palaeoenvironmental and palaeo-drainage changes through the Quaternary and associated to (neo)tectonic processes. In addition to river and wind-reworked Kalahari sands, the sediments include diatomites and carbonate deposits, forming inverted reliefs and originating from palustrine palaeo-environments. The Linyanti-Chobe basin is at the convergence of several ecoregions from tropical and subtropical grasslands to savannas and shrubland biomes. The hydrological cycle in the northern Chobe Enclave is governed by a complex interplay between the Okavango, Kwando, and Upper Zambezi drainage basins, which originate from tropical watersheds of the Angolan highlands. Finally, the widespread development of termite mounds impacts the diversity of soils and sediments of the northern Chobe Enclave, which is also reflected in the vegetation.

2.1 Introduction

2.1.1 Where Is the Chobe Enclave and Why Is it so Interesting?

Landscape evolution in the Chobe-Linyanti basin is closely associated with active tectonics and surface processes. Sedimentary basins forming under extensional tectonic regimes are important records of geological history, among other types of depositional environments. The architectures of these basins and the basin-fill are influenced by the rheological structure of the lithosphere, the availability of crustal discontinuities that can be tensionally reactivated, the mode and amount of extension, and the lithological composition of pre- and syn-rift sediments (Ziegler and Cloetingh 2004). An important factor in controlling geomorphic processes during landscape evolution can be the topography of a region affected by recent and/or active processes such as faulting (Mayer 1986; Cox 1994; Bishop 2007; Giaconia et al. 2012a, 2012b). Therefore, it is crucial to report the underlying geology in order to understand the way landforms evolve. The study site, as a part of the Middle Kalahari Basin of northern Botswana, is situated in the northern Chobe Enclave, an administrative district, close to the Chobe-Linyanti depocenter (Fig. 2.1). It is bounded by the Linyanti river and Lake Liambezi in the north, bordering the eastern part of the Caprivi Strip, and the Savuti and Chobe rivers in the west and south, respectively. It is an agricultural area between relatively pristine national parks covered mostly by the Kalahari sands with unexpected occurrences of carbonate beds (Diaz et al. 2019). Equally so, the various types of sedimentary deposits (Fig. 2.1), including diatomites, fluvial, and aeolian sands, span the site. Palaeo-shorelines within the Middle Kalahari have been investigated as Quaternary landform relicts, which formed under different hydrological conditions (e.g., Burrough and Thomas 2008; Burrough et al. 2009a, 2009b; Shaw et al. 1988). Some investigations focused on understanding geomorphological features, such as sand ridges associated with lacustrine systems, namely, the Mababe Depression, Lake Ngami, and the Makgadikgadi Pan (Grey and Cooke 1977; Grove 1969; Shaw 1985). Understanding the timing of formation of these sand ridges has been helped by thermoluminescence (TL) and optically stimulated luminescence (OSL) dating techniques (e.g., Cooke and Verstappen 1984; Shaw 1985; Burrough et al. 2007; Burrough and Thomas 2008; Ringrose et al. 2008; Burrough et al. 2009a, 2009b). Burrough and Thomas (2008) reported OSL ages of sand ridges from the Mababe Depression and Lake Ngami consistent in ages with sand ridges in the northern Chobe Enclave. However, given the nature of emplacement of these sand ridges and associated sedimentary deposits, such as

carbonate beds (Diaz et al. 2019), and the complexity of interpreting the emplacement of geomorphological features, some questions remain unanswered, such as:

- What is the origin of the sediments forming the sandy landforms?
- What is the origin of the carbonate deposits?
- What depositional environments and landscapes are recognized?
- What could be the main processes at work in this landscape?

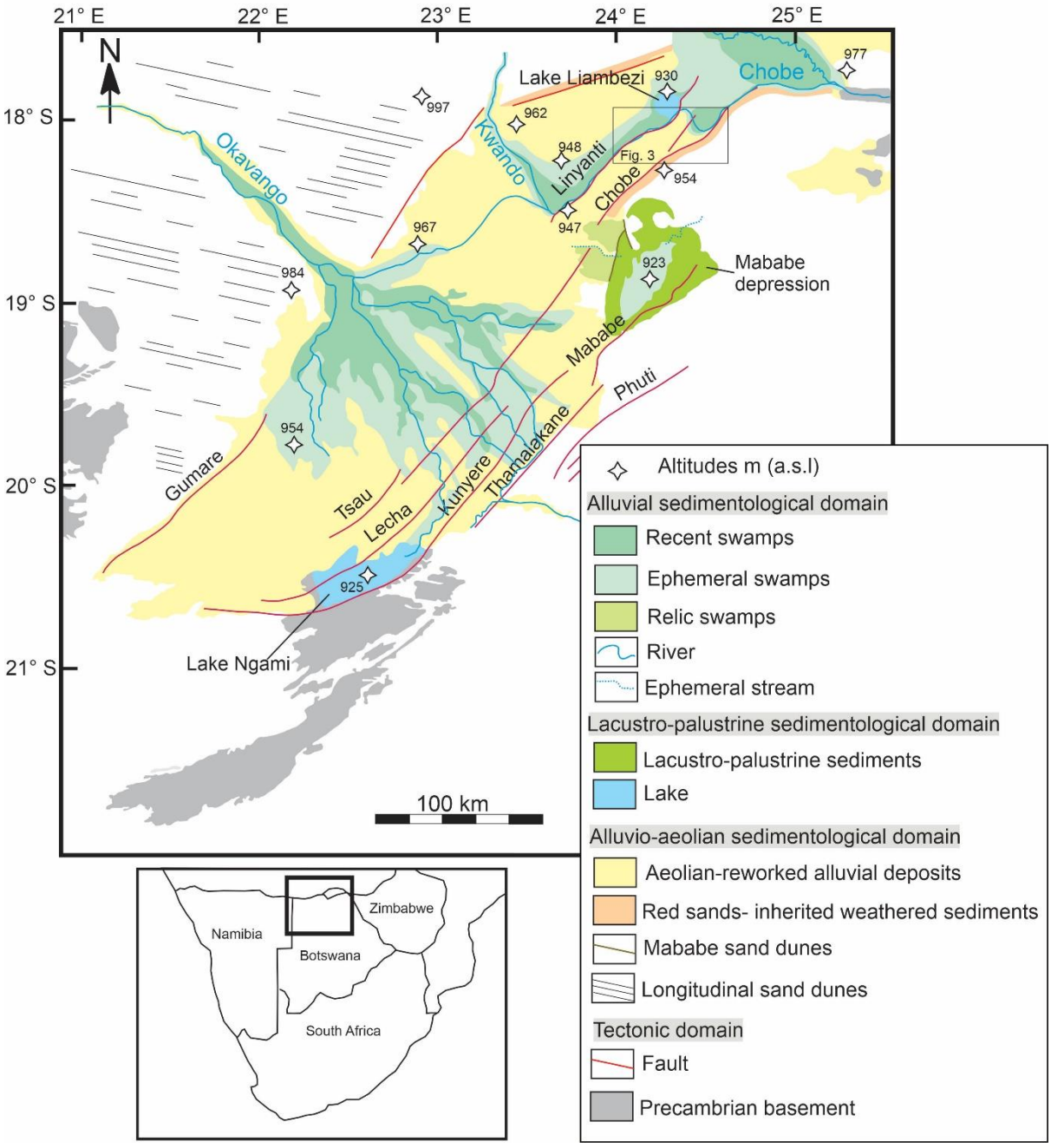

Figure 2.1: Map of the sedimentary domains, Okavango region.

The area is also characterized by a large diversity of soils and vegetation (Romanens et al. 2019; Vittoz et al. 2020). The region covered in this study is unique as it mirrors some aspects of the inland alluvial fans of the Okavango and Kwando rivers, as geologic and tectonic processes extend into this arid to semiarid region, hence establishing a regional-scale and even local-scale zoning of the same large-scale vegetation zones adjacent to the subtropical swamps/flooded areas. The Linyanti-Chobe basin, in particular, is at the convergence of several ecoregions that are all part of the "tropical and subtropical grasslands, savannas and shrubland" biome. It includes the Zambezian flooded grasslands, the Zambezian and mopane woodlands, the Kalahari Acacia-Baikiaea woodlands, and the Kalahari xeric savannah. The Linyanti-Chobe basin flora thus consists of a mix of species from these contrasting, neighboring ecosystems. Finally, the hydrological cycle in the Chobe Enclave is governed by a complex interplay between the Okavango, Kwando, and Upper Zambezi drainage basins. In addition to local rainfall, it receives waters from the Okavango, Kwando-Linyanti, and Zambezi-Chobe River systems, which drain tropical watersheds in the Angolan highlands.

Topography and Climate of the Chobe Enclave

Tectonics influenced both the topography and hydrologic conditions of the study region, possibly altering palustrine/shallow lacustrine and sedimentary budgets. The middle Kalahari is a semiarid environment with a record of wetter climate in the past (Cooke 1975; Shaw and Cooke 1986), and depositional environments that preserve a complex history of Quaternary environmental change (Thomas and Shaw 1991, 2002). Today, northern Botswana is classified as a hot semiarid (steppe) climate (BSh) (Peel et al. 2007). This type of climate is characterized by a mean annual temperature above 22 °C, low mean annual precipitation of which 90 % falls between October and April (Skarpe et al. 2014). The northern Chobe Enclave district (average precipitation of 650 mm; Jones 2002) has a wet season from November to March with average minimum and maximum temperatures of 20 °C and 32 °C, respectively, and a dry season from April to October with average minimum and maximum temperatures of 13 °C and 30 °C, respectively.

2.1.2 Hydrological Setting of the Chobe-Linyanti Basin

As noted above, this region is bounded by the Linyanti river and Lake Liambezi in the north and the Savuti and Chobe rivers in the west and south, respectively. These bounding rivers are part of a complex drainage system that includes all three of the regionally important rivers of the Okavango, the Kwando, and the Zambezi (McCarthy et al. 2000). The headwaters of the catchments

to the Okavango, Kwando, and Zambezi are characterized by a humid, subtropical climate with a mean annual precipitation of up to 1300 mm, decreasing down to about 570 mm in the region of the Chobe Enclave district. The rainy season in the headwater region, as well as the study region, is commonly between November and March (Mizlow et al. 2009) and the intensity depends critically on fluctuations in the positioning of the Intertropical Convergence Zone (e.g., McCarthy et al. 2000). The discharge of the three river systems, along their course which is individually >1800 km, provides a maximum flooding to their respective distal wetlands, towards the south, with a delay of about 6 months. The Okavango's and Kwando's maximum floods occur from June to August (e.g., Pricope 2013), while the Zambezi has an earlier annual flood pulse that may spill over into the Linyanti-Chobe wetlands through the Bukalo Channel, as well as the Chobe River. The flooding in the Linyanti-Chobe basin thus peaks between March and May, a few weeks after the Zambezi reaches its maximum discharge (Tweddle and Hay 2011; Pricope 2013). The Okavango waters penetrate the Linyanti-Chobe basin only during exceptional floods via the Selinda spillway. The relative exchange from the Zambezi and/or the Okavango/Kwando into the Linyanti-Chobe area may well have been more important during the past humid periods, and the existence of a larger palaeo-lake during the Quaternary is postulated (Burrough and Thomas 2008), as supported by inherited geomorphological features in the landscape.

The complexity of the drainage system in the Chobe Enclave is related to uplift along the Okavango-Kalahari-Zimbabwe axis and extension of the East African Rift system during the Cretaceous (Moore and Larkin 2001; Tooth et al. this book). The Kwando River has been deviated from the Zambezi due to faulting along the Linyanti fault, creating the endoreic systems and resultant wetlands of the Linyanti river and Lake Liambezi. The southern bounding fault of the Chobe, in turn, separated the Kwando from the Chobe River, together with movements along the Linyanti fault, also limiting the Linyanti overflow into the Chobe River. Instead, the Chobe River and its wetlands may now receive backflow waters from the Zambezi (Moore and Larkin 2001; Tooth et al. this book). However, depending on the relative amounts of precipitation in the Okavango, the Kwando, and finally also the Zambezi catchments, additional water in the Linyanti-Liambezi basin may enter via the Selinda spillway from the Okavango drainage basin and/or via the Bukalo Channel from the Zambezi drainage basin (McCarthy et al. 2000). Depending on the water levels in the Linyanti and Lake Liambezi drainage system, the Chobe River serves as the major surface outflow (Seaman et al. 1978; Burrough and Thomas 2008; Kurugundla et al. 2010; Peel et al. 2015) and finally returns the waters through a confluence with the Zambezi River further south.

2.2 Geological settings

2.2.1 Structural Context

The northern Chobe Enclave district forms part of the Linyanti-Chobe sub-basin, bounded by the Linyanti and Chobe faults (Fig. 2.1). The Linyanti-Chobe sub-basin together with the Ngami and Mababe basins are the three characteristic syntectonic depocenters (Kinabo et al. 2007) within the large structural depression known as the Okavango Graben. This structural depression is made up of a series of NE-SW trending normal to dextral strike-slip faults (Modisi et al. 2000; Campbell et al. 2006; Bufford et al. 2012). The bounding faults of the Okavango Graben in the southern part form an en-echelon pattern with a direction following the strike of the Precambrian basement structures (Mallick et al. 1981; Moorkamp et al. 2019). The Okavango Graben has been associated with the formation of the southwestern branch of the East African Rift system (Modisi et al. 2000; Alvarez and Hogan 2013); however, Pastier et al. (2017) argued that the tectonic structure of the Okavango Graben better fits a trans-tensional basin model. Trans-tensional or pull-apart basins are topographic depressions that form at releasing bends or steps in a basement strike-slip fault system, with basin margin characterized by the developments of en-echelon oblique—extensional faults that soft- or hard-link with increasing displacement in the principal displacement zones (Wu et al. 2009). Kinabo et al. (2008) coupled analysis of Shuttle Radar Topography Mission (SRTM), Digital Elevation Model (DEM), and aeromagnetic data in the Chobe region and revealed the development of soft linkage on segments of the Linyanti fault and evidence of a hard linkage forming between two en-echelon right-stepping segments of the Chobe fault.

2.2.2 Bedrock Geology

The Ghanzi-Chobe basin in northwestern Botswana consists of a linear belt of volcano-sedimentary sequences that were deposited during Meso-Neoproterozoic times following extension tectonics associated with the Namaqua orogeny (Modisi et al. 2000). This basin was subsequently deformed as part of the continent-wide tectonic event, the Pan-African Damara orogeny, resulting in the inversion of the Proterozoic volcano-sedimentary basins and formation of a fold belt along the northern margin of the Kalahari Craton (Modie 1996). Sediments of the Mesozoic Karoo Supergroup then became part of this fault-bounded graben system (Bordy et al. 2010). The giant Okavango dyke swarm cut across the basin during this time (Le Gall et al. 2002). Significantly, this

sequence in northwestern Botswana was further affected by the reactivation of ancient faults in Pan-African belts, resulting in the Proterozoic NE-SW strike (Pastier et al. 2017). Thus, the Ghanzi-Chobe basin in northwestern Botswana preserves an important record of subsequent tectonic and depositional events that brought together two prominent southern African cratons – the Kalahari and Congo cratons.

Surficial Sedimentary Geology

The Kalahari sands mainly dominate the sediments observed at the ground surface of the area. They outcrop as the upper part of a sedimentary body of more than 200 m in thickness (Thomas and Shaw 1991). Two other sedimentary units, not documented in the region, have also been identified: continental carbonate landmasses (described as "islands" in this chapter) and diatomites.

First, X-ray diffraction (XRD) analyses confirm the almost pure quartz nature of the sands in the region. They are usually extremely well sorted and are present in all types of sediments and soils, whatever their nature (Fig. 2.2). They obviously belong to the large body of the Kalahari sands (Table 2.1). They are also found associated with finer fractions, likely originating from (i) a fine loess fraction and/or dust (Crouvi et al. 2010), (ii) diatoms, or (iii) pedogenic redistribution and neoformation, the latter including the role of termites (see below; Jouquet and Lepage 2002; Jouquet et al. 2011). Their ubiquity, and their mostly aeolian and fluvial reworked nature at the surface of the landscape (Thomas and Shaw 1991, 2002), make these sands suitable for OSL dating (see below).

Second, carbonate formations in the region appear as limited landmasses identified as "islands" in the sand sea (Fig. 2.3). They have variable thicknesses but are frequently thicker than 1 m (Figs. 2.4 and 2.5e– g). In the literature, these carbonate layers are usually defined as "calcrete". Although this term refers to a large variety of processes explaining their formation (and consequently palaeo-environments; Wright, 2007), their genesis has been attributed in Botswana to a combination of pedogenic, groundwater, and geochemical-diagenetic processes (Nash et al. 1994; Nash and Shaw 1998; Ringrose et al. 2002, 2014). The beds, hardened to various degrees, include all the features observed in palustrine limestones at the macroscale (e.g., traces of roots, burrows and/or galleries, shells, paleosol imprints) and at the microscale (e.g., desiccation features, redistributions in the micromass and nodulization, multiple vadose and phreatic phases in cements; see Freytet and Verrecchia 2002; Verrecchia 2007).

Consequently, although designated as “calcretes” in the literature (sensu Wright and Tucker 1991), the carbonate beds from the northern Chobe Enclave district could also be described as palustrine limestones. Their position as low relief features in the landscape are due to an inverted relief, emphasizing their inherited nature (Diaz et al. 2019). This raises the question “Is the palustrine origin of these limestones likely?”. Fine carbonate deposits have been observed in the Okavango Delta (McCarthy et al. 2012) in island-mounds forming within the Delta. However, these tree-covered islands do not accumulate significant amounts of calcium carbonate, only traces as subsurface crystals. Their formation is related to the chemistry at the interfaces between fresh groundwater flow and trapped saline groundwater through tree uptake and transpiration (McCarthy et al. 2012), with dust contributing substantially to the material found on the surface of islands (Humphries et al. 2014). If such a process cannot generate large calcium carbonate accumulations, it is for the simple reason that the Okavango waters are presently extremely poor in Ca^{2+}, i.e., 3–7 mg/L on average, with a conductivity of 33–40 µS cm^{-1} (Dr. Mogobe, Okavango Research Institute, Maun; personal communication, spring 2016). But one can imagine a palaeo-river system significantly enriched in Ca^{2+}, in which the same processes at work during large floods could have led to some of the fossil carbonate deposits outcropping today. They could correspond to large ponds and marshes and would constitute precious palaeo-climate and environmental indicators (Diaz et al. 2019; see below) to reconstruct the relationships between the Zambezi-Chobe system and the southern palaeolakes observed by Burrough and Thomas (2008). Presently, most of these outcropping carbonate deposits are karstified and eroded under the present-day climate and weathering conditions.

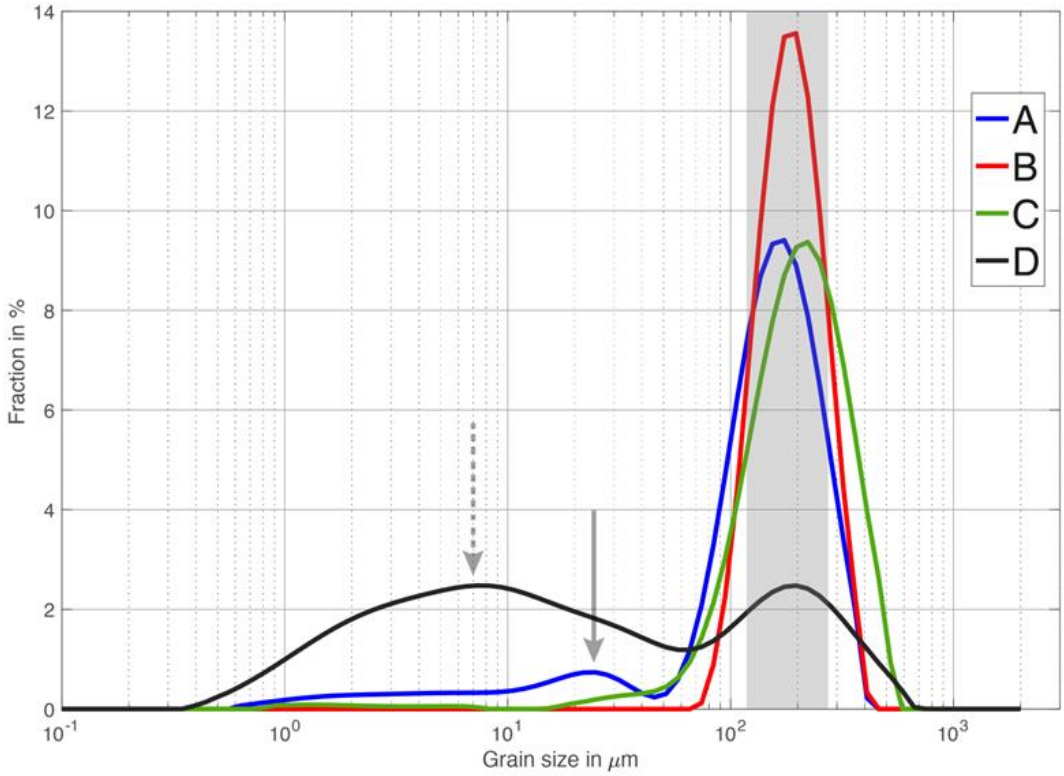

Figure 2.2: Four examples of grain-size distributions from the Chobe Enclave: The Kalahari sand mode is always displayed (shaded area centered on 200 µm). In addition, two modes of fine particles are detected and likely correspond to fine peri-desertic loess (solid arrow at 30 µm) and/or dust/very fine silt due to termite activity and/or diatomite (dashed arrow at 8 µm; see Crouvi et al. 2010 and Sect. 4.3). A) Sandy and homogeneous layer (5.40 m deep), Baobab pit (18°06'10" S, 24°18'30" E, 935 m asl). B) Recent fluvial sand from the Linyanti (18°04'30" S, 24°08'43" E, 937 m asl). C) Recent aeolian sand, east plateau of the Linyanti river (18°10'16" S, 24°14'54" E, 936 m asl). D) Baobab pit, upper layer (soil).

Third, diatomites are easily recognized in the sediments: they form a fine, white material, with a very low density and are sometimes so soft that they can be crushed to a powder in the field. X-ray fluorescence (XRF) analyses confirmed their pure siliceous nature (SiO_2). The presence of quartz, probably of aeolian origin, is also observed using scanning electron microscope (SEM). However, in the study region, diatomites can also be associated to calcite as vein, crack, fracture, and tubular infillings (Fig. 2.6). Such pure diatomites can only form in ponds or shallow lakes, in a range of water salinities, from freshwater to slightly brackish. They must correspond to periods during which wetter conditions prevailed. Their presence can correspond to periods similar to what has been suggested by Burrough and Thomas (2008), i.e., "that increased flow in the Chobe and Zambezi system significantly contributed to the Middle Kalahari lake phases" for the palaeo-lakes

observed in the south and east of the Chobe. It can be hypothesized that their alternation with the carbonate deposits indicates that the Chobe underwent fluctuations in the hydrochemistry of water sources, as well as in climatic conditions. But this theory needs to be properly assessed and documented by further studies.

Table 2.1: Average grain sizes of the Kalahari sands from various locations.

Locations	*Average sizes*	*Authors*
Kalahari dune field	125 to 220 µm	Cook (1980)
Namib sand sea	200 µm	Lancaster (1981)
Kalahari dune crest	175 µm	Watson (1985)
South West Kalahari	190 to 240 µm	Lancaster (1986)
Central Kalahari (Ghanzi)	170 to 225 µm	Wang et al. (2007)
Central Kalahari (Tshane)	210 to 230 µm	Wang et al. (2007)
Northern Botswana	200 µm	Thomas and Shaw (1991)
Namib sand sea	170-340 µm	Crouvi et al. (2010)

2.2.3 Insights into the Quaternary in the Chobe-Lynianti Region

2.2.3.1 Quaternary Palaeo-Lakes and the Chobe-Lynianti Region

The endorheic nature of the basin has led to aeolian, fluvial, and/or lacustrine sedimentary accumulations since the Cretaceous (Grove 1969). Regarding the Quaternary palaeodrainage history, it has mostly been reconstructed through geological and geomorphological archive studies (e.g., Thomas and Shaw 2002; Burrough et al. 2007; Moore et al. 2012). Fossil landforms, such as sand dunes, pans, sand ridges, and carbonate islands (Diaz et al. 2019; Fig. 2.3), testify to changes in hydrological conditions. However, the present-day semiarid climate leads to the deflation of sedimentary archival deposits and does not favor the preservation of organic proxies (Thomas and Burrough 2012). Regional palaeo-environmental records are thus fragmentary and difficult to assess (e.g., Cordova et al. 2017), making interpretations sometimes invalidated, particularly regarding influences of climate change and/or tectonic events on the palaeo-drainage (Moore et al. 2012; Bäumle and Himmelsbach 2018). In the Okavango region, extensive geomorphological evidence for large palaeo-lake exist, referring to wetter climate periods (Grove 1969). Most previous research has focused on palaeolakes in this region, notably Lake Ngami (Huntsman-Mapila et al. 2006), Lake Mababe (Gamrod 2009), and Lake Makgadikgadi (Thomas and Shaw 1991). Burrough and Thomas (2008) proposed that these palaeo-lakes might have coalesced into a single large Mega-Kalahari Lake during previous humid periods. OSL dating of the main palaeo-lake shorelines (beach ridges) in

the Okavango region suggested that high lake levels occurred during the Holocene and Late Pleistocene at 8.5 ± 0.2 ka, 17.1 ± 1.6 ka, 26.8 ± 1.2 ka, 38.7 ± 1.8 ka, 64.2 ± 2.0 ka, 92.2 ± 1.5 ka, and 104.6 ± 3.1 ka (Burrough and Thomas 2008; Burrough et al. 2009a, 2009b). However, it seems that tectonic processes also played a critical role in the drainage evolution. Moore et al. (2012) reviewed the Plio-Pleistocene history of the main rivers in the region belonging to the Congo Basin and the Upper Zambezi Basin. They proposed a model in which the general drainage conditions resulted in smaller lakes, whereas larger lakes were controlled by climate feedbacks, such as the rainfall and evaporation balance. The authors recognized different palaeo-lake systems: Palaeo-Lake Deception with a fossil sand ridge at 995 m (McFarlane and Eckardt 2008), Palaeo-Lake Makgadikgadi with fossil sand ridges at 945 m (Thomas and Shaw 1991; Burrough and Thomas 2008), and Palaeo-Lake Thamalakane with fossil sand ridges at 936 m, 920 m, and 912 m (Grey and Cooke 1977). They proposed one mega-lake (Palaeo-Lake Deception and after Palaeo-Lake Makgadikgadi) during the Early Pleistocene (<500 ka) that progressively contracted, rather than oscillated, due to a reduction of inflow from the tributaries of the Upper Zambezi palaeo-river system that were cut off by tectonic subsidence and lifting, inducing headward erosion and river capturing (Bäumle and Himmelsbach 2018). The decrease of water inputs from the Boteti River controlled by the fault system at the foot of the Okavango Delta caused the Palaeo-Lake Thamalakane to shrink, indicated by a shoreline decreasing from 920 to 912 m between 300 and 100 ka. The 912 m lake would have desiccated in the last 100 ka (Moore et al. 2012).

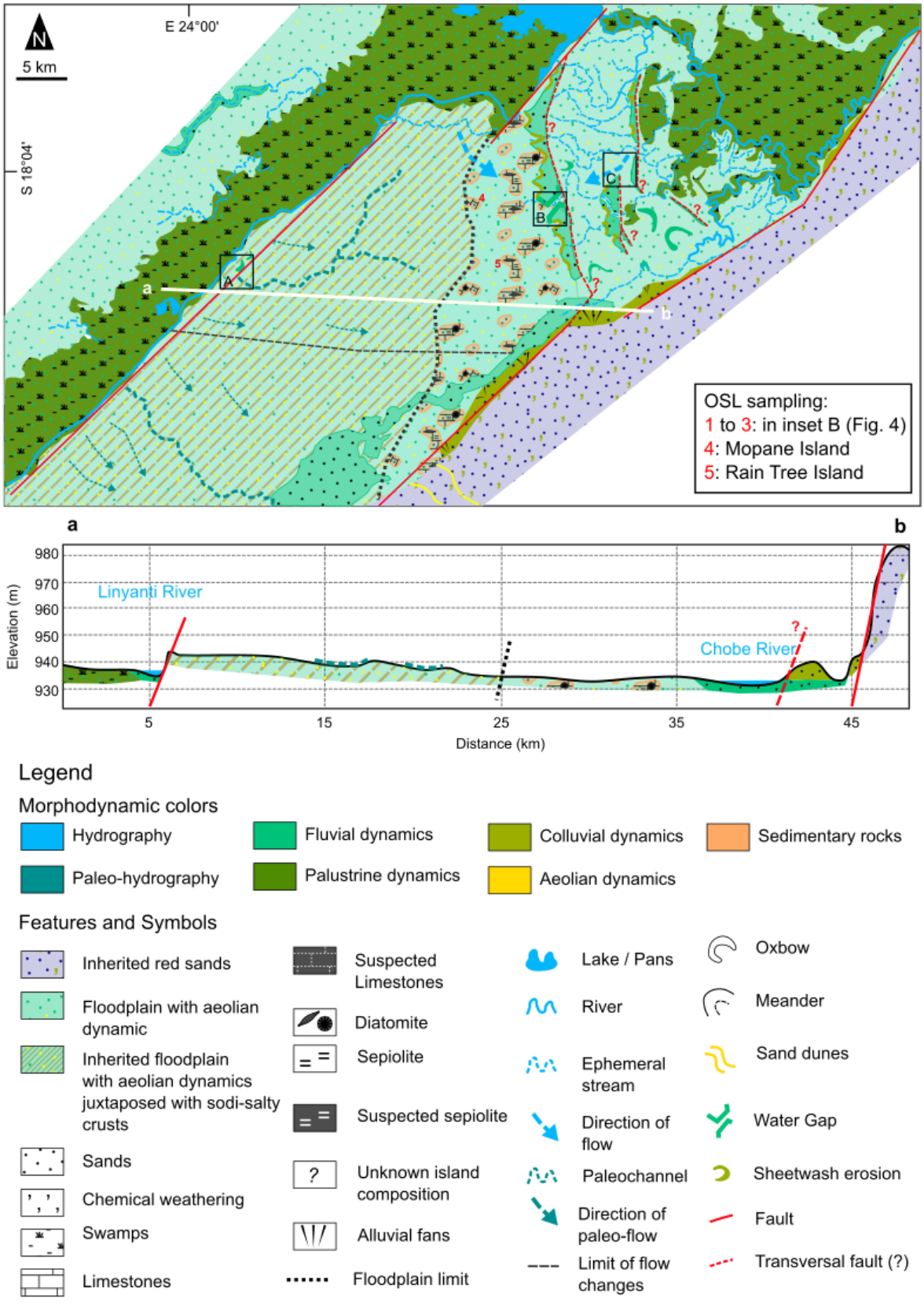

Figure 2.3: Geomorphological map from the Chobe Enclave and elevation profile through the Chobe Enclave

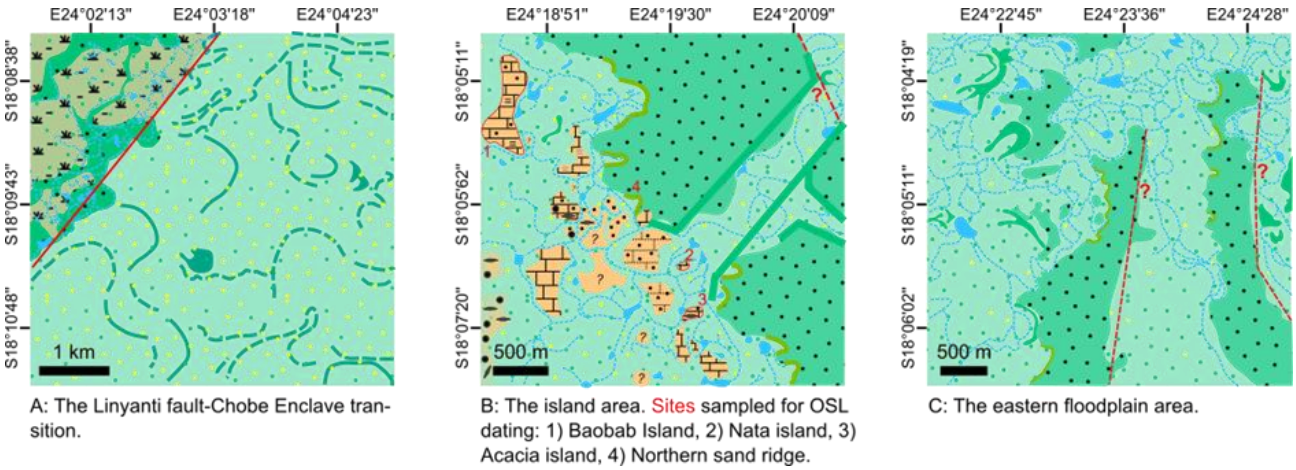

A: The Linyanti fault-Chobe Enclave transition.

B: The island area. Sites sampled for OSL dating: 1) Baobab Island, 2) Nata island, 3) Acacia island, 4) Northern sand ridge.

C: The eastern floodplain area.

Figure 2.4: Detailed geomorphological maps in three key areas from west to east (see Fig. 2.3 for location). A) Paleo-floodplain, B) the island area, C) the sand ridge area. The red numbers correspond to the sites where samples were taken for OSL measurements. Red question marks refer to potential transversal faults. See legend in Fig. 2.3.

2.2.3.2 The Carbonate Islands from the Chobe-Lynianti Region

Carbonate islands of various sizes and surrounded by ephemeral waterbodies are a common feature of the landscape (Figs. 2,3 and 2.4; Diaz et al. 2019). The precise origin and timing of such landforms remain unclear, but they are hypothesized to have been formed in response to regional palaeo-hydrological changes, making them interesting archives for the region. Different successions of sedimentary beds are exposed in quarries (Figs. 2.5e–g and 2.6). The Baobab Island (site 1, Fig. 2.4) is one of these quarries opened in an island. The other studied islands (sites 2, 3, 4, and 5, Figs. 2.3, 2.4 and 2.7) refer to outcrops; the sands below the carbonate layers are described from pits dug in the alluvial plain surrounding the carbonate island, as illustrated in the supplementary materials from Diaz et al. (2019).

The Baobab Island quarry is 5 m deep and the only place where the Kalahari sands can be reached directly below the carbonate beds. These sands have a thickness of 1.30 m (Fig. 2.5 f). They are enriched in secondary silica concretions, as nodules or rhizoliths. The sands become carbonate-rich just below, and at the contact, with the overlying carbonate layer with a wellmarked boundary between the sand-rich layers and the carbonate bed. The bottom part of the carbonate bed includes few small carbonate nodules, increasing in size and abundance toward the surface. Siliceous nodules display the same distribution as the carbonate ones. The uppermost 1.70 m of the pit comprises a hard carbonate bed without any apparent nodules.

The pit from site 2 (3 m deep) was observed next to Nata Island (Fig. 2.4b) located between the northern and the southern N-S sand ridges. The elevation of the island compared to the surrounding sediments is about 2.5 m. A sandy layer, about 1.60 m thick and enriched in siliceous nodules, forms the bottom part of the pit. It is overlaid by a 40 cm-thick grey sandy layer without any siliceous nodules. An organic-rich sandy layer composes the upper part of the outcrop. The carbonate rock from the bed shows root and vegetation tissue debris and dendritic Fe–Mn features. Two 2 m-deep pits were dug at site 3 located next to the most southern N-S sand ridge (Fig. 2.4). The first pit is just next to Acacia Island. Its bottom part is mostly an organic-rich and carbonate-free sand 40 cm in thickness. It is overlaid by a carbonate-rich sandy layer 1.10 m thick, without any organic matter. The uppermost part, 30 cm thick, is organic- and carbonate-rich. The second pit is located within the alluvial plain surrounding Acacia Island. The bottom part is a grey sand-rich layer 20 cm thick with abundant siliceous nodules. It is overlain by a thin sandy layer, 10 cm thick, in turn overlain by a 80 cm organic-rich layer and then, a thin sandy layer (15 cm), the top of the outcrop capped with an organic-rich layer, 75 cm thick. The elevation of the carbonate island compared to the surrounding alluvial plain is about 2 m. The carbonate bed studied was 1 m thick. It is a nodular carbonate rock rich in iron/clay infillings. It seems to overlay a diatomite layer (30 cm thick), showing some dark and carbonate veins forming a grid pattern (Fig. 2.6).

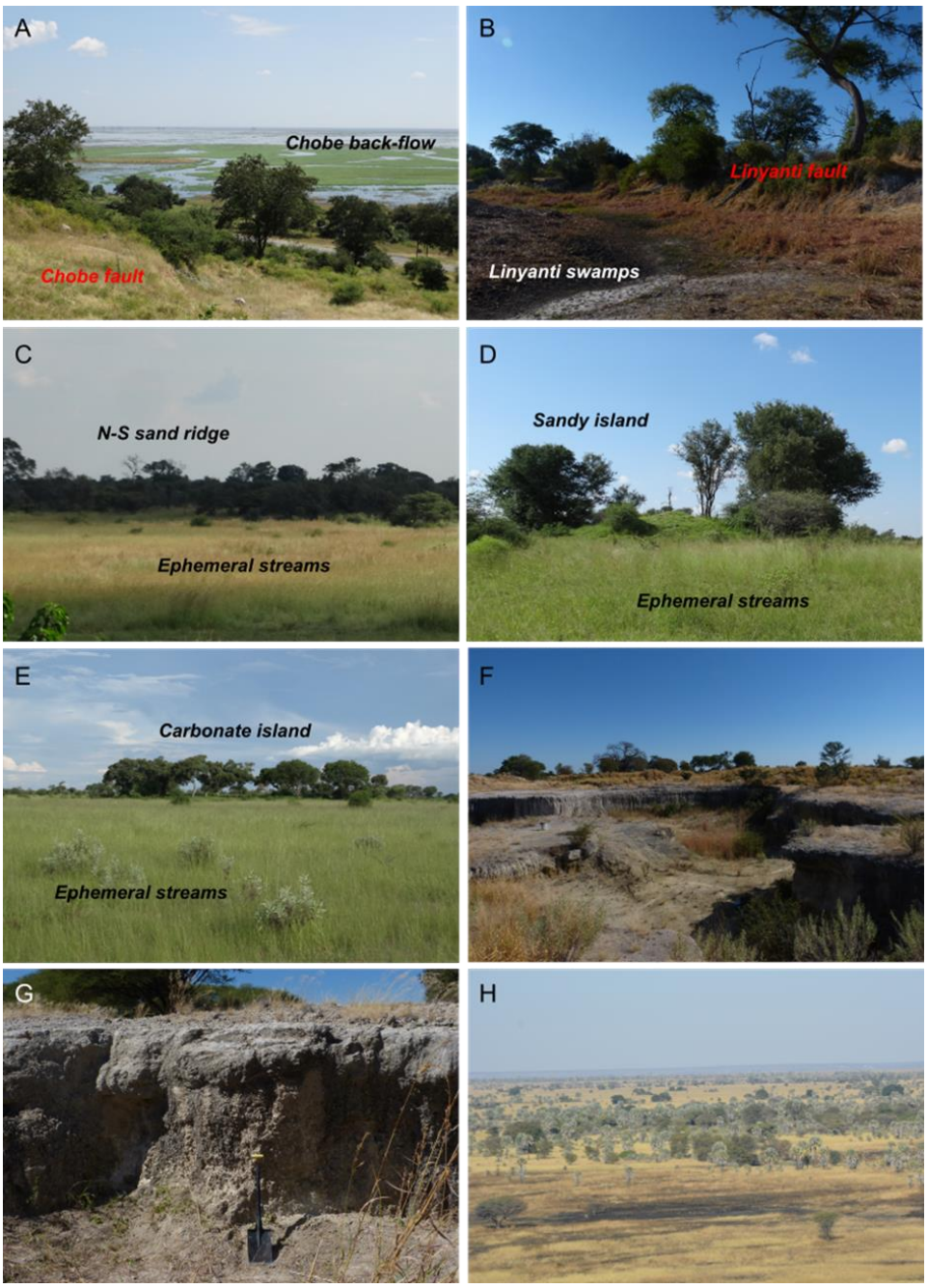

Figure 2.5: Different landscapes and landforms from the Chobe Enclave. a) View from the Chobe fault near Katchikawe on the Chobe backflow, b) view from the Linyanti swamps toward the Linyanti fault during the dry season, c) view on the western side of the N-S sand ridge, slightly elevated with tree vegetation and surrounded by ephemeral streams covered with grass, d) Sandy island covered with trees and surrounded by ephemeral streams covered with grass, e) view of a carbonate island (Diaz et al. 2019) slightly elevated, covered with trees and surrounded by ephemeral streams covered with grass, f) Baobab quarry view with exposure of the carbonate beds (see location on Fig. 2.4b), g) Carbonate layer from another quarry, Acacia pit (see location on Fig. 2.4b), where a diatomitic layer was also observed (Fig. 2.6), h) view on the eastern floodplain with small N-S sand ridges covered by trees and surrounded by ephemeral streams covered with grass during the dry season.

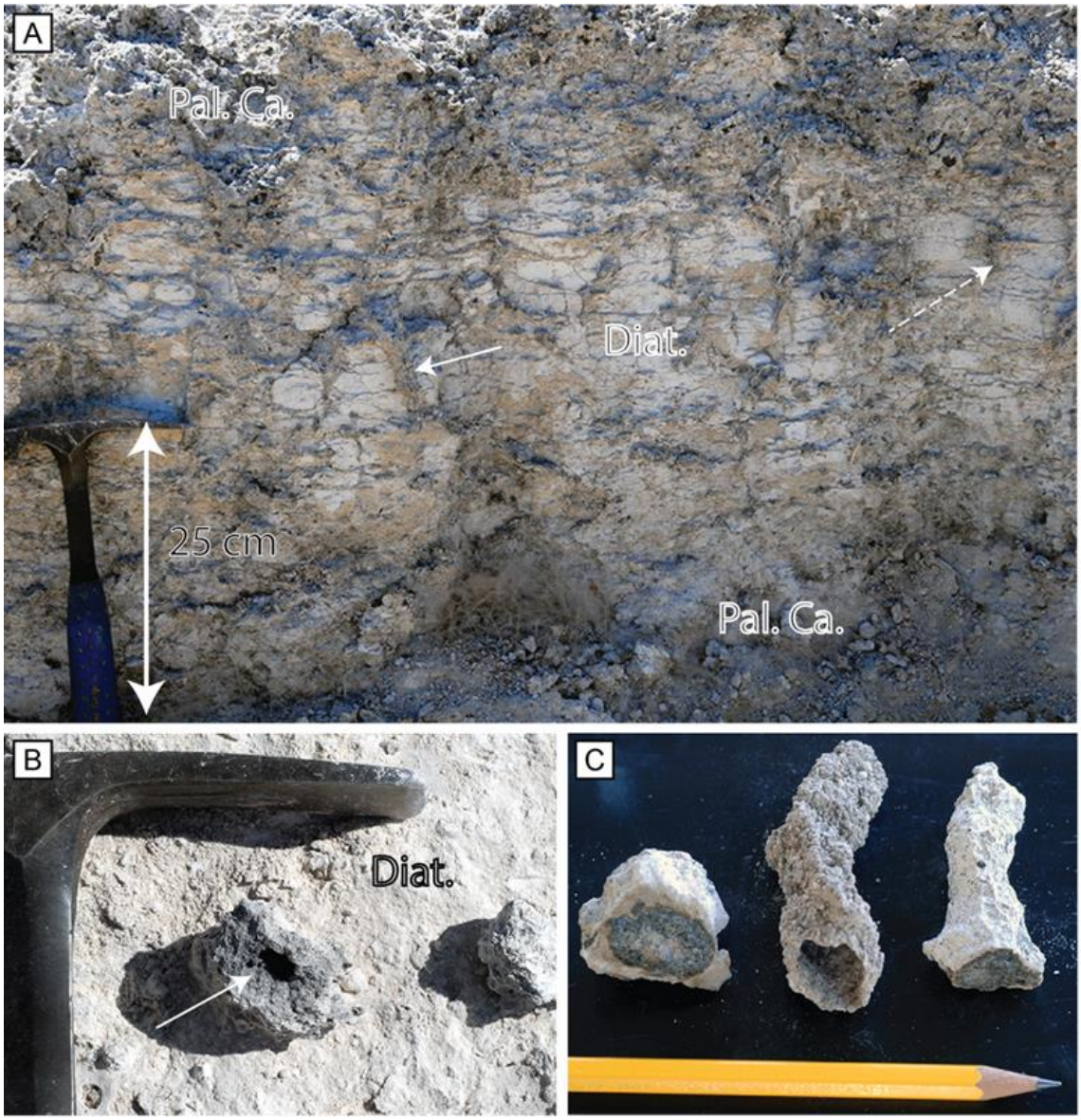

Figure 2.6: Field photographs showing A) the outcrop of a diatomite layer (Diat.) between two palustrine carbonate deposits (Pal.Ca.) at Acacia quarry (18°07'03" S, 24°19'31" E, 933 m asl; see Fig. 2.5g). The age of such deposits is still unknown. There are some diagenetic features, such as burrows or galleries (solid white arrow) and craze planes and fractures (dashed arrow), both infilled with $CaCO_3$. B) Close-up of a carbonate-rich burrow or gallery inside a diatomite layer. C) Comparison between present-day termite gallery (sample in the center) and fossil features found in diatomites. All these hand specimens are cemented by Ca-carbonate.

Another 2 m deep pit was dug next to Mopane Island located 10 km from the N-S sand ridge in the W (site 4, Fig. 2.3). The elevation of this island compared to the surroundings is about 0.5 m. The pit is characterized by a carbonate-rich layer, 20 cm thick, with small roots and a dominance of a sand size fraction (70 %). The layer above is 1.80 m thick and is organic rich, without any carbonate in the fine fraction, but includes carbonate blocks and gravels. The carbonate rock fragments from

the bed are very similar to the Nata Island carbonate layer and comprise tissue debris of roots and plants as well as dendritic Fe–Mn features. A 2 m deep pit was dug next to Rain Tree Island located 10 km from the N-S sand ridge in the W (site 5, Fig.2.3) in the surrounding alluvial floodplain. The elevation of the carbonate bed compared to the floodplain is about 2.5 to 3 m. The lowest part is a white sandy layer (10 cm thick) having abundant siliceous nodules. It is overlain by an organic-rich sandy layer (30 cm thick), in turn overlain by a grey sandy layer (20 cm thick). Above this light-colored sandy layer, there is a second organic-rich layer (20 cm thick) with an organic content increasing toward the upper part of the pit (1.10 m thick). The carbonate rock from the bed is very similar to those of Nata and Mopane Islands. Tissue debris of roots and plants, as well as dendritic Fe–Mn features, are present.

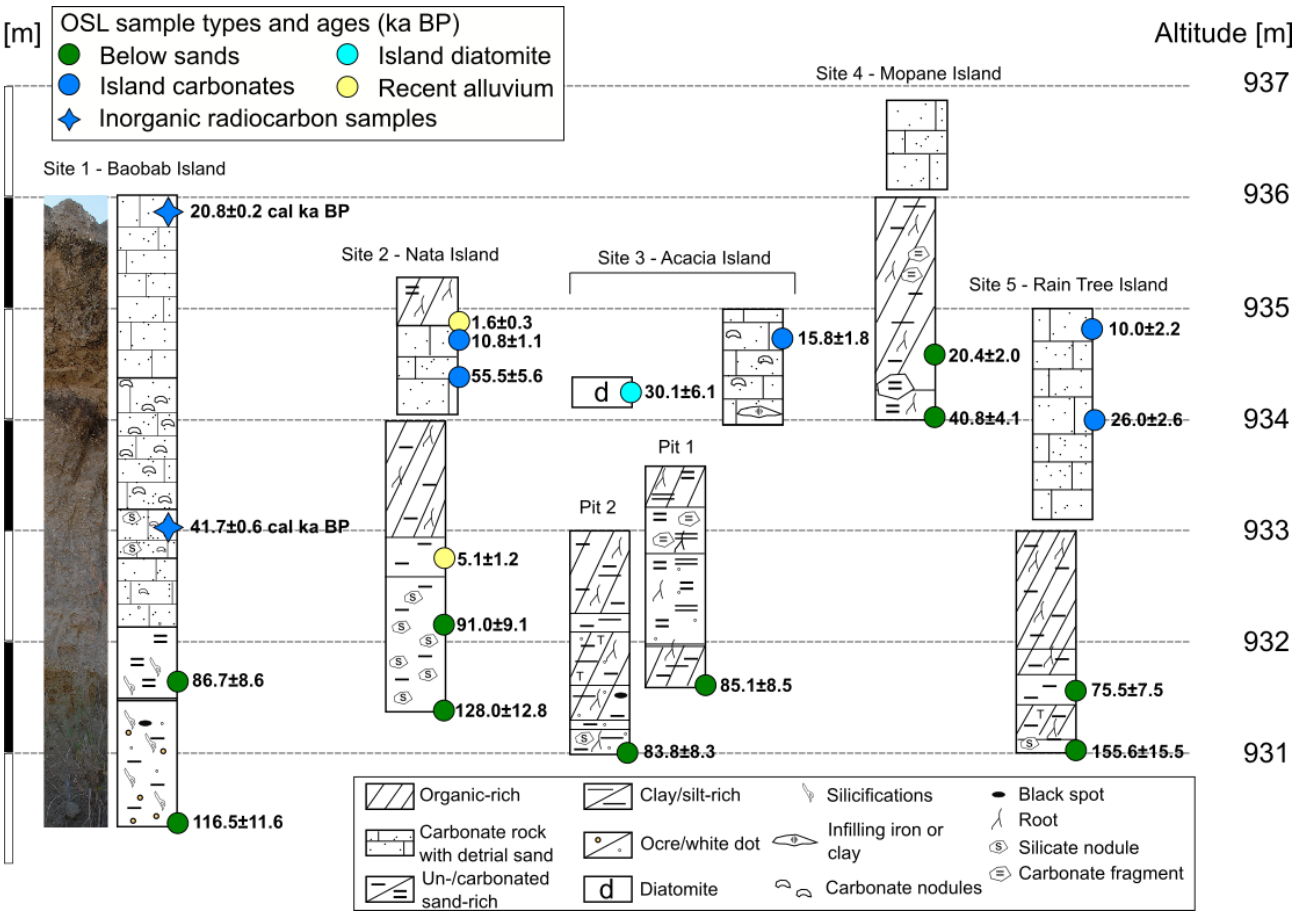

Figure 2.7: Descriptions of the pits and/or soil profiles in each site represented in Figs. 6.3 and 6.4b, with OSL (circles) and radiocarbon (four-branches stars) ages of the different key sedimentary layers.

Thin section observations of carbonate rock samples suggest that the carbonate precipitation occurred in palustrine environments. A petrographic study showed that the quartz

deposition in the palustrine environment would have been contemporaneous to the carbonate precipitation (Diaz et al. 2019). Consequently, to assess the timing of the carbonate island formation, optically stimulated luminescence dating (OSL) was used on quartz from key sedimentary layers (Fig. 2.5); (i) quartz from sandy layers situated below the carbonate islands (green circles in Fig. 2.5), (ii) quartz from sands trapped within the carbonate rock composing the island carbonate beds (blue circles), and (iii) quartz from sandy layers situated above the island carbonate beds (yellow circles). At Baobab Island, the ages of the carbonate rocks were determined using radiocarbon dating on the inorganic carbon fraction (four-branches blue stars). Finally, quartz extracted from the diatomite described at Acacia Island have been used for OSL dating (light blue circle). It can be hypothesized that OSL and radiocarbon ages from the key sedimentary layers may give an indication of the ages of the respective phases (i) the pre-palustrine carbonate, (ii) the palustrine carbonate, and (iii) the post-palustrine carbonate formations, respectively (Fig. 2.7).

Resulting ages show that the pre-palustrine carbonate formation phase would have occurred before 75 ka BP (before MIS 4). There are two younger samples from site 2 that deposited during MIS 2 (20.4 ka BP) and MIS 3 (40.8 ka BP). Were they already deposited during a different phase? The difference between the carbonate island and the top of the sand pit was only 0.5 m instead of 2 m for the other sites. Could this suggest that erosion was less intense in site 4? And that we are measuring alluvium sands possibly deposited during the palustrine carbonate formation phase? Indeed, the palustrine carbonate formation phase could have spanned from 55.5 to 10.0 ka BP (MIS 3 and MIS 2). Interestingly, quartz trapped in the diatomite are also from this phase (30.1 ka BP). It seems that the chemistry of waterbodies was not homogeneous. Finally, the post-palustrine carbonate phase would have occurred after 10 ka BP (MIS 1; Fig. 2.7, Diaz et al. 2019). Thus, it seems that, while lakes were forming in the Makgadikgadi Basin, palustrine environments were developing in the Chobe Enclave (Fig. 2.8). There are still questions pending regarding the origin of waters, e.g., were these palustrine areas forming before the onset of the activity of the Linyanti fault, allowing waters from the Linyanti to enter directly in the Chobe? Bäumle and Himmelsbach's (2018) work on the Linyanti aquifer proposes that palaeo-lakes along the Linyanti could have formed at the beginning of the extension of the graben system occurring during the Early and Middle Pleistocene, contemporaneously to Palaeo-Lake Makgadikgadi. The continuous development of the graben system during the Late Pleistocene led to the present-day Linyanti swamps. Consequently, the Chobe islands seem to be contemporaneous to the development of the graben system, cutting off more and more the inflow from the Linyanti through time, until a tipping point after which only occasional inflows prevailed, such as today (Fig. 2.8). Moreover, it seems that the water inflow

would have been at least sufficient to sustain a palustrine environment and the formation of carbonate until 10 ka BP. After that, the carbonate-rich palustrine system dried out and started to be differentially eroded and solely recent alluvial sands were deposited (MIS 1; Fig. 2.8).

2.3 Geomorphology and Landforms of the Northern Chobe Enclave District

2.3.1 Importance of Hydrology in Shaping Geomorphological Features

The fault systems of the Linyanti and the Chobe control the hydrological settings in the study area. These settings are the main factors controlling the landforms in the enclave. Due to the uplifts linked to the faults, the general topographic slope in the Chobe Basin is <0.02 % on average over long distances. The slope is decreasing from SW to NE, as well as from NW to SE. It increases again close to the Chobe strike-slip fault. This slope configuration induces the development of anastomosed river systems that are completely dry in the western part and become ephemeral to continuous going to the east. This hydrological gradient from W to E induces landforms associated with different morphodynamic processes found in three typical areas (Fig. 2.4) as described below: the western palaeo-floodplain, the island area, and the eastern floodplain area.

2.3.2 The Western Palaeo-Floodplain

The southwestern part of the northern Chobe Enclave district is characterized by an inherited floodplain composed by old fluvial sediments reworked by aeolian processes (Fig. 2.3). Numerous palaeo-channels are observable, having flow directions to the E in the northeastern part and to the SSW in the southwestern part. A soil and vegetation study of the area (Romanens et al. 2019 showed that there is a sodium-rich layer at the soil surface or under a layer of reworked aeolian sands and between the palaeo-channels. Such a formation is probably inherited but its extent under the whole palaeo-floodplain remains unclear. Its origin can be attributed to a palaeo-hydrological system similar to what is observed today in the Okavango Delta. A detailed geomorphological map (Fig. 2.4a) shows the Linyanti swamps, and the inherited floodplain delimited by the Linyanti fault (Fig. 2.5b). The palaeo-channel configurations at this boundary suggest an older connection with the Linyanti river.

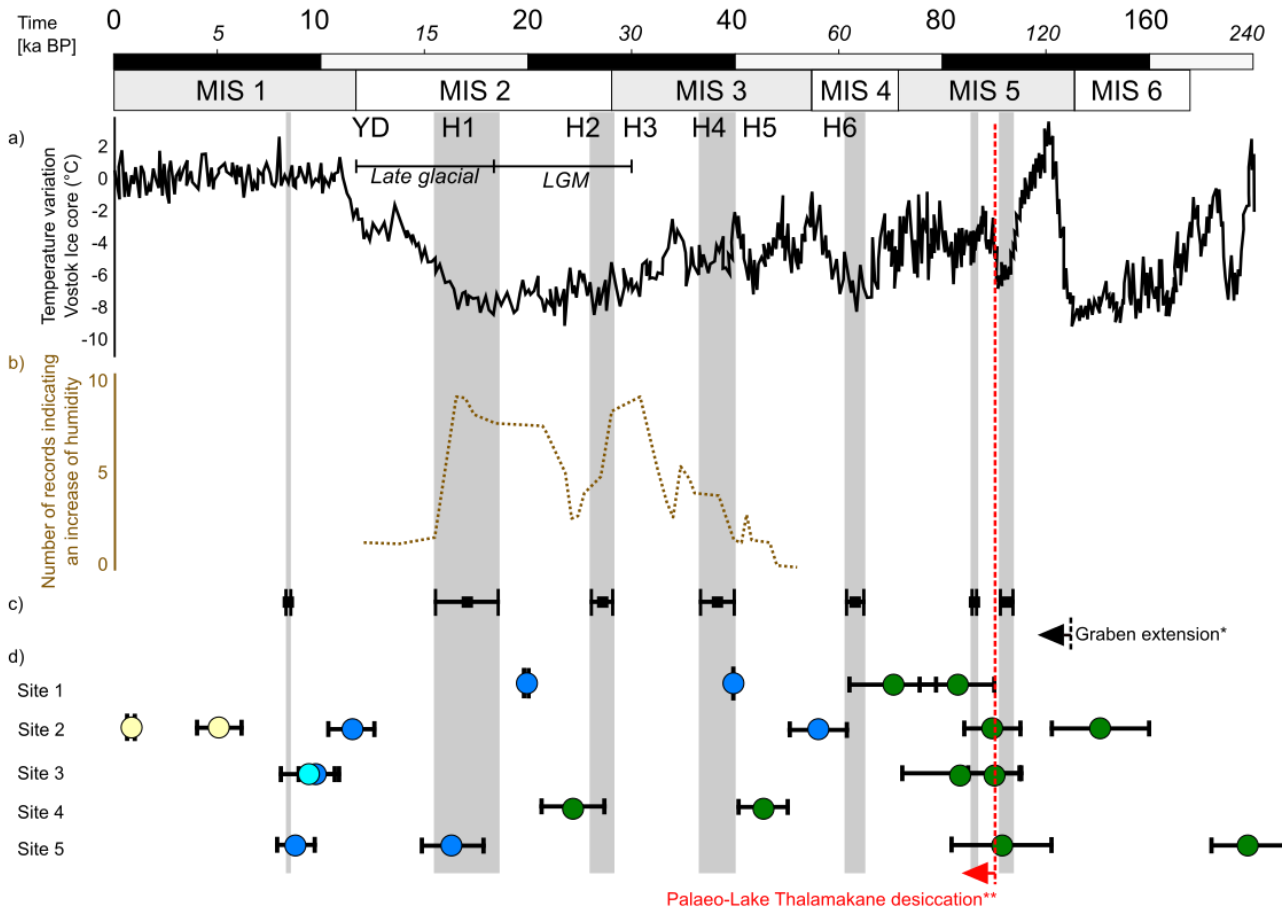

*Figure 2.8: Comparison of the carbonate island ages (circles and four-branches stars) with other types of archives. a) Temperature variations assessed from 2H in the Vostok Ice Core (Petit et al. 1999); data are available online (https://cdiac.ess-dive.lbl.gov/ftp/trends/temp/vostok/vostok.1999.temp.dat); b) Numerous records in the Kalahari area are interpreted as an increase in humidity (Chase and Meadows 2007); the grey bars refer to lake highstands of the Mega lake Makgadikgadi (Burrough and Thomas 2008). *Graben extension in the Linyanti fault area (Bäumle and Himmelsbach 2018), **Thamalakane fault activation inducing the formation of the Okavango Delta and the desiccation of the Palaeo-Lake Thamalakane (Moore et al. 2012).*

2.3.3 The Island Area

Lying between the palaeo-floodplain in the west and the floodplain in the east, the landscape of the island area (Figs. 2.3 and 2.5d– g) is dominated by the presence of islands the size of several hundred squared meters and a height of a few meters. Ephemeral river channels occasionally surround them and, when the water input is sufficient, small pans form (Fig. 2.4b). Sedimentary rocks of different natures form the islands, i.e., carbonate rocks, diatomite, sepiolite layers, amorphous silica-rich sands, and quartz sands (see above). Some of the islands have been

documented (Diaz et al. 2019) but the composition of other islands can only be suggested (dashed lines in Fig. 2.4b) based on field observations; finally, some have an unknown composition (marked with "?" in Fig.2.4b). The succession of islands and channels forms an undulating landscape, which attenuates and finally disappears completely to the west (black dashed line in Fig. 2.3). In the east, a NNE-SSW sand ridge, around 20 km long and 2 km large, marks the limit with the eastern floodplain (Fig. 2.5c). It is composed by fluvial sands undergoing erosion due to sheet wash and forming triangular morphologies along their western side. On the eastern side, the sand ridge has a straight border possibly associated to an NNW-SSE transferal fault. The sand ridge is split into two halves by a river coming from the eastern floodplain, forming a water gap (Fig. 2.4b).

2.3.4 The Eastern Floodplain Area

In the eastern floodplain, smaller sand ridges, having the same characteristics as the one presented above, are present. These ridges are also crosscut by rivers forming sand patches that might have been attached to the ridges before (Fig. 2.4c). The number of ephemeral streams is increasing, and their anastomosed nature creates numerous oxbows. The water can accumulate in multiple pans, which can be connected. Further to the east of the sand ridges, permanent rivers are flowing from Lake Liambezi (from WNW to ESE) and from the Chobe River backflow (from NNE to SSW; Fig. 2.5a, h). Large swamps are forming around their confluence and sand ridges counter the extent of these swamps in the west (Fig. 2.3). Finally, two different landscapes are found at the borders of the area. In the north, the Linyanti swamps form around the Linyanti river, flowing along the fault from the Linyanti delta, towards Lake Liambezi. In the south along the Chobe fault, the slope increases abruptly (about 60 m) as illustrated by the elevation profile (Fig. 2.3). At the top of the slope, red sands, a color resulting from aluminumand iron-rich coatings around quartz grains, are covering the landscape and are likely inherited from past pedogenic weathering. At the foot of the Chobe fault towards the study area, colluvial fans are forming in contact with the alluvial sediments deposited by the Chobe River (Fig. 2.3).

2.3.5 The Complexity of the Chobe's Geomorphology

The geomorphology of the drier Linyanti-Chobe basin is thus complex. A relative chronology of events can be proposed, as also supported by the regional Quaternary chronology (see above): first, red sands formed on a palaeo-surface, observed today at the top of the Chobe fault. They can

be considered as paleosols, possibly very old and inherited from a period before the Chobe fault activation by the extension of the graben system (Pliocene? Before megalakes?). The Chobe extension started and led to possible water accumulation along the Chobe fault. While the graben system was still active, the Linyanti fault formed. This event led to palustrine-lacustrine-fluvial environments from which the palaeo-floodplain and the island landforms are inherited. According to OSL dating, carbonate deposition occurred from 55 to 10 ka BP, contemporaneous to Palaeo-Lake Thalamakane retraction in the SSW. Tectonic events might have affected the drainage, inducing drier conditions through time, cutting off the Upper Zambezi and the Linyanti inputs. From 10 to 5 ka BP, the Linyanti inputs should have been stopped, due to continuous lifting, leading to the fossilization of the palaeo floodplain and carbonate rich palustrine environments. Since this time, relief inversion could have occurred with the preferential erosion of sands around the carbonate-rich formations that are observed today as elevated carbonate islands (Diaz et al. 2019).

2.4 Landscape Components of the Chobe Enclave

2.4.1 Water in the Linyanti-Chobe Region

Both surface and groundwaters of the study region can be compared to the Okavango and the Zambezi (Dyer 2017). While the Okavango Delta hydrology has been particularly well studied over the last few decades (e.g., McCarthy et al. 1991; McCarthy and Ellery 1998; McCarthy et al. 1998; 2000; McCarthy 2006; Atekwana et al. 2016; Akondi et al. 2019), the Kwando and Zambezi rivers, which may also be of importance to the Chobe region, have been less studied so far (Tooth et al. this book). By analogy to the previous studies in the region (McCarthy, 2006; Atekwana et al. 2016; Akondi et al. 2019), the surface waters of the region can be classified as calcium-magnesium-(sodium)-bicarbonate type waters for the major rivers (Okavango, Kwando/ Linyanti, and Zambezi; Fig. 2.9). The Okavango waters, however, have a larger proportion of potassium, whereas the Zambezi waters have a higher electrical conductivity. While the dissolved elemental proportions in the groundwaters do not change markedly relative to the surface waters, they have a higher overall conductivity (ion concentrations and total dissolved ions) compared to the large river entries. Consequently, a more marked change is noted for the Makgadikgadi pan surface waters and extremely evaporated terminal swamp waters of the Linyanti/Chobe as these become sodium-(potassium)- chloride type waters with locally also important sulfate concentrations, notably in the Linyanti/Chobe area. These highly evaporated terminal waters also reach calcite and/or anhydrite saturation (Dyer 2017; Atekwana et al. 2016). Zambezi river waters have a higher Ca/Mg compared

to the Okavango River waters, which may indicate geologically slightly different catchments. As the pH of the Zambezi River is about 7.5, while that of the Okavango is about 6.9, this could indicate the presence of carbonate-bearing rocks in the Zambezi basin. The Okavango waters, in contrast, are more concentrated in sodium and potassium compared to the Zambezi River, suggesting that sodium and potassium as well as Ca are likely derived from silicate (feldspar) weathering. These trends in the major ion compositions are clearly represented in a modified Gibbs diagram (Fig. 2.9).

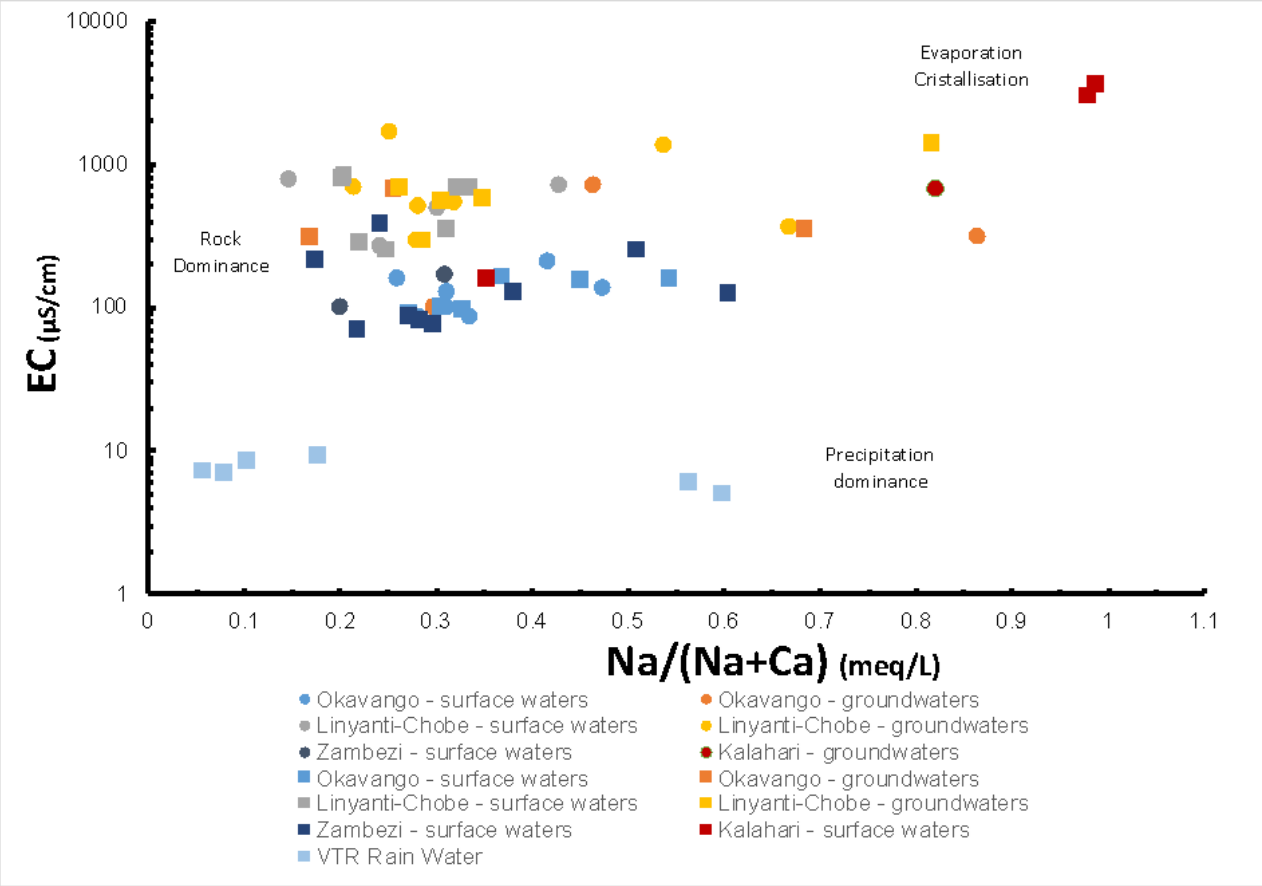

Figure 2.9: Modified Gibbs diagram illustrating the changes in Na and Ca concentrations as a function of source terrain, evaporation-crystallization processes in the studied region.

2.4.2 Vegetation and Soils

Eight plant communities can be distinguished in the Chobe Enclave (Vittoz et al. 2020): three grassland units, three woodland units, and two forest units (Fig. 2.10; Table 2.2). Their spatial distribution depends on the fine microtopography of the northern Chobe region. Based on the vegetation map (Fig. 2.11) and the geomorphology, the study area can be divided into four areas: (1) the floodplains along the Linyanti river, characterized by a gradient of flood duration and

frequency; (2) a mosaic of Combretum woodlands and dambo grasslands in the island area, with contrasted topography positions and substrates; (3) a mosaic of mopane woodlands and sandveld in the western palaeo-floodplain, similarly related to topography; (4) and the Baikiaea forests on red sands, located on the eastern side of the Chobe Fault, extending to the Chobe Forest Reserve. In a parallel study, five soil types were recognized in the study region (Romanens et al. 2019). The following soil types were found (Figs. 2.12 and 2.13), named according to the WRB (IUSS Working Group WRB, 2014):

- Arenosols are largely dominated by sand along the whole profile, generally poor in nutrients and organic matter (Skarpe et al. 2014).
- Kastanozems are characterized by a dark, organic topsoil, saturated with bases, and by a calcium-rich horizon.
- Chernozems and Phaeozems have a high organic content in most of their profile, with a black topsoil horizon; compared to Phaeozems, the Chernozems are characterized by a calcium-rich horizon.
- Solonchaks and Solonetz are characterized by a salt- or sodium-rich horizon in their profile, the second being richer in clays.
- Calcisols contain calcium-rich horizons but compared to Kastanozems, are not particularly rich in organic carbon.

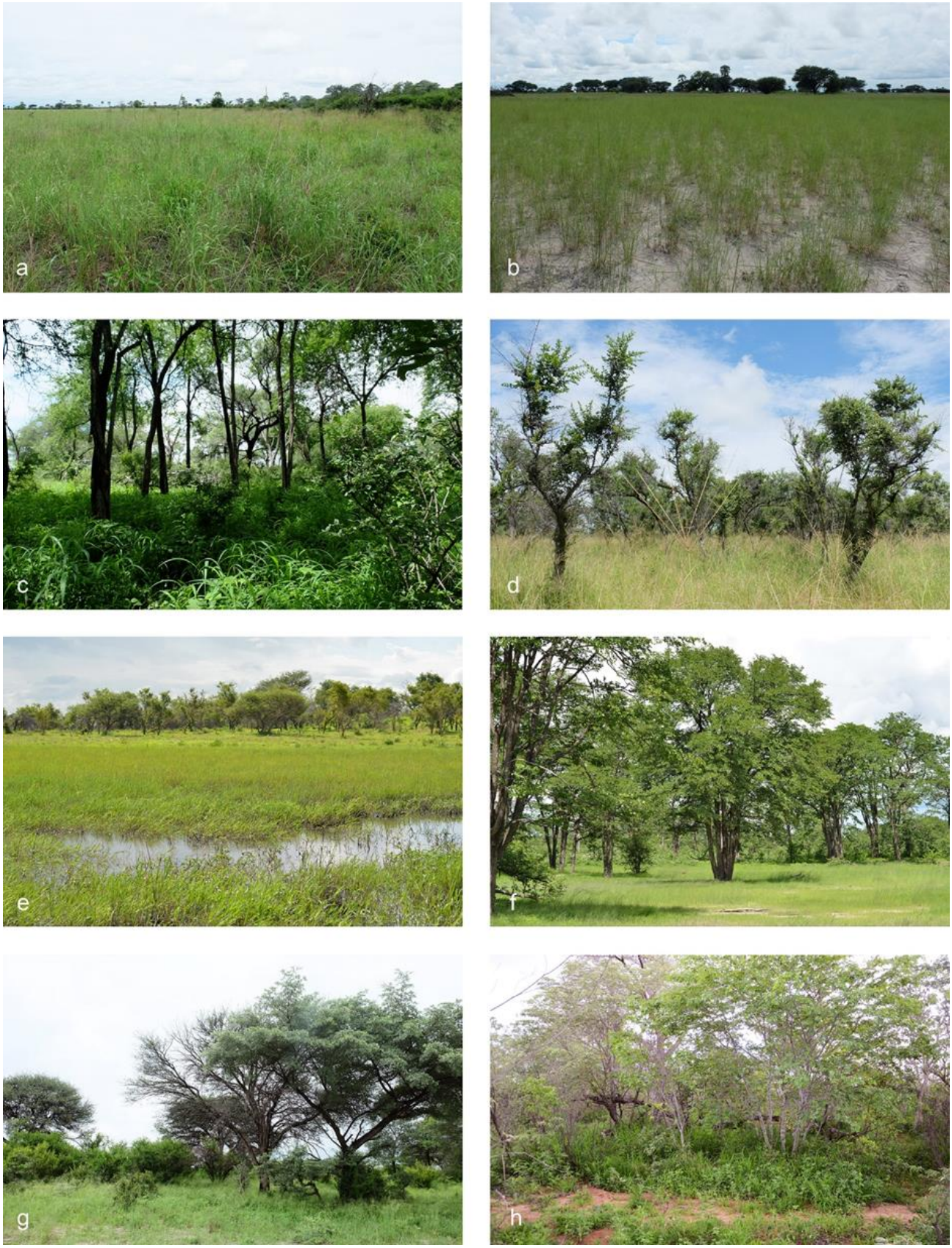

Figure 2.10: Illustrations of the vegetation units. a) Wet floodplain; b) Dry floodplain grassland; c) Riverine forest; d) Combretum woodland; e) Dambo grassland; f) Mopane woodland; g) Sandveld; h) Baikiaea forest (Photos: F. Pellacani, a, b, c, d, g; P. Vittoz, e, f, h).

Table 2.2: Scientific names used in Vittoz et al. (in press) for the different plant communities.

Vegetation unit	*Scientific name (Vittoz et al. 2020)*
Dry floodplain grassland	*Aristida junciformis–Aristida meridionalis* Grassland
Riverine forest	*Croton megalobotrys–Setaria verticillata* Forest
Combretum woodland	*Eragrostis superba–Combretum hereroense* Woodland
Dambo grassland	*Geigeria schinzii–Setaria sphacelata* Grassland
Mopane woodland	*Colophospermum mopane–Jasminum stenolobum* Woodland
Sandveld	*Ipomoea chloroneura–Oxygonum alatum* Woodland
Baikiaea forest	*Baikiaea plurijuga–Baphia massaiensis* Forest

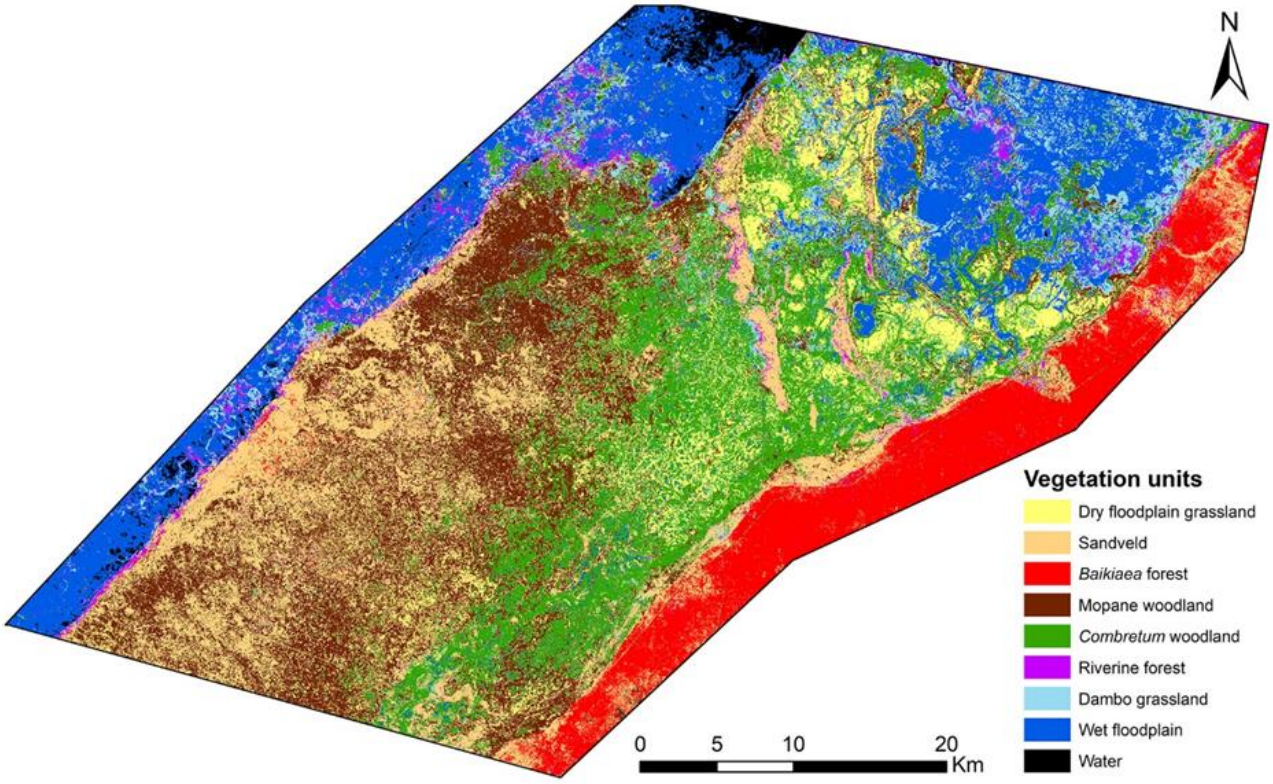

Figure 2.11: Vegetation map of the Chobe Enclave, with vegetation unit groups according to landscape areas. The Linyanti River is delineated by the dark blue line.

2.4.3 Floodplains

The wettest parts of the floodplains were not considered in detail. However, a high diversity of plant communities is expected, close to the one observed in the Okavango Delta (Sianga and Fynn

2017). These plant communities are related to the water depth in permanently flooded areas (Ellery and Ellery this book) and the importance and recurrence of flood events by the Linyanti river in the seasonal swamps (Murray-Hudson et al. 2011; Pricope 2013). The dry floodplain grasslands are present on higher topographic positions, which are flooded at a low frequency, possibly not each year or not at all, but are still under the seasonal influence of a high-water table. This plant community has a low cover of grasses (~40 %), established on former alluvial deposits, with a very high sand proportion (~98 %; soils classified as Arenosols) related to a very low Cation Exchange Capacity (CEC). The dominant species are the grasses *Aristida meridionalis*, *A. junciformis*, and *Hyperthelia dissoluta*, and the forbs *Dicerocaryum eriocarpum* and *Meeremia tridentata* are some of the typical species encountered. These dry floodplain grasslands are characterized by numerous termite mounds (Mujinya et al. 2010, 2014), often occupied by trees (McCarthy 1998; McCarthy et al. 1998), some of them found almost exclusively in such situations (e.g., Phoenix reclinata, Imperata cylindrica; Roodt 1998). Riverine forests form a species-rich community, encountered as small fragments on prominences in or along the floodplain of the Linyanti river. It has the highest mean tree cover (~50 %) and the tallest trees (~8.5 m) of all vegetation units, their density and size related to their possibility to reach a permanent water table with their roots. The alkaline soils (Kastanozems) are dominated by sand but with 15–33% of silt, probably due to the high density of termite mounds. *Berchemia discolor*, *Vachellia tortilis, Croton megalobotrys, Combretum mossambicense*, and *Dichrostachys cinerea* are some of the typical trees and shrubs, often climbed by *Capparis tomentosa. Kigelia africana, Terminalia prunioides,* and *Ficus thonningii* are less frequent woody species but encountered only in riverine forests. Some typical species in the understory are the grasses *Setaria verticillata, Panicum maximum*, and *Urochloa trichopus* and the forbs *Ipomoea dichroa*, *Acalypha fimbriata, Justicia heterocarpa, Achyranthes aspera, Dicliptera paniculata, Commelina petersii, Cyathula orthacantha,* and *Leonotis nepetifolia*.

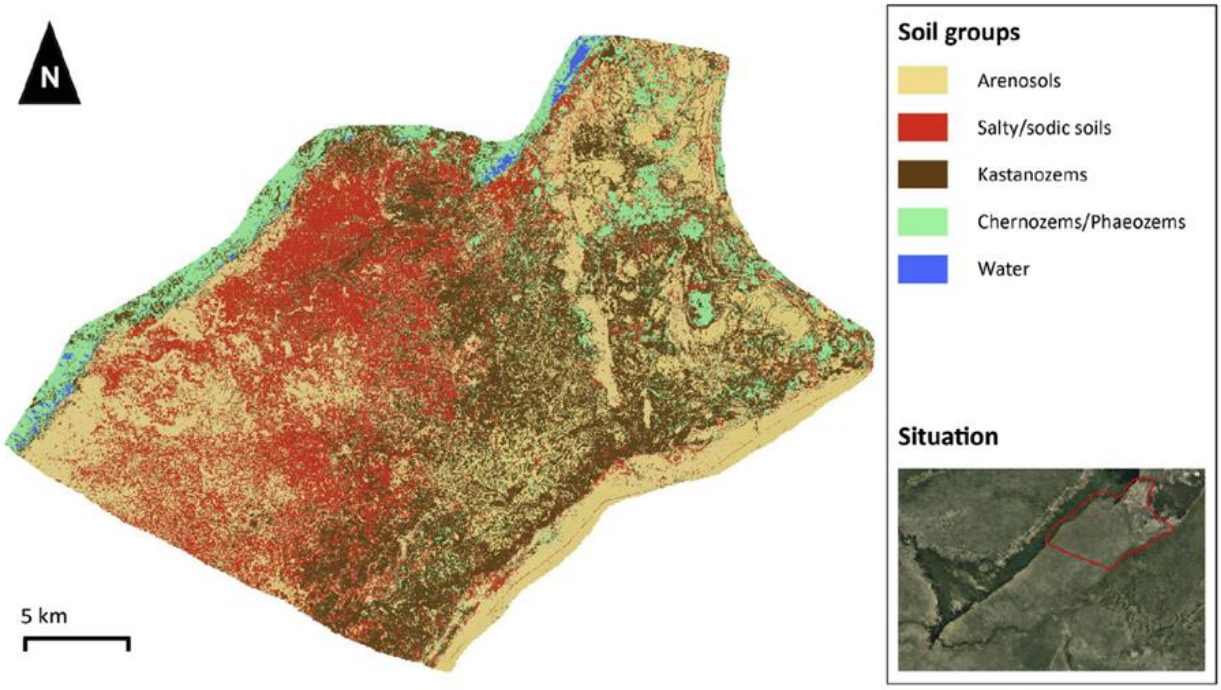

Figure 2.12: Soil map of the northeastern part of the Chobe Enclave. This map was produced by conducting parallel soil (Romanens et al. 2019) and vegetation studies (Vittoz et al. 2020) and the soil map was partly based on the vegetation map.

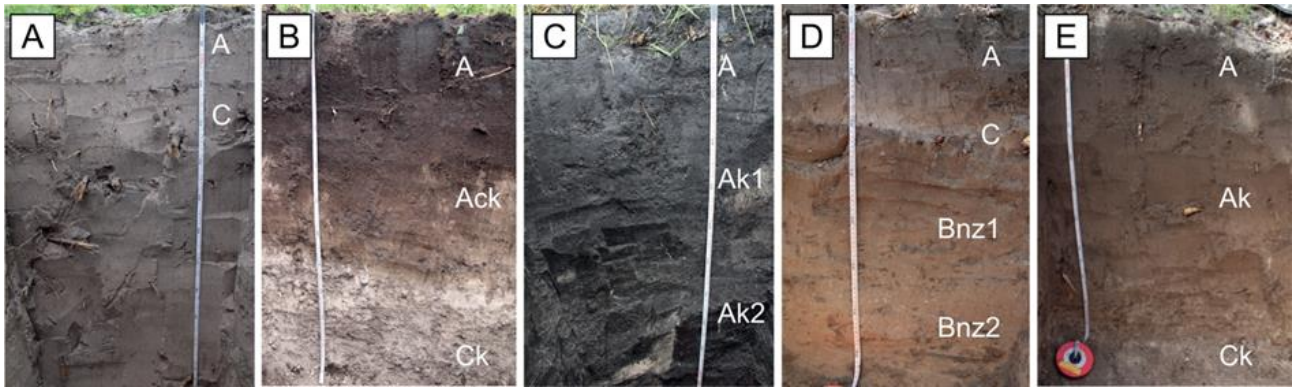

Figure 2.13: Examples of soils found in the Chobe Enclave. a) Arenosol: soil of floodplains and wind-reworked areas. b) Kastanozem: soil found on sandy areas and diatomitic/carbonate islands. c) Chernozem: soil of the humid depressions (dambos) with some hydromorphic properties. d) Solonetz: soil often developed under Mopane woodlands. e) Calcisol: soil easily formed on carbonate islands. Letters on pictures refer to the nomenclature of horizons (for more details, see IUSS Working Group WRB 2014 and Romanens et al. 2019).

2.4.4 Islands

Two plant communities are distributed in this area according to the topography. The Combretum woodlands is found on small islands underlain by carbonate beds. The soils (Kastanozems) are characterized by the highest clay content of the study area (14–20 %) that favors a high CEC dominated by calcium, promoting an alkaline pH (7.8– 8.8). The typical trees are *Combretum hereroense*, *Sclerocarya birrea subsp. caffra*, *Senegalia nigrescens*, and *Vachellia hebeclada.* The grasses *Eragrostis superba*, *Heteropogon contortus, Digitaria eriantha*, and *Cenchrus ciliaris*, and the forbs *Rhynchosia minima, Hoslundia opposita* and *Hibiscus caesius*, and *Solanum panduriforme* are frequently encountered.

The dambo grasslands are found in pans. This community occupies shallow, depressions that are waterlogged during the wet season (Acres et al. 1985). Without a river draining them, fine mineral materials tend to accumulate, and the waterlogging restrains organic matter mineralization. Hence, the soils (Chernozems or Phaeozems) show the lowest sand content (19–29%) but the highest silt (59–68%) and organic carbon (3–5%) contents of all the plant communities in the Chobe Enclave. The high CEC is dominated by calcium, resulting in a neutral to alkaline soil pH. Grasses largely dominate the community, with *Setaria sphacelata, Digitaria milanjiana, Hyparrhenia rufa, Bothriochloa bladhii, Cymbopogon caesius, Panicum repens*, and *Trachypogon spicatus* as frequent or dominant species.

2.4.5 Western Palaeo-Floodplain

The western palaeo-floodplain is similarly characterized by a mosaic of two vegetation units according to topography. The area is a fossil delta with islands separated by channels inherited from ancient hydrological dynamics, before being separated from the Linyanti river by tectonic activity (Kinabo et al. 2008; Fynn et al. 2014).

The islands are occupied by the mopane woodlands. Some areas are characterized by tall *Colophospermum mopane* trees, while in other places the species is limited to stunted specimens, with a low tree cover. It seems that these sizes are related to different soil conditions: stunted mopanes grow on silty soils characterized by a high CEC, saturated by sodium, and with high alkaline pH (9.5–10), classified as Solonchaks. In contrast, tall trees occupy soils with a sandy upper horizon, with moderate alkaline pH (7.0– 8.2), but with the presence of a sodic horizon below 30 cm (Solonetz or other soil types, like Calcisols, with a salic horizons). These high sodium concentrations suggest that these areas have an origin comparable to the present islands in the Okavango Delta (Ramberg and Wolski 2008; McCarthy et al. 2012). Besides mopane, the typical species are the grasses

Schmidtia pappophoroides, Aristida adscensionis, and *Digitaria eriantha*; the sedge *Kyllinga buchananii*; and the forbs *Ipomoea coptica* and *Chamaecrista absus*.

The palaeo-channels are filled with leached, river-washed sands (Arenosols) and occupied by sandvelds. Compared to dry floodplain grasslands, this plant community has a higher topographic position, with a complete absence of visible water table during the wet season. Tree and shrub layers are characterized by the presence or dominance of *Senegalia cinerea*, *Terminalia sericea, Grewia retinervis,* and *Dicrostachys cinerea*, and the herb layer by the grasses *Panicum maximum*, *Urochloa trichopus*, and *Digitaria eriantha*, and the forbs *Acanthosicyos naudinianus, Spermacoce senensis, Indigofera flavicans, Gisekia africana, Cleome hirta*, and *Pavonia senegalensis.*

2.4.6 Baikiaea Forest

Southeast of the Chobe Fault, the *Baikiaea* forests have a dense woody stratum. This vegetation unit, which covers a large area in Chobe National Park (*Baikiaea plurijuga– Combretum apiculatum* woodland) according to Skarpe et al. (2014), grows on thick, reddish Kalahari sands. The soils are classified as Arenosols and their red color is due to an iron and aluminum-rich oxyhydroxide coating, which is responsible for acidic conditions (pH 5.7–6.0). This area is completely disconnected from the rivers and the plants have to rely only on rainwater. Trees and shrubs show high diversity, the most frequent species being *Combretum elaeagnoides, Baikiaea plurijuga, Baphia massaiensis, Croton gratissimus,* and *Bauhinia petersiana*. The grasses *Dactyloctenium giganteum, Panicum maximum, Urochloa trichopus*, and *Digitaria eriantha*, and the forbs *Jacquemontia tamnifolia, Ipomoea pes-tigridis, Vigna unguiculata, Chamaecrista absus*, and *Harpagophytum zeyheri* are constant or locally important species.

2.4.7 The Role of Termites

The most notable species of termites encountered in the northern Chobe Enclave district are the fungus-growing termites (FGT) (subfamily Macrotermitinae, Isoptera). They are important for two reasons: (i) their large iconus epigeal mounds can be seen from afar and (ii) their ability to modify the distribution of sediments and soils in order to build their nest (Jouquet and Lepage 2002; Mujinya et al. 2011). Fungus-growing termites are a subfamily composed of 12 genera and 345 species. One of these genera, *Odontotermes* (142 species) present in this region, tends to build cryptic subterranean fungus-chambers 20–50 cm below ground. An important species found in the

area is the *Trinervitermes trinervoides*, also commonly known as snouted harverster termite for the protruding portion of their face. These are non fungus-growing termites and do not build large fungus-chamber but only small scattered domed mound of only a few centimeters high. The most common species observed in the study area is *Macrotermes michaelseni*, a FGT species part of the *Macrotermes* genus (65 species). It has long been considered as an ecosystem engineer (Jones 1990) for the modifications it brings to the soil, its ability to concentrate nutrients, and its capacity to create patches of fertile land in tropical and subtropical savanna ecosystems (Jouquet and Tavernier 2005; Corenblit et al. 2016).

Figure 2.14: a) Young active termite mound of the Macrotermes michaelseni species, situated on a diatomaceous soil in an open grassland on the eastern side of the Chobe Enclave. b) A non-re-colonized relic termite mound of the Macrotermes michaelseni species. Its size is impressive.

2.4.8 The Potential Impact of Termites in Savanna Ecosystems of the Chobe Enclave

Fungus-growing termites have shared an exosymbiosis since 30 Ma (Roberts et al. 2016) with a fungi belonging to the *Termitomyces* genus. In order to maintain the symbiosis, *Macrotermitinae* must maintain specific hydric and thermic conditions in their nests. Therefore, fungus-growing termites build large biogenic structures in which they are able to increase the alkalinity of soils by an order of magnitude of 3–4. They also increase their carbonate content, the C/N ratio, and concentrate nutrients such as potassium and phosphorus. FGT modify the chemical compositions and mineralogical propreties of clays through the process of selection and transportation of sand grains in their buccal cavity, where they are mixed with saliva (Jouquet et al. 2011). They also act as accelerating agents of clay alteration and chemical weathering in tropical ecosystems. The activities of FGT tend to slightly raise the land surface locally, providing some recolonization advantages. They form a pattern of fertile lands by concentrating nutrients and enhance the growth of vegetation by creating islands of fertility (see above; Dangerfield et al. 1998). The selection of very fine sands, in order to meet the construction requirement for their mounds, create patches of clayey sands that have the property to retain water for long periods of time, producing scattered pockets of water in semiarid regions such as the Chobe-Linyanti region (Pennisi et al. 2015).

Different stages of FGT mounds can be observed in the northern Chobe Enclave district (i) active termite mounds (Fig. 2.14a), generally between 50 cm and a few meters high; they are homogenous and hard consolidated forms; (ii) mounds that have been recently abandoned by the termite colony, due to a predator or a natural hazard; their shape appears as similar to a flattened promontoir with broken pieces laying on the adjacent ground; they can be recolonized by the same species of termites; (iii) relic termite mounds (Fig. 2.14b); these mounds have seen many stages of occupation over a relatively long period of time, from a few dozen years up to hundreds of years and their size can reach 18 m in diameter and be 7 m high. These relic mounds can probably be considered as geomorphological objects by their size, their impact on the environment, and their role in the ecosystem. They are distinctive features in the landscape of which many animals take advantage, such as snakes, monkeys, leopards, lions, elephants, as well as plants (including trees).

Like in many parts of Africa, people from the study region are using mounds for different purposes, e.g., soil amendment, geophagy (Mills 2008), or building material. Their volume is considerable: a single mound in the Chobe had an above ground volume of 1,350 m^3. They also can remain for long periods of time: FGT relic mound ages have been estimated by optically stimulated luminescence (Kristensen et al. 2015) to be 4,000 yrs old in Ghana and to be 2,200 yrs old using 14C in Congo (Erens et al. 2015).

2.4.9 Hydric Gradients Influencing FGT Activities

In regard to termite activities, two gradients are observed in the Chobe Enclave: (i) an EW gradient assigned to the topographic flooding pattern and (ii) a NS gradient attributed to the distance to the Linyanti river in the north. Distribution of *Macrotermes* mounds in the landscape represent these gradients fairly well. In the eastern part of the enclave, large active mounds, similar to the one encountered in the center of the Okavango Delta today, dominate the topography. Moving further west, these big mounds become less common and after a short distance toward the center of the enclave, they totally disappear. In reference to the NS gradient, within the riverine woodland of the Linyanti river, all mound stages are observed (active, abandoned, or relic). Moving south, the active termite mounds are rarer, most of them being abandoned; finally, in the middle part of the enclave, there are no active *Macrotermes* mounds.

2.4.10 Termites Influence the Evolution of the Landscape

Regarding the formation of islands, Dangerfield et al. (1998) were the first to describe the role of FGT in the context of the Okavango Delta. A similar process may have existed for most of the northern Chobe Enclave's past. FGT are probably still involved in the geomorphological shaping of the region through this specific island formation process found in its eastern part. The sediment composition of the islands being an important factor, a recent study quantified the way in which FGT modify local soil grain-size distributions to make the building material for their nest (Van Thuyne et al. 2021). When built on a coarse sand soil, FGT tend to moderately increase the upper part with finer material and tend to increase substantially the lower part in finer material, whereas, when built on a silt soil, the opposite is observed. Once abandoned and destroyed by erosion, the altered soil material consequently modifies the grainsize distribution of the local sediments. The above-mentioned modifications brought by FGT have considerable importance and impact on this semiarid region. For example, the soil pH is often low and the soil remains deficient in many nutritive elements: the mounds are able to provide better soil conditions with a more alkaline pH and a higher nutritive content. The mounds have also the capacity to retain water for long period of time, (i) favoring a de-aridification process (Pennisi et al. 2015), (ii) offering a fire protection in these savanna-prone fire zones, and (iii) contributing to higher stability and resilience of the ecosystem (Pringle et al. 2010).

2.5 Challenges and Conclusions

The northern Chobe Enclave district constitutes a fascinating location in order to understand the complex relationships between the development of landforms in a high African plateau under the influence of trans-tensional pull-apart basins and the various external agents at work during the Quaternary. At the crossroads of various rivers and influenced by neotectonics, large parts of the landscape are not yet explained: issues such as (i) how did the syntectonic depocenters evolve through the Quaternary? Or (ii) what are the ages of the various faults and water gaps affecting the region? The presence of large palustrine carbonate deposits is not totally explained: how were such deposits possible in the past? And what would have been the environmental conditions that enabled such calcium carbonate accumulations in an essentially siliceous basin? In addition, if the source of carbon can easily be identified (CO_2 and organic matter), where is the source of calcium?

This chapter presented a limited state of the art of the science conducted in the area. The present-day composition of the various water bodies cannot totally explain the diversity of the geochemical nature of the sediments. Nevertheless, it seems likely that the large presence of sodium in soils and sediments could be related to some water bodies, associated with efficient evaporation processes. The vegetation is perfectly adapted to the landscape constraints. Another important point is the role of termites: they redistribute the particle sizes of sediments at the surface of the geomorphological features and partly shape the landscape. Today, the main exogenous parameters affecting the landscape seem to be wind, water balance (rain and the prominent role of rivers and floodplains), as well as the biological impact of the living realm. But the conditions prevailing today were probably different during the past, making the reconstruction of the landscape history challenging.

Acknowledgements

The authors would like to thank Prof. Frank D. Eckardt for his confidence and his help in writing this Chapter, the Ministry of Environment, Natural Resources Conservation, and Tourism of the Republic of Botswana as well as the Chobe Enclave Conservation Trust for the research permits, without which these studies would not have been possible. L. Ballif, S. Dyer, F. Pellacani, and R. Romanens are thanked for providing documents and data. The authors would like to acknowledge all the staff from the Van Thuyne-Ridge Research Center in the Chobe Enclave for their support in the field and base camp. K. Verrecchia kindly edited the manuscript. Prof. Susan Ringrose and an anonymous reviewer kindly improved the first version of this Chapter. This research has been funded by the University of Lausanne (International Relations), the Herbette Foundation, and grants from the Swiss National Foundation nos P2LAP2_174595 to ND and 200021_172944 to EPV.

References

Acres BD, Rains AB, King RB, Lawton RM, Mitchell AJB, Rackham LJ (1985) African dambos: their distribution, characteristics and use. Zeitschrift fur Geomorphologie, 52, 62-83.

Akondi RN, Atekwana EA, Molwalefhe L (2019) Origin and chemical and isotopic evolution of dissolved inorganic carbon (DIC) in groundwater of the Okavango Delta, Botswana, Hydrological Sciences Journal, 64: 105-120.

Alvarez NA, Hogan JP (2013) The role of tectonic inheritance in the geometry and location of continental rifts-An example from the Okavango Rift Zone, Botswana. Geological Society of America Abstracts with Programs, 45, 7: 832.

Atekwana EA, Molwalefhe L, Kgaodi O, Cruse AM (2016) Effect of evapotranspiration on dissolved inorganic carbon and stable carbon isotopic evolution in rivers in semi-arid climates: The Okavango Delta in North West Botswana. Journal of Hydrology, 7: 1-13.

Bäumle R, Himmelsbach T (2018) Exploration of deep, previously unknown semi-fossil aquifers of the Kalahari Basin (southern Africa). Grundwasser 23: 29-45.

Bishop P (2007) Long-term landscape evolution: Linking tectonics and surface processes. Earth Surface Processes and Landforms, 32: 329–365.

Bordy EM, Segwabe T, Makuke B (2010) Sedimentology of the Upper Triassic-Lower Jurassic (?) Mosolotsane Formation (Karoo Supergroup), Kalahari Karoo Basin, Botswana, Journal of African Earth Sciences58: 127-140.

Bufford KM, Atekwana EA, Abdelsalam MG, Shemang E, Atekwana EA, Mickus K, Moidaki M, Modisi MP, Molwalefhe L (2012) Geometry and faults tectonic activity of the Okavango Rift Zone, Botswana: evidence from magnetotelluric and electrical resistivity tomography imaging. J. Afr. Earth Sci. 65: 61–71.

Burrough SL, Thomas DSG, Shaw PA, Bailey RM (2007) Multiphase Quaternary highstands at Lake Ngami, Kalahari, northern Botswana. Palaeogeography, Palaeoclimatology, Palaeoecology, 253, 3–4: 280–299.

Burrough SL, Thomas DSG (2008) Late Quaternary lake-level fluctuations in the Mababe depression: middle Kalahari palaeolakes and the role of Zambezi inflows. Quat. Res. 69: 388–403.

Burrough SL, Thomas DSG, Bailey M (2009) Mega-Lake in the Kalahari: a late Pleistocene record of the Palaeolake Makgadikgadi system. Quat. Res. 28: 1392–1411.

Burrough SL, Thomas DSG, Singarayer JS (2009) Late Quaternary hydrological dynamics in the Middle Kalahari: Forcing and feedbacks. Earth-Science Reviews, 96: 313-326.

Campbell G, Johnson S, Bakaya T, Kumer H, Nsatsi J (2006) Airborne geophysical mapping of aquifer water quality and structural controls in the Lower Okavango Delta, Botswana. South African Journal of Geology 109: 475–494.

Chase BM, Meadows ME (2007) Late Quaternary dynamics of southern Africa's winter rainfall zone. Earth-Science Reviews, 84: 103-138.

Clarke CE, Majodina TO, du Plessis A, Andreoli MAG (2016) The use of X-ray tomography in defining the spatial distribution of barite in the fluvially derived palaeosols of Vaalputs, Northern Cape Province, South Africa. Geoderma 267: 48–57.

Cook HJ (1980) Landform evolution in the context of climatic change and neo-tectonism in the Middle Kalahari of north-central Botswana. Transactions of the Institute of British Geographers 5: 80-99.

Cooke HJ (1975) The paleo-climatic significance of caves and adjacent landforms in western Ngamiland, Botswana. Geographical Journal 141: 430–444.

Cordova CE, Scott L, Chase BM, Chevalier M (2017) Late Pleistocene-Holocene vegetation and climate change in the Middle Kalahari, Lake Ngami, Botswana. Quaternary Science Reviews, 171: 199-215.

Corenblit D, Corbara B, Steiger J (2016) Biogeomorphic Ecosystems within Stressful and Disturbed Environments: A Focus on Termites and Pioneer Plants. In: Johnson EA, Martin YE (eds) A Biogeoscience Approach to Ecosystems. Cambridge University Press, Cambridge, pp 456–474

Cox RT (1994) Analysis of drainage-basin symmetry as a rapid technique to identify areas of possible Quaternary tilt-block tectonics: An example from the Mississippi Embayment. Geological Society of America Bulletin, 106: 571–581.

Crouvi O, Amit R, Enzel Y, Gillespie AR (2010) Active sand seas and the formation of desert loess. Quaternary Science Reviews 29: 2087- 2098.

Dangerfield JM, McCarthy TS, Ellery WN (1998) The mound-building termite Macrotermes michaelseni as an ecosystem engineer. Journal of Tropical Ecology, 14: 507-520.

Diaz N, Armitage SJ, Verrecchia EP, Herman F (2019) OSL dating of a carbonate island in the Chobe Enclave, NW Botswana. Quaternary Geochronology 49: 172-176.

Durand N, Monger HC, Canti MG, Verrecchia EP (2018) Calcium Carbonate Features - Chapter 9. In : Stoops G, Mees F, Marcelino V (eds) Interpretation of Micromorphological Features of Soils and Regoliths. 2nd Ed., Elsevier, Amsterdam: 205-258.

Dyer S (2017) Water cycle in the Northern Kalahari. Unpubl. Master of Science in Biogeosciences, Univ. of Lausanne..

Ellery WN, Ellery K (2020) The Okavango Delta as a peatland landscape. In: Eckardt FD (ed) Landscapes and landforms of Botswana. Springer, Berlin.

Erens H, Boudin M, Mees F, Mujinya BB, Baert G, Van Strydonk M, Boeckx P, Van Ranst E (2015) The age of large termite mounds—radiocarbon dating of Macrotermes falciger mounds of the Miombo woodland of Katanga, DR Congo. Palaeogeography, Palaeoclimatology, Palaeoecology 435: 265–271.

Freytet P, Plaziat J-C (1982) Continental carbonate sedimentation and pedogenesis – Late Cretaceous and Early Tertiary of Southern France. In: Purser BH (ed.) Contribution to Sedimentology, 12, Schweizerbart'sche Verlag, Stuttgart.

Freytet P, Verrecchia EP (2002) Lacustrine and palustrine carbonate petrography: an overview. J. Paleolimnology 27: 221-237.

Fynn RW, Chase M, Röder A (2014) Functional habitat heterogeneity and large herbivore seasonal habitat selection in northern Botswana. South African Journal of Wildlife Research 44: 1-15

Galan E, Carretero MI (1999) A New Approach to Compositional Limits for Sepiolite and Palygorskite. Clays and Clay Minerals 47: 399–409

Galan E, Pozo M (2011) Chapter 6 - Palygorskite and sepiolite deposits in continental environments. Description, Genetic Patterns and Sedimentary Settings. In: Galàn E, Singer A (eds) Developments in Clay Science. Elsevier, Amsterdam, pp 125-173.

Gamrod JL (2009) Paleolimnological records of environmental change preserved in Paleo-Lake Mababe, northwest Botswana. Doctoral dissertation, Oklahoma State University.

Giaconia F, Booth-Rea G, Martinez-Martinez JM, Azañon JM, Peréz-Peña JV (2012) Geomorphic analysis of the Sierra Cabrera, an active pop-up in the constrictional domain of conjugate strike-slip faults: The Palomares and Polopos fault zones (eastern Betics, Spain). Geomorphology, 580: 27–42.

Giaconia F, Booth-Rea G, Martínez-Martínez JM, Azañón JM, Pérez-Peña JV, Pérez-Romero J, Villegas I (2012) Geomorphic evidence of active tectonics in the Sierra Alhamilla (eastern Betics, SE Spain). Geomorphology, 145– 146: 90–106.

Grey DRC, Cooke HJ (1977) Some problems in the Quaternary evolution of the landforms of northern Botswana. Catena 4: 123–133.

Grove AT (1969) Landforms and climatic change in the Kalahari and Ngamiland. Geogr. J. 135, 191–212.

Hanor JS (2000) Barite–Celestine Geochemistry and Environments of Formation. Reviews in Mineralogy and Geochemistry 40: 193–275.

Holt JA, Lepage M (2000) Termites and Soil Properties. In: Abe T., Bignell D.E., Higashi M. (eds) Termites: Evolution, Sociality, Symbioses, Ecology. Springer, Dordrecht, Chapter 18: 389-407.

Humphries MS, McCarthy TS, Cooper GRJ, Stewart RA, Stewart RD (2014) The role of airborne dust in the growth of tree islands in the Okavango Delta, Botswana. Geomorphology 206: 307–317.

Huntsman-Mapila P, Ringrose S, Mackay AW, Downey WS, Modisi M, Coetzee SH, Vanderpost C (2006) Use of the geochemical and biological sedimentary record in establishing palaeo-environments and climate change in the Lake Ngami basin, NW Botswana. Quaternary International, 148: 51-64.

Irkec T, Ünlü T (1993) An example to sepiolite formation in volcanic belts by hydrothermal alteration: Kibriscik (Bolu) sepiolite occurrence Mineral Research Exploration Bulletin 115: 49-68.

IUSS Working GroupWRB (2014) World Reference Base for Soil Resources 2014: International Soil Classification System for Naming Soils and Creating Legends for Soil Maps. FAO, Rome

Joly F (1962) Principes pour une méthode de cartographie géomorphologique. Bulletin de l'Association de géographes français, 309-310: 270-278.

Jones BF, Conko KM (2011) Chapter 3 - Environmental Influences on the Occurrences of Sepiolite and Palygorskite: A Brief Review. In: Galàn E, Singer A (eds) Developments in Clay Science. Elsevier, Amsterdam, pp 69–83.

Jones JA (1990) Termites, soil fertility and carbon cycling in dry tropical Africa: a hypothesis. Journal of Tropical Ecology, 6: 291-305.

Jones MB (1988) Photosynthetic responses of C3 and C4 wetland species in a tropical swamp. Journ. Ecol. 76: 253-262.

Jouquet P, Lepage M (2002) Termite soil preferences and particle selections: strategies related to ecological requirements. Insectes Sociaux, 49: 1-7

Jouquet P, Tavernier V (2005) Nests of subterranean fungus-growing termites (Isoptera, Macrotermitinae) as nutrient patches for grasses in savanna ecosystems. African Journal of Ecology, 43: 191-196.

Jouquet P, Traoré S, Choosai C, Hartmann C, Bignell D (2011) Influence of termites on ecosystem functioning. Ecosystem services provided by termites. European Journal of Soil Biology, 47: 215-222.

Kinabo BD, Atekwana EA, Hogan JP, Modisi MP, Wheaton DD, Kampunzu AB (2007) Early structural development of the Okavango rift zone NW Botswana. J. Afr. Sci. 48: 125–136.

Kinabo BD, Hogan JP, Atekwana EA, Abdelsalam MG, Modisi MP (2008) Fault growth and propagation during incipient continental rifting: Insights from a combined aeromagnetic and

Shuttle Radar Topography Mission digital elevation model investigation of the Okavango Rift Zone, northwest Botswana, Tectonics, 27, TC3013, doi:10.1029/2007TC002154.

Kristensen JA, Thomsen KJ, Murray AS, Buylaert J-P, Jain M, Breuning-Madsen H (2015) Quantification of termite bioturbation in a savannah ecosystem: Application of OSL dating. Quaternary Geochronology, 30: 334-341.

Kurugundla CN, Dikgola K, Kalaote K (2010) Restoration and Rehabilitation of Zibadianja Lagoon in Kwando-Linyanti River System in Botswana. Botswana Notes and Records, 2010: 79-89.

Lancaster N (1981) Grain size characteristics of Namib Desert linear Dunes ». Sedimentology, 28(1): 115–122.

Lancaster N (1986) Grain size characteristics of linear dunes in the southwestern Kalahari. Journal of Sedimentary Petrology 56: 395-400.

Le Gall B, Tshoso G, Jourdan F, Feraud G, Bertrand H, Tiercelin JJ, Kampunzu AB, Modisi MP, Dyment J, Maia M (2002) $^{40}Ar/^{39}Ar$ geochronology and structural data from the giant Okavango and related mafic dyke swarms, Karoo igneous province, northern Botswana. Earth and Planetary Science Letters202: 595-606.

Mallick DIJ, Habgood F, Skinner AC (1981) A geological interpretation of Landsat imagery and air photography of Botswana. Overseas Geology and Mineral Resources, 56, Institute of Geological Sciences: London, 36pp.

Mayer L (1986) Tectonic geomorphology of escarpments and mountain fronts. In R. E. Wallace (Ed.), Active tectonics, Studies in Geophysics, Washington, DC, National Academy Press: 125–135.

McCarthy TS (1998) The role of biota in the initiation and growth of islands on the floodplain of the Okavango alluvial fan, Botswana. Earth Surface Processes and Landforms, 23: 291-316.

McCarthy TS (2006) Groundwater in the wetlands of the Okavango Delta, Botswana, and its contribution to the structure and function of the ecosystem. Journal of Hydrology 320: 264–282.

McCarthy TS, Ellery WN (1998) The Okavango Delta. Transactions of the Royal Society of South Africa 53: 157–182.

McCarthy TS, Bloem A, Larkin PA (1998) Observations on the hydrology and geohydrology of the Okavango Delta. South African Journal of Geology 101: 101–117.

McCarthy TS, McIver JR, Verhagen B (1991) Groundwater evolution, chemical sedimentation and carbonate brine for-mation on an island in the Okavango Delta swamp, Botswana. Applied Geochemistry 6: 577–596.

McCarthy TS, Cooper GJR, Tyson PD, Ellery WN (2000) Seasonal flooding in the Okavango Delta - recent history and future prospects. South African Journal of Science 96: 25–33.

McCarthy TS, Humphries MS, Mahomed I, Le Roux P, Verhagen BT (2012) Island forming processes in the Okavango Delta, Botswana. Geomorphology 179: 249-257.

McFarlane MJ, Eckardt FD (2008) Lake Deception: A new Makgadikgadi palaeolake. Botswana Notes and Records, 38: 195–201.

Mees F, Van Ranst, E (2011) Micromorphology of sepiolite occurrences in recent lacustrine deposits affected by soil development. Soil Research 49: 547-557.

Mendelson J, vanderPost C, Ramberg L, Murray-Hudson M, Wolski P, Mosepele K (2010) Okavango Delta: Floods of Life. Raison Publ., Windhoek, Namibia.

Mills AJ (2008) Fungus culturing, nutrient mining and geophagy. A geochemical investigation of Macrotermes and Trinervitermes mounds in southern Africa. Journal of Zoology 278: 24-35.

Milzow C, Kgotlhang L, Bauer-Gottwein P, et al (2009) Regional review: the hydrology of the Okavango Delta, Botswana—processes, data and modelling. Hydrogeol J 17:1297–1328.

Modie BN (1996) Depositional environments of the Meso- to Neoproterozoic Ghanzi-Chobe belt, northwest Botswana. Journal of African Earth Sciences, 22: 255-268.

Modisi MP, Atekwana EA, Kampunzu AB, Ngwisanyi TH (2000) Rift kinematics during the incipient stages of continental extension: evidence from the nascent Okavango rift basin, northwest Botswana. Geology 28: 939–942.

Moore AE, Larkin PA (2001) Drainage evolution in south-central Africa since the break-up of Gondwana. South African Journal of Geology 104: 47–68.

Moore AE, Cotterill FPD, Eckardt FD (2012) The evolution and ages of Makgadikgadi palaeo-lakes: consilient evidence from Kalahari drainage evolution south-central Africa. South African Journal of Geology 115: 385-413.

Moorkamp M, Fishwick S, Walker RJ, Jones AG (2019) Geophysical evidence for crustal and mantle weak zones controlling intra-plate seismicity–the 2017 Botswana earthquake sequence. Earth and Planetary Science Letters 506: 175-183

Mujinya BB, Van Ranst E, Verdoodt A, Baert G, Ngongo LM (2010) Termite bioturbation effects on electro-chemical properties of Ferralsols in the Upper Katanga (D.R. Congo). Geoderma 158: 233-241

Mujinya BB, Mees F, Boeckx P, Bodé S, Baert G, Erens H, Delefortrie S, Verdoodt A, Ngongo M, Van Ranst E (2011) The origin of carbonates in termite mounds of the Lubumbashi area, D.R. Congo. Geoderma 165: 95-105

Mujinya BB, Adam M, Mees F, Bogaert J, Vranken I, Erens H, Baert G, Ngongo M, Vanranst E (2014) Spatial patterns and morphology of termite (*Macrotermes falciger*) mounds in the Upper Katanga, DR Congo. Catena 114: 97-106

Murray-Hudson M, Combs F, Wolski P, Brown MT (2011) A vegetation-based hierarchical classification for seasonally pulsed floodplains in the Okavango Delta, Botswana. African Journal of Aquatic Science 36**:** 223-234

Nash DJ, Shaw PA (1998) Silica and carbonate relationships in silcrete-calcrete intergrade duricrusts from the Kalahari of Botswana and Namibia. Journal of African Earth Sciences 27:11–25

Nash DJ, Thomas DSG, Shaw PA (1994) Siliceous duricrusts as palaeoclimatic indicators: evidence from the Kalahari desert of Botswana. Palaeogeography, Palaeoclimatology, Palaeoecology 112:279–295

Nash DJ, Mclaren SJ, Webb JA (2004) Petrology, geochemistry and environmental significance of silcrete-calcrete intergrade duricrusts at Kang Pan and Tswaane, central Kalahari, Botswana. Earth Surface Processes and Landforms 29: 1559–1586

Pastier A-M, Dauteuil O, Murray-Hudson M, Moreau F, Walpersdorf A, Makati K (2017) Is the Okavango Delta the terminus of the East African Rift System? Towards a new geodynamic model: Geodetic study and geophysical review. Tectonophysics, 712 –713 : 469–481

Peel MC, Finlayson BL, McMahon TA (2007) Updated world map of the Köppen-Geiger climate classification. Hydrology and Earth System Sciences 11: 1633-1644

Peel RA, Tweddle D, Simasiku EK, Martin GD, Lubanda J, Hay CJ, Weyl OLF (2015) Ecology, fish and fishery of Lake Liambezi, a recently refilled floodplain lake in the Zambezi Region, Namibia. African Journal of Aquatic Science 40: 417-424

Pennisi E, Doak D, Tarnita C (2015) Africa's soil engineers: Termites. Science, 347, 6222: 596-597

Pozo M, Calvo JP (2018) An Overview of Authigenic Magnesian Clays. Minerals 8: 520-542

Pricope NG (2013) Variable-source flood pulsing in a semi-arid transboundary watershed: the Chobe River, Botswana and Namibia. Environmental Monitoring and Assessment 185: 1883-1906

Pringle RM, Doak DF, Brody AK, Jocqué R, Palmer TM (2010) Spatial pattern enhances ecosystem functioning in an African savanna. – PLoS Biol. 8: e1000377.

Ramberg L, Wolski P (2008) Growing islands and sinking solutes: processes maintaining the endorheic Okavango Delta as a freshwater system. Plant Ecology 196: 215-231

Ringrose S, Cassidy L, Diskin S, Coetzee S, Matheson W, Mackay AW, Harris C (2014) Diagenetic transformations and silcrete–calcrete intergrade duricrust formation in palaeo-estuary sediments. Earth Surface Processes and Landforms 39:1167–1187

Ringrose S, Kampunzu AB, Vink BW, Matheson W, Downey WS (2002) Origin and palaeo-environments of calcareous sediments in the Moshaweng dry valley, southeast Botswana. Earth Surface Processes and Landforms 27:591–611

Ringrose S, Huntsman-Mapila P, Downey W, Coetzee S, Fey M, Vanderpost C, Vink B, Kemosidile T, Kolokose D (2008) Diagenesis in Okavango fan and adjacent dune deposits with implications for the record of palaeo-environmental change in Makgadikgadi–Okavango–Zambezi basin, northern Botswana. Geomorphology 101: 544–557

Roberts M, Tod C, Aanen DK, Norbe T (2016) Oligocene Termite nests with In Situ Fungus Gardens from the Rukwa Rift Basin, Tanzania, Support a Paleogene African Origin for Insect Agriculture. Plos One, 11 (16): e0156847

Robins CR, Brock-Hon AL, Buck BJ (2012) Conceptual Mineral Genesis Models for Calcic Pendants and Petrocalcic Horizons, Nevada. Soil Science Society of America Journal 76: 1887–1903

Romanens R, Pellacani F, Mainga A, Fynn R, Vittoz P, Verrecchia EP (2019) Soil diversity and major soil processes in the Kalahari basin, Botswana. Geoderma Regional 19: e00236

Roodt V (1998) Trees and shrubs of the Okavango delta: medicinal uses and nutritional value. Shell Oil Botswana (Pty) Ltd, Maun

Sage RF (2004) The evolution of C4 photosynthesis. New Phytol. 161: 341-370

Sawula G, Martins E (1991) Major ion chemistry of the lower Boro River, Okavango Delta, Botswana. Freshwater Biol 26: 481–493

Seaman MT, Scott WE, Walmsley RD, van der Waal BCW, Toerien DF (1978) A limnological investigation of Lake Liambezi. Caprivi. Journal of the Limnological Society of Southern Africa 4: 129-144

Sebag D, Verrecchia EP, Durand A (1999) Biogeochemical cycle of silica in an apolyhaline interdunal Holocene lake (Chad, N'Guigmi region, Niger), Naturwissenchaften 86: 475-478

Shaw PA (1985) The desiccation of lake Ngami: an historical perspective. Geography. J. 151: 318–326

Shaw PA, Cooke HJ (1986) Geomorphic evidence for the late Quaternary paleoclimates of the Middle Kalahari of northern Botswana. Catena 13: 349–359

Shaw PA, Cooke HJ, Thomas DSG (1988) Recent advances in the study of Quaternary landforms in Botswana. Palaeoecology of Africa 19: 15–26

Sianga K, Fynn R (2017) The vegetation and wildlife habitats of the Savuti-Mababe-Linyanti ecosystem, northern Botswana. Koedoe 59: 1-16

Singer A, Kirsten W, Bühmann C (1995) Fibrous clay minerals in the soils of Namaqualand, South Africa: characteristics and formation. Geoderma 66: 43–70

Stoops GJ, Zavaleta A (1978) Micromorphological evidence of barite neoformation in soils. Geoderma 20: 63–70

Su C, Zhong D, Qin P, Wang A (2020) Mineral precipitation sequence and formation of the lacustrine hydrothermal sediments in the Lower Cretaceous Tenggeer Formation in the Baiyinchagan Sag, China. Sedimentary Geology 398: 105586

Thomas DSG, Shaw PA (1991) The Kalahari Environment. Cambridge University Press, Cambridge, UK.

Thomas DSG, Shaw PA (2002) Late Quaternary environmental change in central southern Africa: new data, synthesis, issues and prospects. Quaternary Science Review 21: 783-797

Thomas DSG, Burrough SL (2012) Interpreting geoproxies of Late Quaternary climate change in Africa drylands: implications for understanding environmental change and early human behavior. Quaternary International 253: 5-17

Tooth S, Vandewalle M, Goodin D, Alexander KA (2020) Anatomy of a wetland in a dryland: the Chobe-Zambezi channel-floodplain system. In: Eckardt FD (ed) Landscapes and landforms of Botswana. Springer: XXX-XXX

Tweedle D, Hay CJ (2011) Fish Protection Areas: Documentation for their establishment in Sikunga and Impalila Conservancies. Report for the WWF, 2011, 1-19

Verrecchia EP (2008) Lacustrine and Palustrine Geochemical Sediments. In: Nash DJ, McLaren S (eds) Geochemical Sediments and Landscapes. Blackwell Publ., Oxford, pp 298–329

Verrecchia EP, Verrecchia KE (1994) Needle-fiber calcite: a critical review and a proposed classification, J. Sedim. Res. A64: 650-664

Verrecchia EP, Freytet P, Verrecchia KE, Dumont J-L (1995) Spherulites in calcrete laminar crust: biogenic $CaCO_3$ precipitation as a major contributor to crust formation, J. Sedim. Res. A65: 690-700

Vittoz P, Pellacani F, Romanens R, Mainga A, Verrecchia EP, Fynn RWS (*in press*) Plant community diversity in the Chobe Enclave, Botswana: insights for functional habitat heterogeneity for herbivores. Koedoe

Wang L, D'Odorico PD, Ringrose S, Coetzee S, Macko SA (2007) Biogeochemistry of Kalahari sands. Journal of Arid Environments 71: 259-279

Wang MK, Tseng PC, Chang SS, Ray DT, Shau YH, Shen YW, Chen RC, Chiang PN (2009) Origin and mineralogy of sepiolite and palygorskite from the Tuluanshan Formation, Eastern Taiwan. Clays and Clay Minerals 57: 521–30

Watson A (1986) Grain size variations on a longitudinal dune and a barchan dune. Sedimentary Geology 46(1–2): 49–66

Wright VP (2007) Calcrete. In: Nash DJ, McLaren SJ (eds) Geochemical sediments and landscapes, Balckwell Publ., Oxford, pp. 10-45

Wright VP, Tucker ME (1991) Calcretes: an introduction. In: Wright VP, Tucker ME (eds) Calcretes. Blackwell, Oxford, IAS reprint series 2: 1–22

Wu JE, McClay K, Whitehouse P, Dooley T (2009) 4d analogue modelling of transtensional pull-apart basins. Mar. Pet. Geol. 26: 1608–1623

Yalçin H, Bozkaya Ö (2011) Chapter 7 - Sepiolite–Palygorskite Occurrences in Turkey. In: Galàn E, Singer A (eds) Developments in Clay Science. Elsevier, Amsterdam, pp 175–200

Zamanian K, Pustovoytov K, Kuzyakov Y (2016) Pedogenic carbonates: forms and formation processes. Earth-Science Reviews 157: 1-17

Ziegler PA, Cloetingh S (2004) Dynamic processes controlling evolution of rifted basins. Earth-Science Reviews 64: 1–50

CHAPTER 3

Geometry of sedimentary deposits and evolution of the landforms in the Chobe Enclave, Northen Botswana

Setting up an ERT survey profile

3. Geometry of sedimentary deposits and evolution of the landforms in the Chobe Enclave, Northern Botswana

Published as:

Mokatse, T., Vainer, S., Irving, J., Schmidt, C., Kgosidintsi, B., Shemang, E., & Verrecchia, E. P. (2022). Geometry of sedimentary deposits and evolution of the landforms in the Chobe Enclave, Northern Botswana. *Geomorphology*, *415*, 108406.

In this chapter, personal work entails ERT field acquisition, data processing, sample preparation, grain size analyses and writing of the paper.

Synopsis

The conceptualization of the study was motivated by the completion of the state-of-the-art overview of Chapter 2. This was because main research questions were outlined, and the general framework of the research put into perspective. It was important to now understand the landscape and the associated sedimentological and geomorphological features. As such, geophysical techniques were ideal to understand the subsurface structure and the depth of various lithological units. ERT and GPR are complementary methods for varying ground conditions, such as contrasting resistive and conductive grounds. The inversion of the ERT raw data enabled to view the contacts and depths of different units, whereas GPR data allowed depiction of architecture of the associated sediments.

Abstract:

The imprint of neotectonics is frequently obscured in low-relief environments by the sedimentary cover. This is the case in the Chobe Enclave, part of a pristine region of the Middle Kalahari Basin in northern Botswana, where numerous fossil landforms, such as sand dunes, pans, sand ridges, and carbonate islands, can be observed but whose detailed origins are unclear. In this study, a combination of near-surface geophysical surveys, sedimentological analysis, and optically-stimulated luminescence (OSL) dating were used to study the relationship between landscape development and neotectonic activity in one region of the Chobe Enclave. Specifically, electrical resistivity tomography (ERT) and ground penetrating radar (GPR) surveys were used to define the lateral and vertical distribution of sedimentary deposits associated with a prominent sand ridge and its margins. Sedimentological analysis and OSL dating of soil samples from pits taken along the survey lines were then used to calibrate the geophysical results and establish a chronostratigraphical framework. Our results lead to the following hypotheses regarding the evolution of this part of the Chobe landscape: (i) during the Late Pleistocene (> ~25 ka), fluvial channels were buried due to epeirogenic movements, resulting in paleo-channels; (ii) between ~25 ka and ~6 ka, a paleo-lake shoreline formed, which resulted in the linear eastern margin observed on the considered sand ridge. Erosional bounding surfaces suggest the syndepositional uplift of the sand ridge morphologies during this time; (iii) a neotectonic influence on the evolution of the landscape is revealed by the incision of the sand ridge forming fluvial watergaps since ~6 ka ago; and (iv) due to continuous aeolian and fluvial reworking, the western-most ridge became gradually isolated from the floodplain resulting in an inherited relief. In conclusion, this investigation allowed the deformation caused by epeirogenic movements acting on a low relief landscape to be characterized in terms of landforms and sedimentary body properties.

Keywords:

Sand ridges; Neotectonics; Watergaps; Grain-size distributions; Middle Kalahari.

3.1 Introduction

Recent and ongoing tectonics can affect landscape-shaping processes and their resultant landforms at various scales (Keller and Pinter, 1996; Holbrook and Schumm, 1999; Schumm et al., 2002). However, the imprint of neotectonics is frequently obscured in low-relief environments by the sedimentary cover, hampering identification of the origin of different landforms (Ruszkiczay-Rüdiger et al., 2009). Tectonically influenced landscapes are usually identified by a series of geomorphological indicators, such as entrenched channels, a high degree of incision along the channels flowing across active faults, or a sudden change in channel morphology (e.g., Rhea, 1993; Schumm et al., 2002; Bishop et al., 2003; Riquelme et al., 2003; Silva et al., 2003). The Chobe Enclave, situated in northern Botswana, is bounded by the Chobe and Linyanti faults and has a generally flat topography. It has a variety of landforms, most notable of which are sand ridges, which have been previously interpreted as relict beach ridges of a former lacustrine environment (Shaw and Thomas, 1988; Burrough and Thomas, 2008). The significance of these sand ridges for palaeoenvironmental and palaeoclimatological reconstructions was outlined in the context of OSL-derived lake stage chronologies (Burrough and Thomas, 2008). A tectonic origin for the topographic variations along the ridges in the region was also mentioned (Gumbricht et al., 2001). While all of this work has brought improved understanding of the origin of the sand ridges in the Chobe Enclave, the details regarding the influence of tectonics on their development, and on the landscape evolution in general, have been largely ignored. Further, the way that the internal architecture of these sand ridges could have been affected by neotectonics (McFarlane and Eckardt, 2007; Nash and Eckardt, 2015; Eckardt et al., 2016) remains unclear. Therefore, there is a noticeable knowledge gap concerning the occurrence and impact of neotectonic activity in the Chobe Enclave. This is addressed in this work, which represents a case study for understanding the propagation of upper crust deformation in incipient rifting settings and the resultant effect on landforms.

In this study, we focus on the western-most sand ridge, which is the main geomorphological feature in the Chobe Enclave (Fig. 3.1c). We use a combination of near-surface geophysical surveys, optically-stimulated luminescence (OSL) dating, and sedimentological analyses to study the structure, lithostratigraphy, and chronology of this ridge. The main objectives of our work are: (i) to define the lateral and vertical distribution of sedimentary bodies and the boundaries of the various lithologies; (ii) to outline the possible presence of structures that could be related to neotectonic processes; and (iii) to document the influence of different deformational mechanisms. To this end,

we conducted electrical resistivity tomography (ERT) and ground-penetrating radar (GPR) surveys over various parts of the ridge, where sediment samples were collected for OSL dating and sedimentological analyses. Together, these four methods provide highly complementary information for the characterization of Quaternary sediments (e.g., Aitken, 1998; Baines et al., 2002; Wisen et al., 2005; Bristow et al., 2005, 2007; Burrough and Thomas, 2008; Bristow, 2009). The establishment of a chronostratigraphical framework allows the temporal development of the inspected landforms to be drawn, ultimately gaining understanding about their evolution within the context of regional processes.

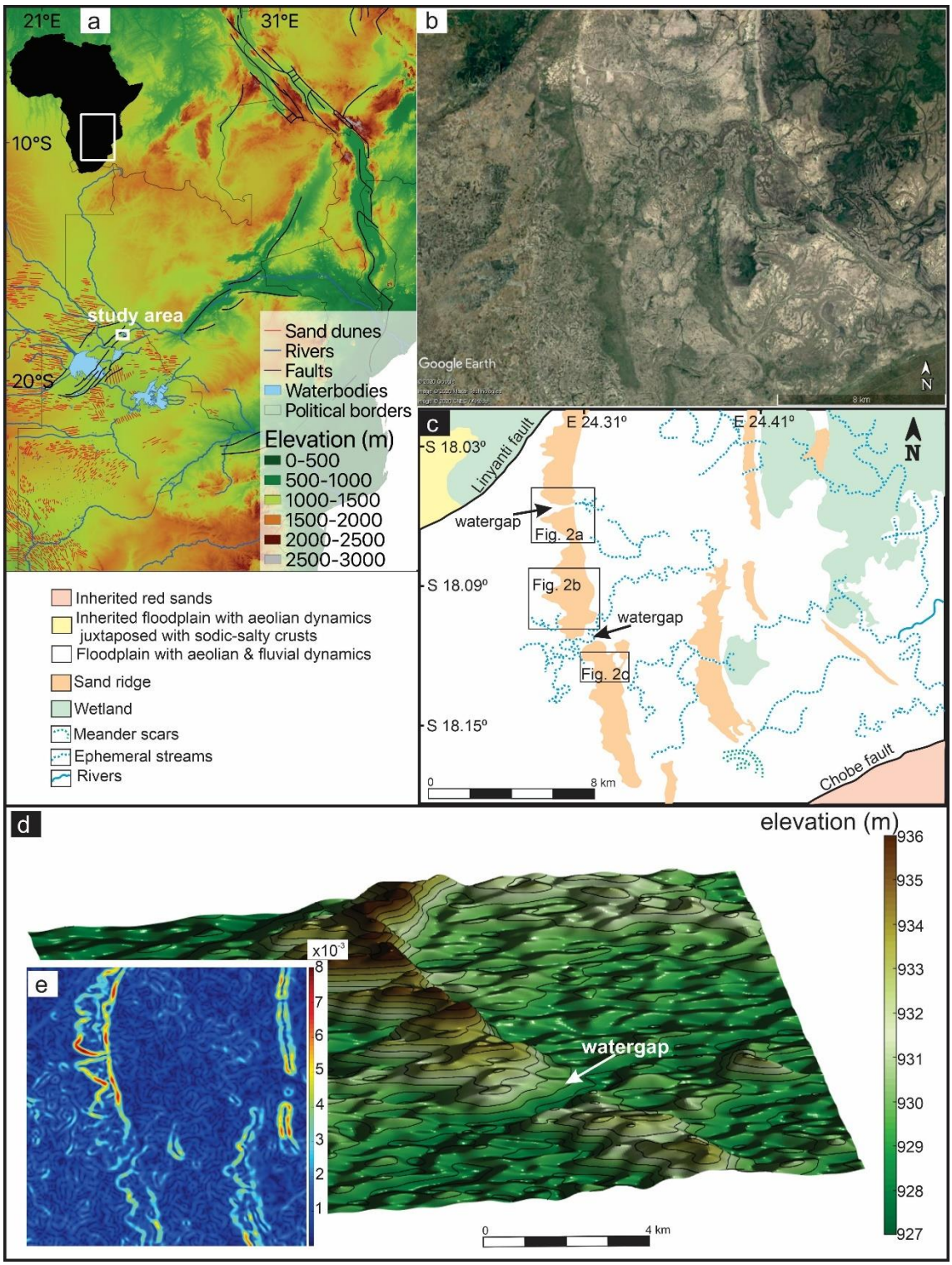

Figure 3.1: (a) *Main rivers, sand dune fields, and faults superimposed on the topography of southern Africa based on SRTM 30 sec DEM (NASA JPL, 2013). Faults of the East African Rift System (EARS) are after Chorowicz (2005) and their possible extension to the Okavango Graben (OG) are modified from Kinabo et al. (2008).* ***(b)*** *Satellite image of the study area (Google Earth, 2020).* ***(c)*** *Geomorphological interpretation of the area depicting main landforms with localities of study sites mentioned in Fig. 3.2.* ***(d)*** *Digital elevation model of the studied sand ridge and adjacent floodplain constructed from Google Earth data.* ***(e)*** *Slope values of the western part of Figure 3.1b and c.*

3.2 Geological setting

3.2.1 Structural context of the Chobe Enclave

On a regional scale, the Chobe Enclave is situated in the Middle Kalahari Basin, where several deformational mechanisms of different amplitude and temporal reoccurrence exist. Occupying the largest portion of the Intracratonic Kalahari Basin (Vainer et al., 2018), the Middle Kalahari is breached by the southwestward propagation of the more discretely deformed East African Rift System (EARS), and is considered to represent settings typical of incipient rifting (Fairhead and Girdler, 1969; Huntsman-Mapila et al., 2009; Kinabo et al., 2008). Based on the structures of the underlying mantle and crust, the Middle Kalahari is classified as a passive rift (Yu et al., 2015a, 2015b, 2017). The basin that overlies Proterozoic and Mesozoic rift structures (Dixey, 1956; Modisi et al., 2000; Doucouré and de Wit, 2003) is situated between elevated structural arches (Gumbricht et al., 2001). This led recent seismic tomography and magnetotelluric studies to suggest that deformation is triggered by inter-cratonic strains between the surrounding Archean cratons (Pastier et al., 2017; Yu et al., 2017). The differential deformation of the uplifted structural axes within the Kalahari Basin (Moore, 1999) resulted in the formation of several sub-basins, including the Makgadikgadi-Okavango-Zambezi basin (MOZB; McCarthy, 2013; Ringrose et al., 2005) of the Middle Kalahari, that was established in the early Pleistocene (Vainer et al., 2021a). The later segmentation of the MOZB into the current configuration that occupies the Chobe Enclave (Fig. 3.1b, c) is the result of Quaternary tectonics, which is assumed to be reflected in the sedimentary bodies that occupy this structural trough. Like the more developed basins in the EARS, grabens and half grabens provide space for sedimentation and the accumulation of waterbodies, whereas transfer zones link the depressed blocks and transport displacement strains between individual fault and basin segments (Gawthorpe and Hurst, 1993, McCarthy, 2013). Locally, the Chobe Enclave is bounded by the Linyanti (to the northwest) and the Chobe (to the southeast) faults (Fig. 3.1c), which breach the vast intracratonic Kalahari Basin to form this sub-basin within the high African plateau (Fig. 3.1a). Together with the Ngami and Mababe sub-basins, the Chobe Enclave comprises a syntectonic depocenter within the structural depression of the Okavango Graben (OG), which is the northern segment of the larger MOZB. This structural depression is made up of a series of NE-SW trending normal to dextral strike-slip faults (Modisi et al., 2000; Campbell et al., 2006; Bufford et al., 2012). The bounding faults of the OG on the southern part that extends into the Chobe Enclave were formed in an *en-echelon* pattern with a direction following the strike of the Precambrian basement

structures (Mallick et al., 1981; Moorkamp et al., 2019). The OG has been associated with the formation of the southwestern branch of the EARS (Modisi et al., 2000; Alvarez Naranjo and Hogan, 2013). However, Pastier et al. (2017) argued that the tectonic structure of the OG better fits a transtensional basin model. Kinabo et al. (2008) coupled analysis of Shuttle Radar Topography Mission, Digital Elevation Model, and aeromagnetic data in the Chobe Enclave and revealed the development of soft linkage on segments of the Linyanti fault and evidence of a hard linkage forming between two *en-echelon* right-stepping segments of the Chobe fault.

3.2.2 Surficial geology and geomorphology of the Chobe Enclave

The Chobe Enclave was developed within the vast (10^6 km^2), elevated (~1000 m asl), erosional surface of the Central African Plateau, which was established by the Pliocene (Partridge, 1998; Burke and Gunnel, 2008; Daly et al., 2020) following discrete epeirogenic flexuring (Vainer et al., 2018, 2021a). Although later tectonic activity occurred, the general topography of the Chobe Enclave remains fairly flat. Even so, fluvial watergaps serve as notable geomorphological indicators in the Chobe Enclave and attribute for tectonic influence on the landscape, evidenced by incision across sand ridges (Fig. 3.1d). Two slopes are predominant in the area, one gently decreases from SW to NE, and the other from NW to SE, with a value of less than 0.02% on average (Fig. 3.1e). This configuration promotes the existence of anastomosed fluvial systems, which are completely dry in the western part and become ephemeral to permanently flowing rivers to the east (Fig. 3.1b, c). The Chobe Enclave is mostly covered by unconsolidated sand that was introduced to the southern parts of the Kalahari approximately 2 Ma ago (Vainer et al., 2021b).

Cenozoic deposition of Kalahari Group sediments in the Chobe Enclave resulted in the accumulation of alluvial, lacustrine, fluvial, and aeolian deposits (Huntsman-Mapila et al., 2005; Podgorski et al., 2013). Sand ridges are the dominant landforms in the area (Mokatse et al., 2022), and are considered to represent late Quaternary paleolacustrine shorelines (Shaw and Thomas, 1988) formed under hydrological conditions different from the present-day (Grove, 1969; Cooke, 1980; Mallick et al., 1981; Shaw and Cooke, 1986; Shaw et al., 1988, 1997; Ringrose et al., 1999, 2005, 2009; Burrough and Thomas 2008; Burrough et al., 2009; Moore et al., 2012). These ridges have been mostly studied in order to understand how they might relate to paleohydrological and paleoclimatological processes (Fig. 3.1c; Burrough et al., 2007; Burrough and Thomas, 2008).

The Chobe Enclave also includes carbonate deposits in an otherwise large siliceous-dominated basin. These deposits, which were described as palustrine limestones (Diaz et al., 2019), outcrop in

the landscape as "*islands*" among the sands and are mostly observed in the central part of the Chobe Enclave, between the paleo-floodplain in the west and the large present-day floodplain in the east (Mokatse et al., 2022). These "islands" are also associated with diatomites in an unclear geometrical relationship, suggesting periods of wetter conditions and increased flows into the basin from the Chobe and Zambezi fluvial systems. Such paleo-flows likely contributed to the formation of lacustrine/palustrine deposits and were presumably developing during the surge of paleo-lakes witnessed in the south and the east of the Chobe Enclave by Burrough et al. (2009).

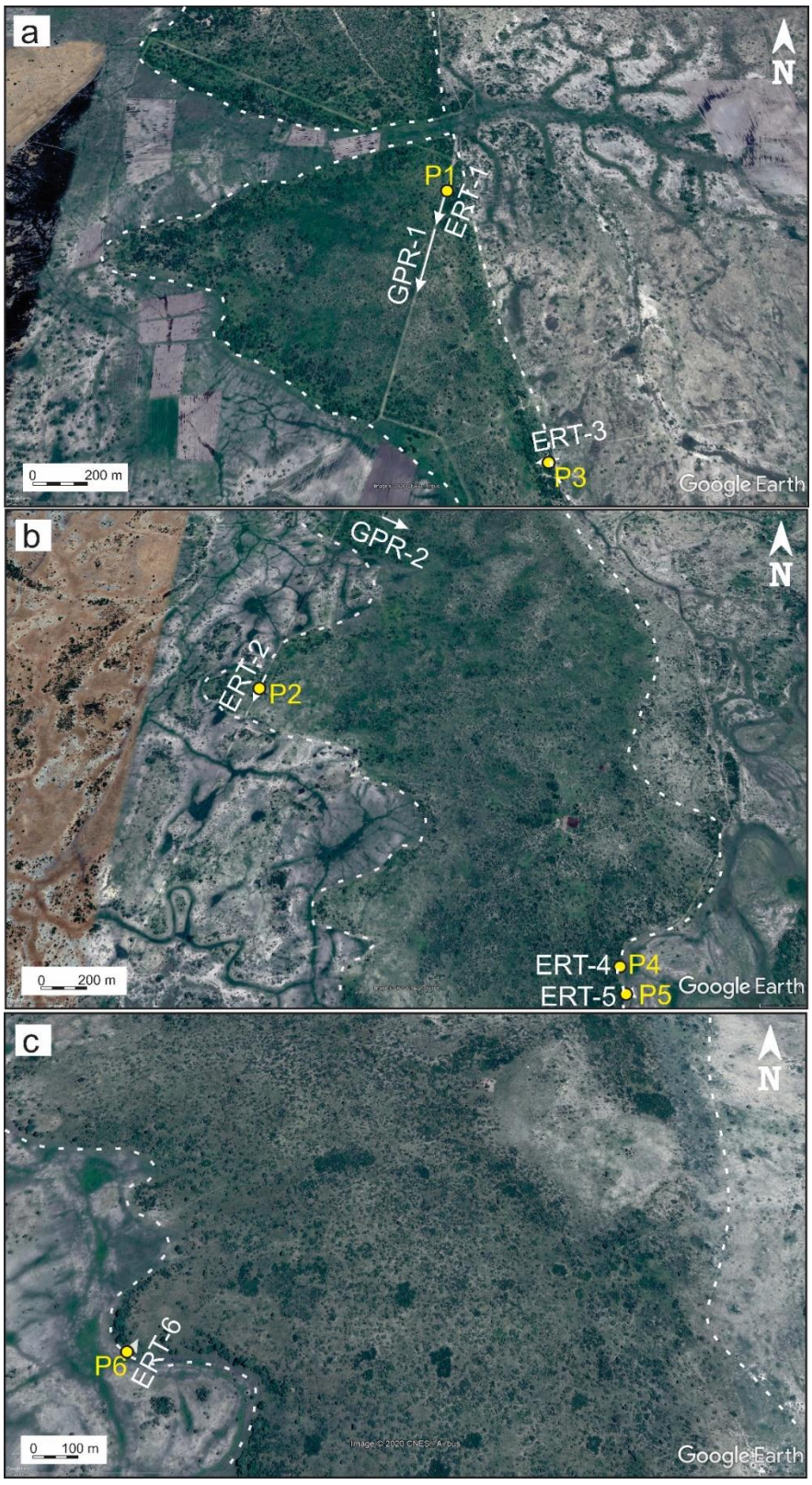

Figure 3.2: *Satellite images (Google Earth, 2020) showing the locations of ERT and GPR survey lines and corresponding pits (P). White arrows represent the direction and distance of geophysical surveys on the ground. White dashed lines represent the margins of the western-most sand ridge in the Chobe Enclave. The locations of images (a), (b) and (c) are shown in Fig. 3.1 (c).*

3.3 Methods

3.3.1 Site selection

This study focuses on the western-most north-south-trending sand ridge in the Chobe Enclave (Fig. 3.1c-e). Two key locations were targeted for data acquisition: (i) the sand ridge itself, to record morphological characteristics, which are critical to explain its origin and changes with time, and (ii) the sand ridge margins, which are pertinent to observe changes across the contact between the ridge and the floodplain.

3.3.2 Geophysical surveys

Electrical Resistivity Tomography (ERT)

ERT is an efficient and non-invasive geophysical technique that has been widely employed to image the spatial distribution of electrical resistivity in the shallow subsurface (e.g., Barber and Brown, 1984; Loke and Baker, 1996; Storz et al., 2000). In August 2020, a total of 6 ERT surveys were conducted in the study region (Fig. 3.2). Four of these surveys (ERT3, 4, 5 and 6) were at the sand ridge margins, where a transition from the fine sand of the ridge to the silt-rich sediments of the floodplain was recorded, whereas two surveys (ERT1 and 2) were acquired on the sand ridge itself. The latter two surveys represented regions where ERT imaging was possible on the sand ridge. In other locations, the highly resistive nature of the sand did not permit current flow into the ground, despite attempts to improve electrode coupling by watering with saline solution.

The ERT measurements were carried out using an IRIS Syscal Pro Switch 48-channel resistivity meter. The electrode spacing along the profiles was set to either 1 m or 2 m, and data were acquired using both the dipole-dipole and Wenner–Schlumberger electrode array configurations (Table 3.1). A Leica Geosystems differential GPS was used to measure the precise location and elevation of each electrode. Profiles ERT-1 and ERT-2, for which the line length exceeds the spacing times the number of available electrodes, were collected using a roll-along strategy. A pulse duration of 500 ms and a target of 50 mV for the potential readings were set as criteria for the current injection. For each resistivity quadripole, a total of four repeat measurements were performed in order to improve data quality and to help identify erroneous values.

Pre-processing of the ERT data was carried out using the Prosys II software and included deleting all resistance values where the relative standard deviation of the repeat quadripole measurements was greater than 3%, or where the measured electric potential had a value < 5 mV. In order to prepare the data for the 2D inversion procedure, the precise x-y locations of each electrode were also projected onto a best-fitting straight line. To invert the measurements, the Boundless Electrical Resistivity Tomography (BERT) software package was employed (Günther and Rücker, 2019). The prior constraints placed on the resistivity model for the inversion were carefully evaluated and the same inversion settings were used for all of the apparent resistivity datasets. Specifically, we considered smooth (L2-norm) prior model constraints with the inversion parameter *zweight* set to 0.5 in order to reflect a balance between an isotropic (*zweight*=1) and strongly layered (*zweight*=0.1) resistivity distribution. Moreover, the regularization parameter *lambda,* which controls the balance between fitting the ERT measurements and respecting the prior smoothness constraints, was chosen to provide a normalized chi-squared data misfit approximately equal to one, in accordance with the assumed level of error on the potential measurements. Interpretation of the models was aided by lithological logs from pits acquired along the survey lines (Fig. 3.2).

Table 3.1: Characteristics of the ERT profile lines considered in this study**.**

Profile line	Profile orientation	Profile length (m)	Number of electrodes	Electrode spacing (m)	Electrode array
ERT-1	NE - SW	214	48	2	Dipole-dipole & Wenner-Schlumberger
ERT-2	NE - SW	214	48	2	Dipole-dipole & Wenner-Schlumberger
ERT-3	E - W	94	48	2	Dipole-dipole & Wenner-Schlumberger
ERT-4	E - W	47	48	1	Dipole-dipole & Wenner-Schlumberger
ERT-5	E - W	47	48	1	Dipole-dipole & Wenner-Schlumberger
ERT-6	SW - NE	47	48	1	Dipole-dipole & Wenner-Schlumberger

Ground Penetrating Radar (GPR)

GPR allows the imaging of changes in electrical properties near the Earth's surface by recording the reflections of an emitted electromagnetic pulse from subsurface interfaces across which such properties change (Annan and Davis, 1992; Neal, 2004). Two GPR profiles were acquired at the study site (Fig. 3.2). Both were located on the sand ridge, where fine sand contributes to a highly

electrically resistive environment which is ideally suited for GPR surveying. In contrast, at the sand ridge margins, the GPR method was not applicable because of the presence of silt-rich floodplain sediments, whose high electrical conductivity strongly attenuated the propagating GPR pulse.

The GPR data acquisition was carried out using a Mala ProEx system with 100 MHz rugged terrain antennas, which was connected to a GPS. The 100 MHz antennas allowed for a depth of penetration of approximately 12 m and were chosen because of their higher resolution compared to lower frequency antennas available for the same system (Neal, 2004). The spacing between the transmitter and receiver antennas was 2.2 m. Data were recorded using a 500 ns time window and each recorded trace was stacked 16 times in order to improve the signal-to-noise ratio (Table 3.2). Traces were acquired continuously while moving the antennas at an approximately constant speed, resulting in an average trace spacing along the profile of roughly 14 cm.

The GPR datasets were processed using the ReflexW software. The processing was rather standard and consisted of the following steps: (i) data binning to create an even trace spacing; (ii) "dewow" to remove the low-frequency transient upon which the GPR reflections are superimposed; (iii) time-zero adjustment to calibrate the data to the emission time of the transmitted pulse; (iv) application of a time-varying gain function to compensate for attenuation and the geometrical spreading of energy; (v) frequency-wavenumber migration (Stolt, 1978) using a constant velocity of 0.15 m/ns in order to collapse diffraction hyperbolae and to reposition reflectors to their correct positions in depth; and (vi) correction for topography along the profile.

Table 3.2: Characteristics of the GPR profile lines considered in this study**.**

Profile line	Profile orientation	Profile length (m)	Time window (ns)	Number of stacks	Antennae separation (m)	Traces	Antenna frequency (MHz)
GPR-1	NE - SW	200	500	16	2.2	1697	100
GPR-2	NW - SE	220	500	16	2.2	1535	100

3.3.3 Sample analyses

Pit sample analyses

Six pit sites were located along the ERT and GPR survey lines to provide a ground control of the lithology (Fig. 3.2). This is a pertinent way to contribute to a well-informed interpretation of the various lithologies and to the assessment of the spatial distribution of surficial sediments. The characterization of the pit sites was based on field observations and particle size distribution (PSD) analyses carried out on 35 samples. The PSD were obtained using a laser diffraction Beckmann Coulter LS 13 320 on the < 2 mm size fraction after leaching with 10% hydrochloric acid. Samples were first classified under the Folk (1954)'s classification scheme as general descriptors, and statistics calculated using the Folk and Ward formula (Folk and Ward, 1957). The processing of PSD data was conducted to confirm the differences between the various position of groups of samples from the sand ridge and its margins. This was done by using various modes of their PSD, which essentially aided to identify the origin of the sediments. The PSD curves were all plotted together in order to observe the overall variations of their shapes. Moreover, End-Member Mixing Analysis (EMMA) was performed based on the algorithm provided by Dietze et al. (2012) and run within the MATLAB computing environment. It was applied to all PSD curves to recognize the possible contributions of the various sedimentary sources. After identification of the end-members, each sample was described in terms of relative contribution of each end-member to its PSD. Sediments associated with a specific sedimentary process usually have a characteristic PSD referred as an end member. Essentially, the observed PSD can be considered as a result of a mixing process of a finite number of end members resulting in a complex spectrum. EMMA of sediment PSD demonstrates one way of discretizing the continuum of selective entrainment, transport, and deposition of sediments, providing deeper insights into the sedimentary environment and climatic conditions involved (Prins et al. 2002, 2007; Dietze et al. 2013a, b; Schmidt et al., 2021).

Optically Stimulated Luminescence (OSL)

Sampling and preparation

One to two samples were collected from each pit to determine through OSL dating when the detrital material was last exposed to sunlight (Aitken, 1998). Sampling was completed using light-sealed tubes hammered into pit walls, at least 30 cm above the carbonate deposits, where present. Samples were then dry-sieved in subdued red-light conditions into the 180-212 μm size fraction. Quartz was isolated by dissolving carbonate and oxidizing organic matter with 10% HCl and 30%

H_2O_2, respectively, and from other minerals by two-step heavy liquid separation using sodium polytungstate. The fraction with a density between 2.62 and 2.70 g cm^{-3} was etched for 40 min with 40% HF and subsequently treated with 10% HCl for dissolution of potential Ca-fluoride precipitates.

Equivalent dose estimation

Luminescence measurements were performed on a Risø TL/OSL-DA 20 instrument with a $^{90}Sr/^{90}Y$ β-source that delivers a dose rate of 0.144 Gy s^{-1} to quartz coarse grains on stainless steel discs (Risø calibration quartz batches 71, 90, and 113). OSL signals were stimulated by an array of blue (470 ± 5 nm) LEDs with a nominal power density of 36 mW cm^{-2} for 38 s and collected by an EMI 9235QB15 photomultiplier tube with a 7.5 mm Hoya U340 glass filter in front of it. To establish the dose response curve (DRC), signals were integrated over the first 0.7 s of the decay curve and a background averaged from the last 2 s was subtracted. The DRC was fitted with a single saturating exponential function and the equivalent dose (D_e) determined through interpolation using the Analyst software (v3.24; Duller, 2015).

Preparatory tests were performed to determine the most suitable measurement parameters for D_e determination (e.g., Kim et al., 2009). Thus, dose recovery and preheat plateau tests (DRT and PPT, respectively) were carried out on 15 aliquots from three samples collected at 1.05 m deep in Pit 1, 1.40 m deep in Pit 2, and 2.05 m deep in Pit 4 (Fig. 3.2), testing the temperature range between 180 and 260 °C at 20 °C increments. For the DRTs, the natural signal was bleached in a Hönle UVACube for 30 min and samples were given a β-dose in the range of the natural dose. In addition to multi-grain measurements on 1 mm aliquots, single-grain analyses of 500 grains were performed for samples collected at 1.05 m deep in Pit 1 and 2.05 m deep in Pit 4.

Equivalent doses were determined on 40 to 48 aliquots per sample by applying the single-aliquot regeneration method (SAR; Murray and Wintle, 2000). Aliquots were accepted for age calculation if the recycling ratio was in the range of 0.9–1.1, recuperation rate was <5%, and a test dose signal error was <10%. Furthermore, the IR-depletion ratio test (Mauz and Lang, 2004) was applied to all measurements to assure the purity of quartz. For samples that displayed a scattered D_e distribution or considerable percentage of rejected aliquots, an additional set of 24 or 48 aliquots was measured to ensure a statistically valid dose determination. The central age model (CAM; Galbraith et al., 1999) and minimum age model (MAM; Galbraith et al., 1999) were applied to all accepted D_e values

via the **R**-package 'Luminescence' v0.9.10 (Kreutzer et al., 2012; R Core Team, 2021). The model parameter representing the overdispersion (σ_b) was estimated from the DRT.

Dose rate estimation

Present day water content was determined based on weight loss after drying samples at 40 °C and carbonate content was determined based on weight loss after dissolution in 10% HCl. As of our understanding of the depositional environments, current moisture content does not reflect a representative value for the burial period, thus a higher water content of 10±3 % was assigned to represent a former palustrine-lacustrine environment (Diaz et al., 2019).

The concentrations of U, Th and K were determined at Actlabs (Canada) via fusion inductively coupled plasma mass spectrometry (FUS-ICP-MS; Table 2). Current sample depth was considered to estimate the cosmic dose rate. The overall dose rates and luminescence ages were calculated with DRAC (v1.2; Durcan et al. 2015) using conversion factors from Guérin et al. (2011), α-attenuation factors from Brennan et al. (1991) and β-attenuation factors from Guérin et al. (2012).

3.4 Results

3.4.1 Lithological Observations and Particle-Size Distributions

Pits 1 and 2 are located on sand ridges, whereas Pits 3, 4, 5, and 6 on their margins (Fig. 3.2). The compilation of data from these localities is crucial for the understanding of the long-term development of the geomorphological features as well as to observe the temporal field relationships between the ridges and their surroundings (Fig. 3.3a, b).

The lithological logs are generalized to the dominant lithology and show a succession from silt-rich to sand-rich sediments, interbedded with sandy carbonate (Fig. 3a). Pit 1 (2.27 m deep) consists of a sandy carbonate layer of ~47 cm thickness appearing between two fine sand units, whereas Pit 2 (with a maximum depth of 1.30 m) consists of fine sands overlying a sandy carbonate layer. This pit is situated at the highest elevation, i.e., ~941 m. At Pit 3 (1.68 m deep), a sandy carbonate bed is overlain by fine sands. Sample H5P3 (Fig. 3.3a) contained amorphous siliceous aggregates and was not included in the end-member analysis to avoid inaccurate interpretation of the results. Pit 4 (2.2 m deep) and Pit 5 (2.18 m deep) are dominated by fine sands. Lastly, Pit 6 is positioned at the lowest

elevation of ~935 m with a depth of 2 m and is dominated by fine sands in contact with silt-rich sediments at its bottom.

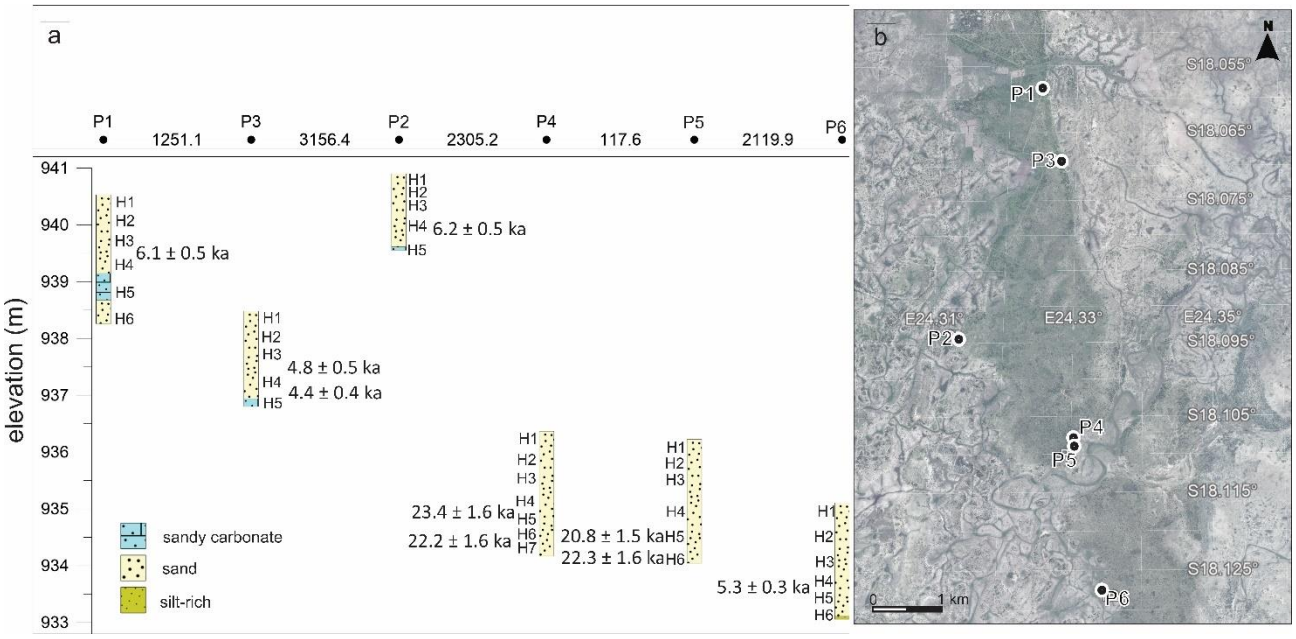

Figure 3.3: (a) *Lithological logs and corresponding OSL ages: classes are generalized from the particle size distribution analysis using the classification scheme by Folk (1954). Pit sites are denoted by P1 to P6. H1 to H6 refer to sample positions in each pit. Along the horizontal axis, figures between the pit numbers (P1 to P6) refer to the distance (in metres) between two successive pits from north to south. The y-axis refers to the altitude (in metres) at the top of the pit.* ***(b)*** *Locations of the pits referred to in (a). See also Figure 3.2.*

EMMA processing allowed four statistical sedimentary contributors (labeled EM1, 2, 3, and 4) to be identified (Fig. 3.4). The EM1 curve has a leptokurtic shape with a single mode in the sand fraction at 120 µm, corresponding to a very well sorted sand. In EM 2, two distinct maxima are observed with a mode at 120 µm and the other at 250 µm, showing a mixing association of two sandy compartments. The EM3 curve displays a leptokurtic shape with a mode at 250 µm, emphasizing a very well sorted sand. Finally, EM4 has a leptokurtic shape with a mode at 250 µm and a minor platykurtic distribution centered in the silt fraction, around 15 µm (Fig. 3.4a). The weight of the distinctive EMs in each PSD allowed groups of samples to be sorted, underlying the prominent role of the sandy fractions, except when EM4 is present in a large proportion.

The sand ridge (Pits 1 and 2) is mainly characterized by EM2 in the bottom part, whereas the upper parts are comprised of EM1, EM3 and EM4 (Fig. 3.4b). This transition is clearly evident only on the sand ridge. On the other hand, the sand ridge margins are characterized by two distinct

patterns. The first pattern, recognized in Pits 4 and 5, is dominated by EM3 and a minor contribution of EM1 and EM4 (Fig. 3.4b). EM3 represents very well sorted sand. The second pattern, observed in Pits 3 and 6, is mostly EM1 and EM4 with minor EM3 (Fig. 3.4a). Furthermore, the transition in all sites is prominent, as the EMMA results (Fig. 3.4b) display a clear picture of evolution of the PSD for each site, from the sand ridge to its margins. This is an equally important step in emphasizing how end-members successfully characterize the variability of the curves (Fig. 3.4), ultimately giving insight into possible sedimentary sources across the region.

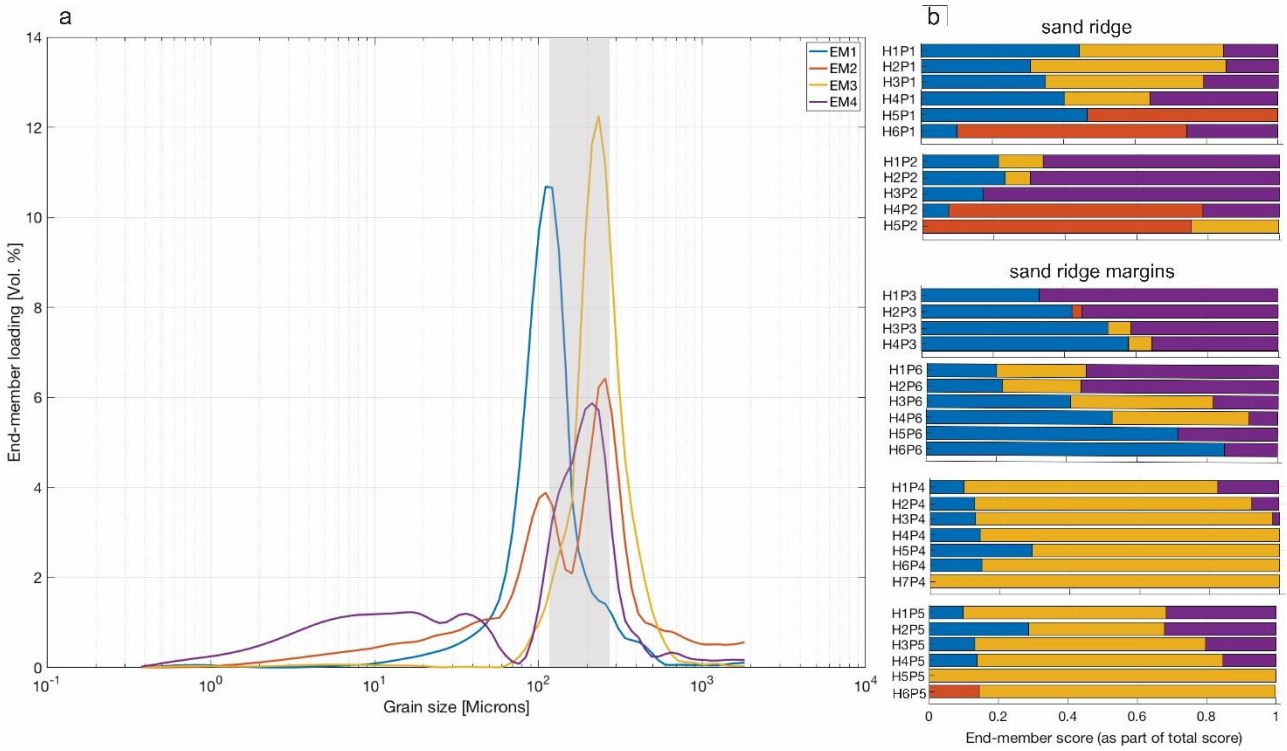

Figure 3.4: (a) *PSD plot of end-members determined via End-Member Mixing Analysis (EMMA). The Kalahari sand mode is displayed as a shaded area centred on 200 µm.* ***(b)*** *Bar chart of the end-member contributions to each sample.*

3.4.2 Electrical Resistivity Tomography (ERT) Profiles

All the ERT inversion results presented in this work correspond to the dipole-dipole electrode array configuration, which has improved lateral resolution characteristics compared to the Wenner-Schlumberger configuration (Loke, 2004). This made it easier in our interpretations to define the lateral distribution of sedimentary bodies.

Sand ridge

Profile ERT-1 is 214-m long and was acquired along the sand ridge in a NE-SW direction (Fig. 3.2a). The ERT inversion results for this profile (Fig. 3.5a) show a near-surface layer having increasing thickness towards the SW, whose resistivity values range between 200 and 4000 Ωm. This layer corresponds to moderately sorted fine sands observed in Pit 1 (Fig. 3.3a), where variations in resistivity are likely controlled by the amount of silt present. Below these fine sands, the resistivity values along the profile are seen to decrease (< 100 Ωm), which we interpret as indicating a transition from fine sand to silt-rich floodplain deposits. Within these deposits, zones of increased resistivity can be observed on the left-hand side of the profile, which may represent paleo-channels consisting of fine sand. These channels are located between approximately 8 and 20 m depth.

Profile ERT-2 was acquired across the sand ridge in a NE-SW direction (Fig. 3.2b). Similarly, the corresponding ERT inversion results (Fig. 3.5b) show a relatively resistive layer at the top overlying a dominant conductive layer of values <100 Ωm. However, the upper layer is discontinuous with the middle section showing zones we interpret as paleo-channels closer to the surface. Our interpretation of this profile (Fig. 3.5b) shows a fine sand layer overlying silt-rich floodplain deposits, with an eroded surface from 30 to 112 m. Paleo-channels can be identified within the floodplain at a depth of approximately 2 to 5 m.

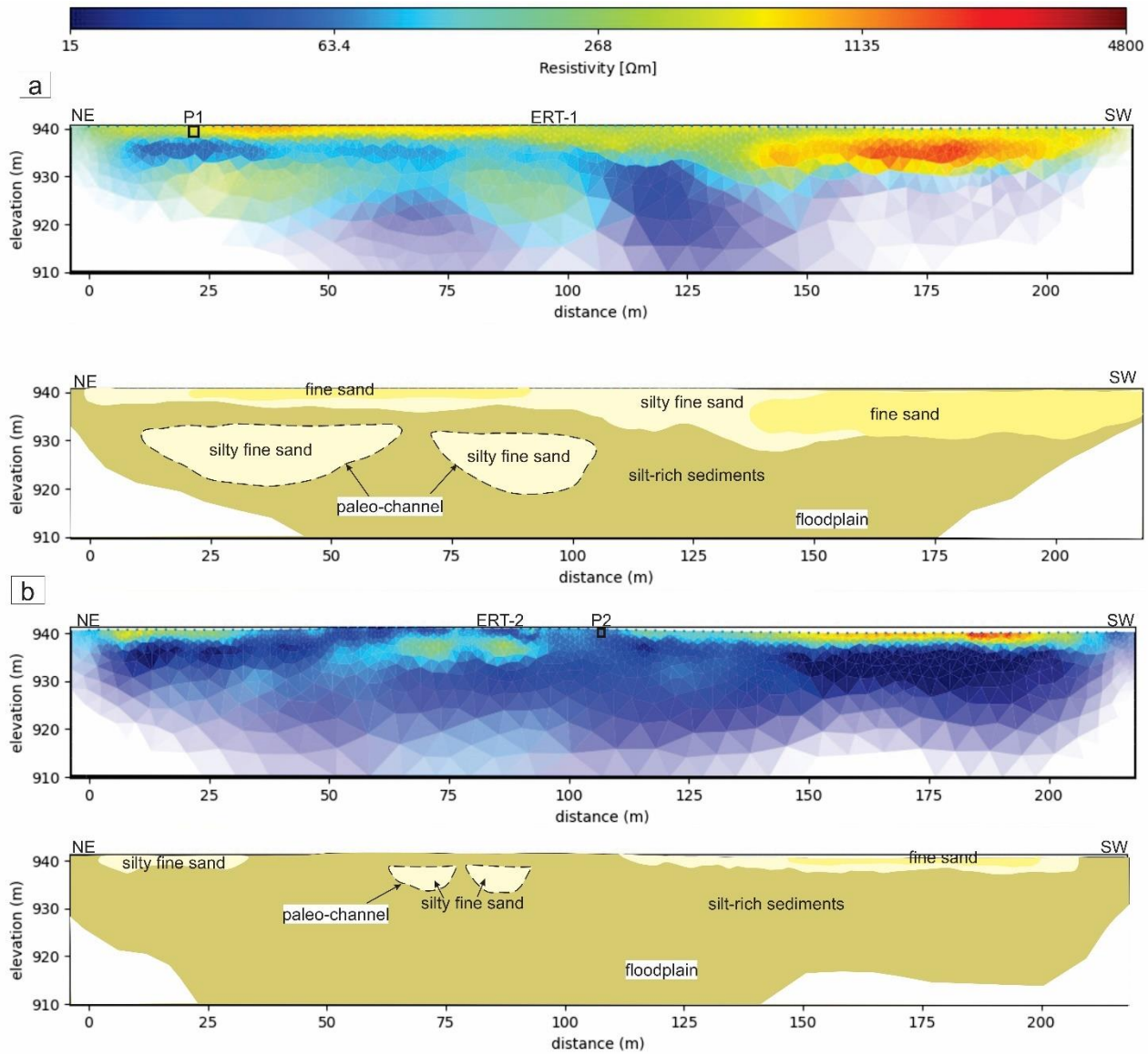

***Figure 3.5**: Dipole-dipole ERT profiles (a) ERT-1, and (b) ERT-2, which were acquired along the sand ridge (Fig. 3.2). Shown are the inversion results and their interpretations based on the observed resistivity values and sedimentological data.*

Sand ridge margins

The sand ridge margins correspond to a transition between the floodplain and the sand ridge. Profile ERT-3 is situated on the eastern margin of the sand ridge in the southern part of the study area (Fig. 3.2a). The corresponding ERT inversion results (Fig. 3.6a) show a more resistive layer at the surface from approximately 30 m onwards, whose thickness increases towards the west. This layer has been identified as fine sand in Pit 3 (Fig. 3.3a). Below the fine sand, is a section dominated by a conductive layer of values ~20 to ~100 Ωm, corresponding to the silt-rich sediments of the floodplain. Within this conductive floodplain, a relatively resistive feature is displayed and

interpreted as a paleo-channel. Profile ERT-4 crosses the sand ridge margin from N to S (Fig. 3.2b). Here, the ERT inversion results (Fig. 3.6b) again show a resistive upper layer, representing fine sand, overlying a more conductive layer corresponding to silt-rich sediments observed in Pit 4 (Fig. 3.3a). Likewise, Profile ERT-5 runs across a sand ridge margin dominated by a resistive layer (>200 Ωm) from 20 to 47 m, which corresponds to fine sand in Pit 5 (Fig. 3.3a). The fine sand is underlain by a more conductive layer (<70 Ωm) representing silt-rich sediments of the floodplain. Finally, profile ERT-6 (Fig. 3.2c) runs along the N-S trending sand ridge margin in the southern part of the study area. The ERT inversion results (Fig. 3.7b) show consistency with previously presented data having a more resistive upper layer with values >600 Ωm (fine sand), and a relatively conductive lower layer (<60 Ωm) corresponding to silt-rich sediments of the floodplain below Pit 6 (Fig. 3.3a). It is important to note that the conductivity will vary depending on the moisture or clay content of the floodplain sediments.

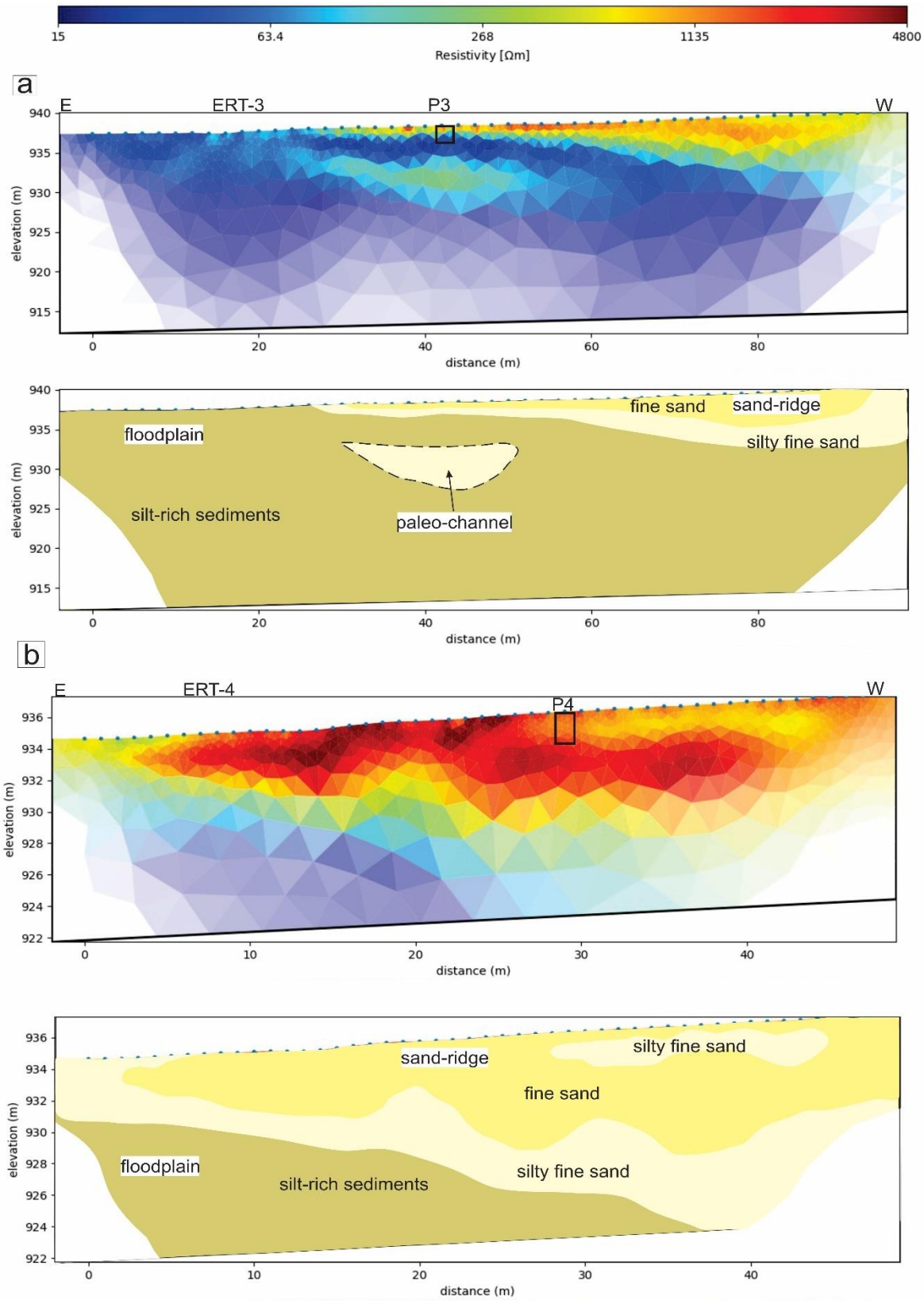

***Figure 3.6**: Dipole-dipole ERT profiles (a) ERT-3 and (b) ERT-4 across sand ridge margins (Fig. 3.2). Shown are the inversion results and their interpretations based on the observed resistivity values and sedimentological data.*

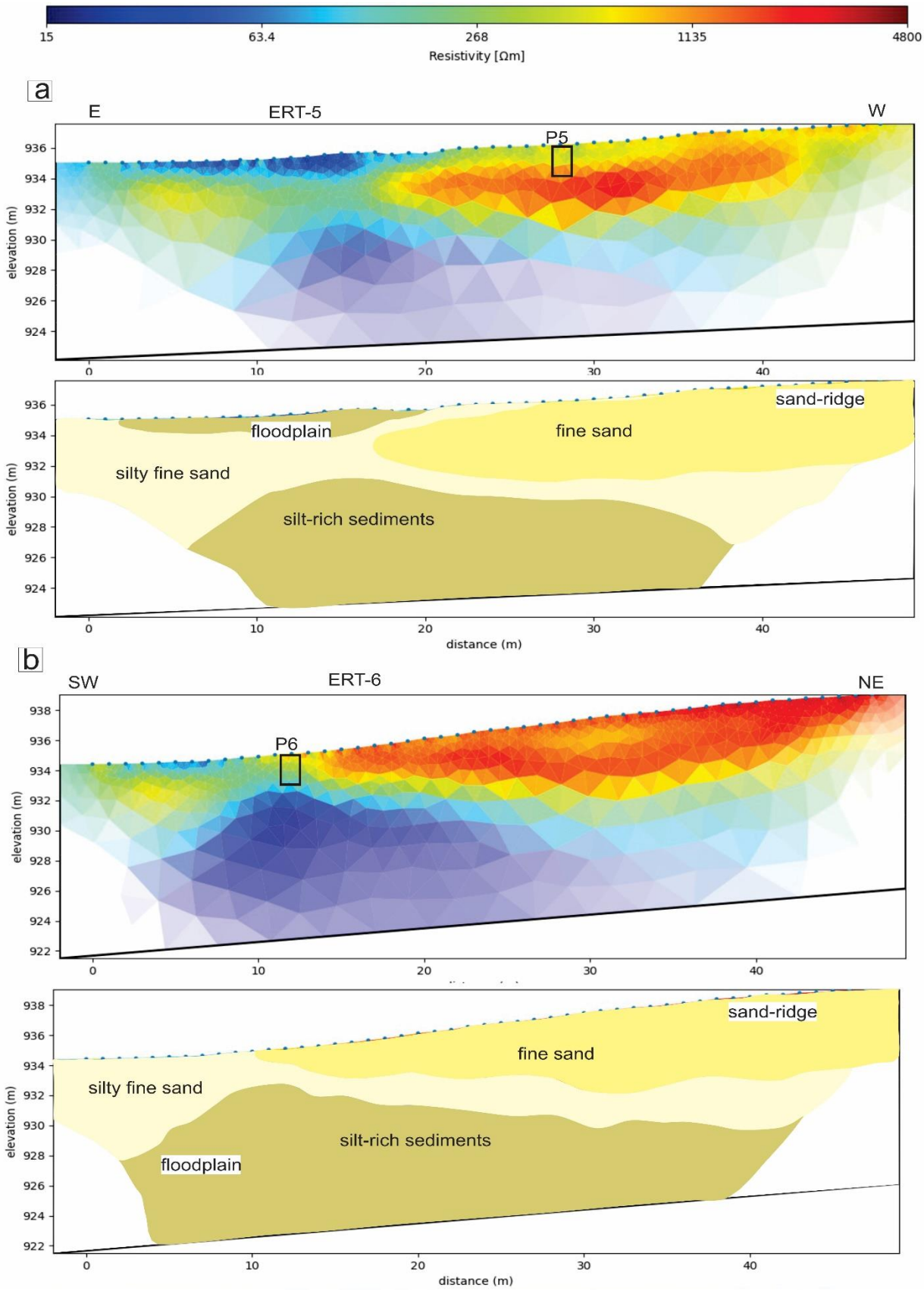

***Figure 3.7**: Dipole-dipole ERT profiles (a) ERT-5 and (b) ERT-6 across sand ridge margins (Fig. 3.2). Shown are the inversion results and their interpretations based on the observed resistivity values and sedimentological data.*

3.4.3 Ground-Penetrating Radar (GPR) Profiles

Profile GPR-1 is 200-m long and was acquired along the sand ridge in a NE-SW direction (Fig. 3.2a). The GPR results (Fig. 3.8a) show two continuous reflectors at approximately 2 to 4 m depth. The upper reflector terminates on the lower one, revealing the internal structure and relative chronology (Bristow and Jol, 2003) within the ridge. Profile GPR-2 is 220-m long and was acquired along the sand ridge in a NW-SE direction (Fig. 3.2b). Similarly, the GPR results (Fig. 3.8b) show two continuous reflectors running subparallel to the ground surface, each occurring between depths of ~2 to ~4 m and ~6 to ~8 m. The lower reflector occurs closer to the boundary of high signal attenuation hence appearing less continuous. Diffraction hyperbolae appearing on both profiles at an apparent depth of ~7 to 10 m are caused by trees along the survey line. The maximum GPR penetration depth along these profiles is approximately 12 m.

The Chobe Enclave sand ridges are thus characterized by prominent continuous reflectors consistent throughout the area with varying thickness, whereas the surrounding floodplains show high signal attenuation because of their increased fine sediments and/or moisture content. The interpreted models (Fig. 3.8a, b) emphasize some continuous bounding surfaces, characterized by continuous reflectors along the sand ridge, and a transition zone, defined by a boundary of high signal attenuation. Generally, this is consistent with the ERT inversion results showing a transition between the resistive sand ridge and the conductive silt-rich floodplain.

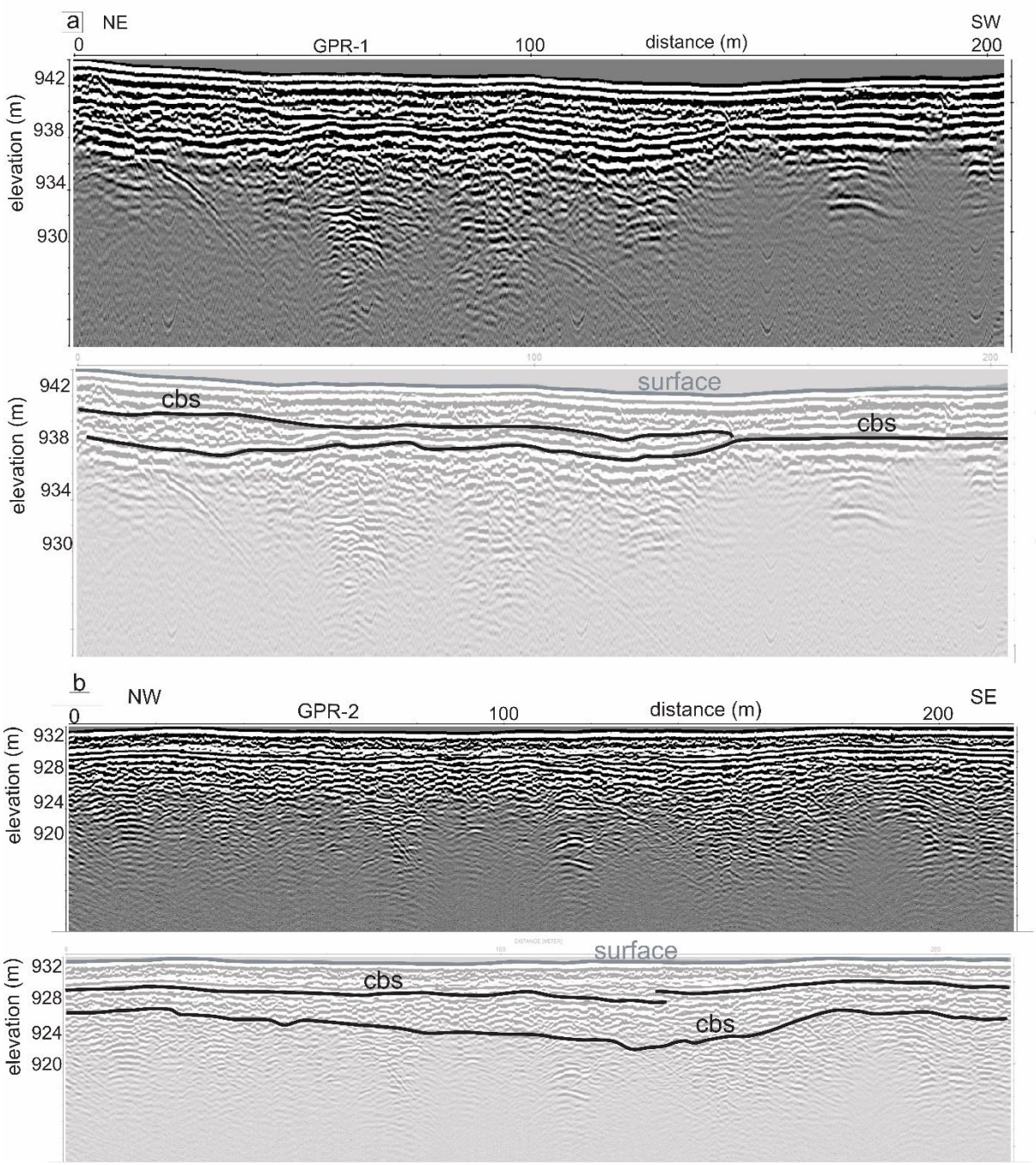

***Figure 3.8**: GPR profiles **(a)** GPR-1, and **(b)** GPR-2, which were acquired along the sand ridge (Fig. 3.2).* Shown are the processed 100-MHz reflection data *and their interpretations. (cbs=continuous bounding surface).*

3.4.4 Optically stimulated luminescence (OSL) results

All processed samples were dry with <0.5% water content (except for OP5-103 with <2% water) and contained neglectable amount of carbonate and feldspar (Table 3.3). Preheat plateau tests (PPT) imply that a preheat temperature of 200 °C is collectively best suited for all samples (Fig. 3.9); this

temperature along with a cut heat to 200 °C was utilized during D_e measurements. Dose recovery tests (DRT) carried out with this preheat temperature resulted in dose reproducibility within 4%, 2%, and 1% for samples OP1-105, OP2-140, OP4-205, respectively. D_e values from single-grain measurements are indistinguishable (within error) for sample OP1-105 and higher by 4% for sample OP4-205 than the multi-grain D_e (Fig. 3.9). Central age model (CAM) and minimum age model (MAM) results in pits 2, 4, and 6 agree within 1σ uncertainty. In pits 1, 3, and 5, over 40% of variance subsists between CAM and MAM, and CAM ages are presented (Table 3.3).

The effects of inter-grain variability in the degree of bleaching, β micro-dosimetry effects, bioturbation, and grain-to-grain differences in OSL characteristics for an analogous set of samples were discussed in Burrough et al. (2009). These authors concluded that the most suitable age model for this type of sediment is the CAM. They also estimated the internal activities of ^{238}U, ^{232}Th, and ^{40}K within the quartz grains, showing that the internal α- and β-dose would not push the age estimates outside of the assigned 1σ uncertainties and would not affect age clusters calculated subsequently. Therefore, CAM ages were calculated based on the dose rate estimated from the radioelement concentrations measured within bulk samples and the corresponding cosmic dose. The resultant ages are in stratigraphic order within 1σ uncertainties and are clustered into two age groups that range between 23.4 ka and 20.8 ka and between 6.2 ka and 4.4 ka. The older age group is found between 2.1 m and 1.7 m depths in pits 4 and 6 while in pits 1, 2, 3, and 5, where maximal sampling depth is 1.4 m, samples display a Holocene age.

Table 3.3: OSL ages of the studied samples, based on the Central Age Model (CAM).

Sample	Pit no	Depth [cm]	Accepted/ measured aliquots	K [wt.%]	1σ	Th [ppm]	1σ	U [ppm]	1σ	$CaCO_3$ [wt.%]	Measured H_2O [wt.%]	Estimated H_2O [wt.%]	1σ	Dose rate [Gy ka^{-1}]	1σ	D_e [Gy]	1σ	Overdispersion [%]	1σ	**Age [ka]**	**1σ**
OP1-105	P1	105	35/35	0.06	0.01	0.6	0.08	0.4	0.02	1.6	0.1	10	3	0.372	0.022	2.26	0.13	35	4	**6.1**	**0.5**
OP2-140	P6	140	46/46	0.07	0.01	1.0	0.14	0.3	0.02	0.0	0.1	10	3	0.377	0.022	2.00	0.03	9	1	**5.3**	**0.3**
OP3-105	P3	105	78/94	0.09	0.01	0.8	0.11	0.3	0.02	1.2	0.3	10	3	0.390	0.022	1.89	0.15	66	6	**4.8**	**0.5**
OP3-120	P3	120	73/81	0.09	0.01	0.8	0.11	0.3	0.02	5.1	0.5	10	3	0.387	0.022	1.69	0.13	70	6	**4.4**	**0.4**
OP4-185	P4	185	43/47	0.06	0.01	0.6	0.08	0.2	0.01	0.0	0.0	10	3	0.314	0.020	7.35	0.18	15	2	**23.4**	**1.6**
OP4-205	P4	205	48/48	0.02	0.00	0.3	0.04	0.2	0.01	0.0	0.0	10	3	0.256	0.018	5.67	0.12	14	2	**22.2**	**1.6**
OP5-103	P2	103	43/48	0.13	0.02	0.8	0.11	0.2	0.01	1.8	1.7	10	3	0.406	0.025	2.50	0.14	35	4	**6.2**	**0.5**
OP6-170	P5	170	65/70	0.03	0.00	0.4	0.06	0.2	0.01	0.0	0.0	10	3	0.278	0.019	5.78	0.12	19	2	**20.8**	**1.5**
OP6-210	P5	210	58/72	0.03	0.00	0.4	0.06	0.2	0.01	0.0	0.0	10	3	0.270	0.019	6.02	0.15	20	2	**22.3**	**1.6**

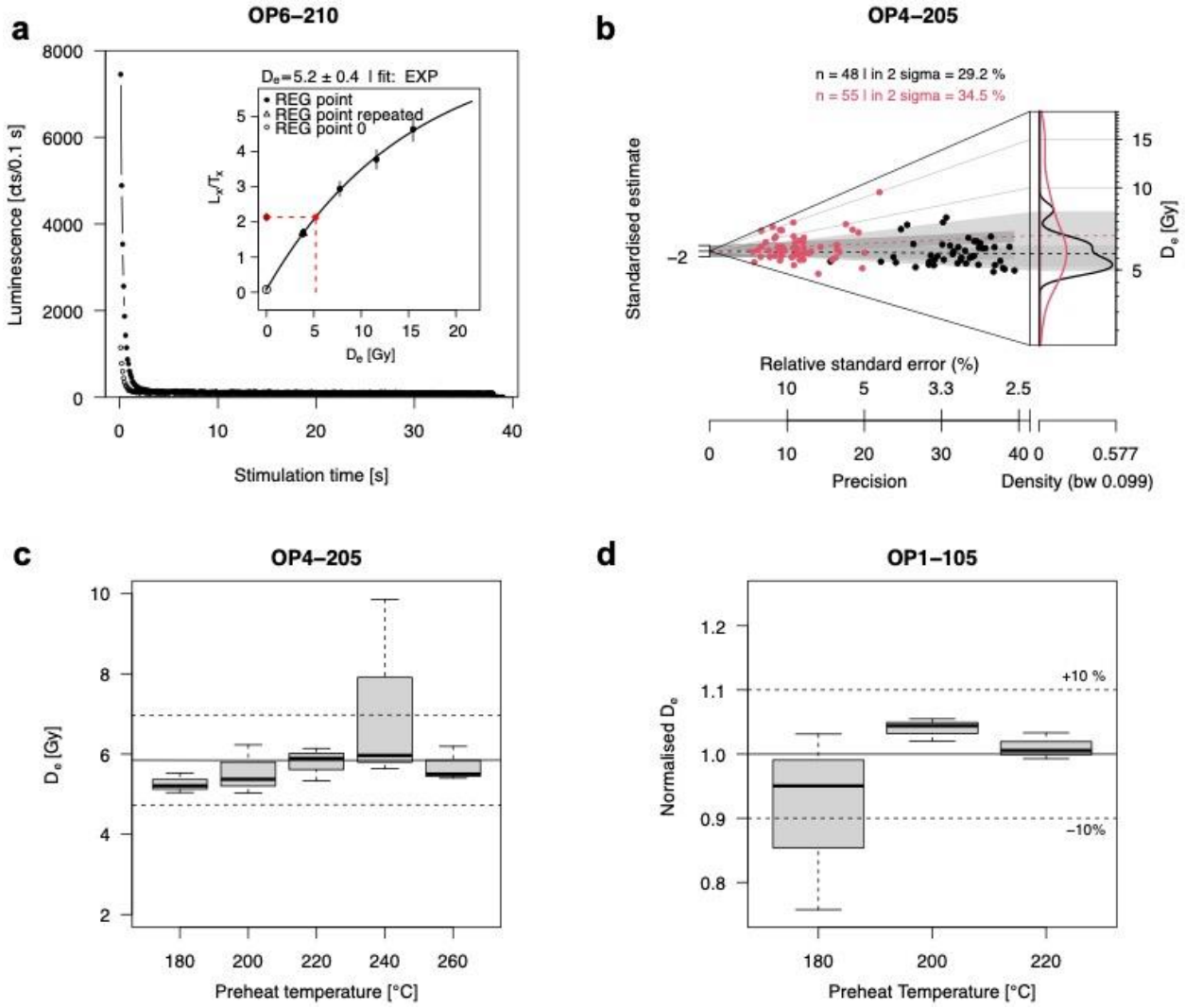

Figure 3.9: *Luminescence characteristics of the analysed quartz samples from the Chobe enclave. (a) OSL decay curves of one aliquot of sample OP6-210. Solid symbols denote the natural decay curve; open symbols represent the decay curve corresponding to the first test dose. The inset shows a representative dose response curve of the same sample, fitted with a single saturating exponential function. (b) Abanico plot (Dietze et al., 2016) of the multi-grain (black) and single-grain (red) D_e distributions of sample OP4-205 (weighted mean as central value). (c) Boxplot of the preheat plateau test results of sample OP4-205. Three aliquots were analysed for each preheat temperature. The solid black line marks the average dose of all shown aliquots (5.85 Gy); the dashed lines represent the standard deviation from this value. (d) Boxplot of the dose recovery test results of sample OP1-105. The recovery dose administered was 2.15 Gy. Three aliquots were analysed for each preheat temperature.*

3.5 Discussion

3.5.1 Geometry and internal structures of landforms

The sand ridge – The remnant asymmetrical and linear morphology of sand ridges in the Chobe Enclave remains sparsely vegetated with elevations reaching as high as 936 m (Fig. 3.1d). Secondly, the eastern margins of individual ridges show a sharp linear contact with the floodplain, whereas their western margins display typical *en-chevron* shapes (Fig. 3.2). This geometry is the consequence of sheetwash erosion on slopes of asymmetrical structural reliefs in arid and semiarid zones (Parsons and Abrahams, 2009), the longest slope dipping into the direction of the open *en-chevron* V-shape (Fig. 3.1). Nevertheless, some steep slopes enclose these geomorphological features (Fig. 3.1e), emphasizing some inheritance: indeed, the sand-ridge appears as a fossil relief, shaped in a different environment than at present, in order to get the *en-chevron* morphology. Today, however, erosion seems to equally affect both sides of the ridge (Fig. 3.1d). Moreover, the Chobe Enclave sand ridges have been formerly reported as floodplain beach ridges that were emplaced synchronously with Lake Thamalakane phases (Burrough and Thomas, 2008). Typically, beach ridges refer to stabilized, aeolian, relict wave-built shoreline features, which may consist of either siliciclastic or calcareous clastic material. Before they were stabilized, they would either have a regressive or transgressive history (Otvos, 2000). On the other hand, the internal structure of sand ridges from GPR profiles indicates the presence of bounding surfaces (Fig. 3.8), emphasized by continuous sub-horizontal reflectors. These internal structures suggest the past occurrence of *different depositional events within the ridges*. The processed GPR reflection data allowed the internal structure of the sand ridge to be observed to a depth of 8 m and prominent radar surfaces were identified as continuous bounding surface (*cbs)*. Below these features, there is a boundary of high signal attenuation, indicating a finer conductive unit below or a zone of higher moisture content. This latter could represent the floodplain deposits or finer sediments with higher moisture content. The *cbs* correspond to possible *erosional bounding surfaces* and are characterized by continuous sub-horizontal reflectors along the sand ridge. From the above evidence, the internal structure of the sand ridge likely relates to a transition zone from the upper dry sand with erosional surfaces to lower floodplain deposits / finer sediments with high moisture content. Consequently, the erosional bounding surfaces observed in the deep

parts of the sand ridge could originate either from a lacustrine (associated to shore erosion due to paleo-lakes) or an aeolian environment, or a result of both.

Furthermore, there are different sedimentary sources identified corresponding to specific origins found in the landscape of the Chobe Enclave from the interpretation of the EMMA of the PSD data. The main sedimentary sources from different bodies can be mixed in various proportions (Van Thuyne et al., 2021). Results from the *sand ridge and its margins* show similar groups of grain size contributors, but with distinct variations individually. The Kalahari sands constitute the prominent sedimentary source, characterized by the modes centered around 200 µm (Mokatse et al., 2022 and references therein) and corresponding to EM3 (Fig. 3.4a, b). This source has endured different phases of erosion and reworking with different proportions observed across study sites (Fig. 3.4b). Another depositional phase of the Kalahari sand is noted on the sand ridge margins, where two age clusters are observed (Fig. 3.4b). The first one shows the presence of the Kalahari sand, dominant in Pits 4 and 5 and represented by EM3, with ages ranging from 23.4 to 20.8 ka. The second cluster shows a larger contribution of EM1 and EM4 with ages ranging from 5.3 to 4.4 ka. The sediments from these sites include a proportion of reworked Kalahari sands, desert loess, and a diatomite mud fraction (Van Thuyne et al., 2021). EM4 displays the platykurtic curve of diatomite mud with the influence of a desert loess fraction. The last depositional phase observed occurred on the sand ridge, displaying the onset of EM2 at the bottom, and contribution of EM1 and EM4 at the top (Fig. 3.4b). It is evident that EM2 is particularly distinct on the sand ridge with ages ranging from 6.2 to 6.1 ka. The occurrence of EM2 on the sand ridge marks the deposition of reworked material of EM3 and EM1. The sand ridge and its margins compose of a mixture of one or more grain size signatures, each corresponding to a specific source. Consequently, it is revealed that the Kalahari sands (EM3) constitute the parental material of the coarse fraction dominating on the sand ridge margins. On the other hand, the sand ridge margins show a transition to a dominant presence of fine sand (EM1) and diatomite mud (EM4). Lastly, a mixture of Kalahari sands and fine sand demonstrated by EM2 thrives on sand ridges with an increased reworking of Kalahari sand, diatomite mud, and fine sand on the upper portions of the ridges.

The floodplain – The spatial distribution of the various lithologies was assessed using ERT, which showed the presence of resistive units within floodplain deposits that we interpret as

evidence of *paleo-channels* (Figs. 3.5 to 3.7). Indeed, these features likely correspond to silty fine sand bodies within the conductive silt-rich floodplain sediments. Most of the Chobe Enclave landscape is occupied by the floodplain undergoing aeolian and fluvial dynamics (Mokatse et al., 2022), and its extent limits are bounded by the Chobe and Linyanti faults. However, the sand ridge overlying the floodplain deposits displays quite astonishing features on its margins with the floodplain. These are the sharp linear contact on eastern margins and *en-chevron* patterns on the western margins. Moreover, one key feature is the antecedent drainage pattern cutting through the sand ridges (a watergap), an identification of a tectonically controlled geomorphological feature.

3.5.2 The suspected role of neotectonic activity

The present-day entrenched and anastomosed fluvial system (Fig. 3.1b, c) suggests that fluvial deflection in the Chobe is controlled by epeirogenic movements (Holbrook and Schumm, 1999). Indeed, the deflection of channels into the sagging basin, that is illustrated to have happened in the past by the presence of the paleo-channels revealed in this work, implies subsidence within the flanking structural highs. As it typically occurs in low-relief areas that experience a discrete topographical disturbance, deflection of a river during an uplift or into a zone of subsidence will manifest as an abrupt shift in the river course coincident with the deformed zone (Holbrook and Schumm, 1999). This is observed in the Chobe Enclave, where *fluvial watergaps* cut through sand ridges (Fig. 3.1b, c). Such features, observed at lower elevations are typical geomorphological indicators that usually attributes for a neotectonically influenced landscape (Clark, 1989). Furthermore, the *en-chevron* morphology displayed on the western margins and sharp linear contact on the eastern margins of the sand ridge in the Chobe Enclave are similar features to those observed on the Magikwe ridge (Burrough and Thomas, 2008, their Fig. 2) in the tilted Mababe basin (Gumbricht et al., 2001), with both Magikwe ridge and the Chobe Enclave sand ridge being incised by *fluvial watergaps*. Although small-scale neotectonic activity is not easily visible, GPR imaging of the subsurface and OSL dating of the sand ridges and sand ridge margins suggest some tectonic uplift. The resultant ages showed two clusters corresponding to the sand ridges and sand ridge margins, respectively. On the sand ridges, Pits 1 and 2 display consistent ages between 6.1 ± 0.5 and 6.2 ± 0.5 ka (Fig. 3.3a), whereas on the sand ridge margins there are two recognizable age sub-

clusters. The first cluster observed in Pits 4 and 5 provides late Pleistocene ages from 20.8 ± 1.5 to 23.4 ± 1.6 ka and the second, in Pits 3 and 6, Holocene ages from 4.4 ± 0.4 to 5.3 ± 0.3 ka (Fig. 3.3a). In addition, the syndepositional uplift of the ridge is further evidenced by the presence of erosional bounding surfaces. Geochronology of the sand ridge and sand ridge margins is further supported by the PSD curves using end-member contributions (Fig. 3.4a). Specifically, on the sand ridge, which is evidently dominated by the contribution of EM2, it is the only site with this signature. This observation possibly links the onset of EM2 on the sand ridge with the syndepositional uplift event. These observations must reflect the deformation caused by epeirogenic movements acting on the low relief landscape of the Chobe Enclave at the time. Indeed, the topographic positions of studied pits and their corresponding sedimentary signatures show evidence of variability of sediments because of erosion. The sedimentary signatures from end-member contributions in the PSD support this as well, due to the reworking of sediments. This strongly suggests that an erosional phase could have been triggered by a possible neotectonic activity, the latter providing some relief potential for sediment reworking and erosion in this otherwise very flat topography.

The development of the large-scale Chobe Enclave landscape is hypothesized to have begun with high displacement rate along the Chobe fault (Alvarez Naranjo, 2016). The Chobe fault is considered as the main border fault of the Okavango Graben; its nucleation points on the surface and its propagation direction along strike is NE – SW (Kinabo et al., 2008; Alvarez Naranjo, 2016). This configuration (zone of high displacement) resulted in a depocenter forming the Chobe-Linyanti sub-basin (Kinabo et al., 2007), where the formation of sharp linear eastern margin of the sand ridge indicative of wet (lake shoreline?) conditions likely began because of the subsidence of the Chobe fault hanging wall (Fig. 3.10). At this time, the subsidence of the Chobe fault hanging wall resulted in burial of a distributary channel system, observed as paleo-channels in this study. Evidence for fault segments linkage of Linyanti fault confirms its development (Kinabo et al., 2008), this resulting in uplift of the footwall and erosion. This ultimately triggers the erosion on the western margins of the sand ridge found in the Chobe Enclave and giving rise to the development of the current landscape.

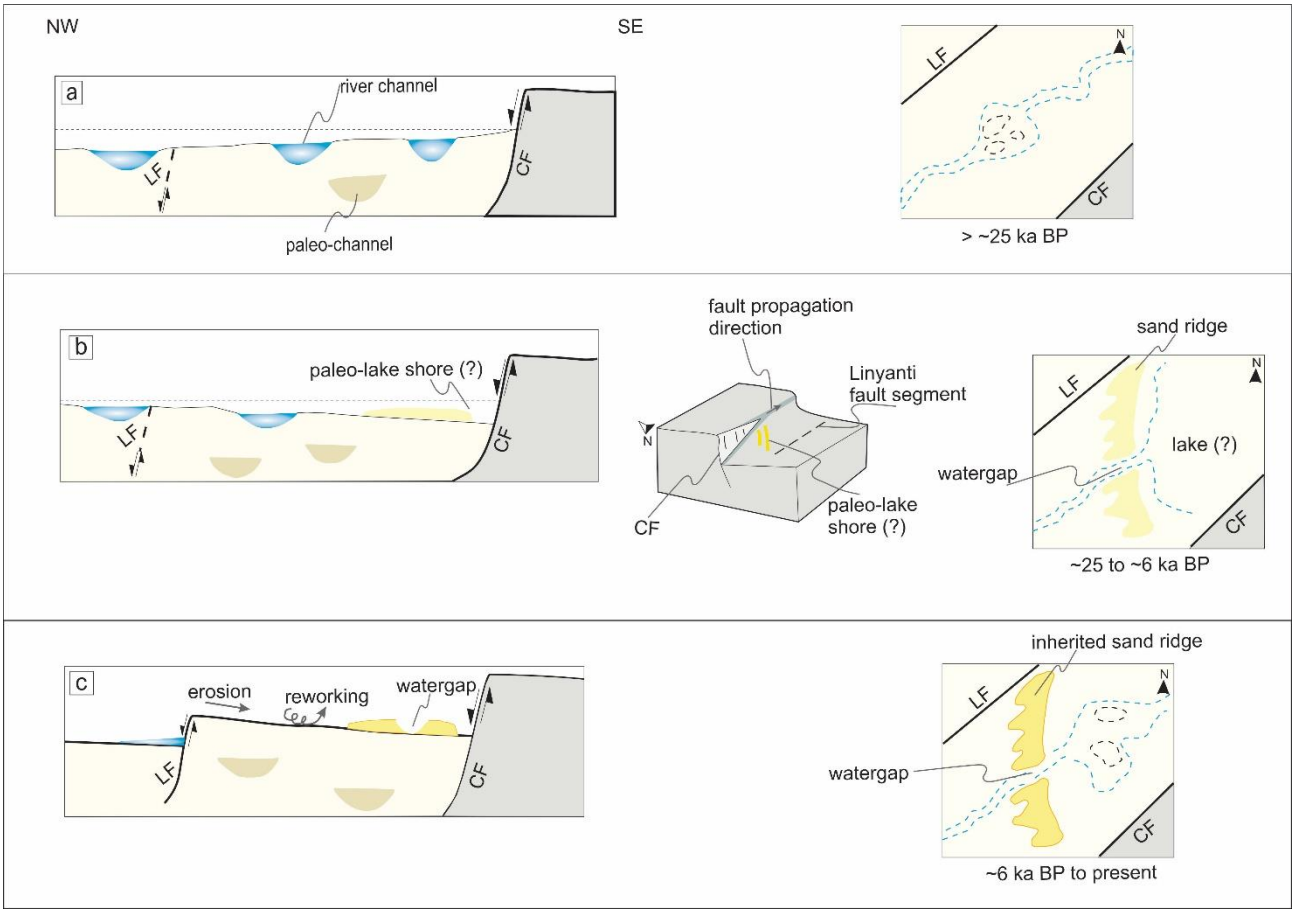

***Figure 3.10**: Schematic diagram illustrating the landscape evolution of the Chobe Enclave during the Late Pleistocene to Holocene (for details see text). LF - Linyanti fault, CF - Chobe fault.*

3.5.3 Evolution of depositional environments and Chobe Enclave's landscape

The Middle Kalahari paleolake system has been a major component for understanding late Quaternary climate and hydrological dynamics. The existence of a megalake system was proposed due to a consistency in ridge altitudes within basins of this system, with major lake highstands identified from OSL dating (Burrough et al., 2009, their Fig. 4). According to Burrough et al. (2009), the paleolacustrine environment gave rise to paleolake shorelines common to the western margins of the basins. The 'wave-built' shorelines on the western margins of paleolake Makgadikgadi are considered to be constructed by an easterly wind component of the climate system. However, it is first necessary to state that the landscape formation of the Chobe Enclave occurred in an environment situated between two faults (Linyanti and Chobe), where linkages between fault segments have prevailed and proven to exert profound influence on development of neotectonics and fluvial activities. Consequently,

the drainage patterns of the fluvial systems in the Chobe Enclave, and this part of the Middle Kalahari, were certainly influenced by these fault zones, their linkage between these zones, and the preexisting basement fabrics (Kinabo et al., 2008). This was undoubtedly a factor controlling the Late Pleistocene to Holocene landscape in the Chobe Enclave.

The evolution of the region (Fig. 3.10) can be summarized as follows: (1) the propagation of the NE-SW trending Chobe fault resulted in high displacement along the fault. Before ~25 ka (Fig. 3.10a), the fluvial systems endured burial of channels with continuous deposition across the landscape. Silty fine sand paleo-channels formed within the silt-rich floodplain deposits overlain by fine sand of the ridges. The sizes of the paleo-channels varied depending on their probable depositional patterns (Fig. 3.10a). These depositional patterns were the result of fluvial deflection due to epeirogenic movements (Holbrook and Schumm, 1999). (2) During a second step of neotectonic uplift events, between ~25 and ~6 ka (Fig. 3.10b), syntectonic deposition occurred and the continued propagation of the Chobe fault formed a depocenter making part of the Chobe-Linyanti sub-basin (Kinabo et al., 2007). During this time, some sand ridges formed. This syndepositional uplift of the sand ridge morphologies is attested by the presence of erosional bounding surfaces. This configuration triggered the formation of sharp linear eastern margin of the sand ridge, also representing a possible paleo-lake/marsh shore. Moreover, during this period, there is a prominent continued erosional phase, revealing the existence of carbonate islands emerging from the floodplain areas and creating a topographical inversion relief within the basin (Mokatse et al., 2022). Indeed, the presence of these palustrine carbonates refers to periods and/or areas of reduced clastic input and may be used as an indicator of the aggradation rate at work in the floodplain (Alonso-Zarza, 2003), as well as a change in the water chemistry. The carbonate precipitation events in the Chobe Enclave occurred irregularly, since at least ~75 ka (Diaz et al., 2019; Mokatse et al., 2022); they witness changes and some disorganization in the hydrological network, probably associated with phases triggered by neotectonics, although some climate influence cannot be totally discarded. Nevertheless, it is certainly during this phase, between ~25 and ~6 ka, that the watergaps started to form. (3) Finally, from ~ 6 ka to present day (Fig. 10c), continued fault growth and propagation of the Linyanti fault resulted in uplift of the footwall, which induced erosion to the NE of the Chobe Enclave. This contributed to essentially erode the western margins of the present-day sand ridge as well and deepen the fluvial watergaps. The sand ridge was progressively isolated from the floodplain level and constitutes an inherited relief,

presently eroded on both of its flanks, due to aeolian and fluvial reworking as a continuous phase of the landscape shaping.

3.6. Conclusions

A combination of ERT, GPR, OSL, and sedimentological data was used to investigate the geometry, internal structure, and history of the Chobe Enclave's landforms. Different depositional environments were recorded during the Late Pleistocene to Holocene in the Chobe Enclave. Throughout this time, the reworking and deposition allowed the Kalahari sand to be mixed with various proportions of different sedimentary sources from desert loess to diatomite mud. The Late Pleistocene (> ~25 ka) is characterized by burial of fluvial channels due to epeirogenic movements revealed as paleo-channels today. During ~25 ka to ~6 ka, a hypothetical paleo-lake shoreline formed, resulting in the linear eastern margin of the sand ridge. Furthermore, since ~6 ka, the neotectonic influence on the evolution of the landscape and drainage is attested by the incision of the sand ridge, forming fluvial watergaps. As this study gives insight on possible influence of neotectonics on the landscape, further work is needed to validate and explore the extent of neotectonics as well as development of the eastern-most sand ridges in the Chobe Enclave.

Acknowledgements

The authors acknowledge the Ministry of Environment, Natural Resources Conservation and Tourism of the Republic of Botswana as well as the Chobe Enclave Conservation Trust for the research permits, without which this study would not have been possible, as well as the Botswana International University of Science and Technology and the University of Lausanne. The authors also warmly thank Dr Nathalie Diaz for her advice. This work has been supported by a Swiss National Foundation grant no 200021_172944 to EPV.

References

Aitken, M. J. 1998. An Introduction to Optical Dating. The Dating of Quaternary Sediments by the Use of Photon-Stimulated Luminescence. Oxford, New York, Tokyo: Oxford University Press, 267 pp.

Alonso-Zarza, A.M., 2003. Palaeoenvironmental significance of palustrine carbonates and calcretes in the geological record. Earth-Science Reviews, 60(3-4), 261-298.

Alvarez Naranjo, A., 2016. The role of pre-existing basement fabrics in the initiation of continental rifting: The Okavango Rift Zone, Botswana. Doctoral Dissertations. 2642. https://scholarsmine.mst.edu/doctoral_dissertations/2642.

Alvarez Naranjo, A., Hogan, J.P., 2013. The role of tectonic inheritance in the geometry and location of continental rifts-An example from the Okavango Rift Zone, Botswana. Geological Society of America Abstracts with Programs. Vol. 45, No. 7, 832.

Annan, A.P., Davis, J.L., 1992. Design and development of a digital ground penetrating radar system. In: Pilon, J. (Ed.), GroundPenetrating Radar. Geol. Surv. Can. Pap. 90-4, 15–23.

Baines, D., Smith, D.G., Froese, D.G., Bauman, P., Nimeck, G., 2002. Electrical resistivity ground imaging (ERGI): a new tool for mapping the lithology and geometry of channel-belts and valley-fills. Sedimentology, 49(3), 441-449.

Barber, D.C., Brown, B.H., 1984. Applied potential tomography. Journal of Physics E: Scientific Instruments, 17(9), 723-733.

Bishop, M.P., Shroder Jr, J.F., Colby, J.D., 2003. Remote sensing and geomorphometry for studying relief production in high mountains. Geomorphology, 55(1-4), 345-361.

Brennan, B.J., Lyons, R.G., Phillips, S.W., 1991. Attenuation of alpha particle track dose for spherical grains. International Journal of Radiation Applications and Instrumentation. Part D. Nuclear Tracks and Radiation Measurements, 18(1-2), 249-253.

Bristow, C.S., 2009. Ground penetrating radar in aeolian dune sands, in: Jol, H.M. (Ed.), Ground Penetrating Radar: Theory and Applications. Elsevier Science: Amsterdam, The Netherlands, pp. 273-297.

Bristow, C.S., Duller, G.A.T., Lancaster, N., 2007. Age and dynamics of linear dunes in the Namib Desert. Geology, 35(6), 555-558.

Bristow, C.S., Jol, H.M., 2003. An introduction to ground penetrating radar (GPR) in sediments. Geological Society, London, Special Publications, 211(1), 1-7.

Bristow, C.S., Lancaster, N., Duller, G.A.T., 2005. Combining ground penetrating radar surveys and optical dating to determine dune migration in Namibia. Journal of the Geological Society, 162(2), 315-321.

Bufford, K.M., Atekwana, E.A., Abdelsalam, M.G., Shemang, E., Atekwana, E.A., Mickus, K., Molwalefhe, L., 2012. Geometry and faults tectonic activity of the Okavango Rift Zone, Botswana: Evidence from magnetotelluric and electrical resistivity tomography imaging. Journal of African Earth Sciences, 65, 61-71.

Burke, K., Gunnell, Y., 2008. The African erosion surface: a continental-scale synthesis of geomorphology, tectonics, and environmental change over the past 180 million years (Vol. 201). Memoir of the Geological Society of America 201, 1-66.

Burrough, S.L., Thomas, D.S., Shaw, P.A., Bailey, R.M., 2007. Multiphase quaternary highstands at lake Ngami, Kalahari, northern Botswana. Palaeogeography, Palaeoclimatology, Palaeoecology, 253(3-4), 280-299.

Burrough, S.L., Thomas, D.S.G., 2008. Late Quaternary lake-level fluctuations in the Mababe Depression: Middle Kalahari palaeolakes and the role of Zambezi inflows. Quaternary Research, 69(3), 388-403.

Burrough, S.L., Thomas, D.S., Singarayer, J.S., 2009. Late Quaternary hydrological dynamics in the Middle Kalahari: forcing and feedbacks. Earth-Science Reviews, 96(4), 313-326.

Campbell, G., Johnson, S., Bakaya, T., Kumar, H., Nsatsi, J., 2006. Airborne geophysical mapping of aquifer water quality and structural controls in the Lower Okavango Delta, Botswana. South African Journal of Geology, 109(4), 475-494.

Chorowicz, J., 2005. The east African rift system. Journal of African Earth Sciences, 43(1-3), 379-410.

Clark, G.M., 1989. Central and southern Appalachian water and wind gap origins: Review and new data. Geomorphology, 2(1-3), 209-232.

Cooke, H.J., 1980. Landform evolution in the context of climatic change and neo-tectonism in the Middle Kalahari of north-central Botswana. Transactions of the Institute of British Geographers, 5 (1), 80-99.

Daly, M.C., Green, P., Watts, A.B., Davies, O., Chibesakunda, F., Walker, R., 2020. Tectonics and landscape of the Central African Plateau and their implications for a propagating Southwestern Rift in Africa. Geochemistry, Geophysics, Geosystems, 21(6), e2019GC008746.

Diaz, N., Armitage, S.J., Verrecchia, E.P., Herman, F., 2019. OSL dating of a carbonate island in the Chobe Enclave, NW Botswana. Quaternary Geochronology, 49, 172-176.

Dietze, E., Hartmann, K., Diekmann, B., IJmker, J., Lehmkuhl, F., Opitz, S., Borchers, A., 2012. An end-member algorithm for deciphering modern detrital processes from lake sediments of Lake Donggi Cona, NE Tibetan Plateau, China. Sedimentary Geology, 243, 169-180.

Dietze, M., Kreutzer, S., Burow, C., Fuchs, M.C., Fischer, M., Schmidt, C., 2016. The abanico plot: visualising chronometric data with individual standard errors. Quaternary Geochronology, 31, 12-18.

Dietze, E., Maussion F., Ahlborn, M., Diekmann, B., Hartmann, K., Henkel, K., Kasper, T., Lockot, G., Opitz, S., Haberzettl, T., 2013a. Sediment transport processes across the Tibetan Plateau inferred from robust grain size end-members in lake sediments. Clim Past 9:4855–4892.

Dietze, E., Wünnemann, B., Hartmann, K., Diekmann, B., Jin, H., Stauch, G., Yang, S., Lehmkuhl, F., 2013b. Early to mid-Holocene lake high-stand sediments at Lake Donggi Cona, northeastern Tibetan Plateau, China. Quat Res 79:325–336.

Dixey, F., 1956. The east African rift system. HM Stationery Office.

Doucouré, C.M., de Wit, M.J., 2003. Old inherited origin for the present near-bimodal topography of Africa. Journal of African Earth Sciences, 36(4), 371-388.

Duller, G.A.T., 2015. The analyst software package for luminescence data: overview and recent improvements. Ancient TL 33, 35-42.

Durcan, J.A., King, G.E., Duller, G.A.T., 2015. DRAC: dose rate and age calculator for trapped charge dating. Quat. Geochronol. 28, 54-61.

Eckardt, F.E., Flügel, T., Cotterill, F., Rowe, C., McFarlane, M., 2016. Kalahari tectonic landforms and processes beyond the Okavango Graben. Quaternary International, 404, 194.

Fairhead, J.D., Girdler, R.W., 1969. How far does the rift system extend through Africa? Nature, 221(5185), 1018-1020.

Folk, R.L., 1954. The distinction between grain size and mineral composition in sedimentary-rock nomenclature. Journal of Geology 62: 344–359.

Folk, R.L., Ward, W.C., 1957. Brazos River bar: a study in the significance of grain size parameters. Journal of Sedimentary Petrology 27 (1), 3–26.

Galbraith, R.F., Roberts, R.G., Laslett, G.M., Yoshida, H., Olley, J.M., 1999. Optical Dating of Single and Multiple Grains of Quartz from Jinmium Rock Shelter, Northern Australia: Part I, Experimental Design and Statistical Models. Archaeometry 41, 339-364.

Gawthorpe, R.L., Hurst, J.M., 1993. Transfer zones in extensional basins: their structural style and influence on drainage development and stratigraphy. J. Geol. Soc. London, 150, 1137–1152.

Google Earth, 2020. Chobe region, Botswana. Pro V 7.3.4.8573, CNES/Airbus 2020. http://www.earth.google.com.

Grove, A.T., 1969. Landforms and climatic change in the Kalahari and Ngamiland. The Geographical Journal, 135(2), 191-212.

Guérin, G., Mercier, N., Adamiec, G., 2011. Dose-rate conversion factors: update. Ancient TL, 29(1), 5-8.

Guérin, G., Mercier, N., Nathan, R., Adamiec, G., Lefrais, Y., 2012. On the use of the infinite matrix assumption and associated concepts: a critical review. Radiation Measurements, 47(9), 778-785.

Gumbricht, T., McCarthy, T.S., Merry, C.L., 2001. The topography of the Okavango Delta, Botswana, and its tectonic and sedimentological implications. South African Journal of Geology, 104(3), 243-264.

Günther, T., Rücker, C., 2019. Boundless Electrical Resistivity Tomography BERT v2. 2–the user tutorial, LIAG Hannover, TU Berlin, http://www.resistivity.net/download/bert-tutorial.pdf.

Holbrook, J., Schumm, S.A., 1999. Geomorphic and sedimentary response of rivers to tectonic deformation: a brief review and critique of a tool for recognizing subtle epeirogenic deformation in modern and ancient settings. Tectonophysics, 305(1-3), 287-306.

Huntsman-Mapila, P., Kampunzu, A.B., Vink, B., Ringrose, S., 2005. Cryptic indicators of provenance from the geochemistry of the Okavango Delta sediments, Botswana. Sedimentary Geology, 174(1-2), 123-148.

Huntsman-Mapila, P., Tiercelin, J.J., Benoit, M., Ringrose, S., Diskin, S., Cotten, J., Hémond, C., 2009. Sediment geochemistry and tectonic setting: Application of discrimination diagrams to early stages of intracontinental rift evolution, with examples from the Okavango and Southern Tanganyika rift basins. Journal of African Earth Sciences, 53(1-2), 33-44.

Keller, E.A., Pinter, N., 1996. Active Tectonics. Prentice-Hall, Upper Saddle River, 338 pp.

Kim, J.C., Duller, G.A.T., Roberts, H.M., Wintle, A.G., Lee, Y.I., Yi, S.B., 2009. Dose dependence of thermally transferred optically stimulated luminescence signals in quartz. Radiation Measurements, 44(2), 132-143.

Kinabo, B.D., Atekwana, E.A., Hogan, J.P., Modisi, M.P., Wheaton, D.D., Kampunzu, A.B., 2007. Early structural development of the Okavango rift zone, NW Botswana. J. Afr. Earth Sci. 48, 125–136.

Kinabo, B.D., Hogan, J.P., Atekwana, E.A., Abdelsalam, M.G., Modisi, M.P., 2008. Fault growth and propagation during incipient continental rifting: Insights from a combined aeromagnetic and Shuttle Radar Topography Mission digital elevation model investigation of the Okavango Rift Zone, northwest Botswana. Tectonics 27, TC3013Natu.

Kreutzer, S., Schmidt, C., Fuchs, M.C., Dietze, M., Fischer, M., Fuchs, M., 2012. Introducing an R package for luminescence dating analysis. Ancient TL 30 (1), 1-8.

Loke, M.H. (2004) Rapid 2-D Resistivity & IP inversion using the least-squares method. Wenner (a,b,g), dipole-dipole, inline pole-pole, pole-dipole, equatorial dipole-dipole, Wenner-Schlumberger and non-conventional arrays on land, underwater and cross-borehole surveys. RES2DINV ver. 3.54 Manual. Geotomo Software.

Loke, M.H., Barker, R.D., 1996. Rapid least-squares inversion of apparent resistivity pseudosections by a quasi-Newton method1. Geophysical prospecting, 44(1), 131-152.

Mallick, D.I.J., Habgood, F., Skinner, A.C., 1981. A geological interpretation of Landsat imagery and air photography of Botswana. Overseas Geology and Mineral Resources, 56, Institute of Geological Sciences: London, 36 pp.

Mauz, B., Lang, A., 2004. Removal of the feldspar-derived luminescence component from polymineral fine silt samples for optical dating applications: evaluation of chemical treatment protocols and quality control procedures. Ancient TL, 22(1), 1-8.

McCarthy, T.S., 2013. The Okavango Delta and its place in the geomorphological evolution of southern Africa. South African Journal of Geology, 116(1), 1-54.

McFarlane, M.J., Eckardt, F.D., 2007. Palaeodune morphology associated with the Gumare fault of the Okavango graben in the Botswana/Namibia borderland: a new model of tectonic influence. South African Journal of Geology, 110(4), 535-542.

Modisi, M.P., Atekwana, E.A., Kampunzu, A.B., Ngwisanyi, T.H., 2000. Rift kinematics during the incipient stages of continental extension: Evidence from the nascent Okavango rift basin, northwest Botswana. Geology, 28(10), 939-942.

Mokatse, T., Diaz, N., Shemang, E., Van Thuyne, J., Vittoz, P., Vennemann, T., Verrecchia, E.P., 2022. Landscapes and landforms of the Chobe Enclave, Northern Botswana, in: Eckardt, F. (Ed.), Landscapes and Landforms of Botswana. Springer-Nature, Dordrecht, 91-116. doi.org/10.1007/978-3-030-86102-5_6.

Moore, A.E., 1999. A reappraisal of epeirogenic flexure axes in southern Africa. South African Journal of Geology, 102, 363-376.

Moore, A.E., Cotterill, F.P.D., Eckardt, F.D., 2012. The evolution and ages of Makgadikgadi palaeo-lakes: consilient evidence from Kalahari drainage evolution south-central Africa. South African Journal of Geology, 115(3), 385-413.

Moorkamp, M., Fishwick, S., Walker, R.J., Jones, A.G., 2019. Geophysical evidence for crustal and mantle weak zones controlling intra-plate seismicity–the 2017 Botswana earthquake sequence. Earth and Planetary Science Letters, 506, 175-183.

Murray, A.S., Wintle, A.G., 2000. Luminescence dating of quartz using an improved single-aliquot regenerative-dose protocol. Radiation Measurements 32, 57–73.

Nasa, J.P.L., 2013. NASA shuttle radar topography mission global 1 arc second. Nasa Lp Daac, 15.

Nash, D.J., Eckardt, F.D., 2015. Drainage development, neotectonics and base-level change in the Kalahari Desert, southern Africa. South African Geographical Journal, 98(2), 308-320.

Neal, A., 2004. Ground-penetrating radar and its use in sedimentology: principles, problems and progress. Earth-science reviews, 66(3-4), 261-330.

Otvos, E.G., 2000. Beach ridges—definitions and significance. Geomorphology, 32(1-2), 83-108.

Parsons, A.J., Abrahams, A.D., 2009. Geomorphology of desert environments, in: Parsons, A.J., Abrahams, A.D. (Eds.), Geomorphology of Desert Environments. Springer Nature, Dordrecht, pp. 3-7.

Partridge, T.C., 1998. Of diamonds, dinosaurs and diastrophism: 150 million years of landscape evolution in southern Africa. South African Journal of Geology, 101(3), 167-184.

Pastier, A.-M., Dauteuil, O., Murray-Hudson, M., Moreau, F., Walpersdorf, A., Makati, K., 2017. Is the Okavango Delta the terminus of the East African Rift System? Towards a new geodynamic model: Geodetic study and geophysical review. Tectonophysics, 712 –713, 469–481.

Podgorski, J. E., Green, A. G., Kgotlhang, L., Kinzelbach, W. K., Kalscheuer, T., Auken, E., & Ngwisanyi, T. (2013). Paleo-megalake and paleo-megafan in southern Africa. *Geology*, *41*(11), 1155-1158.

Prins, M.A., Bouwer, L.M., Beets, C.J., Troelstra, S.R., Weltje, G.J., Kruk, R.W., Vroon, P. Z., 2002. Ocean circulation and iceberg discharge in the glacial North Atlantic: Inferences from unmixing of sediment size distributions. Geology, 30(6), 555-558.

Prins, M.A., Vriend, M., Nugteren, G., Vandenberghe, J., Lu, H., Zheng, H., Weltje, G.J., 2007. Late Quaternary aeolian dust input variability on the Chinese Loess Plateau: inferences from unmixing of loess grain-size records. Quaternary Science Reviews, 26(1-2), 230-242.

R Core Team, 2021. R: a Language and Environment for Statistical Computing. R Foundation for Statistical Computing, Vienna, Austria. https://www.R-project.org/.

Rhea, S., 1993. Geomorphic observations of rivers in the Oregon Coast Range from a regional reconnaissance perspective. Geomorphology, *6*(2), 135-150.

Ringrose, S., Downey, B., Genecke, D., Sefe, F., Vink, B., 1999. Nature of sedimentary deposits in the western Makgadikgadi basin, Botswana. Journal of arid environments, 43(4), 375-397.

Ringrose, S., Huntsman-Mapila, P., Kampunzu, H., Downey, W.D., Coetzee, S., Vink, B., Vanderpost, C., 2005. Geomorphological and geochemical evidence for palaeo feature formation in the northern Makgadikgadi sub-basin, Botswana. Palaeogeography, Palaeoclimatology and Palaeoecology, 217, 265-287.

Ringrose, S., Harris, C., Huntsman-Mapila, P., Vink, B.W., Diskins, S., Vanderpost, C., Matheson, W., 2009. Origins of strandline duricrusts around the Makgadikgadi Pans (Botswana Kalahari) as deduced from their chemical and isotope composition. Sedimentary Geology, 219(1-4), 262-279.

Riquelme, R., Martinod, J., Hérail, G., Darrozes, J., Charrier, R., 2003. A geomorphological approach to determining the Neogene to Recent tectonic deformation in the Coastal Cordillera of northern Chile (Atacama). Tectonophysics, 361(3-4), 255-275.

Ruszkiczay-Rüdiger, Z., Fodor, L., Horváth, E., Telbisz, T., 2009. Discrimination of fluvial, eolian and neotectonic features in a low hilly landscape: A DEM-based morphotectonic analysis in the Central Pannonian Basin, Hungary. Geomorphology, 104(3-4), 203-217.

Schmidt, C., Zeeden, C., Krauß, L., Lehmkuhl, F., Zöller, L., 2021. A chronological and palaeoenvironmental re-evaluation of two loess-palaeosol records in the northern Harz foreland, Germany, based on innovative modelling tools. Boreas 50, 746-763.

Schumm, S.A., Dumont, J.F., Holbrook, M.J., 2002. Active Tectonics and Alluvial Rivers. Cambridge University Press, Cambridge, 276 pp.

Silva, P.G., Goy, J.L., Zazo, C., Bardaj, T., 2003. Fault-generated mountain fronts in southeast Spain: geomorphologic assessment of tectonic and seismic activity. Geomorphology, 50(1-3), 203-225.

Shaw, P.A., Cooke, H.J., 1986. Geomorphic evidence for the late Quaternary palaeoclimates of the middle Kalahari of northern Botswana. Catena, 13(4), 349-359.

Shaw, P.A., Thomas, D.S.G., 1988. Lake Caprivi: a late Quaternary link between the Zambezi and middle Kalahari drainage systems. Zeitschrift für Geomorphologie 32 (3), 329-337.

Shaw, P.A., Cooke, H.J., Thomas, D.S.G., 1988. Recent advances in the study of Quaternary landforms in Botswana. Collection Palaeoecology of Africa 19, 15-26.

Shaw, P.A., Stokes, S., Thomas, D.S.G., Davies, F.B.M., Holmgren, K., 1997. Palaeoecology and age of a Quaternary high lake level in the Makgadikgadi Basin of the Middle Kalahari, Botswana. South African Journal of Science, 93(6), 273-276.

Stolt, R.H., 1978. Migration by Fourier transform. Geophysics 43, 23–48.

Storz, H., Storz, W., Jacobs, F., 2000. Electrical resistivity tomography to investigate geological structures of the earth's upper crust. Geophysical prospecting, 48(3), 455-472.

Vainer, S., Erel, Y., Matmon, A., 2018. Provenance and depositional environments of Quaternary sediments in the southern Kalahari Basin. Chemical Geology, 476, 352-369.

Vainer, S., Matmon, A., Erel, Y., Hidy, A.J., Crouvi, O., De Wit, M., Geller, Y., ASTER Team, 2021a. Landscape responses to intraplate deformation in the Kalahari constrained by sediment provenance and chronology in the Okavango Basin. Basin Research, 33(2), 1170-1193.

Vainer, S., Matmon, A., Dor, Y.B., Verrecchia, E., Aumaitre, G., 2021b. Eolian chronology reveals causal links between tectonics, climate, and erg generation. PRE_PRINT-Researchsquare. : https://doi.org/10.21203/rs.3.rs-801542/v1.

Van Thuyne, J., Darini, I., Mainga, A., Verrecchia, E.P., 2021. Are fungus-growing termites super sediment-sorting insects of subtropical environments? Journal of Arid Environments, 193, 104566.

Wisen, R., Auken, E., Dahlin, T., 2005. Combination of 1D laterally constrained inversion and 2D smooth inversion of resistivity data with a priori data from boreholes. European Association of Geoscientists & Engineers, Near Surface Geophysics 3, 71–79.

Yu, Y., Gao, S.S., Moidaki, M., Reed, C.A., Liu, K.H., 2015a. Seismic anisotropy beneath the incipient Okavango rift: implications for rifting initiation. Earth Planet. Sci. Lett. 430, 1–8.

Yu, Y., Liu, K.H., Moidaki, M., Reed, C.A., Gao, S.S., 2015b. No thermal anomalies in the mantle transition zone beneath an incipient continental rift: evidence from the first receiver function study across the Okavango rift zone, Botswana. Geophys. J. Int. 202 (2), 1407–1418.

Yu, Y., Liu, K.H., Huang, Z., Zhao, D., Reed, C.A., Moidaki, M., Lei, J., Gao, S.S., 2017. Mantle structure beneath the incipient Okavango rift zone in southern Africa. Geosphere 13 (1), 102–111.

CHAPTER 4

Sepiolite as a multifactorial indicator of paleoenvironments in the Chobe Enclave

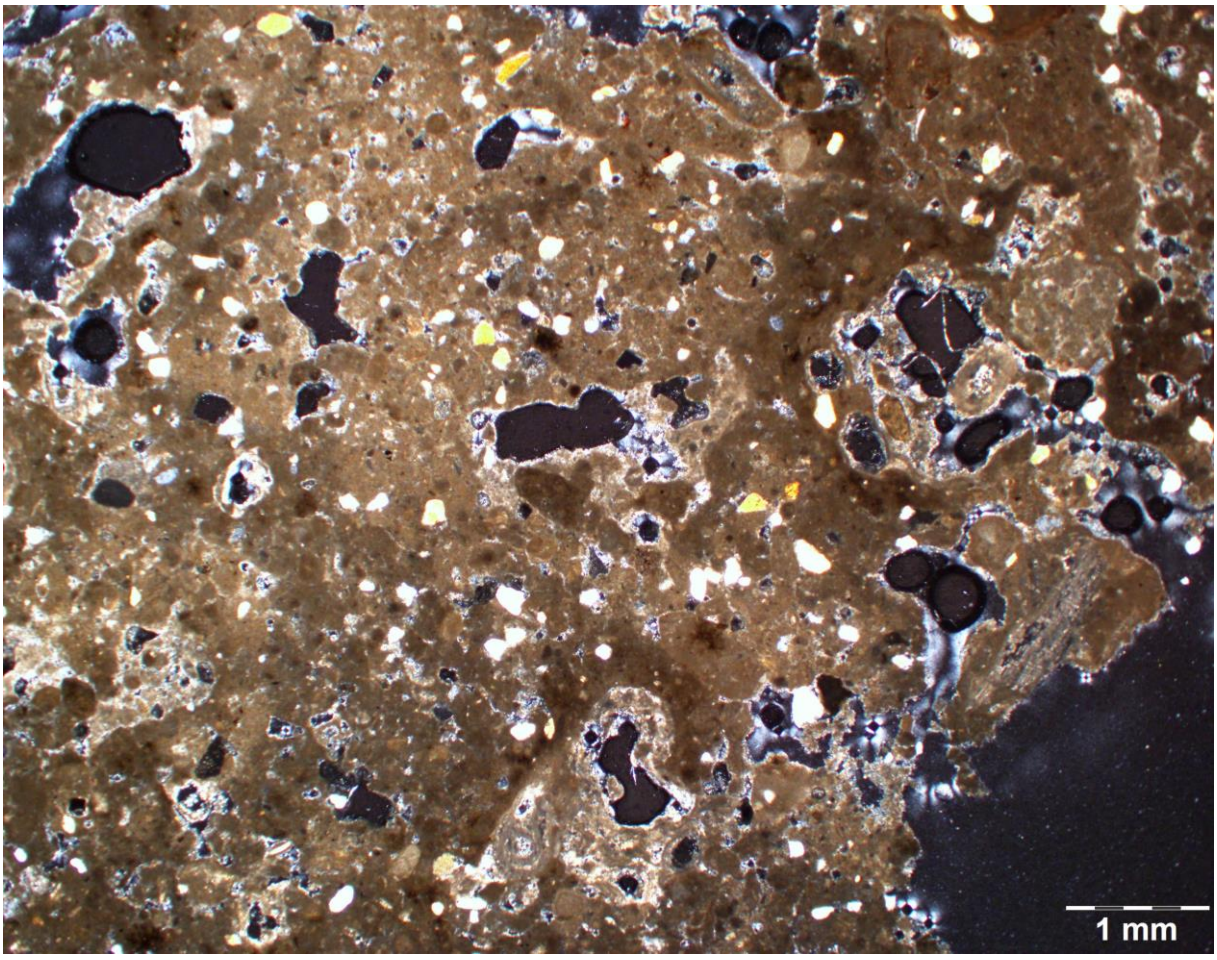

Optical microphotograph of a palustrine carbonate with trapped quartz grains

4. Sepiolite as a multifactorial indicator of paleoenvironments in the Chobe Enclave (northern Botswana)

Published as

Mokatse, T., Prud'Homme, C., Vainer, S., Adatte, T., Shemang, E., Verrecchia, E. P. (2023). Sepiolite as a multifactorial indicator of paleoenvironments in the Chobe Enclave (northern Botswana). *Sedimentary Geology*, *454*, 106459.

In this chapter, personal work entails fieldwork and data collection, preparation of samples (grain size distributions, bulk and clay fractions), writing of the paper.

Synopsis

The concept of this paper was motivated by the completion of Chapter 3. After successfully delineating the geometry of the sedimentary deposits in the region associated with the landforms, it was important to understand the mineralogy of the system which surprisingly revealed the occurrence of fibrous clay minerals from X-ray diffraction studies and scanning electron microscopy. This paved the way to investigate the nature and significance of this mineral occurrence.

Abstract

The origin and evolution of clay minerals in sedimentary basins is usually influenced by changes in depositional hydrochemistry. The formation and preservation of rare fibrous magnesium-rich clay minerals, like sepiolite, is of interest in the Chobe Enclave, northern Botswana, as it occurred in a siliceous-rich intra-cratonic basin. New X-Ray diffraction (XRD) data, scanning electron (SEM) and transmission electron (TEM) microscopy analyses, as well as geochemical data, are used to study the origin of authigenic sepiolite and the sub-environments related to its formation in the Chobe Enclave. The paleoenvironment record during the Late Pleistocene to Holocene demonstrates that the deposition in the region was preceded by an alluvial fan/fluvial deposits in humid conditions. The upper-basin catchment yielded a clay assemblage, including kaolinite and minor smectite amounts, now preserved in the Chobe as a detrital phase. The alluvial fan deposits were later overlain by deposits from lacustrine/palustrine environments where significant hydrochemical changes took place: during these changes, a fibrous clay mineral (authigenic sepiolite) formed in shallow lake/marshes in a closed system with low energy, under the influence of magnesium-rich and alkaline waters. The mineralogical and geometrical (diagenetic) relationships between the palustrine deposits (carbonate facies) and sepiolite point to a sequence of precipitation from an evaporitic system in which calcite, sepiolite, and finally amorphous silica follow one another. In addition, although the sepiolite parent solution was enriched from a water source concentrated in Mg^{2+}, the presence of Ba^{2+} ions also emphasize some spells of hydrothermal activity.

4.1 Introduction

Clay minerals form under different geological environments and their depositional and diagenetic assemblages in sedimentary basins constitute a potential record of morphological, tectonic, and climatic conditions that prevailed during their formation (Webster and Jones, 1994; Lopez and Gonzalez, 1995; Akbulut and Kadir, 2003; Cuevas et al., 2003; Hong et al., 2007). Because the origin of the clay minerals can be either authigenic or detrital (Chamley, 1989), changes in depositional hydrochemistry that can be caused by tectonics and drainage evolution affecting source area lithology, influence the characteristics of clay mineral assemblages. The changing depositional hydrochemistry involves varying parameters, such as pH, ion species and concentrations in both surface and pore waters. In sedimentary environments, neoformation (or authigenesis) can take place in both syngenetic and diagenetic settings, whereas transformation is mainly related to diagenesis with formation of specific clay minerals depending on physicochemical conditions (Chamley, 1989). Sepiolite, a relatively rare clay mineral in nature, is a fibrous clay mineral of the following average structural formula: $Mg_4Si_6O_{15}(OH)_2.6H_2O$ (Galán and Singer, 2011). The sepiolite structure is composed of a 2:1 type ribbon with four octahedral positions occupied by Mg^{2+} and sometimes by Al^{3+} or Fe^{3+} (Fersmann, 1913; Shannon, 1929; Kauffman, 1943; Galán and Singer, 2011). Its origin commonly lies on authigenic processes, i.e., its precipitation takes place directly from a solution in which the main sepiolite components, namely magnesium and silicon, are present in high concentrations (Mizutani et al., 1991; Galán and Carretero, 1999; Akbulut and Kadir, 2003; Wang et al., 2009). The first step necessary to precipitate sepiolite consists of an increase in Mg^{2+} and Si^{4+} ion activities in the solution, as well as the persistence of low Al^{3+} activity (Birsoy, 2002). So far, these conditions were observed in two different environments: (1) the most documented is related to the alteration and weathering of volcanic rocks (Yalçin and Bozkaya, 2011) as well as low temperature hydrothermalism (Irkec and Ünlü, 1993; Galán and Pozo, 2011), and (2) the transformation of previous sedimentary minerals, such as dolomite or smectite (Jones and Conko, 2011). Once the required ions are in the solution, sepiolite precipitation can be triggered by progressive and increasing concentrations of Mg^{2+} and Si^{4+} ions in the parent solution, frequently obtained during evaporation (Helgeson et al., 1969). Furthermore, a high pH (usually > 8-9) and a low

concentration of impurities within a low energy waterbody, constitute ideal conditions to form the fibrous crystals of sepiolite (Pozo and Calvo, 2018).

Sepiolite is principally observed in lacustrine to palustrine environments with high evaporation rates, due to prevalent semiarid to arid climate conditions (Stoessel and Hay, 1978; Tateo et al., 2001; Garcia-Romero et al., 2007; Draidia et al., 2016). However, its occurrence in a large sandy silica-rich basin has only been scarcely documented (Pardo et al., 2009; Miller et al., 2010). Moreover, critical questions arise relating to the source of Ca being able to form carbonate beds associated with sepiolite in a highly siliceous environment. Some decimeter-thick deposits, with the presence of various amounts of sepiolite, have been investigated to characterize these clay minerals and to provide clues about the major processes at play. Therefore, this study aims at assessing the sub-environments and their relation to the formation of sepiolite in the Chobe Enclave, located in Northern Botswana.

The following questions are investigated: (1) What lithofacies are associated with the fibrous clay minerals? (2) What could be at the origin of the input of Mg^{2+}, river transportation or hydrothermal input? (3) Was the increase of the pH solution obtained through evaporation and/or degassing? (4) And finally, what does sepiolite precipitation mean in terms of paleoenvironmental reconstruction?

4.2 Geological settings

Northern Botswana (Fig. 4.1) is characterized by large Quaternary sandy deposits of several hundred meters thick laying on a crustal basement constituted by Neoproterozoic formations, which are parts of the Kwando complex (Key and Ayres, 2000; Lehmann et al., 2015). These formations belong to the Ghanzi Chobe Belt, an igneous and metamorphic region set up during the Neoproterozoic and observed from West Botswana to the Chobe Enclave (Schwartz, 1996; Modie, 2000). Moreover, a “Karoo basalt formation” spreads out in the northern Botswana and is part of the Large Igneous Province (LIP), which formed between 179 and 181 Ma ago, as the last volcanic formation described in this area, with some dolerite dykes (Le Gall et al., 2002; Jourdan et al., 2004).

The Chobe Enclave is an extensional basin bounded by two major faults, the Chobe Fault (southeast) and the Linyanti Fault (northwest; Fig. 4.1). The tectonic nature of the basin can have multiple origins and is located between the East African Rift System at the

northeastern part of the Chobe Enclave and the structural depression of the Okavango Basin at its southwestern part (Vainer et al., 2021). These large tectonic structures possess a different extensional scheme, but both develop a succession of horst/graben systems affected by normal faulting (Gumbricht et al., 2001; Chorowicz, 2005). However, in this area of southern Africa, the topography is characterized by large plateaus with a flat relief (Mokatse et al., 2022a).

The Chobe Enclave forms part of Chobe-Linyanti sub-basin, infilled with Quaternary sediments largely dominated by sands deposited in semiarid conditions (Burrough et al., 2007, 2009). This basin is situated inside the intracratonic Kalahari Basin, where Plio-Pleistocene aeolian and fluvial sands, as well as sandstones, represent the most common sediments (Thomas and Shaw, 1990; Haddon and McCarthy, 2005; Matmon et al., 2015; Vainer et al., 2021, 2022). In the Chobe Enclave, the Quaternary deposits, probably between 50 and 100 m thick (Thomas and Shaw, 1991), overlay a Proterozoic metamorphic and magmatic basement. In terms of drainage, two main rivers flow into the Chobe Enclave, the Kwando/Linyanti in the southwest, and the Chobe in the northeast (Fig. 4.1). Finally, it must be noted that hydrothermalism is locally evidenced at the present-day by the presence of hot springs in the northern part of Chobe Enclave (Mukwati et al., 2018). These hot springs undoubtedly point to the influence of active neotectonics in the region.

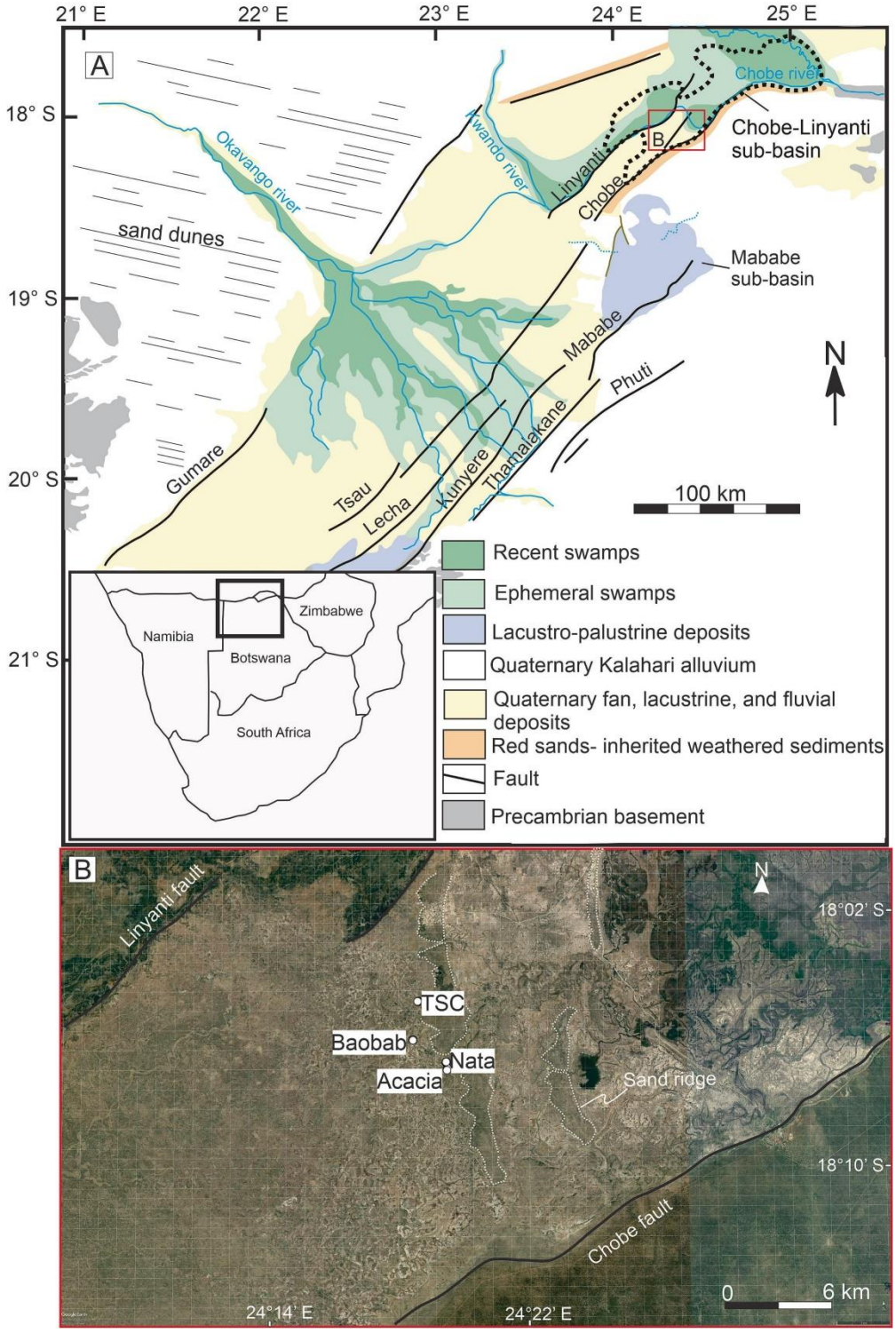

Figure 4.1: (A) Lower-left corner, map of Southern Africa with a black frame referring to the regional map in A; regional and surficial geological map of the Okavango–Linyanti graben showing the study area within the Chobe–Linyanti sub-basin (dotted line). The red rectangle refers to the area in B. (B) Satellite image showing the location of the sites (Google Earth, 2022). The Chobe and Linyanti faults are emphasized by a bold black line and sand ridges by fine dotted white lines.

4.3 Material and methods

4.3.1 Study sites

The study sites in the Chobe Enclave, i.e. (i) TSC site, (ii) Baobab quarry, (iii) Nata site and (iv) Acacia quarry (Fig. 4.1) are located on a paleo-floodplain and in a fossil carbonate-rich palustrine environment with a variety of closely associated carbonates, diatomites, and sandy deposits. Descriptions and interpretations of the facies associations were conducted at these four main sites (Fig. 4.2) across the landscape, where preferential erosion of sands around the carbonate-rich formations are observed today as elevated carbonate islands (inverted relief; Diaz et al., 2019).

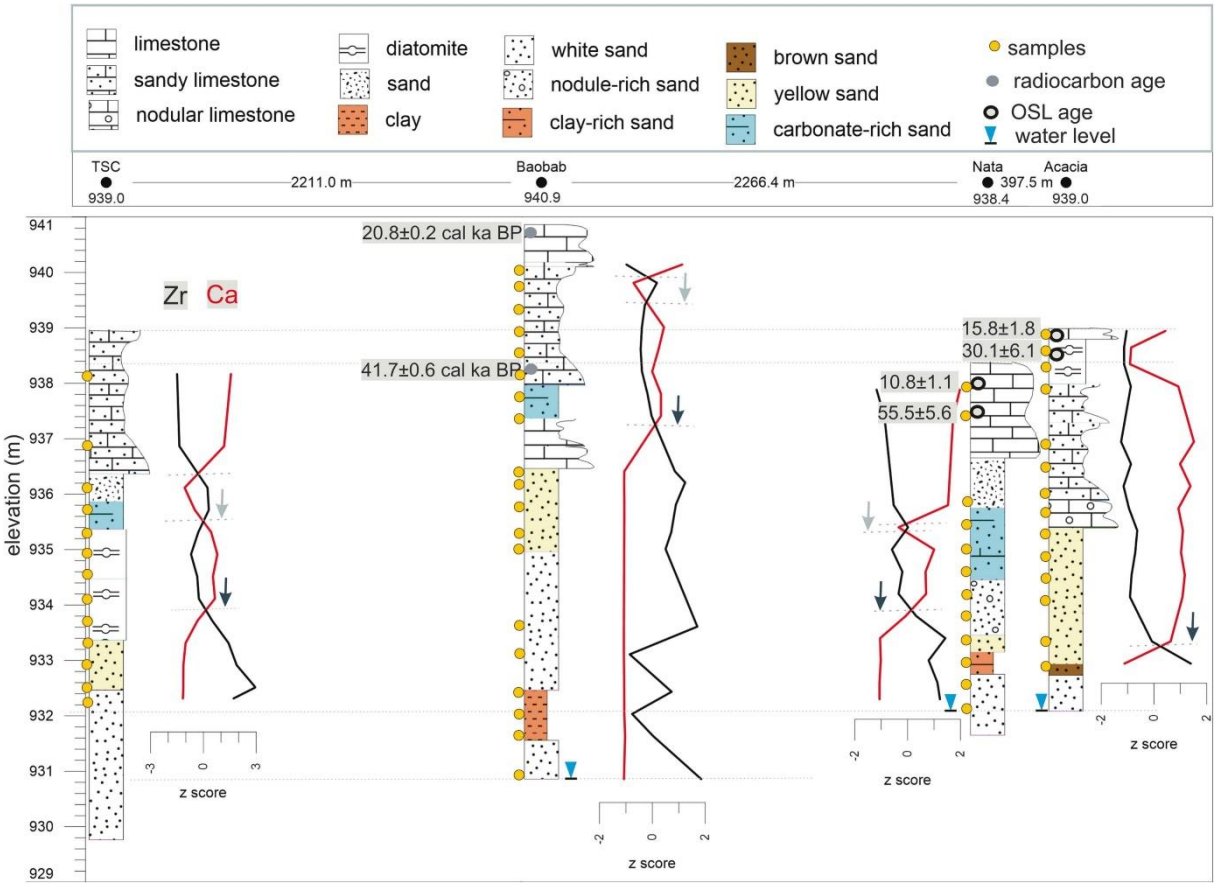

Figure 4.2. Lithological logs showing variations in Ca and Zr contents expressed in standardized units, OSL and radiocarbon ages (Diaz et al., 2019; Mokatse et al., 2022a), and altitudinal relationships across study sites. The selection of these variables is based on the PCA results as they are strongly anti-correlated along the first principal component (see Fig. 4.8). The black arrows indicate sediment input during wet periods, and the gray arrows indicate reworking/detrital input (see discussion in the text).

4.3.2 X-ray diffraction analysis (XRD)

XRD analyses of the whole-rock and clay mineral <2 µm fraction (Adatte et al., 1996; Godet et al., 2008) were carried out using an ARL Thermo X'tra X-ray diffractometer at the University of Lausanne on fifty-four (54) samples. The samples were prepared following the procedure of Kübler (1987) and Adatte et al. (1996). Whole-rock mineralogy characterization were performed on randomly oriented powder of the bulk sample. Whole-rock composition was determined by XRD based on methods described by Klug and Alexander (1974), Kübler (1987) and Rolli (1990). This method for semi-quantitative analysis of the whole-rock mineralogy used external standards. Clay crystals were separated from the whole rock by removing carbonate in a 10% HCl solution for 20 min, by controlling and adjusting the pH, and stirred using air injection. An ultrasonic bath tank was used to break aggregates, followed by centrifugation and repeated washing of the insoluble residue until the solution reached pH = 7. The <2 µm grain size fraction was obtained by sedimentation based on Stokes Law. The obtained solution was placed on a watch glass to evaporate prior to analysis. XRD analyses of oriented clay samples were made after air drying at room temperature and ethylene-glycol solvated conditions. The intensities of selected XRD peaks characterizing each clay mineral present in the size fraction (e.g., kaolinite, sepiolite, smectite, chlorite) were measured for a semi-quantitative estimate of the proportion of clay minerals present in the <2 µm fraction. Therefore, clay minerals are given in relative percent abundance without correction factors. Content in swelling (% smectite) is estimated by using the method of Moore and Reynolds (1989). In addition to clay minerals, a semi-quantitative calculation of other mineral proportions in the bulk fraction was applied to identify their assemblages associated to sepiolite.

4.3.3 Optical and electron microscopy

Samples were observed using optical and electronic microscopy i.e., a scanning electron microscope (SEM) as well as a transmission electron microscope (TEM). The observation of thin sections was performed using an Olympus BX61 optical microscope to identify the various minerals and amorphous phases. Analyses were carried out on selected fragments of fresh samples on stubs. In addition, a SEM was used to observe at high magnification the

relationship between quartz, calcite, amorphous silica, and sepiolite on freshly fractured samples. Observations were conducted at the University of Lausanne with a Tescan Mira II LMU coupled to an EDX Penta-FET 3x detector after gold coating of fresh samples and examined by secondary electron images for textural analysis. The working conditions were 20.00 kV and a working distance of ~15.0 mm. Finally, a TEM (Philips CM-200) with a high-resolution camera device was used at the CSEM (Centre Suisse d'Electronique et de Microtechnique, Neuchâtel, Switzerland) to observe the structure of the clay minerals at high resolution. The settings were the following: the beam was accelerated at 200 kV and the working distance was 360 mm; the fraction <2 µm was dispersed in distilled water and deposited as a drop, and then evaporated on copper grids used for observations under TEM.

4.3.4 Geochemical analyses and data processing

An approximation of the geochemical compositions of the fibrous clays was obtained with an EDAX microprobe (Oxford Instrument) coupled with the TEM used for observations of the clay structure: EDAX analyses were performed on the same samples. EDAX results were expressed in weight %. Relative contributions of Si, Mg, and Al+Fe have been standardized, plotted in a ternary diagram, and compared to contents in sepiolite and palygorskite from the literature (based on Suarez and Garcia-Romero, 2011).

The bulk elemental chemistry of the samples was obtained using a PANalytical Axiosm AX X-ray fluorescence device at the University of Lausanne. All samples were analyzed for major and trace elements according to two different methods. For major elements, the bulk rock powder was heated to 1050°C (fusion temperature) with $B_4Li_2O_7$, and for trace elements, crushed samples were mixed with wax and pressed.

The relationships between the different variables (mineralogical as well as geochemical) were assessed using principal component analyses (PCA). Data were standardized before processing with MatlabTM 2022a version. Moreover, proportions of clay minerals form a simplex i.e., the sum of the variables in each item (proportions) is a constant common to all items (100%), destroying the potential independence of variances and covariances and leading to Pearson's spurious correlations. To avoid such unwanted correlations, only two standardized clay variables were used, sepiolite and kaolinite

(authigenic and detrital respectively) in order to break the simplex for PCA, and each of the minerals is used as a proxy for contrasting environments.

4.4 Results

4.4.1 Macroscale distribution and facies associations

TSC site – The section is approximately 6.6 m deep (Fig. 4.3A), located in the Chobe Enclave floodplain west of the N-S sand ridge (Fig. 4.1). The top of the section is composed of a 2.6 m-thick sandy limestone with a heterogeneous karstic surface; this layer consists of a mixture of 0.3 m-maximum diameter clasts within a microcrystalline matrix. Below this carbonate layer, a < 1 m-thick carbonate-rich sand bed makes the transition to a ~2 m-thick diatomite earth formed by a fine, white material with a very low density and easily crushed to powder in the field. These diatomite beds include some carbonate-rich material. The diatomite bed is underlain by white sands, typical of the Kalahari Sand (Mokatse et al., 2022a). This white sand includes some siliceous nodules. Between the diatomite and the white sands, a brown/yellow sand (~1 m thick) layer is enriched in $CaCO_3$ nodules, with bioturbations.

Baobab quarry – The section refers to a ~10 m high quarry wall (Fig. 4.3B) made up with varying lithologies from palustrine carbonate (Diaz et al., 2019) to sand. The palustrine carbonate displays different facies: a sandy limestone overlain by a brecciated carbonate layer with carbonate nodules. Below the sandy carbonate, there is a layer of soft laminated carbonate of ~0.4 m thick. Generally, the boundary between the carbonate beds and the below sands is pronounced. In some places, the contact is characterized by carbonate-rich sands. Moreover, there is a sharp contact of brown/yellow sands between the white sand and the carbonate units. This observation is similar to the aforementioned TSC island site. Lastly, one key feature is the occurrence of a clay-rich layer (~0.9 m thick) between two white sand units (in orange in Fig. 4.3B). These white sand units have occasional siliceous concretions, and groundwater intersected at ~10 m in depth.

Nata site – The site outcrops in a fluvial watergap cutting across the N-S sand ridge (Fig. 4.1). It is made up of a ~1.7 m-thick limestone unit overlying a carbonate-rich material (Fig. 4.3C). This material consists of $CaCO_3$ nodules of various sizes (pluri-centimeters) and has a sharp

contact with the white sand below. The sharp contact is composed of yellow sand with a clayey-sandy layer.

Acacia quarry – The quarry section is ~6 m deep with a 0.2-m thick top part consisting of a thin limestone layer overlying a 0.8-m thick diatomite bed (Fig. 4.3D). The diatomite is made of a white material with a low density with some siliceous centimetric nodules. Below is a sandy limestone with a lower contact enriched in CaCO3 nodules. As observed at TSC site and Baobab quarry, the contact between the sandy limestone and the white sand below is made up of a yellow/brown sand. This is a significant feature, and the brown/yellow sands can be considered as a transition between two different paleoenvironments.

To summarize, all the outcrops include Kalahari Sands at their base. The transitions towards the top sandy limestones are made of some yellow sands with carbonate and occasionally, the presence of diatomitic layers.

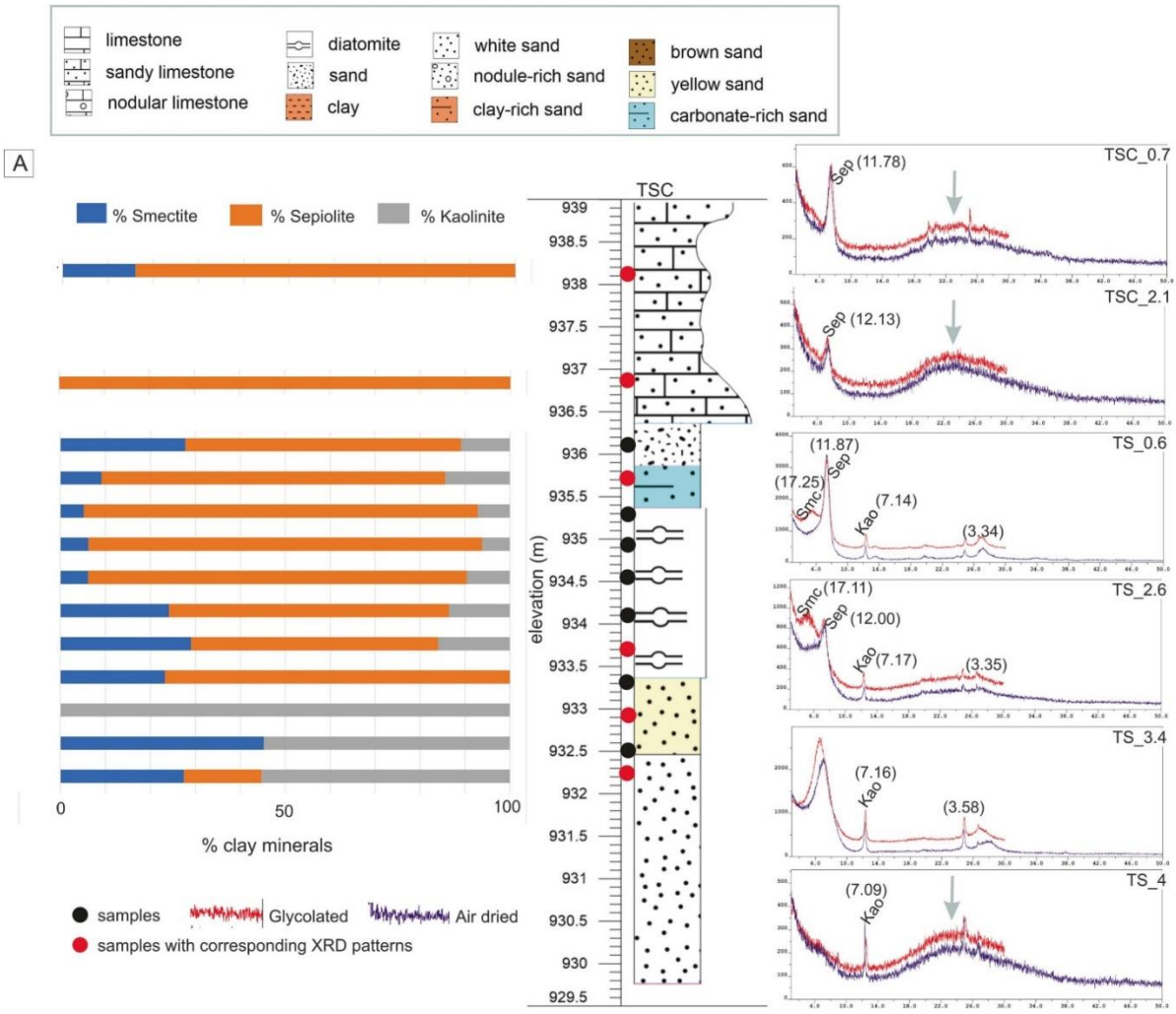
limestone
sandy limestone
nodular limestone
diatomite
sand
clay
white sand
nodule-rich sand
clay-rich sand
brown sand
yellow sand
carbonate-rich sand
A
% Smectite
% Sepiolite
% Kaolinite
0
50
100
% clay minerals
samples
Glycolated
Air dried
samples with corresponding XRD patterns
TSC
elevation (m)
939
938.5
938
937.5
937
936.5
936
935.5
935
934.5
934
933.5
933
932.5
932
931.5
931
930.5
930
929.5
TSC_0.7
Sep (11.78)
TSC_2.1
Sep (12.13)
TS_0.6
(11.87)
Sep
(17.25)
Smc
(7.14)
Kao
(3.34)
TS_2.6
Smc (17.11)
Sep
(12.00)
Kao (7.17)
(3.35)
TS_3.4
(7.16)
Kao
(3.58)
TS_4
(7.09)
Kao

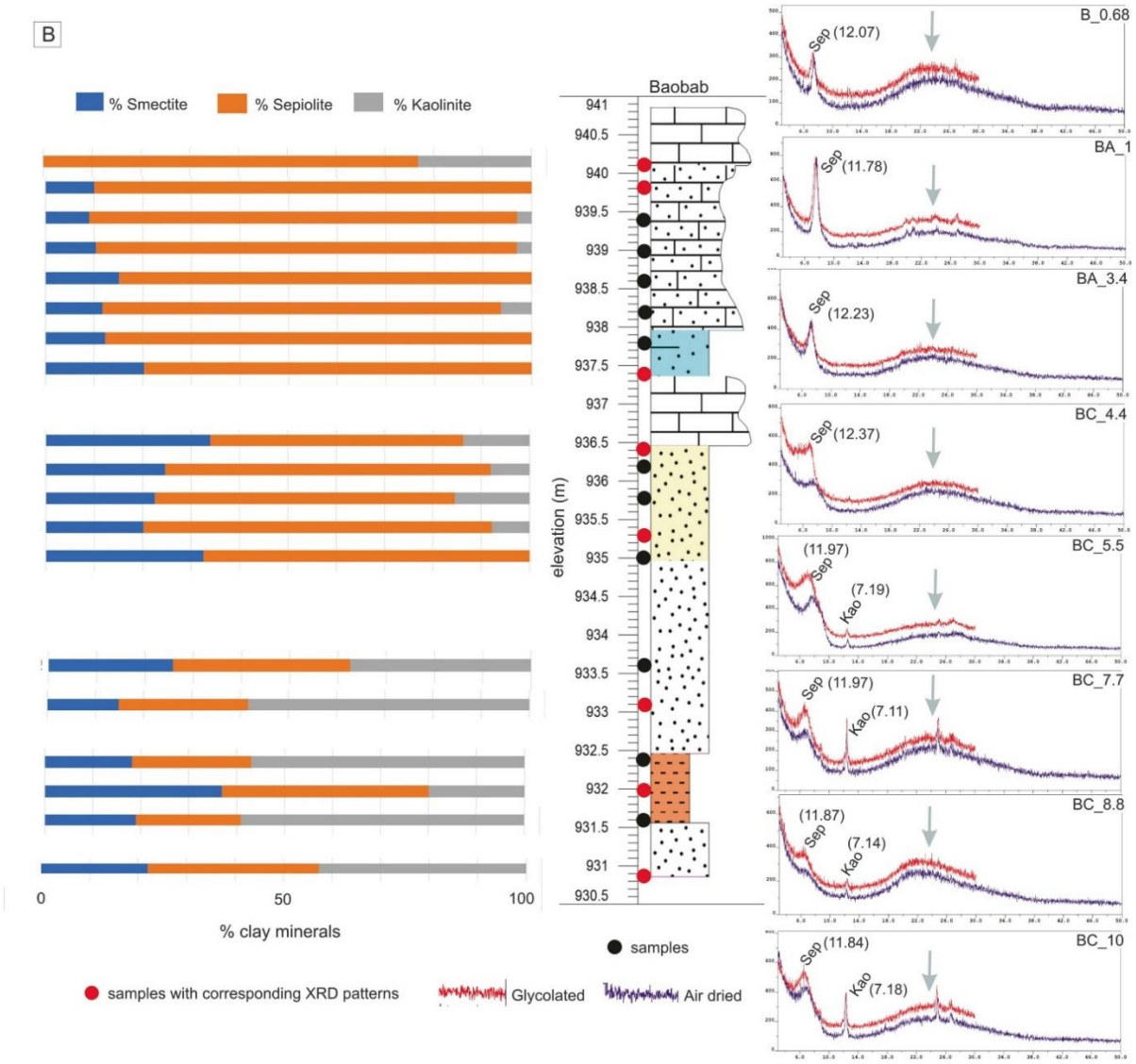
B
% Smectite
% Sepiolite
% Kaolinite
0
50
100
% clay minerals
Baobab
941
940.5
940
939.5
939
938.5
938
937.5
937
936.5
936
935.5
935
934.5
934
933.5
933
932.5
932
931.5
931
930.5
elevation (m)
samples
samples with corresponding XRD patterns
Glycolated
Air dried
B_0.68
Sep (12.07)
BA_1
Sep (11.78)
BA_3.4
Sep (12.23)
BC_4.4
Sep (12.37)
BC_5.5
(11.97)
Sep
(7.19)
Kao
BC_7.7
Sep (11.97)
Kao (7.11)
BC_8.8
(11.87)
Sep
(7.14)
Kao
BC_10
Sep (11.84)
Kao (7.18)

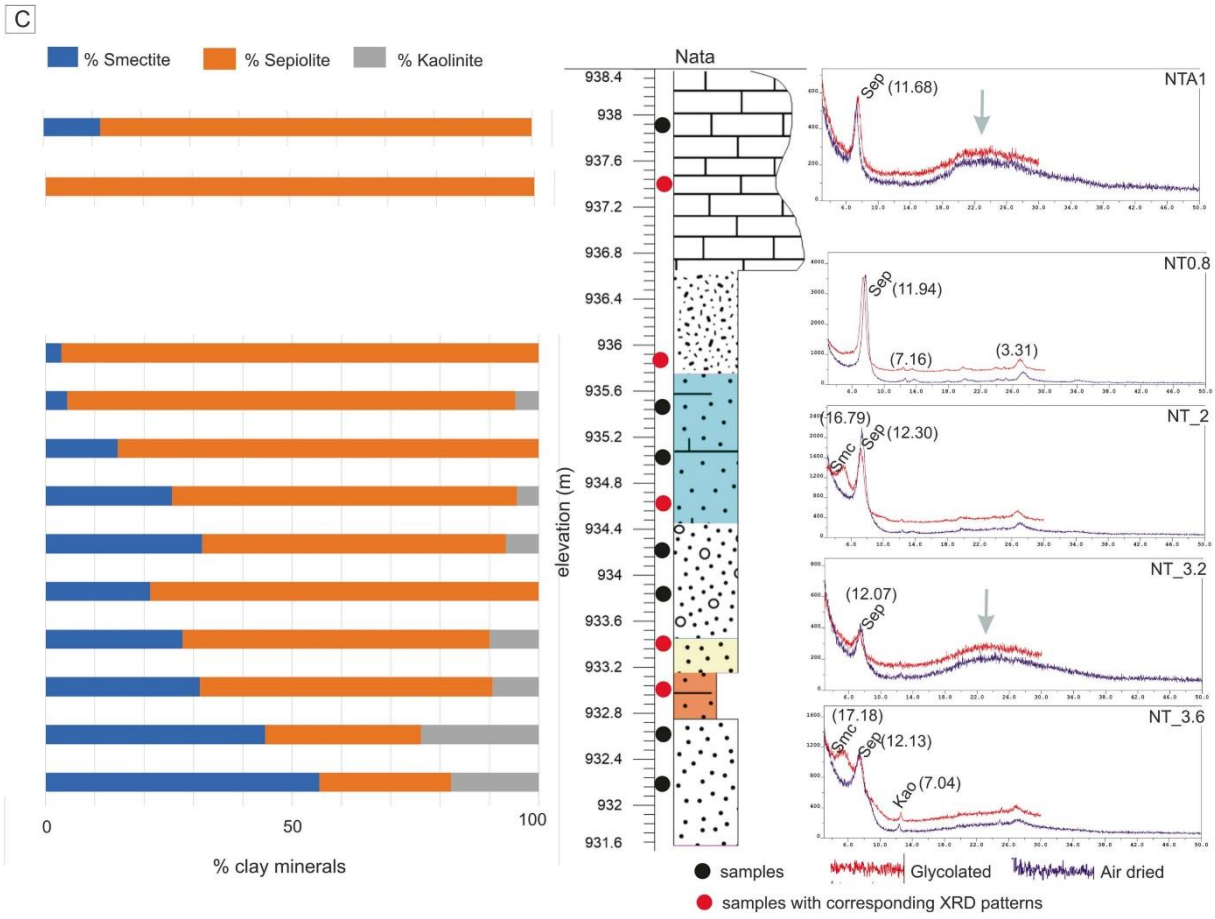
C
% Smectite
% Sepiolite
% Kaolinite
0
50
100
% clay minerals
Nata
938.4
938
937.6
937.2
936.8
936.4
936
935.6
935.2
934.8
934.4
934
933.6
933.2
932.8
932.4
932
931.6
elevation (m)
NTA1
Sep (11.68)
NT0.8
Sep (11.94)
(7.16)
(3.31)
NT_2
(16.79)
Smc
Sep (12.30)
NT_3.2
(12.07)
Sep
NT_3.6
(17.18)
Smc
Sep (12.13)
Kao (7.04)
samples
Glycolated
Air dried
samples with corresponding XRD patterns

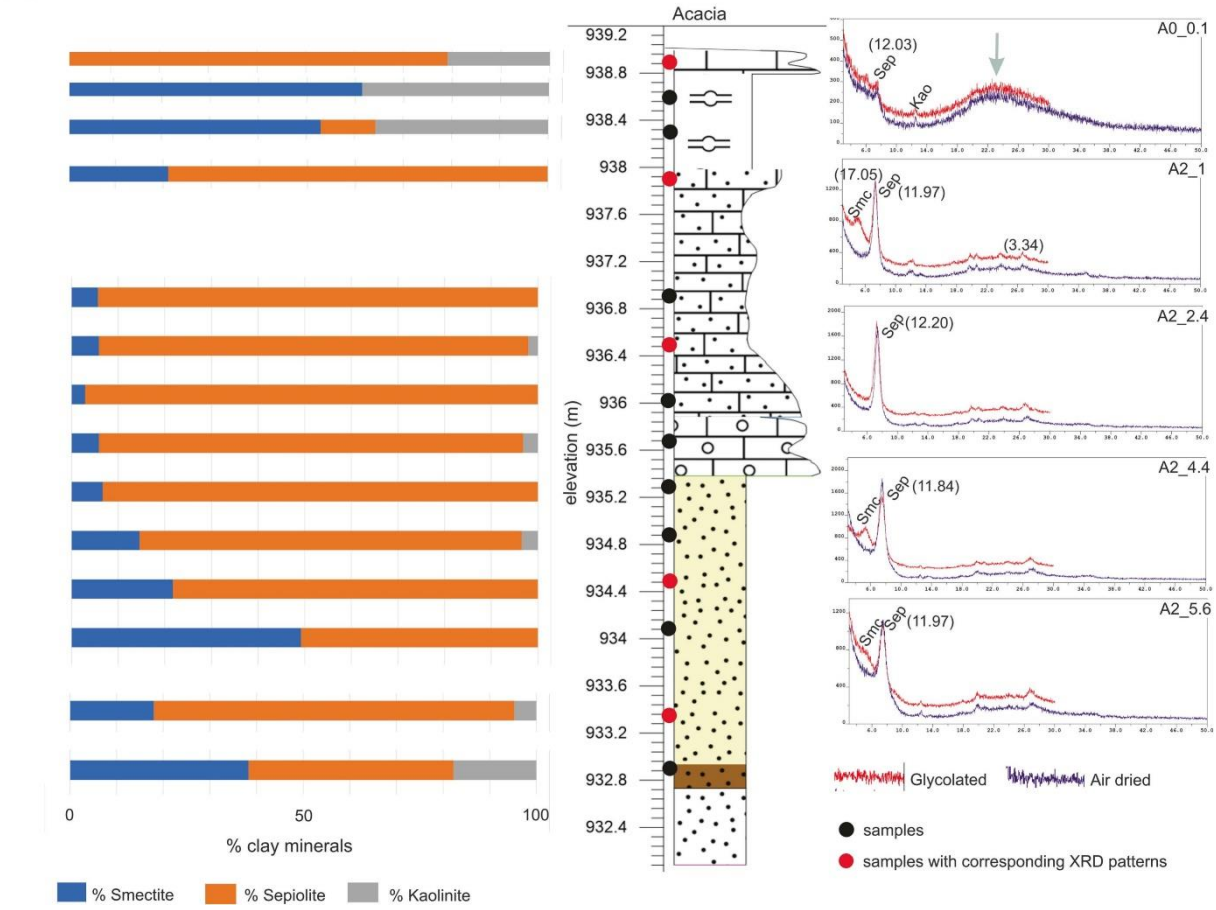

Figure 4.3. Lithological log of the four study sites with corresponding clay mineral abundances and XRD patterns of the clay size fraction (<2 µm). Sep = sepiolite, Smc = smectite and Kao = kaolinite. (A) TSC site. (B) Baobab quarry. (C) Nata site (D) Acacia quarry. The gray arrow shows the diffuse peak over the angular range 14° to 36° indicating the presence of amorphous silica. The d-spacing is given in angstrom (Å).

4.4.2 Microscale distribution and fabric of the Chobe Enclave sepiolite

The proportions of phyllosilicates in the minerals present in the outcrops vary from 0 to 72% (see Suppl. Mat. Table 4.1) with an average value of 23% and a standard deviation of 14%. When present, the proportions of sepiolite can reach 100% among the phyllosilicates. Only two samples are totally devoid of this clay mineral. Within the phyllosilicates, sepiolite proportions in the Chobe Enclave sites have an average value of 69% with a standard deviation of 26%, making sepiolite the most prominent clay mineral of the area.

The distribution of sepiolite at the microscale allowed its relationship with other minerals to be assessed and to shed light on the sedimentological and chemical conditions

that prevailed during its formation. The crystal morphology was first described using TEM as it is a pertinent approach to investigate, through the crystal shape, the potential in situ or reworked (detrital) origin of the mineral. Soil micromorphology descriptions have been used on multiple thin sections from sepiolite-rich layers. The following section describes their main characteristics observed in carbonate-rich and diatomite samples (carbonate and diatomite facies) containing sepiolite.

Carbonate facies are composed of microcrystalline, sandy, and nodular limestone with occasional diatomite facies intercalations (Fig. 4.2). These samples display a random distribution pattern with a single spaced porphyric c/f-related distribution (Figs 4.4A, B). The coarse fraction is formed by quartz grains whose proportions are constant in the samples (around 30%). Quartz grains are usually smooth, with a high to moderate sphericity and roundness, and well sorted. Their grain-size mode is around 200 µm and their leptokurtic distribution has been attested using conventional measurement of their grain-size distributions: these sands are mineralogically, as well as in terms of grain-size, like those forming the aeolian Kalahari Sand (Thomas and Shaw, 1991; Vainer et al., 2018, 2022; Mokatse et al., 2022a). In addition to quartz grains, pedofeatures such as nodules, are frequently observed. They can be made of calcium carbonate (micritic disorthic nodules) or of amorphous to cryptocrystalline silica, attested using a first order retardation plate shifting the birefringence colors to the second order (Fig. 4.4C). The presence of amorphous silica associated with sedimentary deposits of the Kalahari Basin has already been documented (McCarthy and Ellery, 1995; Ringrose et al., 2008; Diaz et al., 2019). Regarding the micromass, which constitutes 65% of the thin section area, its mineralogy is complex: it is a mixed phase of abundant sepiolite, with traces of carbonate and a clay size diatomitic mud. In addition to the micromass, other intrusive pedofeatures are present (forming around 5% of the thin section) i.e., coatings around quartz grains, which can vary from calcite to sepiolite.

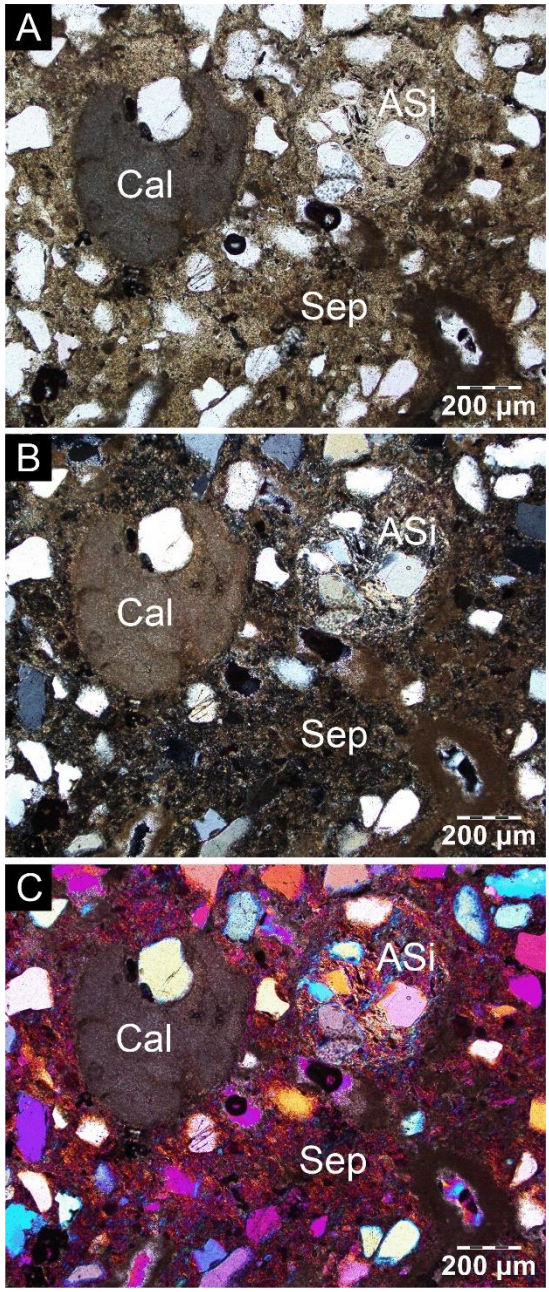

Figure 4.4: Optical microscope images of a sample with a high sepiolite content. The groundmass includes pure sepiolite (Sep) in the micromass, which is also coating some quartz grains (in white in A; in white to dark gray in B). The presence of calcite is attested by a nodule of micrite (Cal) and there is only scarce micrite in the micromass. Moreover, another nodule, this time of amorphous silica (ASi) emphasizes the presence in the thin section of other siliceous phases than clay minerals. (A) Natural light (PPL). (B) Crossed-polarized light (XPL). (C) Cross-polarized transmitted light with the first order retardation plate (gypsum plate) inserted into the light path; the use of the gypsum plate facilitates the identification of silica-rich phases by shifting the color of quartz, sepiolite, and amorphous silica to a higher order i.e., bright blue, yellow, and pink; calcite remains the same as in XPL.

SEM investigations on sepiolite-rich samples of each location studied allowed the geometry between the various mineral phases to be clarified. As expected, crystals of

homogenous fibrous sepiolite form mineral grain coatings (Fig. 4.5A) but also impregnate the groundmass (Fig. 4.5B), forming a dense mesh in the micromass, confirming the fabric observed under the optical microscope. Coatings are commonly observed on quartz grains and diatoms, but also on and next to rhombohedral calcite crystals (Fig. 4.5C). In samples with high contents of sepiolite, large cements of amorphous silica precipitate in a botryoidal pattern associated with individual spheres (Fig. 4.5D). Such facies could attest supersaturation spans, regarding the silicon ion, affecting the parent solution, and therefore some variability in pH towards alkalinity (Arbey, 1980). The differentiation between quartz grains, amorphous silica, or diatoms on one side, and sepiolite crystals on the other side, remains somehow challenging at some places, as the surface of the former minerals often show dissolution features associated with visibly authigenic sepiolite. The thickness of sepiolite coatings varies but can reach about ten microns for the thickest ones. Finally, TEM images confirmed the perfectly fibrous aspect of sepiolite, sometimes forming sheets, as documented in the literature (Wang et al., 2009). Individual fiber crystals have variable sizes but are 10 nm-large on average (Fig. 4.5E, F). The sheet-like arrangements of sepiolite crystals can form thin layers on large areas (Fig. 4.5E, F), which may coalesce (hundreds of μm^2) and finally coat quartz grains (Fig. 4.5A).

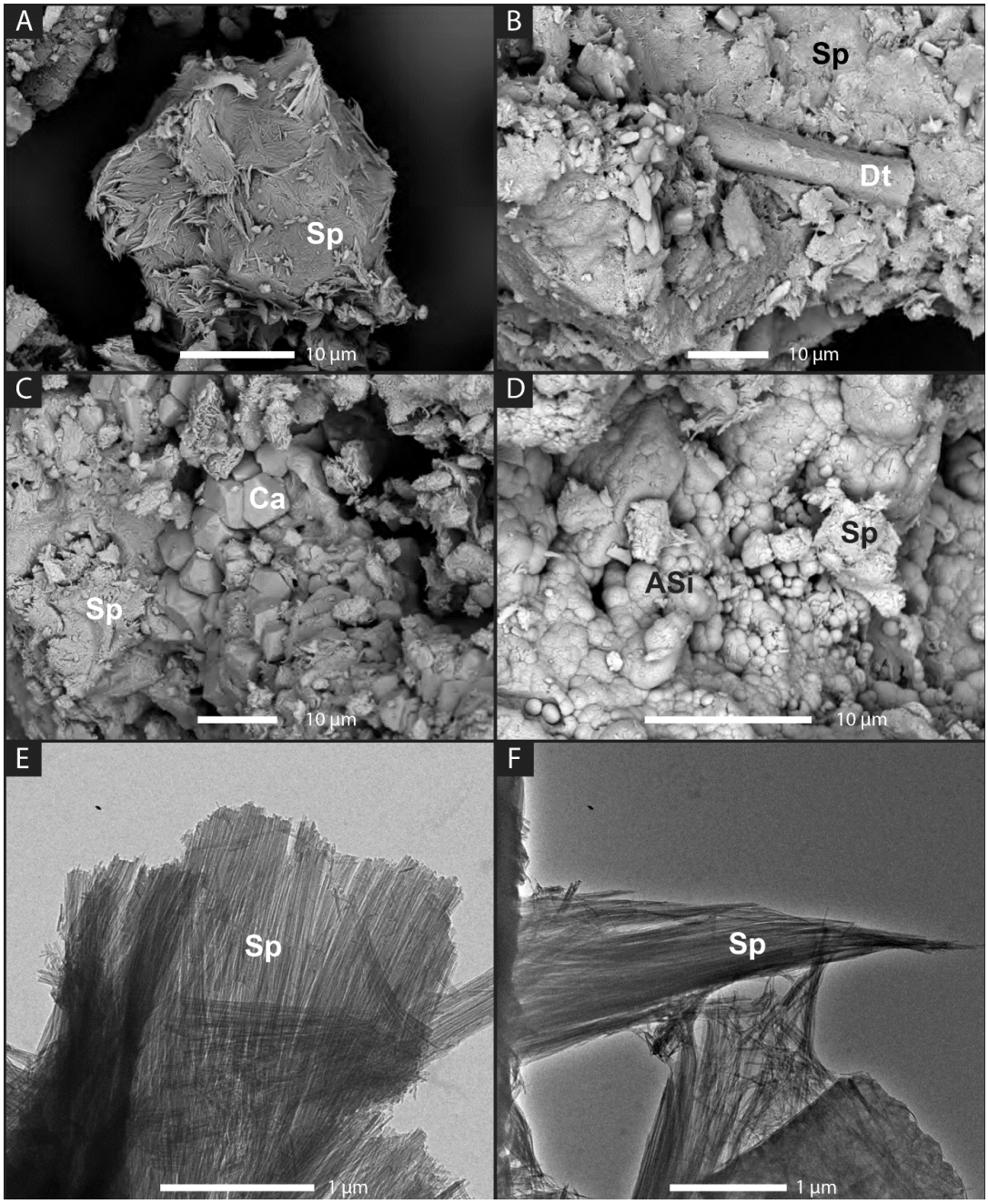

Figure 4.5: Scanning electron microscope (SEM) and transmission electron microscope (TEM) images of sepiolite. A) SEM micrograph of a sepiolite (Sp) coating on a quartz grain showing a random orientation of crystals with fusiform shape tips. B) SEM view of a preserved diatom (Dt) in a sepiolite (Sp) matrix with some fine silt-size quartz. Sepiolite crystals are thinner and smaller than in A). C) SEM view of a rhombohedral calcite cement (Ca) associated and partly covered by sepiolite crystals (Sp). D) SEM image showing amorphous silica spheres (ASi) arranged in a botryoidal texture and precipitated inside a pore in a sepiolite (Sp) matrix. The C) and D) SEM view emphasize the following succession of minerals: calcite precipitated first, then sepiolite, and finally amorphous silica. E) TEM image showing the fibrous structure of the sepiolite (Sp) and particularly a large sheet of sepiolite fibers. F) TEM view of fusiform sepiolite (Sp) arrangements.

In conclusion, microscopical investigations allow a succession of sediments and phases to be assigned: quartz grains from the Kalahari Sands constitute the coarse fraction of the beds. A diatomite mud is frequently associated to this sand, forming the initial groundmass. This groundmass is then enriched in calcium carbonate as either traces of micrite in the micromass or as disorthic to anorthic micritic nodules. Impregnative sepiolite invades the micromass and coats large grains (quartz sand), the diatomite micromass, and pore walls. Finally, an amorphous siliceous phase, in a botryoidal pattern associated with individual spheres, ends this mineralogical sequence. This sequence must reflect the evolving composition of the solution in the environment. Regarding sepiolite, its silicon part can easily be provided by the environment, rich in siliceous components, whereas the origin of the Mg^{2+} remains unsolved.

4.4.3 Minerals associated with sepiolite

Analyses of bulk-XRD samples are dominated by three main types of minerals: quartz (and amorphous silica), calcite, and phyllosilicates, which were identified using a semi-quantitative method (see Suppl. Mat. Table 4.1). Quartz is always present in the samples and constitutes almost 100% of the mineral fraction in the deepest deposits found at each location. These layers correspond to the Kalahari Sands. The composition of sediments changes along the outcrops with varying proportions of calcite, with a content reaching sometimes ~80 % in the carbonate-rich layers, e.g., in TSC and Nata sites. The clay mineral XRD analyses display sepiolite dominated sections, mostly occurring in carbonates associated with some smectite and kaolinite. The presence of kaolinite and smectite would indicate a greater contribution from the detrital material, probably originating from the weathering of the Karoo basalts (Garzanti et al., 2014). Barite ($BaSO_4$) has also been detected in some samples but (i) it cannot be quantified due to the low intensity of their respective peaks, and (ii) occurs mostly as an accessory mineral and represents < 5%. However, the presence of barite associated with palustrine limestone is of interest (Fig. 4.6), as both occurrence of sepiolite and barite raises more questions regarding the sources of Mg and Ba, respectively. There are also some traces of gypsum, which appear only on XRD diffractograms of a few samples, mainly located in the Acacia Quarry and associated to diatoms (amorphous silica phase).

Moreover, in the literature, sepiolite deposits are generally associated with potential sources of magnesium, such as dolomite (Watts, 1980; Galán and Pozo, 2011). Surprisingly, there is no trace of dolomite in the study samples. Consequently, the magnesium ion must originate from another host rock or source to support the precipitation of sepiolite.

Finally, X-ray diffraction (XRD) patterns clearly point to a clay fraction almost exclusively composed of sepiolite, with minor proportions of smectite and kaolinite, although an amorphous silica phase is also present (likely as a diatomite fine earth; Figs 4.3A-D). XRD patterns noticeably record all the expected peaks of sepiolite, according to Galán and Singer (2011), when the clay mineral is present in large amounts; its identification is still easy in diffractograms with peaks of less amplitude.

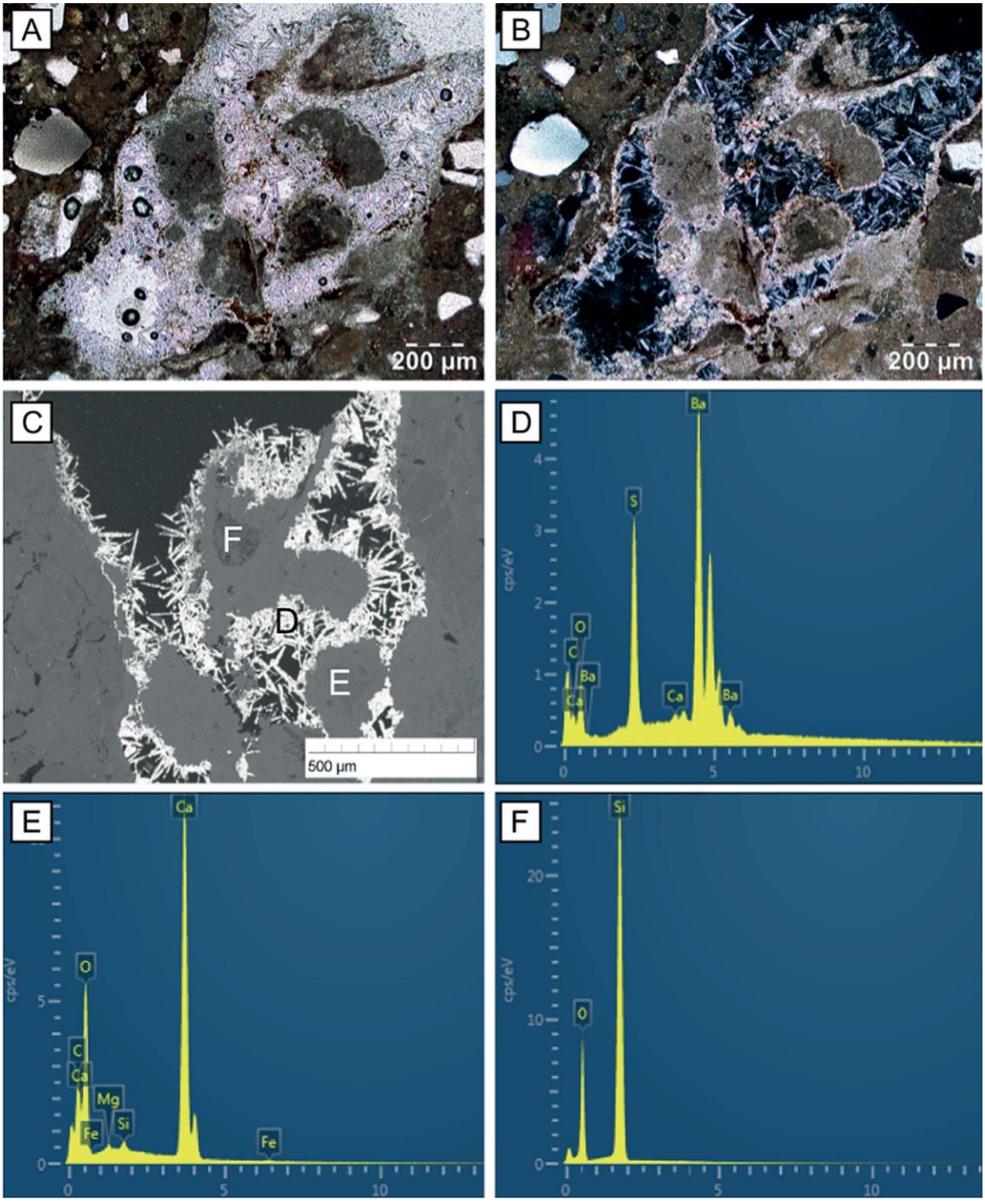

Figure 4.6: A) Thin section of a palustrine limestone in which styloidic crystals of barite formed, attached to micritic clasts of reworked mud. View in plane-polarized light. B) Same view in crossed-polarized light. Bright needles of barite contrast with the extinct background. The large white minerals different from barite are quartz grains. C) Same thin section observed with a scanning electron microscope in backscattered electron mode: barite appears in white (greater atomic number than the compounds of the background). D, E, and F letters refer to the areas analyzed by EDAX. EDAX spectra are the following: D) spectrum of barite crystals; presence of Ba and S, as barite is a barium sulphate; E) spectrum of the calcium carbonate micromass forming the palustrine limestone (presence of Ca); F) quartz grain with essentially silicon (Si).

4.4.4 The chemical composition of sepiolite

Semi-quantitative chemical compositions of sepiolite carried out by TEM-EDAX are plotted on a ternary diagram (Fig. 4.7): the three variables refer to the respective contents in silicon (Si expressed as SiO_2 wt%), magnesium (as MgO wt%), and iron plus aluminum (expressed as [Fe_2O_3 + Al_2O_3] wt%). The selection of these elements is justified by the theoretical composition of sepiolite, which is:

$$\left(Mg_{8-y-z}R^{3+}_{y}\ \square_{z}\right)\left(Si_{12-x}R^{3+}_{x}\right)O_{30}(OH)_4(OH_2)_4R^{2+}_{(x-y+2z)/2}(H_2O)_8$$

according to the review by Suarez and Garcia-Romero (2011) and based on Brauner and Preisinger (1956)'s formula, where cation occupancies (R) are mainly Al^{3+}, Fe^{3+}, Fe^{2+}, Ti^{2+}, rarely Cr^{3+} and Ni^{2+} (with the range of octahedral cations varying between 6.87 and 8.11). Moreover, a similar ternary diagram by Suarez and Garcia-Romero (2011), compiling a large set of data from the literature, is used to compare the amounts of elements found in the Chobe Enclave sepiolite with sepiolite compositions from other sites worldwide (Fig. 4.7). Indeed, the sepiolite compositions from Suarez and Garcia-Romero (2011)'s data set are all included in the green area drawn in figure 5 (for comparison, palygorskite data are clustered in the red area; Fig. 4.7). As expected, the observed samples from the Chobe Enclave (n = 36) are all included in the sepiolite area from Suarez and Garcia-Romero (2011), emphasizing their clear and expected sepiolite composition. Nevertheless, there is a slight dispersion of sepiolite chemical compositions, varying from values situated in the bottom part of the green cluster (Fig. 4.7) to its top where slightly enriched Al-sepiolites are plotted. Although there is a minor superimposition of the respective chemical domains of the two fibrous clays in the reference ternary plot (Suarez and Garcia-Romero, 2011), Al-sepiolite is more likely than palygorskite as this mineral is hardly detected in XRD patterns. In conclusion, XRD and TEM-EDAX analyses of clay fractions highlight the particularly enriched in sepiolite associated to specific deposits of the Chobe Enclave.

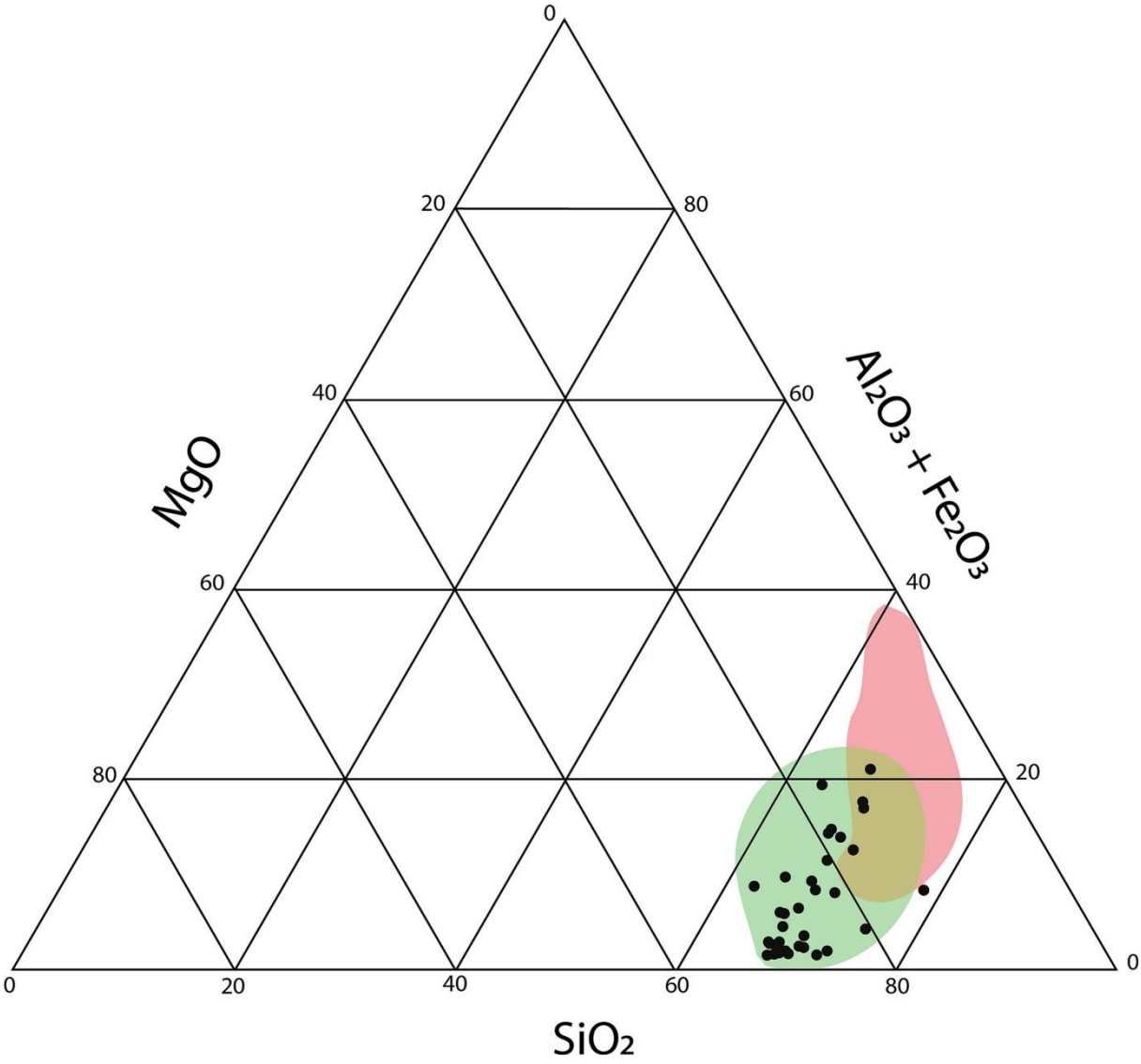

Figure 4.7: Relative contents of Si, Mg, and Al+Fe (expressed as oxides, SiO_2-MgO-Al_2O_3+Fe_2O_3) in sepiolite crystals from study sites and literature plotted in a ternary diagram. Measurements have been performed with an EDAX microprobe coupled to a TEM. Black dots refer to the results from this study, whereas the diversity of sepiolite and palygorskite compositions given in the literature review from Suarez and Garcia-Romero (2011) are symbolized as two clouds in green and red, respectively.

4.4.5 Major and trace elements in sepiolite beds

Contents of major elements in sediments reflect the composition of the three main minerals detected by XRD analyses i.e., quartz, calcite, and sepiolite. Silicon and calcium are the dominant elements, and their respective proportions vary with the rock type, from calcite cemented sandstones to limestones. Samples with sepiolite are enriched in magnesium compared to limestones due to the composition of the fibrous clay. Soil samples of Acacia

quarry contain significant proportions of iron. Fe_2O_3 contents can reach almost 6% in sandy sediments (with 80% SiO_2), whereas limestones contain < 2.5% of Fe_2O_3.

Contents of barium in the different quarries vary from < 100 ppm to almost 2400 ppm. Unexpectedly, these values are high compared to the mean Ba content observed in Karoo basalts and dolerite (< 500 ppm), which are the nearest and most potential sources of Ba easily transportable by rivers. This large difference has been also observed in the Makgadikgadi paleo-lake located in the south of the Chobe Enclave. This paleo-lake deposit contains, at its minimum, 190 ppm of Ba in silcretes but can reach 4820 ppm in deposits composed by a mixed silcrete and calcrete layer (Ringrose et al., 2009). Surprisingly, the Sr content in the Chobe Enclave does not seem to be related to Ba, contrarily to Ringrose et al. (2009).

Finally, in Acacia quarry, sample contents in aluminum are correlated to silica contents. This relationship must be explained by the presence of diatom frustules, which can enhance aluminum enrichment, as suggested by Koning et al. (2007), Michalopoulos et al. (2000), and Ren et al. (2013). Nevertheless, the presence of some Al sources from sepiolite cannot be totally precluded because, as emphasized above in the section about the chemical composition of sepiolite, the presence of some Al-sepiolite remains possible.

To conclude, the results emphasize a mineralogical system with four mineralogical end-members i.e., quartz, calcite, sepiolite, and amorphous silica (in the shape of diatoms or as a secondary amorphous cement). The presence of sepiolite is somehow difficult to explain if it is referred to the conventional environments described in the literature (Galán and Pozo, 2011). Although strong evaporation and the presence of dissolved silica in the water seem likely in this region, the necessary contribution of a magnesium source remains challenging. Indeed, in the literature, sepiolite precipitation is often associated with dissolution of dolomite or alteration of magnesium-rich metamorphic rocks (Galán and Pozo, 2011). In the Chobe Enclave, there is no trace of dolomite and the nearest volcanic rocks (the Karoo Complex) seem unlikely to provide the necessary amount of magnesium to provide surface water with a suitable concentration of Mg^{2+}. Another important discrepancy with literature lies in the fact that the evaporitic mineralogical series, usually associated with sepiolite, is absent in the Chobe Enclave. Only carbonate is formed, whereas gypsum, found in some samples, represents only a minor part of the mineral phase, and is probably related to the activity of termites (Van Thuyne et al., 2021) or to some aeolian contributions (McCarthy, 2013). Finally, the discovery of a large quantity of Ba in the form of barite adds one more

question to the sedimentary settings of the Chobe Enclave. This mineral, seldom associated with sepiolite, could point to a hypothesis not yet discussed, i.e., hydrothermalism.

Consequently, the relationships between the various mineralogical and geochemical variables were assessed using a principal component analysis (PCA). The PCA clearly differentiates between three clusters: a carbonate-sepiolite one, a detrital pole, and a last one related to a likely hydrothermal influence (Fig. 4.8). Planes plotted using PC4 vs. PC1 (Fig. 4.8A) and PC2 vs. PC1 (Fig. 4.8B) account for 54.9 % and 65.0 % of the total data variance, respectively. The first principal component (PC1) shows a positive correlation with Si, Zr, and kaolinite components (Figs. 4.8A, B), and correlates negatively with sepiolite, Mg, Mn, and Ca. The second principal component (PC2) correlates negatively with Fe and K (Fig. 4.8B). Moreover, the fourth principal component (PC4) correlates negatively with only Ba (Fig. 4.8A). A high positive PC1 score indicates detrital material, whereas the carbonate facies have a negative PC1 score. On the other hand, hydrothermalism pole plots in the negative field of PC4 coordinate. Consequently, on one hand, most variations accounted for by PC1 are a function of lithological variation i.e., from the detrital component to the carbonate-sepiolite reactor. On the other hand, variations accounted for by PC4 point to chemical changes due to potential hydrothermal input (Ba variable). In addition, the approaching right angles between Ba and PC1, and Fe-K and PC1, emphasize an absence of linear relationships between these variables and PC1: in other words, these elements are not controlled by the two end-members given above, but are likely to be part of an assemblage associated with either hydrothermalism, for Ba, or with weathering of some mineral phases that host Fe and K. All these relationships will be discussed in the following section.

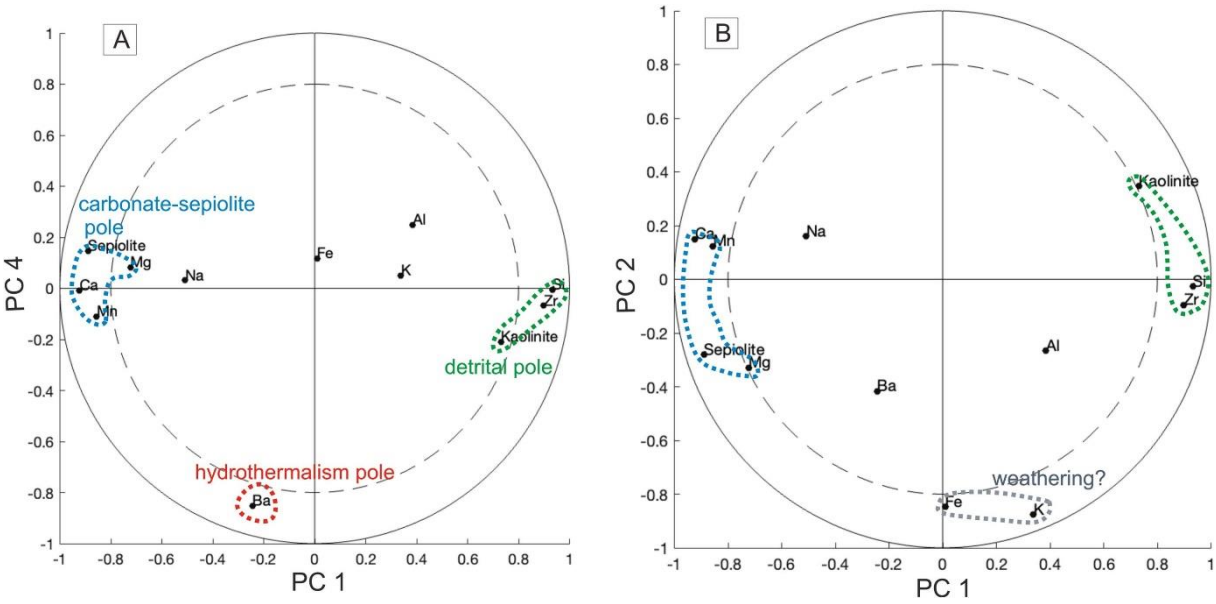

Figure 4.8: Circle of correlations between variables and principal components obtained during PCA of Chobe Enclave samples showing the two planes, (A) PC4 vs PC1 and (B) PC2 vs PC1. Three groups of variables are identified; they refer to three main poles: a carbonate-sepiolite, a detrital, and an hydrothermalism one according to their color. A fourth cluster centered on Fe and K variables could eventually refer to a weathering pole, although still questionable. The plane in A explains 54.9% of the total variance whereas it is 65.03% in plane in B. See also Table 4.1.

Table 4.1: Results of principal component analysis. PC: principal components from 1 to 4. Expl. var.: percentage (%) of explained variance by each PC. Cum. var.: cumulative percentage (%) of explained variance with the first four PC. Numbers under the variables refer to the correlation coefficients between each variable and the PC. This coefficient is calculated as $r_i = \sqrt{\lambda_i} \cdot u_i$ where r_i are the correlation coefficients between the variables and the i^{th} PC, λ_i and u_i the eigenvalue and the eigenvector of the i^{th} PC, respectively. $r_i \geq 0.85$ are in bold.

PC	Expl. var.	Cum. var.	Al	Ca	Fe	K	Mg	Mn	Na	Si	Ba	Zr	Sepiolite	Kaolinite
PC1	47.44	47.44	0.38	**- 0.92**	0.01	0.34	- 0.72	**- 0.86**	- 0.51	**0.93**	- 0.24	**0.90**	**- 0.89**	0.73
PC2	17.59	65.03	- 0.27	0.15	**- 0.85**	**- 0.87**	- 0.33	0.12	0.16	- 0.03	- 0.42	- 0-10	- 0.28	0.35
PC3	10.52	75.55	0.76	- 0.02	- 0.30	0.15	0.26	0.12	0.63	- 0.04	0.14	0.06	- 0.09	0.26
PC4	7.45	83.00	0.25	0.12	- 0.12	0.05	0.08	- 0.11	0.03	- 0.01	**- 0.85**	- 0.07	0.15	- 0.21

4.5 Discussion

The sepiolite precipitation in the Chobe Enclave must reflect a specific type of depositional environment. The geochemical composition of sepiolite, which includes Si and Mg, reflects the enrichment in these elements of the parent solution from which the sepiolite precipitated. In the literature, two main factors contribute to increase the concentration of these elements in a hydro-sedimentary environment: (i) a significant input of ions from rivers or from hydrothermalism (Irkec and Ünlü 1993; Galán and Pozo 2011), and (ii) an evaporative system (Helgeson et al., 1969). Tectonic activity has been obviously operating in the study area, changing the watershed and basin geometry forming and re-shaping various waterbodies in the Kalahari Basin (Shaw and Thomas, 1988; Burrough and Thomas, 2008; Vainer et al., 2021) that are clearly attributed to the result of such tectonic effects (Moore, 1999; Ringrose et al., 2005; McCarthy, 2013). Alongside the influence of neotectonics on the landscape evolution in the Chobe Enclave (Mokatse et al., 2022b), hydrothermal springs of low temperature have been reported in northern Botswana (Niles, 2012; Mukwati et al., 2018). However, the potential influence of hydrothermal springs on the sedimentology of the Chobe-Linyanti sub-basin was never mentioned. Furthermore, the hydrological system of northern Botswana and its history through the Quaternary are complex (Nugent, 1990; Moore et al., 2012). In this context, the settings that governed the precipitation of sepiolite might provide interesting evidence on the paleo-environmental system of the Chobe Enclave during the Quaternary (Fig. 4.2). The following discussion explores the potential origin of parent solutions and the establishment of sub-environments related to sepiolite formation (Tosca and Masterson, 2014). This approach will also be based on a precipitation model for sepiolite in the Chobe Enclave. Finally, potential hydrological and sedimentological properties of the Chobe Enclave area will be introduced with the aim of proposing a reconstruction of the environment in which sepiolite has been precipitated during the Quaternary.

4.5.1 The origin of sepiolite

Source area contributions

One aspect to understand the origin of sepiolite is to decipher the sources of Mg and Si ions. One of the primary concerns about fibrous clay minerals is whether their origin is a transformation of precursor clay minerals or a precipitation directly from solutions (Singer, 1979; Pozo and Galán, 2015). In the Chobe, SEM and TEM analyses reveal the sepiolite to be authigenic (Fig. 4.5), indicating that the parent solution must be concentrated enough in magnesium and dissolved silica to trigger the precipitation of the mineral. In this case, possible water sources constitute relevant concerns to explore in the region. In present-day, the main origin of water flowing to the Chobe Enclave is sourced from the watersheds located in the equatorial Angolan highlands and Zambia. Water is provided to the south by three main rivers: 1) the Kwando-Linyanti, 2) the Cuito spilling in the Okavango from Angola watershed, and 3) the Zambezi from Zambia watershed (Moore et al., 2012; Fig. 4.1). Surface water in the region can be classified as calcium-magnesium-(sodium)-bicarbonate type waters from the aforementioned major rivers. Even so, the geology of the catchments slightly varies as the Zambezi River waters have a higher Ca/Mg compared to the Okavango River waters. In addition, the Zambezi River waters have a pH of around 7.5 compared to about 6.9 of the Okavango, suggesting the presence of carbonate-bearing rocks in the Zambezi basin (Mokatse et al., 2022a). However, the extremely evaporated terminal swamp waters of the Chobe/Linyanti are sodium-(potassium)-chloride type with local sulfate concentrations (Atekwana et al., 2016; Dyer, 2017). Still, there are less recognized mineral phases of evaporites in the studied samples of the Chobe Enclave than would be expected from these different sources.

The deposits in the Chobe Enclave largely show a lower unit dominated by sand-rich material (white sands). This unit contains detrital clays and reworked detrital sediments. Kaolinite and minor smectite are dominant in the white sands (Fig. 4.3A, B). Moreover, this lower unit shows Zr enrichment (Fig. 4.2) that is consistent across all sites, emphasizing a detrital origin (Fig. 4.8). The detrital origin of the clay minerals is also attested by the PCA (Fig. 4.8), hence, suggesting the deposition by fluvial systems which drained relatively wetter climate areas than in present time (Garzanti et al., 2014, 2022). However, it is worth noting the minor contents of sepiolite observed in this unit, which could have likely not formed in situ. Above the lower unit, there is a transition zone denoted by yellow/brown sands. This zone shows significantly lower contents of detrital clays (Fig. 4.3), with a notable enrichment

of Ca (Fig. 4.2). This would emphasize the input from wet periods/spells: indeed, deposition of carbonate in a palustrine environment and diatomite facies occurred preferentially in humid conditions. Following this period, the enrichment of Zr and depletion of Ca (Fig. 4.2) indicate a period of reworking/detrital input. Presently, both the carbonate and diatomite facies host sepiolite (Fig. 4.4) with relatively lower content in diatomites (Figs. 4.3A, D) and higher content in carbonate. This consequently underlines the adequate input of Mg and Si ions in the system able to precipitate sepiolite during the deposition of these beds.

Sepiolite precipitation: was the Chobe Enclave an evaporitic environment?

The conditions in which the sepiolite is stable provide clues about the paleoenvironment they form in. A thermodynamic stability diagram, adapted from Helgeson et al. (1969), shows what a precipitation sequence of minerals must be expected from a water body in a CaO-MgO-SiO_2-CO_2-H_2O evaporitic system of a lake in the Sierra Nevada (Fig. 4.9). Figure 4.9 clearly displays the succession of the mineral phases during the evaporation process i.e., when the solution concentrates with time. The various species in the parent solution ($Si(OH)_4$, Ca^{2+} and Mg^{2+}) exhaust during the sequential precipitation of minerals i.e., calcite first, then sepiolite, and finally amorphous silica. The solution concentration due to the evaporation also triggers an increase in pH, leading to the precipitation of Ca-carbonate from the aqueous solution at pH around 8.4, and amorphous silica at a pH around 8.7. Obviously, as long as there are carbonate and calcium ions in the solution, calcite will precipitate until the Ca^{2+} reservoir is exhausted. The sepiolite precipitation occurs after calcite nucleation at a pH slightly more alkaline (Fig. 4.9). The stability of sepiolite is a function of pH (Galán and Singer, 2011). At this moment, the Mg^{2+} concentration starts to decrease in the aqueous solution as it is integrated into the sepiolite. Regarding the dissolved silica concentration, it continues to increase even if some silicon is incorporated into the fibrous clay. Finally, when Mg^{2+} is exhausted from the parent solution, $Si(OH)_4$ amorphous silica precipitates as the final mineral component. Consequently, the mineralogical assemblage (calcite, sepiolite, and amorphous silica) observed in the Chobe Enclave (Figs 4.4 and 4.5C, D) results from a succession that is identical to the one provided by the model. Indeed, the geometrical relationships between the mineral phases (Fig. 4.5C, D) clearly show the presence of a rhombohedral calcitic cement associated and partly covered by sepiolite crystals, as the clay minerals precipitated after the Ca-carbonate. On top of the

sepiolite and calcite association, spherical amorphous silica precipitated inside a pore coated with sepiolite. This succession highlights the sequence of precipitation i.e., calcite precipitated first, then sepiolite, and finally amorphous silica. Moreover, the presence of sepiolite in palustrine carbonate facies is often considered to be closely related to semiarid evaporitic environments (Singer, 1984; Jones and Galán, 1988; Chamley, 1989 and references therein). However, the absence (or lack) of evaporites in the Chobe Enclave possibly indicates that the sepiolite was not generated under conventional extreme evaporitic conditions, especially since the regional waters are presently enriched in sulphates (see section above). Consequently, another potential and contributing source for ions must be proposed: it is likely that some parent solution was also locally enriched from a water source also concentrated in ions such as Mg^{2+} and Ba^{2+}, a hydrothermal source, a hypothesis discussed in the next section.

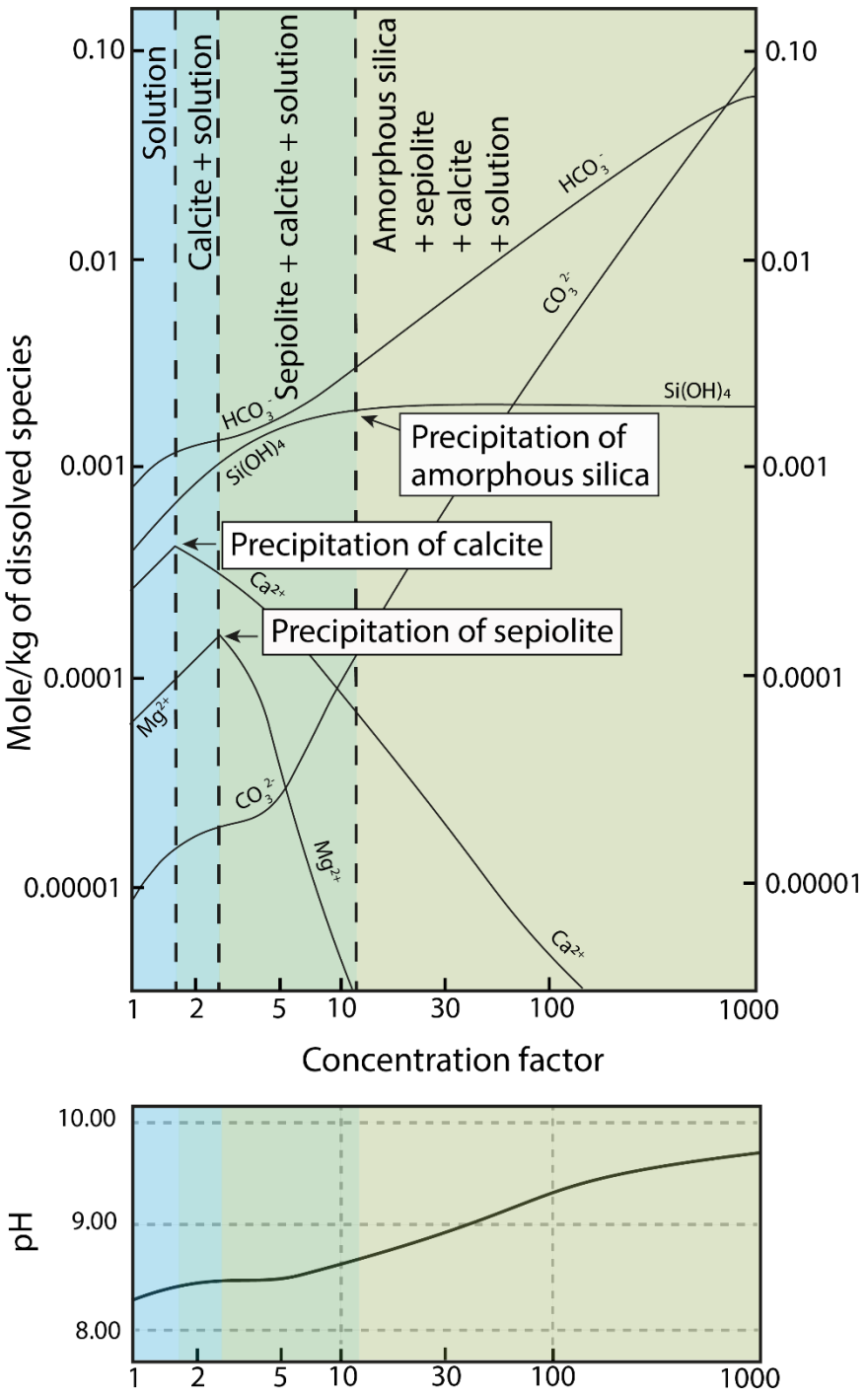

Figure 4.9: Plots of concentrations in various element species and pH values in a water solution during an evaporation process based on Helgeson et al. (1969). The x-axis refers to the concentration factor of the solution, whereas the y-axis refers either to the content in mole.kg^{-1} of dissolved species (top) or to pH (bottom). Calculations have been made by Helgeson et al. (1969) for a system composed by CaO-MgO-CO_2-SiO_2-H_2O at 25°C. Activity coefficients and equilibrium constants used for their diagram come from both their field and computed data (see their paper). Redrawn and adapted from Helgeson et al. (1969)'s Figure 8.

Is hydrothermalism a common feature of the Chobe Enclave?

Barite is often observed associated with carbonates in the Chobe Enclave (Fig. 4.7), raising the same question about the origin of the barium ion. Barite is usually documented in environments under the influence of hydrothermal or evaporation processes (Hanor, 2000) but was also recognized in soils and surficial sediments (Stoops and Zavaleta, 1978). It is frequently associated with sepiolite, calcite, and amorphous silica (Brock-Hon et al., 2012; Robins et al. 2012; Brock-Hon and Elliot, 2013), as it is in the Chobe Enclave (Figs 4.5 and 4.6). In the Chobe samples, barite clearly postdates the silicification process and calcite formation (Fig. 4.6), as also observed by Clarke et al. (2016). Although its formation can be attributed to soil dynamics, it remains difficult to explain the source and presence of barium in the Kalahari Sands prior its remobilization through pedogenic processes. However, the PCA suggests that barium does not show any correlation with the detrital and carbonate-sepiolite end-members (a $\pi/2$ rad angle between the variable poles; Fig. 4.8 and Table 4.1), although accounting for 7.5% of the total variance, which is not negligible. This absence of significant correlation can easily be interpreted as a random process, which is superimposed and associated neither with detrital phases nor with some conventional evaporitic process, as documented by the two poles along PC1 (Fig. 4.8). As in such environments, the barium leached by hydrothermal waters from the basement rock can combine with sulfur, forming barite after silicifications and calcite formation (Su et al. 2020). Even though barite has been clearly identified as a secondary mineral in the Chobe Enclave (Fig. 4.8), its origin and significance still need further investigations. In conclusion, a possible lacustrine hydrothermal contribution seems to be likely in some specific layers (Fig. 4.8), strengthening fortuitously conditions for, eventually, local sepiolite formation.

4.5.2 Sepiolite and the Chobe Enclave evolution during the Quaternary

From the mineralogical and PCA results, clay minerals, such as kaolinite and smectite (although with minor contents), were identified as witnesses of detrital phases. On the other hand, the absence of palygorskite in the Chobe Enclave is pointing to a closed palustrine/lacustrine system, in which the water body was depleted in aluminum and iron (Galán and Singer, 2011; Fig. 4.7). The detrital clays, particularly kaolinite and likely smectite,

are relatively abundant on the lower white sands (alluvial fan/fluvial) of the Chobe Enclave (Fig. 4.3A, B). These detrital phases suggest that kaolinite was produced possibly in humid upper-catchment regions of sub-equatorial Angola and Zambia (Garzanti et al., 2014). Hence, this assemblage associated with the sandy-rich lithology (Fig. 4.2) depicts conditions prior to the palustrine carbonate formation in the Chobe Enclave. This humid event was followed by a dryer episode, which increased the salinity of shallow lakes/marshes in a closed lacustrine/palustrine system with low energy. With favorable depositional conditions i.e., increased pH and requested ionic concentrations, it was possible to precipitate authigenic sepiolite, associated with the palustrine carbonate facies. The environmental conditions, documented from past and present-day systems and favorable for precipitation of fibrous magnesium-rich clays, probably also occurred during the Late Pleistocene to Holocene when palustrine carbonate deposited in the Chobe Enclave. Indeed, the carbonate precipitation events occurred irregularly, since ~75 ka (Diaz et al., 2019; Mokatse et al., 2022a; Fig. 4.2). These palustrine carbonate facies, with the highest authigenic sepiolite content, suggests the presence of a favorable reactor for sepiolite precipitation in semiarid or arid conditions (Helgeson et al., 1969). The presence of amorphous silica, also point to relatively higher alkalinity in the system (Galán and Singer, 2011; Fig. 4.9).

Sediment association found in the Chobe Enclave is closely like the Okavango alluvial fan deposits described by Ringrose et al. (2008). There, the lower part of the deposits, characterized by carbonate as a dense groundmass (McCarthy et al., 2012), directly lies on thick quartz sand layers: this suggests a shallow lake episode in the Chobe Enclave, with a lower water table depth compared to the present level, and provided by a hydrological or climate change (Cordova et al., 2017). Such deposits have been documented in the Madrid Basin where “the sepiolite deposits formed mainly associated with alluvial fan facies, palustrine conditions in marginal lake environments, and associated with other Mg-clays in mud-flat facies” (Pozo and Calvo, 2018). In addition, Ringrose et al. (2008) interpreted the presence of sepiolite as resulting from desiccation events. All these conditions fit with a large alluvial fan/palustrine paleoenvironment, making sepiolite unsurprising as a clay mineral in the Chobe Enclave. Finally, similar sedimentological assemblage and geochemical characteristics are found in a desiccated waterbody in the southern Kalahari Basin (Vainer et al., 2018). In this semiarid environment, Mg-rich clays of sepiolite (Bateman et al., 2003), palygorskite, and montmorillonite dominate the fine fraction. There, Sr isotopic ratios suggest

the incorporation of Mg from the dissolution of adjacent dolomites. Analogously to the Chobe Enclave, Ba is enriched in these southern Kalahari sediments that also contain amorphous phases. These proxies alongside ratios between iron phases and regional field observations led Vainer et al. (2018) to propose an oxygen-poor, brackish, and alkaline waterbody, with an average depth column of 6 m during its ~450 Ka of existence (Matmon et al., 2015). The similarity in the sedimentology and structural settings could imply on the Chobe Enclave as one of several waterbodies filling the Kalahari Basin throughout the Quaternary, such as the current alluvial fan of the Okavango.

As documented above, sepiolite precipitation needs an efficient evaporitic system to concentrate Mg^{2+}, as well as an alkaline pH for keeping $Si(OH)_4$ in solution until both ions reach the needed value of the solubility product for saturation state (Fig. 4.9). A closed lake system provides some necessary but not sufficient conditions to directly precipitate sepiolite from the water: evaporation and hydrology parameters (origin and nature of the fluids) also play a prominent role in the sedimentary process of sepiolite authigenesis.

4.6 Conclusions

The present study documents the occurrence and origin of authigenic sepiolite and demonstrates the possible conditions that were suitable for the formation of fibrous, magnesium-rich clay minerals in the Chobe Enclave. Authigenic sepiolite is reported with fibrous structure associated with carbonate and diatomite deposits. A closed lacustrine/palustrine alkaline system gave rise to high $Si(OH)_4$ and Mg^{2+} concentrations, enabling direct precipitation of sepiolite. A specific sequence of events is observed along pore walls and reflects the evolution of the parent solution and its ionic composition through time in an evaporitic system: firstly, calcite precipitates, secondly, sepiolite formation, followed by precipitation of amorphous silica. While the precipitation of sepiolite can be triggered from river waters transporting Mg^{2+} ions, some other sources of Mg-rich waters could have been provided during spells of hydrothermal activity. Principal component analysis demonstrates that the variability of element contents is controlled by three end-members i.e., detrital, carbonate-sepiolite, and hydrothermalism components, with the latter being asserted by the presence of barium. On one hand, kaolinite and minor smectite occurrences refer to a detrital clay assemblage in the lower units (sand-rich) of the Chobe Enclave, indicating the imprint of

humid conditions (input via large rivers and reworking) prior to carbonate formation. On the other hand, sepiolite is mostly associated to carbonate-diatomite facies in the upper units, indicating its likely formation by direct precipitation from solution (neoformation/authigenesis). Moreover, the formation and preservation of this sepiolite in palustrine carbonate dominated deposits reflect compatibility with the dominance of semiarid climate conditions during the Late Pleistocene to Holocene periods in the region where favorable conditions prevailed.

Acknowledgements

The authors acknowledge the Ministry of Environment, Natural Resources Conservation and Tourism of the Republic of Botswana as well as the Chobe Enclave Conservation Trust for the research permits, without which this study would not have been possible, as well as the Botswana International University of Science and Technology and the University of Lausanne. Special thanks to the Van Thuyne Ridge research center team for assistance with fieldwork and logistics. The authors also thank Mr. Dimitri Rigoussen for his discussions, and the reviewers, who greatly improved the first draft of this manuscript. This work has been supported by a Swiss National Foundation grant no 200021_172944 to EPV.

Supplementary material:

Suppl. Mat. Table 4.1: Bulk-rock mineralogy (XRD). Qz: quartz, Kfs: K-feldspar; Pl: plagioclase; Phyllo: phyllosilicates; Cal: calcite; Hem: hematite; Gth: Goethite. "Unquantified" correspond to organic matter, low-range order minerals or amorphous material.

Samples	Phyllo %	Qz %	Kfs %	Pl %	Cal %	Dol %	Gth%	Unquantified
B_0.68	20.09	34.19	0.00	0.00	43.12	0.00	0.00	2.60
BA_1	29.45	48.34	0.00	1.59	14.23	0.00	0.00	6.39
BA_1.4	19.01	49.26	0.00	1.03	24.51	0.00	0.00	6.20
BA_1.8	18.56	17.42	0.00	0.00	61.15	0.00	0.00	2.87
BA_2.2	7.89	30.90	0.00	0.00	57.34	0.00	0.00	3.88
BA_2.6	13.74	30.93	0.00	0.00	52.56	0.00	0.00	2.76
BA_3	1.89	47.90	0.00	0.00	47.37	0.00	0.00	2.84
BA_3.4	4.23	42.79	0.00	0.00	48.35	0.00	0.00	4.63
BC_4.4	25.13	67.77	0.00	1.52	1.56	0.30	0.00	3.72
BC_4.6	18.78	71.78	1.21	0.37	0.00	0.00	0.00	7.87
BC_5	16.69	80.12	0.00	0.42	0.40	0.00	0.00	2.36
BC_5.5	38.12	60.34	0.00	0.94	0.36	0.00	0.00	0.24
BC_5.8	22.80	73.82	0.00	0.46	0.00	0.00	0.72	2.20
BC_6.3	19.20	78.63	0.00	0.00	0.00	0.00	1.06	1.11
BC_7.4	27.18	70.10	0.00	0.36	0.00	0.00	0.00	2.36
BC_7.7	26.19	71.09	0.00	0.35	0.00	0.00	0.72	1.66
BC_8.4	45.98	47.92	0.65	0.00	0.40	0.00	0.00	5.05
BC_8.8	49.09	37.12	3.45	0.00	1.55	0.00	5.71	3.07
BC_9.2	72.12	9.44	2.21	0.00	1.16	0.00	5.32	9.75
BC_10	34.74	62.28	0.00	0.00	0.00	0.00	0.00	2.98
A0_0.1	24.80	28.96	0.00	0.00	39.09	1.92	0.00	5.23
A1_0.3	55.90	9.26	4.45	0.00	12.13	0.00	0.00	18.26

A1_0.6	54.89	5.21	4.36	0.00	11.99	0.00	10.63	12.93
A2_1	21.98	22.12	0.00	0.00	52.98	0.00	0.00	2.92
A2_2	0.00	31.09	0.00	0.00	67.34	0.00	0.00	1.57
A2_2.4	26.90	18.98	0.00	0.00	47.87	0.00	0.00	6.25
A2_2.8	0.00	25.72	0.00	0.00	70.76	0.00	0.00	3.52
A2_3.2	17.43	26.53	0.00	0.00	51.09	0.00	0.00	4.95
A2_3.6	27.86	20.67	0.00	0.00	45.66	0.00	0.00	5.81
A2_4	23.09	21.89	0.00	0.00	52.12	0.00	0.00	2.90
A2_4.4	27.09	11.61	0.00	0.00	58.06	0.00	0.00	3.24
A2_4.8	29.67	19.67	0.00	0.00	47.82	0.00	0.00	2.84
A2_5.2	24.06	31.13	0.00	0.00	42.31	0.00	0.00	2.49
A2_5.6	24.17	27.93	0.00	0.00	43.76	0.00	0.00	4.14
A2_6	23.62	70.89	0.86	0.00	0.42	0.00	0.00	4.20
NTA_0.5	0.00	13.78	0.00	0.00	80.23	0.00	0.00	5.99
NTA_1	0.00	65.23	0.00	0.00	32.63	0.00	0.00	2.14
NT0.8	16.99	24.76	0.00	0.00	50.34	0.00	0.00	7.91
NT_1.2	26.98	35.09	0.00	0.00	33.37	0.00	0.00	4.56
NT_1.6	30.23	9.67	0.00	0.00	57.23	0.00	0.00	2.87
NT_2	35.23	11.89	0.00	0.00	50.23	0.00	0.00	2.65
NT_2.4	24.87	34.09	0.00	0.00	37.12	0.00	0.00	3.92
NT_2.8	36.76	34.19	0.00	0.00	26.02	0.00	0.00	3.03
NT_3.2	33.10	59.45	1.61	0.00	1.36	0.00	0.00	4.49
NT_3.6	13.90	81.23	0.70	0.00	0.65	0.00	0.00	3.52
NT_4	17.32	73.10	6.58	0.00	0.00	0.00	0.00	3.00
NT_4.3	12.77	82.30	0.70	0.00	0.00	0.00	0.00	4.23
TSC_0.7	0.00	16.24	0.00	0.00	82.09	0.00	0.00	1.67
TSC_2.1	22.67	16.09	0.00	0.00	59.01	0.00	0.00	2.23
TS_0.2	38.11	56.90	1.61	0.00	1.69	0.00	0.00	1.69
TS_0.6	33.89	32.90	1.53	0.00	29.09	0.00	0.00	2.59

TS_1	19.85	26.88	0.00	0.00	50.57	0.00	0.00	2.71
TS_1.4	23.06	26.19	3.22	1.90	43.76	0.00	0.00	1.87
TS_1.8	0.00	34.12	0.00	0.00	63.76	0.00	0.00	2.12
TS_2.2	0.00	53.98	0.00	0.00	43.12	0.00	0.00	2.90
TS_2.6	13.67	62.00	0.00	0.00	21.23	0.00	0.00	3.10
TS_3	21.09	70.65	1.19	0.00	4.20	0.00	0.00	2.87
TS_3.4	22.67	74.00	1.30	0.00	0.00	0.00	0.00	2.03
TS_3.8	24.65	72.75	0.68	0.00	0.00	0.00	0.00	1.92
TS_4	30.67	65.37	0.65	0.00	0.00	0.00	0.00	3.31

Suppl. Mat. Table 4.2: Proportions of the different clay minerals in the clay fraction (< 2 μm). Smc: smectite, Sep: sepiolite; Kao: kaolinite; Chl: chlorite

Sample	Smc %	Sep %	Kao %	Chl %
TSC_0.7	16.09	83.91	0.00	0
TSC_2.1	0.00	100.00	0.00	0
TS_0.2	24.73	54.57	9.67	11.03
TS_0.6	9.13	76.49	14.39	0
TS_1	5.19	87.69	7.12	0
TS_1.4	6.18	87.68	6.15	0
TS_1.8	6.03	82.67	9.37	1.93
TS_2.2	24.13	62.33	13.54	0
TS_2.6	27.54	52.12	15.11	5.22
TS_3	23.26	76.74	0.00	0
TS_3.4	0.00	0.00	100.00	0
TS_3.8	39.11	0.00	47.40	13.48
TS_4	27.48	17.25	55.27	0
B_0.68	0.00	76.82	23.18	0
BA_1	10.01	89.99	0.00	0
BA_1.4	8.67	84.92	2.88	3.52
BA_1.8	9.95	82.97	2.91	4.17
BA_2.2	15.16	84.84	0.00	0
BA_2.6	11.15	77.86	6.00	5
BA_3	12.31	87.69	0.00	0
BA_3.4	20.30	79.70	0.00	0
BC_4.4	31.06	47.78	12.52	8.64
BC_4.6	22.68	61.95	7.40	7.97
BC_5	22.55	62.00	15.45	0
BC_5.5	18.28	65.24	7.05	9.43
BC_5.8	23.28	48.15	0.00	28.57
BC_7.2	21.59	30.68	31.32	16.41
BC_7.7	14.79	26.88	58.33	0
BC_8.4	18.23	24.80	56.97	0
BC_8.8	32.14	37.50	17.37	12.98
BC_9.2	18.98	21.92	59.10	0
BC_10	19.11	30.54	37.10	13.26
NTA_0.5	11.64	88.36	0.00	0
NTA1	0.00	100.00	0.00	0
NT0.8	3.21	96.79	0.00	0
NT_1.2	4.42	90.83	4.75	0
NT_1.6	14.68	85.32	0.00	0
NT_2	25.65	69.92	4.43	0
NT_2.4	31.78	61.57	6.66	0
NT_2.8	21.23	78.77	0.00	0

NT_3.2	25.00	56.08	8.98	9.94
NT_3.6	28.62	54.23	8.57	8.57
NT_4	44.53	31.59	23.87	0
NT_4.3	48.73	23.38	15.62	12.27
A0_0.1	0.00	67.40	17.89	14.71
A1_0.3	52.29	0.00	32.84	14.87
A1_0.6	52.97	11.31	35.72	0
A2_1	21.04	78.96	0.00	0
A2_2	5.69	94.31	0.00	0
A2_2.4	5.76	90.24	1.98	2.02
A2_2.8	2.92	97.08	0.00	0
A2_3.2	5.88	90.95	3.17	0
A2_3.6	6.67	93.33	0.00	0
A2_4	14.59	81.97	3.44	0
A2_4.4	21.74	78.26	0.00	0
A2_4.8	49.22	50.78	0.00	0
A2_5.6	17.98	77.27	4.74	0
A2_6	35.11	40.27	16.30	8.32

References

Adatte, T., Stinnesbeck, W., Keller, G., 1996. Lithostratigraphic and mineralogic correlations of near K/T boundary sediments in northeastern Mexico: Implications for origin and nature of deposition. In: Ryder, G., Fastovsky, D., Gartner, S. (Eds.), The Cretaceous-Tertiary Event and Other Catastrophes in Earth History Geological Society of America Special Paper, 307, 211–226.

Akbulut, A., Kadir, S., 2003. The geology and origin of sepiolite, palygorskite and saponite in Neogene lacustrine sediments of the Serinhisar-Acipayam basin, Denizli, SW Turkey. Clays and Clay Minerals 51(3), 279–92.

Arbey, F., 1980. Les formes de la silice et l'identification des évaporites dans les formations silicifiées. Bull. Cent. Rech. Explot.-Prod. Elf-Aquitaine, 4, 1, 309-365.

Atekwana, E.A., Molwalefhe, L., Kgaodi, O., Cruse, A.M., 2016. Effect of evapotranspiration on dissolved inorganic carbon and stable carbon isotopic evolution in rivers in semi-arid climates: The Okavango Delta in Northwest Botswana. Journal of Hydrology: Regional Studies, 7, 1-13.

Bateman, M.D., Thomas, D.S., Singhvi, A.K., 2003. Extending the aridity record of the Southwest Kalahari: current problems and future perspectives. Quaternary International, 111(1), pp.37-49.

Birsoy, R., 2002. Formation of sepiolite-palygorskite and related minerals from solution. Clays and Clay Minerals, 50(6), 736-745.

Brauner, K., Preisinger, A., 1956. Struktur und Entstehung des Sepioliths. Tschermaks Mineralogische und Petrographische Mitteilungen 6(1–2), 120–40.

Brock-Hon, A.L., Robins, C.R., Buck, B.J., 2012. Micromorphological investigation of pedogenic barite in Mormon Mesa petrocalcic horizons, Nevada USA: Implication for genesis. Geoderma, 179, 1-8.

Brock-Hon, A.L., Elliot, T.R., 2013. Three-Dimensional Investigation of Petrocalcic Materials: Insight into Pedogenic Processes and Future Applications. Soil Science Society of America Journal, 77(4), 1436-1441.

Burrough, S.L., Thomas, D.S.G. 2008. Late Quaternary lake-level fluctuations in the Mababe Depression: Middle Kalahari palaeolakes and the role of Zambezi inflows. Quaternary Research 69, 388-403.

Burrough, S.L., Thomas, D.S.G., Shaw, P.A., Bailey, R.M., 2007. Multiphase Quaternary Highstands at Lake Ngami, Kalahari, Northern Botswana. Palaeogeography, Palaeoclimatology, Palaeoecology, 253(3–4), 280–99.

Burrough, S.L., Thomas, D.S.G., and Bailey, R.M., 2009. Mega-Lake in the Kalahari: A Late Pleistocene record of the Palaeolake Makgadikgadi system. Quaternary Science Reviews 28(15–16), 1392–1411.

Chamley, H., 1989. Clay Sedimentology. Springer-Verlag, Berlin.

Chorowicz, J., 2005. The east African rift system. Journal of African Earth Sciences, 43(1-3), pp.379-410.

Clarke, C.E., Majodina, T.O., Du Plessis, A., Andreoli, M.A.G., 2016. The use of X-ray tomography in defining the spatial distribution of barite in the fluvially derived palaeosols of Vaalputs, Northern Cape Province, South Africa. Geoderma, 267, 48-57.

Cordova, C.E., Scott, L., Chase, B.M., Chevalier, M., 2017. Late Pleistocene-Holocene vegetation and climate change in the Middle Kalahari, Lake Ngami, Botswana. Quaternary Science Reviews 171, 199–215.

Cuevas, J., De La Villa, R.V., Ramirez, S., Petit, S., Meunier, A., Leguey, S., 2003. Chemistry of Mg smectites in lacustrine sediments from the Vicalvatro sepiolite deposit, Madrid Neogene Basin (Spain). Clays and Clay Minerals, 51, 457-472.

Diaz, N., Armitage, S.J., Verrecchia, E.P., Herman, F., 2019. OSL Dating of a carbonate island in the Chobe Enclave, NW Botswana. Quaternary Geochronology 49, 172–76.

Draidia, S., El Ouahabi, M., Daoudi, L., Havenith, H.B., Fagel, N., 2016. Occurrences and genesis of palygorskite/sepiolite and associated minerals in the Barzaman Formation, United Arab Emirates. Clay Minerals 51, no. 05, 763–79.

Dyer, S., 2017. Water cycle in the Northern Kalahari. Unpubl. Master of Science in Biogeosciences, Univ. of Lausanne.

Fersmann, A., 1913. Research on magnesian silicates. Mémoires de l'Académie des sciences de St. Petersburg 32, 321–430.

Galán, E., Carretero, M.I., 1999. A New Approach to Compositional Limits for Sepiolite and Palygorskite. Clays and Clay Minerals 47(4), 399–409.

Galán, E., Pozo, M., 2011. Palygorskite and sepiolite deposits in continental environments. Description, Genetic Patterns and Sedimentary Settings. In Developments in Clay Science, 3:125–73.

Galán, E., Singer, A. (Eds) 2011. Developments in palygorskite-sepiolite research. Development in Clay Science, 3, 501.

García-Romero, E., Suárez, M., Santarén, J., Alvarez, A., 2007. Crystallochemical Characterization of the palygorskite and sepiolite from the Allou Kagne deposit, Senegal. Clays and Clay Minerals 55(6), 606–17.

Garzanti, E., Padoan, M., Setti, M., López-Galindo, A., Villa, I.M., 2014. Provenance versus weathering control on the composition of tropical river mud (southern Africa). Chemical Geology, 366, 61-74.

Garzanti, E., Pastore, G., Stone, A., Vainer, S., Vermeesch, P. and Resentini, A., 2022. Provenance of Kalahari Sand: Paleoweathering and recycling in a linked fluvial-aeolian system. Earth-Science Reviews, 224, p.103867.

Godet, A., Bodin, S., Adatte,T., Föllmi, K.B., 2008. Platform-induced clay-mineral fractionation along a northern Tethyan basin-platform transect: implications for the interpretation of Early Cretaceous climate change (Late Hauterivian-Early Aptian). Cretaceous Research 29(5–6), 830–47.

Google Earth, 2022. Chobe region, Botswana. Pro V 7.3.6.9345, CNES/Airbus 2022. http://www.earth.google.com.

Gumbricht, T., McCarthy, T.S., Merry, C.L., 2001. The topography of the Okavango Delta, Botswana, and its tectonic and sedimentological implications. South African Journal of Geology, 104(3), pp.243-264.

Haddon, I.G., McCarthy, T.S., 2005. The Mesozoic–Cenozoic interior sag basins of Central Africa: the late-cretaceous–Cenozoic Kalahari and Okavango basins. Journal of African Earth Sciences, 43(1-3), 316-333.

Hanor, J.S., 2000. Barite–celestine geochemistry and environments of formation. Reviews in Mineralogy and Geochemistry, 40(1), 193-275.

Helgeson, H. C., Garrels, R. M., Mackenzie, F. T., 1969. Evaluation of irreversible reactions in geochemical processes involving minerals and aqueous solutions—II. Applications. Geochimica et Cosmochimica Acta, 33(8), 451-483.

Hong, H., Yu, N., Xiao, P., Zhu, Y.H., Zhang, K.X., and Xiang, S.Y., 2007. Authigenic palygorskite in Miocene sediments in Linxia basin, Gansu, northwestern China. Clay Minerals, 42, 45-58.

Irkec, T., Ünlü, T., 1993. An example to sepiolite formation in volcanic belts by hydrothermal alteration: Kibriscik (Bolu) sepiolite occurrence Mineral Research Exploration Bulletin, 115, 49-68.

Jones, B.F., Galán, E., 1988. Sepiolite and palygorskite. In: Bailey, S.W. (Ed.), Hydrous Phyllosilicates, Reviews in Mineralogy 19, Mineralogical Society of America, Washington, 631–674.

Jones, B.F., Conko, K.M., 2011. Environmental influences on the occurrences of sepiolite and palygorskite: a brief review. Developments in clay science, 3, 69-83.

Jourdan, F., Féraud, G., Bertrand, H., Kampunzu, A.B., Tshoso, G., Le Gall, B., Tiercelin, J.J., Capiez, P., 2004. The Karoo triple junction questioned: evidence from Jurassic and Proterozoic 40Ar/39Ar ages and geochemistry of giant Okavango dyke swarm (Botswana). Earth and Planetary Science Letters, 222, 989–1006

Kauffman Jr., A.J., 1943. Fibrous sepiolite from Yavapai County, Arizona. American Mineralogist, no. 28, 512–520.

Key, R.M., Ayres, N., 2000. The 1998 edition of the national geological map of Botswana. Journal of African Earth Sciences, 30(3), 427–51.

Klug, H. P., Alexander, L. E., 1974. X-ray diffraction procedures: for polycrystalline and amorphous materials (p. 992).

Koning, E., Gehlen, M., Flank, A.-M., Calas, G., Epping, E, 2007. Rapid post-mortem incorporation of aluminum in diatom frustules: evidence from chemical and structural analyses. Marine Chemistry 106, no. 1–2, 208–22.

Kübler, B., 1987. Cristallinité de l'illite: méthodes normalisées de préparation, méthode normalisée de mesure, méthode automatique normalisée de mesure. Cahiers de l'Institut de Géologie, Université de Neuchâtel, Suisse Série ADX n° 2.

Le Gall, B., Tshoso, G., Jourdan, F., Féraud, G., Bertrand, H., Tiercelin, J.J., Kampunzu, A.B., Modisi, M.P., Dyment, J., Maia, M., 2002. 40Ar/39Ar geochronology and structural data from the giant Okavango and related mafic dyke swarms, Karoo igneous province, northern Botswana. Earth and Planetary Science Letters, 202, 595–606.

Lehmann, J., Master, S., Rankin, W., Milani, L., Kinnaird, J.A., Naydenov, K.V., Saalmann, K. and Kumar, M., 2015. Regional aeromagnetic and stratigraphic correlations of the Kalahari Copperbelt in Namibia and Botswana. Ore Geology Reviews, 71, pp.169-190.

Lopez, F., Gonzalez, J.M.G., 1995. Fibrous clays in the Almazan Basin (Iberian range, Spain): genetic pattern in a calcareous lacustrine environment. Clay Minerals 30(4), 395–406.

Matmon, A., Hidy, A.J., Vainer, S., Crouvi, O., Fink, D., Erel, Y., Arnold, M., Aumaître, G., Bourlès, D., Keddadouche, K. and Horwitz, L.K., 2015. New chronology for the southern Kalahari Group sediments with implications for sediment-cycle dynamics and early hominin occupation. Quaternary Research, 84(1), pp.118-132.

McCarthy, T.S., 2013. The Okavango Delta and its place in the geomorphological evolution of southern Africa. South African Journal of Geology, 116(1), 1-54.

McCarthy, T.S., Ellery, W.N., 1995. Sedimentation on the distal reaches of the Okavango Fan, Botswana, and its bearing on calcrete and silcrete (ganister) formation. Journal of Sedimentary Research, 65(1a), 77-90.

McCarthy, T.S., Humphries, M.S., Mahomed, I., Le Roux, P., Verhagen, B.T., 2012. Island forming processes in the Okavango Delta, Botswana. Geomorphology, 179, 249-257.

Michalopoulos, P., Aller, R.C., Reeder, R.J., 2000. Conversion of diatoms to clays during early diagenesis in tropical, continental shelf muds. Geology 28, no. 12; p. 1095–1098.

Miller, R. M., Pickford, M., Senut, B., 2010. The geology, paleontology and evolution of the Etosha pan, Namibia: implications for terminal Kalahari deposition. South African Journal of Geology 113(3), 307–34.

Mizutani, T., Fukushima, Y., Okada, A., Kamigaito, O., 1991. Hydrothermal synthesis of sepiolite. Clay Minerals 26(03), 441–45.

Modie B.N., 2000. Geology and mineralisation in the Meso- to Neoproterozoic Ghanzi-Chobe belt of northwest Botswana. Journal African Earth Sciences 30 (3), 467–474.

Mokatse, T., Diaz, N., Shemang, E., Van Thuyne, J., Vittoz, P., Vennemann, T., Verrecchia, E.P., 2022a. Landscapes and Landforms of the Chobe Enclave, Northern Botswana. In: Eckardt, F.D., (Ed.), Landscapes and landforms of Botswana, Springer Nature Switzerland, 91-115.

Mokatse, T., Vainer, S., Irving, J., Schmidt, C., Kgosidintsi, B., Shemang, E., Verrecchia, E.P., 2022b. Geometry of sedimentary deposits and evolution of the landforms in the Chobe Enclave, Northern Botswana. Geomorphology, 108406.

Moore, D., Reynolds, R., 1989. X-Ray diffraction and the identification and analysis of clay-minerals: Oxford, Oxford University Press, 332 p.

Moore, A.E., 1999. A reappraisal of epeirogenic flexure axes in southern Africa. South African Journal of Geology, 102(4), 363-376.

Moore, A.E., Cotterill, F.P.D. and Eckardt, F.D., 2012. The evolution and ages of Makgadikgadi palaeo-lakes: consilient evidence from Kalahari drainage evolution south-central Africa. South African Journal of Geology, 115(3), 385-413.

Mukwati, B.T., Tadesse, N., Bagai, Z.B., Laletsang, K., 2018. Hydrogeochemistry of the Kasane Hot Spring, Botswana. Universal Journal of Geoscience 6, 130-145.

Niles, M.C., 2012. Chemical and isotopic analysis of hot springs in Zambia; no evidence for near surface rift-related magmatic body (BSc. thesis). Oklahoma State University, Stillwater.

Nugent, C., 1990. The Zambezi River: tectonism, climatic change and drainage evolution. Palaeogeography Palaeoclimatology Palaeoecology, 78, 55-69.

Pardo, P., Bastida, J., Serrano, F.J., Ibáñez, R., Kojdecki, M.A., 2009. X-Ray Diffraction line-broadening study on two vibrating, dry-milling procedures in kaolinites. Clays and Clay Minerals 57(1), 25–34.

Pozo, M., Calvo, J.P., 2015. Madrid Basin (Spain): A natural lab for the formation and evolution of magnesian clay minerals. In Magnesian Clays: Characterization, Origin and Applications, Pozo, M., Galán, E. (Eds.), AIPEA Educational Series, Pub. No. 2, Digilabs: Bari, Italy, pp. 229-281.

Pozo, M., Calvo, J.P., 2018. An overview of authigenic magnesian clays. Minerals, 8(11), 520.

Pozo, M., Galán, E., 2015. Magnesian clay deposits: Mineralogy and origin. In: Pozo, M., Galán, E. (Eds.), Magnesian Clays: Characterization, Origin and Applications. AIPEA Educational Series, Pub. No. 2, Digilabs, Bari, Italy, pp. 175–227.

Ren, H., Brunelle, B.G., Sigman, D.M., Robinson, R.S., 2013. Diagenetic aluminum uptake into diatom frustules and the preservation of diatom-bound organic nitrogen. Marine Chemistry, 155, 92–101.

Ringrose, S., Huntsman-Mapila, P., Kampunzu, A.B., Downey, W., Coetzee, S., Vink, B., Matheson, W., Vanderpost, C., 2005. Sedimentological and geochemical evidence for palaeo-environmental change in the Makgadikgadi subbasin, in relation to the MOZ rift

depression, Botswana. Palaeogeography, Palaeoclimatology, Palaeoecology, 217(3-4), 265-287.

Ringrose, S., Huntsman-Mapila, P., Downey, W., Coetzee, S., Fey, M., Vanderpost, C., Vink, B., Kemosidile, T., Kolokose, D., 2008. Diagenesis in Okavango fan and adjacent dune deposits with implications for the record of paleo-environmental change in Makgadikgadi–Okavango–Zambezi basin, northern Botswana. Geomorphology, 101(4), 544–57.

Ringrose, S., Harris, C., Huntsman-Mapila, P., Vink, B.W., Diskins, S., Vanderpost, C., Matheson, W., 2009. Origins of strandline duricrusts around the Makgadikgadi Pans (Botswana Kalahari) as deduced from their chemical and isotope composition. Sedimentary Geology, 219, 262-279.

Robins, C.R., Brock-Hon, A.L., Buck, B.J., 2012. Conceptual mineral genesis models for calcic pendants and petrocalcic horizons, Nevada. Soil Science Society of America Journal, 76(5), 1887-1903.

Rolli, M. (1990). Dosage semi-quantitatif RX sur Scintag. Cahiers de l'Institut de Géologie de Neuchâtel, Suisse, v. Série ADX, 1, 49.

Schwartz, M.O., Kwok, Y.Y., Davis, D.W., Akanyang, P., 1996. Geology, geochronology and regional correlation of the Ghanzi Ridge, Botswana. South African Journal of Geology, 99, 245-250.

Shannon, E.V., 1929. Tschermigite, ammoniojarosite, epsomite, celestite and palygorskite from Southern Utah. Proceedings of the United States National Museum, 74 (13), 12.

Shaw, P.A., Thomas, D.S.G., 1988. Lake Caprivi: a late Quaternary link between the Zambezi and middle Kalahari drainage systems. Zeitschrift für Geomorphologie 32, 329-37.

Singer, A., 1979. Palygorskite in sediments: detrital, diagenetic or neoformed—A critical review. Geologische Rundschau, 68, 996–1008.

Singer, A., 1984. Pedogenic palygorskite in the arid environment. In: Singer, A., Gala´n, E. (Eds.), Palygorskite–Sepiolite. Occurrences, Genesis and Uses. Developments in Sedimentology, vol. 37. Elsevier, Amsterdam, 169–177.

Stoessell R.K., Hay, R.L., 1978. The geochemical origin of sepiolite and kerolite at Amboseli, Kenya. Contributions to Mineralogy and Petrology, 65, 255-267.

Stoops, G.J., Zavaleta, A., 1978. Micromorphological evidence of barite neoformation in soils. Geoderma, 20(1), 63-70.

Su, C., Zhong, D., Qin, P., Wang, A., 2020. Mineral precipitation sequence and formation of the lacustrine hydrothermal sediments in the Lower Cretaceous Tenggeer Formation in the Baiyinchagan Sag, China. Sedimentary Geology, 398, 105586.

Suárez, M., García-Romero, E., 2011. Advances in the crystal chemistry of sepiolite and palygorskite. In: Galàn, E., Singer, E., (Eds.), Developments in Clay Science, Elsevier, 33-65,

Tateo, F., Sabbadini, R., Morandi, N., 2000. Palygorskite and sepiolite occurrence in Pliocene lake deposits along the river Nile: evidence of an arid climate. Journal of African Earth Sciences 31(3–4), 633–45.

Thomas, D.S.G., Shaw, P.A., 1990. The deposition and development of the Kalahari Group sediments, Central Southern Africa. Journal of African Earth Sciences 10(1–2), 187–97.

Thomas D.S.G., Shaw, P.A., 1991. The Kalahari environment. Cambridge University Press, 284.

Tosca, N. J., Masterson, A.L., 2014. Chemical controls on incipient Mg-silicate crystallization at 25 C: Implications for early and late diagenesis. Clay Minerals, 49(2), 165-194.

Vainer, S., Erel, Y., Matmon, A., 2018. Provenance and depositional environments of Quaternary sediments in the southern Kalahari Basin. Chemical Geology, 476, 352-369.

Vainer, S., Matmon, A., Erel, Y., Hidy, A.J., Crouvi, O., De Wit, M., Geller, Y. and ASTER Team, 2021. Landscape responses to intraplate deformation in the Kalahari constrained by sediment provenance and chronology in the Okavango Basin. Basin Research, 33(2), pp.1170-1193.

Vainer, S., Matmon, A., Ben Dor, Y., Verrecchia, E.P. and Eckardt, F., 2022. Eolian chronology reveals causal links between tectonics, climate, and erg generation. Nature Communications, 13(1), pp.1-9.

Van Thuyne, J., Darini, I., Mainga, A., Verrecchia, E.P., 2021. Are fungus-growing termites super sediment-sorting insects of subtropical environments? J. of Arid Environments, 193, 104556.

Wang, M.K., Tseng, P.C., Chang, S.S., Ray, D.T., Shau, Y.H., Shen, Y.W. Chen, R.C., Chiang, P.N., 2009. Origin and mineralogy of sepiolite and palygorskite from the Tuluanshan Formation, Eastern Taiwan. Clays and Clay Minerals 57(5), 521–30.

Watts, N.L., 1980. Quaternary pedogenic calcretes from the Kalahari (southern Africa): mineralogy, genesis and diagenesis. Sedimentology, 27(6), 661-686.

Webster, D.M., Jones, B.F., 1994. Paleoenvironmental implications of lacustrine clay minerals from the double lakes formation, southern high plains, Texas. In: Renaut, R.W., Last, W.M. (Eds.), Sedimentology and Geochemistry of Modern and Ancient Saline Lakes. SEPM Spec. Publ. 50, 159–172.

Yalçin, H., Bozkaya, Ö., 2011. Sepiolite–palygorskite occurrences in Turkey. In Developments in clay science (Vol. 3, 175-200). Elsevier.

CHAPTER 5

Late Quaternary evolution of a large floodplain assessed by quartz microtextural analysis (Chobe Enclave, Northern Botswana)

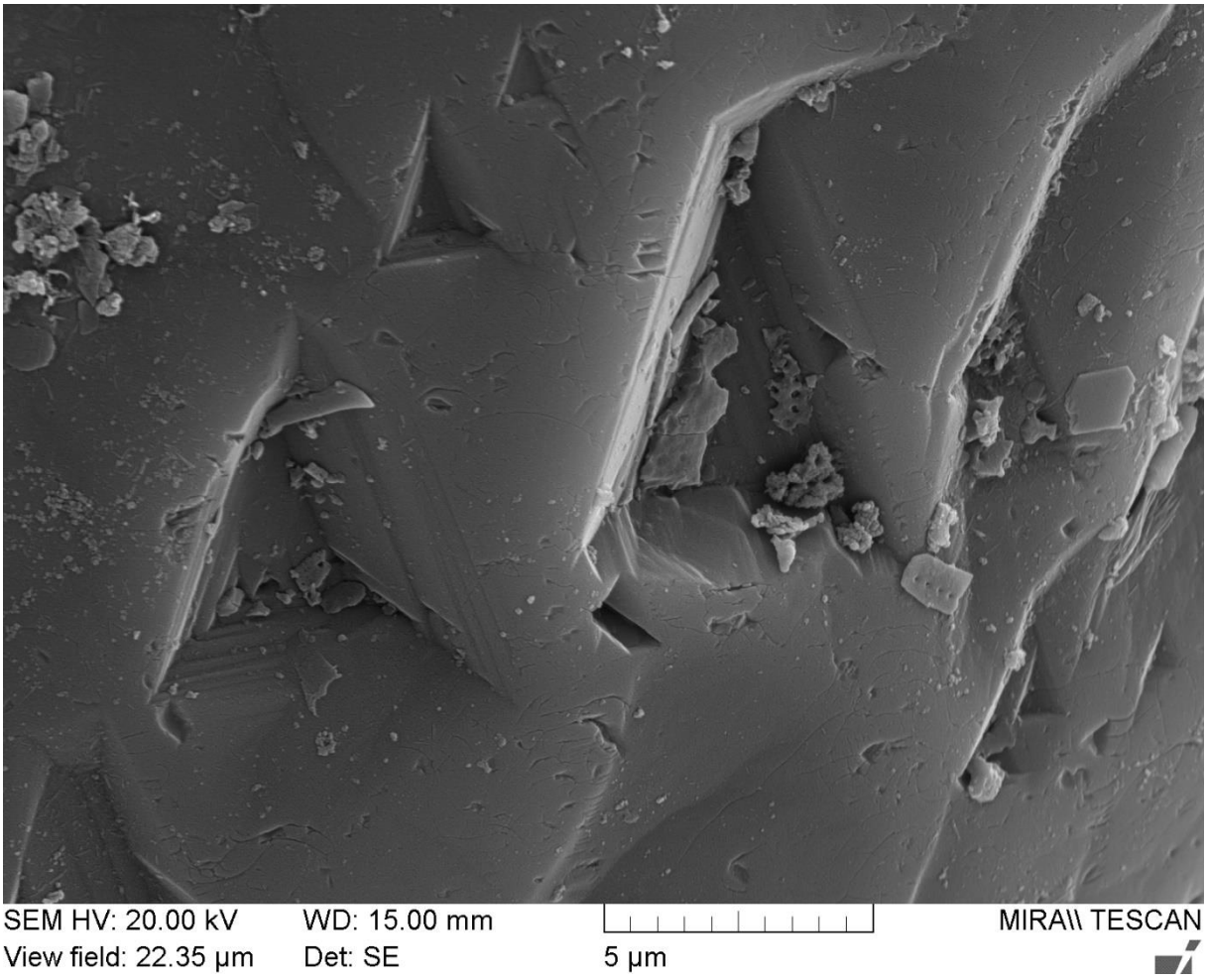

SEM image showing triangular etch pits with adhering particles including diatom fragments.

5. Late Quaternary evolution of a large floodplain assessed by quartz microtextural analysis (Chobe Enclave, Northern Botswana)

(To be sent to *Quaternary International*)

In this chapter, personal work entails: sampling, sample preparation, SEM analysis, literature review and writing.

Synopsis

This chapter focuses on the diversity and long history of quartz grains belonging to the various sedimentary bodies observed in the Chobe Enclave. The relationship between particle size variability in the various sub-environments and the characterization of the main microtextures successions is a crucial step in understanding the evolution of a sandy semi-arid landscape.

Abstract

Analysis of quartz microtextures using scanning electron microscopy is a method performed to reconstruct the sedimentary history of quartz grains. Using this approach, this study focuses on quartz grain microtextures from six different facies observed in the Chobe Enclave floodplain: white pure sands, yellow sands, carbonate-rich sands, clay-rich sands, as well as quartz grains trapped in diatomites and palustrine limestones. This research assesses and documents the succession of depositional environments and aims at the reconstruction of succession/history of quartz grains based on four outcrops. The various facies from the Chobe Enclave floodplain display mostly similar granulometric sand fraction modes and grain-size distributions, emphasizing similar reworking conditions, which led to a homogenization of sands from potentially different sources. A total of 16 microtextures were observed on quartz surfaces from the six sedimentary facies. Results of this study demonstrate the existence of both mechanical and chemical features developed during transportation and deposition of quartz grains in alternating aeolian and subaqueous (mainly fluvial) environments, as well as weathering phases (likely in paleosols or alkaline environments). Quartz microtextures reveal a primary aeolian legacy overprinted by alternating fluvial/palustrine/weathering phases, with some more recent aeolian marks, consistent with the complex history of a paleo-alluvial fan resulting from changes in hydrological conditions as well as tectonic settings during the Late Pleistocene.

5.1 Introduction

Quartz grain microtextures have been extensively studied and used to identify sources of various detrital sediments, as well as to decipher processes endured during transportation and diagenetic history of sediments (Krinsley and Doornkamp, 1973; Vos et al., 2014). This approach is justified and can be achieved because different transport modes imprint distinct microscale features onto quartz grain surfaces. Indeed, quartz grain microtextural analysis is based on the recognition of some specific features (microtextures), their frequencies, and their relative succession at the surface of quartz grains observed with a scanning electron microscope (SEM). Each type of sediment transport imprints a series of microtextures on the grain surface, e.g. turbulent transport in rivers, aeolian reworking, or chemical weathering (Vos et al., 2014). In addition, their relative succession, assessed by the observation of their fresh or smoothed aspect, disturbance, and partial erosion, allows a sequence of events to be reconstructed (Krinsley & Doornkamp, 1973; Mahaney, 2002; Itamiya et al., 2019; J. Li et al., 2021).

The quartz microtextural approach has only been rarely applied to the Late Quaternary sediments that recorded the evolution of southern African plateaus (Bond and Fernandes, 1974; Thomas, 1987), although quartz-rich sediments are extremely common in the strata. Consequently, and after stratigraphic and geophysical investigations (Mokatse et al., 2022a, 2022b), a microtextural analysis is applied to quartz of the Chobe Enclave, Botswana (Fig. 5.1) in order to assess the evolution of the landscape of this southern African plateau.

Accordingly, the current research aims to 1) explore the application of SEM microtextural analysis to assess the depositional environments in Quaternary floodplain strata, and 2) reconstruct the succession of the environments recorded in the Chobe Enclave sedimentary facies, particularly by exploring trends in preserved microtextures as witnesses of sequences of depositional and reworking settings, such as lacustrine, palustrine, aeolian, or pedogenic phases developed after the deposition of sediments in the large fluvial floodplain of the Chobe Enclave.

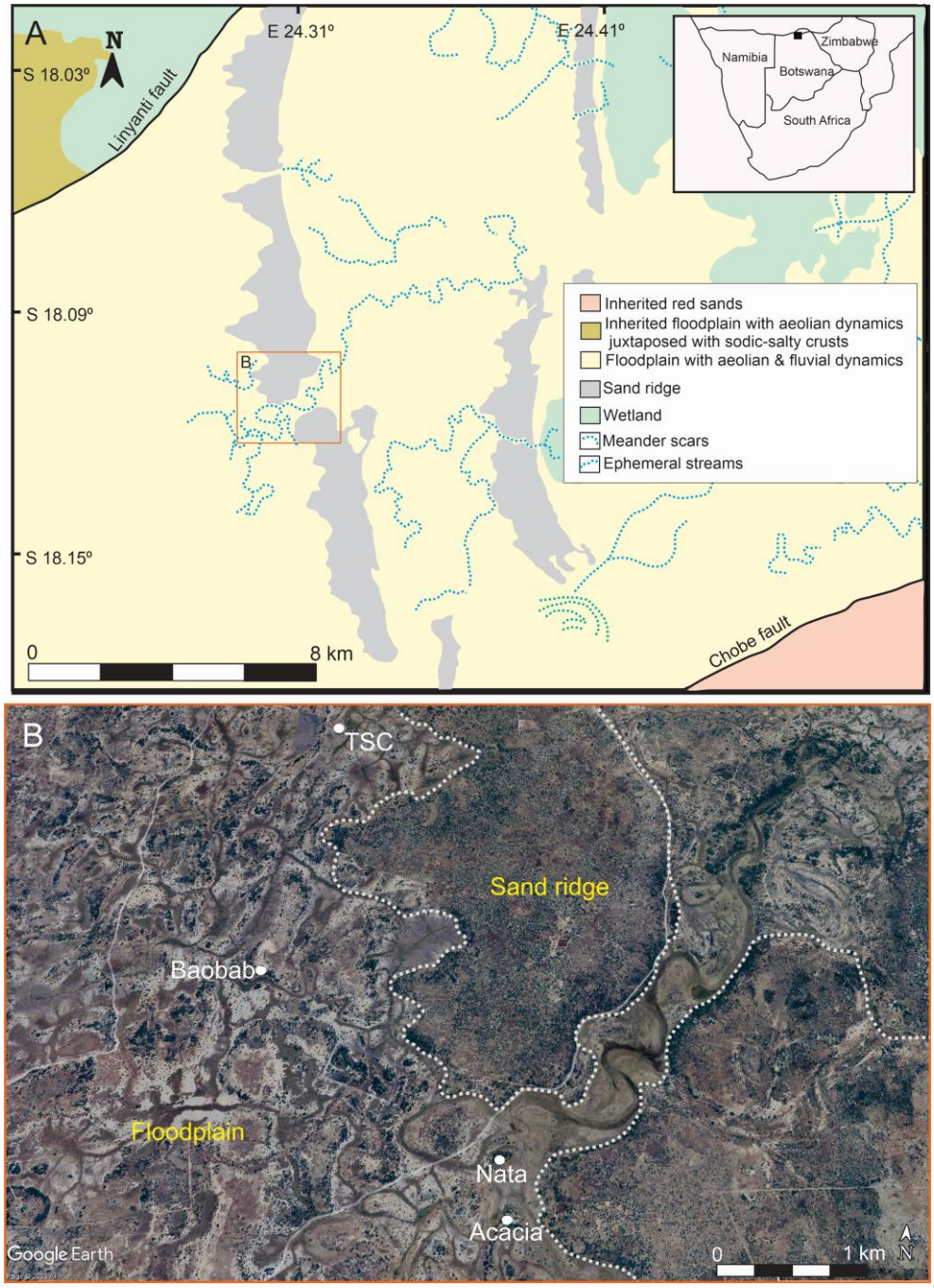

Figure 5.1: A) Geomorphological map of the Chobe Enclave. The red rectangle refers to the area in B. B) Satellite image showing the location of the study sites (Google Earth, 2023). The outline of the sand ridges is depicted by the white dashed line.

5.2 Geological settings

The Chobe Enclave forms part of the Chobe-Linyanti sub-basin, infilled with Quaternary sediments largely dominated by sands deposited in semiarid conditions (Burrough et al., 2007, 2009; Fig. 5.1). The Chobe-Linyanti sub-basin, together with the Ngami and Mababe sub-

basins form within the structural depression of the Okavango Graben (Modisi et al., 2000; Kinabo et al., 2007, 2008). This graben system is a segment of the larger Makgadikgadi-Okavango-Zambezi basin (MOZB), situated inside the intracratonic Kalahari Basin, where Plio-Pleistocene aeolian and fluvial sands, as well as sandstones, represent the most common sediments (Thomas and Shaw, 1990; Haddon and McCarthy, 2005; Matmon et al., 2015; Vainer et al., 2021, 2022). In the Chobe Enclave, the Quaternary deposits, probably between 50 and 100 m thick (Thomas and Shaw, 1991; Vainer et al., submitted), overlay a Proterozoic metamorphic and magmatic basement. In addition, the Chobe Enclave also includes carbonate deposits in an otherwise large siliceous-dominated basin. These deposits, which were described as palustrine limestones (Diaz et al., 2019), outcrop in the landscape as "*islands*" among the sands and are mostly observed in the central part of the Chobe Enclave, between the paleo-floodplain in the west and the large present-day floodplain in the east (Mokatse et al., 2022). These limestones are usually associated with diatomites and significant authigenic fibrous clay minerals (sepiolite; Mokatse et al., 2023), which formed in fluctuating lacustrine/palustrine environments.

5.3 Facies Characteristics

Four outcrops have been studied in the Chobe Enclave (Fig. 5.2). They are extensively described in Mokatse et al. (2022b). Four main facies are recurrent: White sands, Yellow sands, Diatomites, and carbonate-rich sediments and limestones.

The White sand facies forms part of the lowest lithological units of the Chobe Enclave. Samples from these facies consist of almost exclusively well sorted fine quartz sand (Fig. 5.2; Mokatse et al., 2022). The Yellow sand facies often correspond to the transition zone between the White sand facies and the Diatomite, Carbonate-rich, and Limestone facies associations. In the field, they appear as reworked paleosols, their upper and lower boundaries being sometimes sharp erosive ones. Carbonate-rich sands refer to sandy layers that could have been enriched in calcite during a change in the chemistry of the parent solutions circulating in the Chobe Enclave, before the onset of the palustrine (limestone) ecosystem (Fig. 5.2; Fig. 5.3A, B). In addition to the carbonate-rich or palustrine ecosystem, some diatomite deposits are observed: constituted by a mix of crushed and preserved diatomite frustules, they

correspond to a quiet and clear freshwater environment, as observed today in the Okavango Delta (Mokatse et al., 2022a).

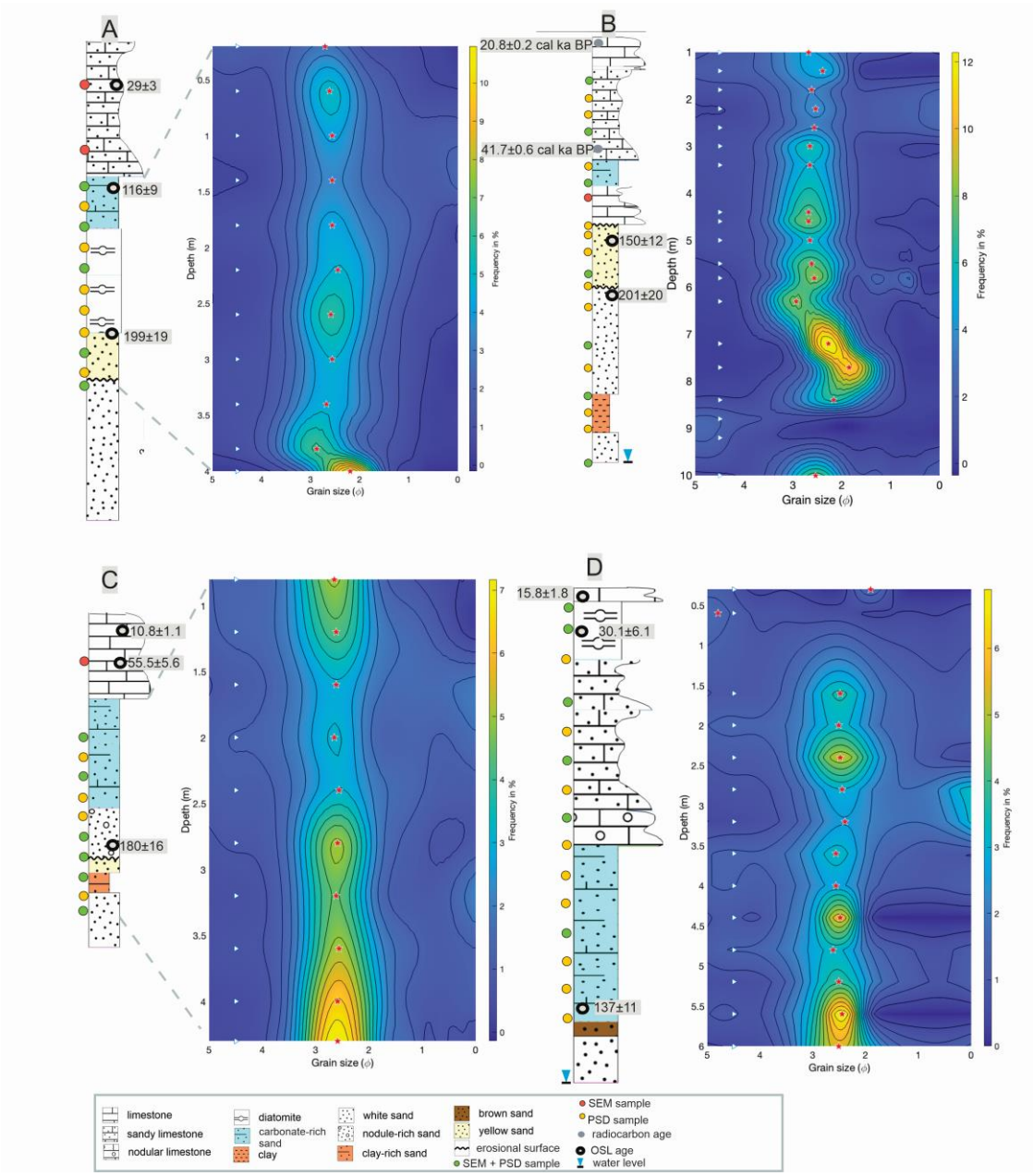

Figure 5.2: Particle size distribution maps of the four studied outcrops following Beierle et al. (2002)'s displaying method, and including OSL and radiocarbon ages (Diaz et al., 2019; Mokatse et al., 2022; Shlomy et al., submitted). The white triangle points to the sample position and the red stars to the mode of each sample. The isovalue curves refer to the grain size frequencies in % (scale on the right-hand side). Grain sizes are expressed following the phi scale. The wavy line at the limit of two facies refers to an erosional contact between the layers.

5.4 Methods

5.4.1 Selection and observation of quartz grains

A total of 54 samples were collected across the Chobe Enclave landscape including the floodplain, fluvial watergaps, and carbonate 'islands' (Fig. 5.1B). The sites were selected to help to detect the morphological diversity of quartz grains across the area. Based on lithological variations (i.e. facies), 28 samples (with ~30 grains per sample) were selected for the observation of quartz microtextures. Each sample was separated into three fractions (100 – 180, 180 – 250 and 250 – 300 µm). All samples were treated to remove carbonate minerals, iron oxides, organic matter, and other small particles attached to the sand grain surfaces (Vos et al., 2014). After treatment, the quartz grains were randomly selected (Mahaney 2002) and placed on SEM stubs for detailed observations. After gold coating, quartz grains were observed using a Tescan Mira II LMU coupled to an EDX Penta-FET 3x detector at the University of Lausanne. Images were created in secondary electron (SE) mode set to 20 kV accelerating potential with a ~ 15 mm working distance. Energy-dispersive spectrum (EDS) analysis enabled verification of the mineralogy of each analyzed grain. Finally, after careful observations and analyses, there was no evident differences in the microtextures observed between the different fractions. Consequently, the different fractions of each sample were pulled together.

Quartz grain microtextures (with some examples in Fig. 5.3C-H) were observed with reference to the Vos et al. (2014)'s classification table. A total of 16 microtextures were observed (Table 5.1; see some prominent microfeatures in Fig. 5.3C-H). The occurrences of each microtexture relative to the total number of grains in a sample were assessed after all grains were inspected. Then, this was followed by grouping of samples based on the interpreted facies associations (limestone, diatomite, carbonate-rich, clay-rich, Yellow sand, and White sand).

Table 5.1: List of microtextural features used in this study (top) and ordinal scale of frequencies (bottom). The classification into mechanical, chemical, and mechanical and chemical microtextures is based on Vos et al. (2014). In the bottom table, frequency intervals used for each ordinal rank are given between parentheses.

Microtextural features		
Mechanical	*Chemical*	*Mechanical and chemical*
Sub-angular	Oriented etch pits	Chattermarks
Sub-rounded	Solution pits	Elongated depressions
Rounded	Silica precipitation	Adhering particles
Conchoidal fractures		
Meandering ridges		
V-shaped percussion cracks		
Upturned plates		
Crescentic percussion marks		
Bulbous edges		
Parallel striations		

Ordinal frequencies	
0 - not observed (0)	3 - moderate (26-49)
1 - rare (1-5)	4 - common (50-74)
2 - sparse (6-25)	5 - abundant (>75)

5.4.2 Numerical assignment of observations

Data were acquired in two different ways. First, the presence of each feature observed on the quartz surface was noted for each of the 30 observed grains in each sample. This means that the obtained counts cannot be > 30. The acquired matrix was used to assess the frequency of features for all samples (to evaluate the most frequent ones), as well as for each sediment facies (to evaluate their potential signatures). Nevertheless, such counting remains partially flawed as its accuracy and precision cannot be ensured, i.e. the obtained numbers does not reflect a calibrated measurement. Consequently, measurements are ranked using an ordinal

scale (Davis, 1986; Vos et al., 2014; Table 5.1), which includes the necessary variability of counting (Table 5.1). The obtained matrix is then transformed to be used in multivariate statistics (see *Data processing and statistics* section below).

5.4.3 Grain size distributions

Grain size distribution analyses of 54 samples were performed using a laser diffraction Beckmann Coulter LS 13 320 on the < 2 mm size fraction after leaching with 10% hydrochloric acid (HCl) and 35% hydrogen peroxide (H_2O_2) for removal of carbonate fraction and organic matter, respectively. Data processing of particle size distributions is developed in the next section.

5.4.4 Data processing and statistics

Matlab™ software (Mathworks, 2022) was applied for all data processing and plots. Statistics and Machine Learning as well as Signal Processing toolboxes, in-house scripts and functions were used to explore data.

Sand modes – The use of interpolation (with a spline function), and a search for local maxima on the grain size distributions obtained in the laboratory, ensured the precise identification of the sand fraction modes. The mode detected in each sample is plotted associated to the particle size distribution maps (see below). In addition, the variability in mode distributions was assessed using boxplots (Suppl. Mat. Fig. SM 5.1A). On each box, the central mark indicates the median, and the bottom and top edges of the box indicate the 25th and 75th percentiles, respectively, the red line referring to the mean. The whiskers extend to the most extreme data points not considered outliers, and the outliers are plotted individually using the '+' marker symbol. Finally, differences among the various facies are assessed using a one-way ANOVA coupled to a multi-compare test (the `multcompare` function in Matlab™; Fig. SM 5.1B).

Particle size distribution (PSD) maps – These maps are based on the method proposed by Beierle et al. (2002). Maps (or surface plots) of grain size data allow qualitative interpretation

of the characteristics of the entire PSD and thus provide important insights into depositional processes and changing environmental conditions. Maps are generated using the "natural" interpolation algorithm of Matlab™: it is a triangulation-based natural neighbor interpolation and represents an efficient tradeoff between linear and cubic interpolations.

Transformation of ordinal data – Values obtained in the ordinal matrix of microtextural features (see above) was changed using the Hellinger transform (Borcard et al., 2011), a conventional transform utilized in ecology for plant counting. The Hellinger transform is defined as:

$$x'_{ij} = \sqrt{\frac{x_{ij}}{x_{i+}}}$$

where *j* is the microtextural feature, *i* the sample, and *i+* the row sum for the i^{th} sample. It is then possible to use the transformed matrix for multivariate analysis (Borcard et al., 2011).

Multivariate analysis using Principal Component Analysis (PCA) – Although MultiDimensional Scaling (MDS) was often applied to microtexture data (Keiser et al., 2015; Passchier et al., 2021), the choice of Principal Component Analysis is justified by the fact that there is no reference profile of microtextures that can apply directly on the dataset. Consequently, looking for the maximized variance in the sample plot, as well as the search of the weight of each variable (in this case, the microfeatures), makes PCA a suitable method. PCA is a method allowing the visualization of how near points are to each other by looking for the eigenvectors and eigenvalues of the correlation matrix of the variables. The projection of sample points in the PCA space produces a representation of the data in a chosen small number of dimensions (dimension reduction with maximum variance; generally, the first two or three dimensions account for most of the variance). Results of the Chobe Enclave samples are plotted in the first two-dimensional space of the two first principal components (PC) that are accounting for 38% of the total variance, which is an unexpectedly reasonable rate regarding the dispersion of the data. A second plot displays the correlation circle on which the coordinates refer to correlation coefficients between the variables (the microfeatures) and the first two PCs. The correlation coefficient is calculated as follows:

$$r = \sqrt{\lambda} \cdot u$$

where *r* is the correlation coefficient of a chosen variable with a chosen PC, λ the eigenvalue of the eigenvector *u*. Two smaller circles of a radius corresponding to a correlation coefficient of r = |0.8| and r = |0.6|, respectively, are drawn inside the correlation circle to appraise the most influential microfeatures (the variables) on the PC (with the highest $|r|$). Finally, confidence ellipsoids (within a confidence interval of 2σ, i.e. 95%) are also calculated in order to compare the microtextural signature of the various facies and their potential overlap.

5.4.5 The chronological approach of the quartz history

The examination of quartz grain surfaces from the different facies in the Chobe Enclave reveals both the presence of mechanical and chemical features with angular to well-rounded outlines (Fig. 5.3; Suppl. Mat. Fig. SM 5.2). By chance, many quartz grains show a remarkable preservation of microtextural relationships, i.e. the relative succession that records the history/chronology of processes endured by quartz grains. Indeed, the observation of the erosion of microfeatures, the degree of preservation of microtextures, their smoothing and the way they overprint each other, allow the multiple consecutive sediment transport modes and paleoenvironments to be characterized and organized following a relative chronology of events (Le Ribault, 1974; Vos et al., 2014; Keiser et al., 2015).

5.5 Results

5.5.1 Grain size distributions and modes of quartz grains in the various outcrops

Boxplots (Suppl. Mat. Fig. 5.1A) show some variability around the mean and median values, and both, one-way ANOVA and multi-comparison, were applied to the data (Suppl. Mat. Fig. 5.1B) to evaluate these differences. Statistical results are summarized in Table 5.2. The high Prob > F value indicates that there are no differences in mode means among the facies groups. This can be verified by a multiple comparison test of the various means using Tukey's honestly significant difference procedure (provided by the "`multcompare`" function in Matlab™). According to the multiple comparison results for all distinct pairs of groups, and if the White sands are considered as the control group (as a signature for the Kalahari Sands' geological

background), no groups have means significantly different from White sands whatever the origin of the sands.

The particle size distribution maps (Fig. 5.2) enable the visualization of the measured sediment grain size variations through the sedimentary logs (Beierle et al., 2002). The grain size distributions slightly vary throughout the floodplain units. They show leptokurtic distributions for the sand fraction, well sorted, with some minor variations along the outcrops, emphasizing some potential reworking and/or local transport processes. At TSC site (Fig. 5.2A), the lower unit (White sand) displays a coarser fraction compared to the whole section. This pattern is also observed at Baobab site (Fig. 5.2B), although a finer fraction occurs between two layers of the lower unit (White sand). On the other hand, Nata site (Fig. 5.2C) displays consistent distributions and modes across all units, a pattern which is similar in Acacia outcrop, except for some finer fractions observed in the upper units (recognized as diatomite and carbonate facies). The modes in diatomites and limestones point to a finer sandy fraction with PSD displaying more platykurtic curves compared with the other facies (Fig. 5.2).

Table 5.2: Results of one-way ANOVA. There are five groups (Limestone, Diatomite, Carbonate-rich sands, Yellow sands, and White sands. SS: sum of squares; Df: degree of freedom; MS: mean squared error; F: the F-satistic; Prob > F: the probability that the test statistic can take a value greater than the value of the computed test statistic.

Source	*SS*	*Df*	*MS*	*F*	*Prob > F*
Group	1489.1	4	372.28	1.82	0.1437
Error	8609.1	42	204.98		
Total	10098.2	46			

5.5.2 Microtextures of the Chobe Enclave quartz grains

The observed quartz microtextures in the whole set of samples consist of oriented etch pits (Fig. 5.3E), V-shaped percussion cracks (Fig. 5.3H), and adhering particles (Fig. 5.3D), with the most common quartz shapes being subrounded (Fig. 5.3C). Other microtextures include conchoidal fractures with solution pits (Fig. 5.3G), followed by numerous crescentic percussion marks (Fig. 5.3F). All the microtextures display similar, but not equal, frequencies by facies (Fig. 5.4). The features occurring commonly at high frequencies in the various facies are the oriented etch pits, the adhering particles, the V-shaped percussion marks, followed by

chattermarks and meandering ridges (Fig. 5.4). Other microtextures are less frequent, but do not appear to be more distinctive of any specific facies.

The Limestone facies observed in the floodplain areas indicate overprinted microtextures, i.e, conchoidal fractures, which are usually curving, breaking patterns found on the quartz grain. However, these features are observed together with crescentic percussion marks, typically cone-shaped cracks on grains, and triangular etch pits. Lastly, one key feature is silica coatings around the quartz grains. This possibly provides insights on the latest processes undergone by the grains (Suppl. Mat. Fig. SM 5.3A).

The diatomite facies displays usually similar patterns as carbonate facies. They include subangular to subrounded quartz grains, dominated by adhering particle features made predominantly of diatom frustules. More ancient observed features, like crescentic percussion marks and triangular etch pits, are commonly enlarged by dissolution (Fig. SM 5.3B).

As for the Yellow sand facies, subangular to well-rounded grains show smoothed edges observed with older features including triangular etch pits, crescentic percussion marks, and notable bulbous edges (Fig. SM 5.3C). The bulbous edges are typically rounded grain edges with a parabolic curve (Mahaney, 2002). As observed on the diatomite facies, there is similarly evidence of earlier formed marks enlarged by dissolution. Finally, silica coatings are other key features observed with numerous adhering particles.

The microtextures of the White sand facies include crescentic percussion marks, V-shaped impact marks, triangular etch pits, and silica coatings (Fig. SM 5.3D). In addition, the grains display smoothed edges bearing the aforementioned features. Interestingly, some adhering particles are observed, specifically some diatom fragments with sizes of < 10 µm. These are finer fragments compared to the ones observed within both the carbonate and diatomite facies.

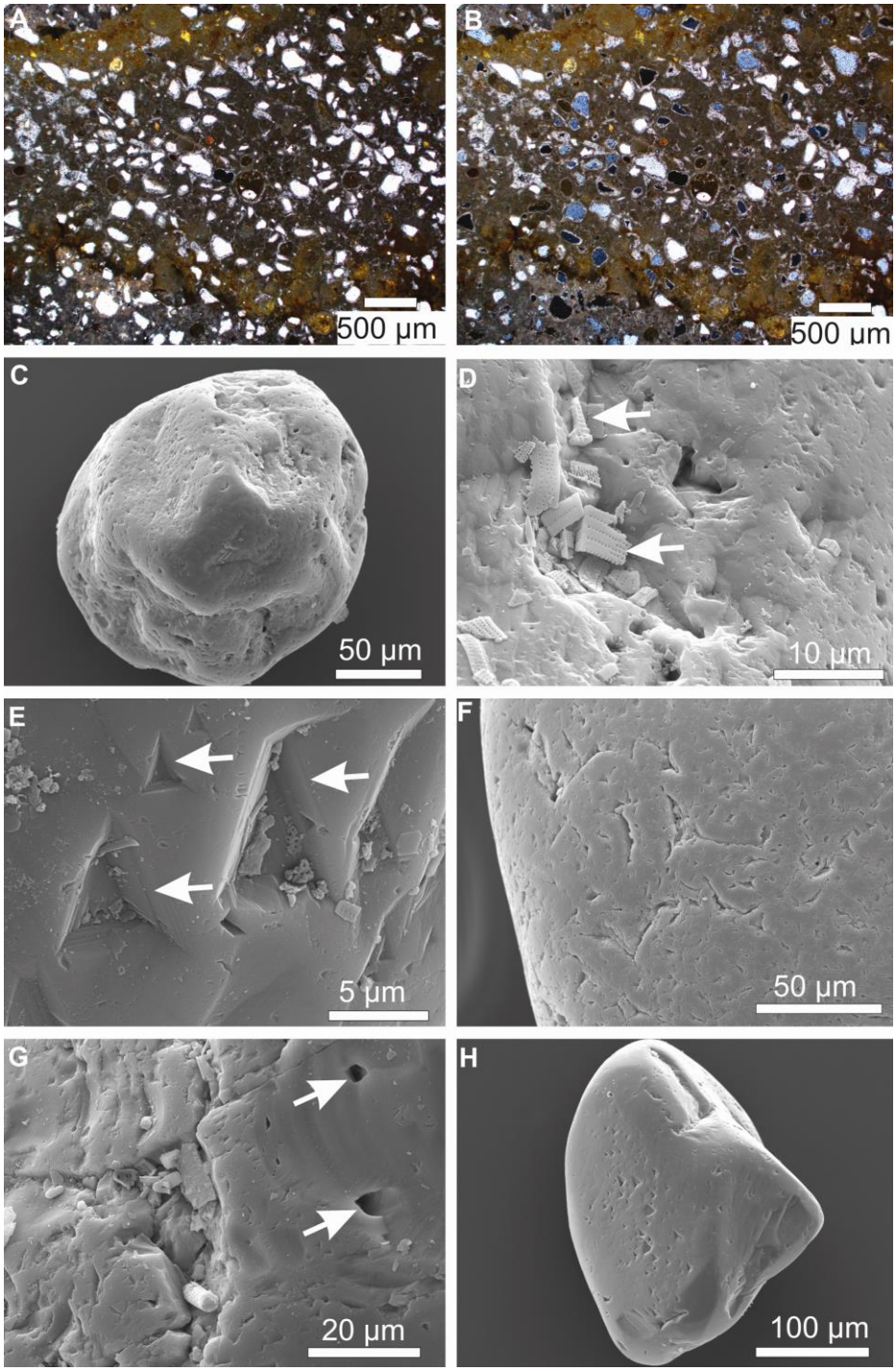

Figure 5.3: A-B) Optical micrograph of a sandy limestone in plane polarized light (PPL), with angular to sub-rounded quartz grains. B) Same view in cross polarized light (XPL), displaying calcite coated quartz grains, also referred as "aureoled quartz" (Freytet and Plaziat, 1982). Such coatings are typical on quartz trapped in palustrine/floodplain carbonate-rich seetings (Freytet and Plaziat, 1982). C-H) SEM images of sand-sized quartz grains in the Chobe Enclave; C) Sub-rounded quartz grain; D) Adhering particles dominated by diatoms in diatomites; E) Triangular etch pits with smoothed edges; F) Numerous crescentic percussion marks; G) Conchoidal fracture with solution pits; H) Sub-angular grain with smoothed triangualr etch pits and V-shaped percussion marks.

5.5.3 Multivariate analysis: results of the PCA

In the PCA ordination, the PC1 and PC2 axes account for about 38 % of the total variance (21.25 % and 16.75 %, respectively). From the PCA graph plotting (Fig. 5.5A), the distribution of the different facies overlaps. However, there is some evidence of coherence of the limestone facies as well as for the White sands. The correlation circle (Fig. 5.5B) plots the correlation coefficients between the variables (microtextural features) and the principal components (PC1 and PC2). The distribution of variables describing the quartz grain microtextures can be related to major processes based on Vos et al. (2014, their Table 2) and Figure 5.4. Accordingly, three poles scatter the variables in the circle area limited by a $r > |0.6|$: two poles along an axis at $3/4\pi$ from the positive direction of the abscissa defining a mechanical axis, and a third pole, perpendicular in the positive direction to the mechanical axis, describing a chemical attractor (Fig. 5.5B). The opposition along the mechanical axis emphasizes two different sets of variables: the upper left hand side quadrant is dominated by fluvial mechanical microtextures, whereas, in the opposite direction, a set of microtextures indicates a mostly aeolian mechanical imprint. This opposition points to the fact that the two mechanical processes are clearly distinct and finally, perpendicular to this mechanical axis, a group of microtextures directly refer to chemical imprints. The presence of this set at $\pi/2$ indicates the absence of relationships between mechanical and chemical imprints, which is expected as chemical imprints can affect a quartz grain at any time during its evolution in the environment.

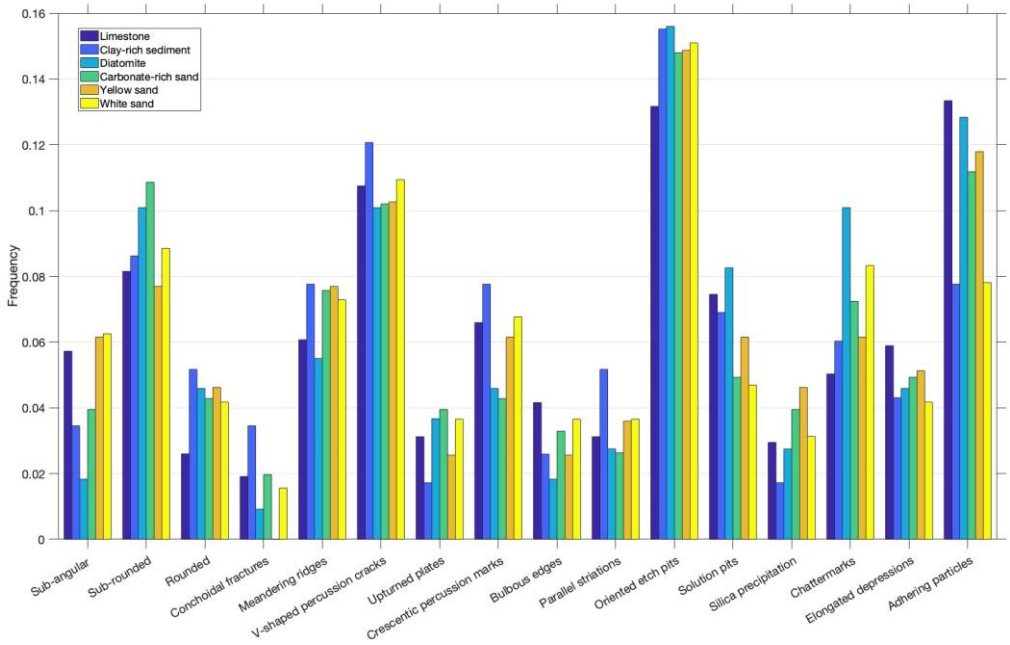

Figure 5.4: Bar chart of the feature frequencies according to the six recognized facies, Limestone, Clay-rich sediment (sand), Diatomite, Carbonate-rich sand, Yellow sand, and White sand. The frequency is the ratio between a given feature occurrence and the total number of feature occurrences. Some features are more frequent than other but there is only some, but no large, differences between facies.

A ternary diagram (Suppl. Mat. Fig. SM 5.4), based on the three groups of selected features identified by the circle of correlation of the PCA (Fig. 5.5B) can be used to plot the samples according to the environmental interpretation of their microtextures (Vos et al., 2014), i.e. fluvial/subaqueous, aeolian, and chemical. In this plot, sample coordinates are calculated using the sample average values for each group of features in the Hellinger matrix. All samples group in a limited area of the ternary diagram, emphasizing that the processes have a similar weight on the microtextures and that quartz grains underwent repeated processes during their evolution in the Chobe Enclave, whatever the facies type. Nevertheless, the ternary diagram does not show the way, aeolian, fluvial, and weathering processes followed one another, an issue that must be explained to understand the succession of the environments through time.

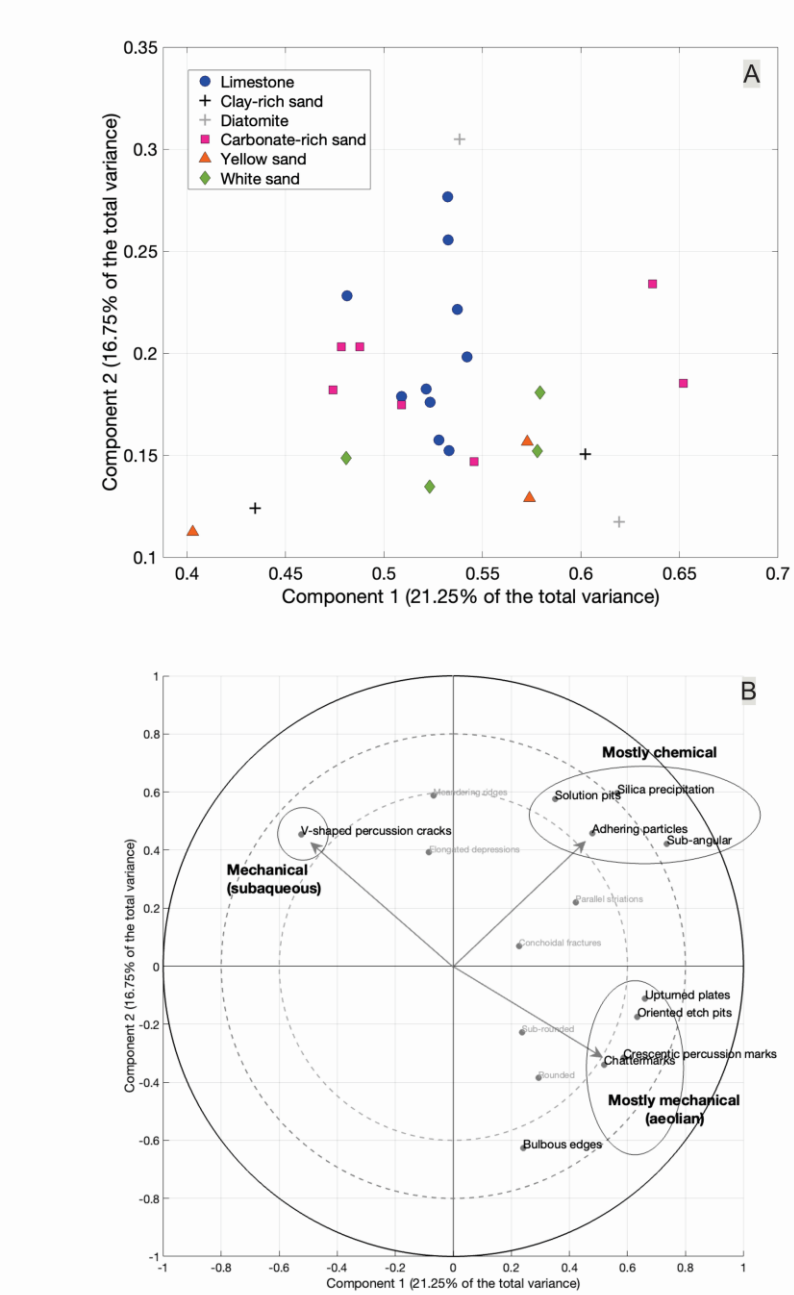

Figure 5.5: Principal Component Analysis (PCA) and circle of correlations. (A) PCA graph plotting the 28 samples by facies. Some of the facies plot as a gathered group (Limestone, White sands), whereas others are more dispersed (Carbonate-rich sands, Yellow sands). The first two principal component space explain 38% of the total variance. (B) Correlation circle on which are plotted the correlation coefficients between the variables (microtextural features) and the two first principal components. The two dotted circles have a radius corresponding to a correlation coefficient of r = |0.8| and r = |0.6|, respectively. Three poles dispatch the variables along the circle with a r > |0.6|: two poles along an axis at 135° from the positive direction of the abscissa defining a mechanical axis, and a third pole, perpendicular in the positive direction to the mechanical axis, describing a chemical attractor. The environmental interpretation of the quartz grain microtextures is based on Vos et al. (2014, their Table 2) and Figure 3 (see also Suppl. Mat.).

5.5.4 Successions of microtextures

The interpretation of the succession of the inherited microtextures is based on differentiated aspects of the features observed on a single grain (freshness, smoothing, enlargement, etc.), and checked with other grains from the same sample to confirm a potential scenario. That is, differences can be made from transportation and sedimentation processes. The features observed are categorized as mechanical, chemical, or mechanical-chemical (Table 5.1). For example, mechanical features observed on grains from the Limestone facies comprise conchoidal fractures (Suppl. Mat. Fig. SM 5.3A). This feature is then overprinted by chemical ones, which are silica coatings and solution pits (Suppl. Mat. Fig. SM 5.3A). In this way, the initial mechanical feature refers to an earlier process, whereas the chemical feature confirms a later occurring process of weathering. These observations essentially prove relative successions of processes and environmental settings between two phases. Consequently, in the Chobe Enclave, the succession of microtextures allows the history of the quartz grains to be reconstructed, as discussed below.

5.6 Discussion

5.6.1 Interpretation of PSD maps and the relationships between modes and facies

The Chobe Enclave floodplain displays a sand fraction with similar granulometric characteristics evidenced from relatively homogeneous modes across the units and sand size distributions as emphasized in the PSD maps (Fig. 5.2). Although somehow coarser than the other facies, the White sands are associated with extremely well sorted, leptokurtic distributions of the sand fraction, which resemble a sub-environment of continuous sorting under possible subaqueous current transport (fluvial). However, it is worth noting that the White sand facies can be interbedded with units of a very fine fraction (Fig. 5.2B), indicating deposition dominated by low-energy episodes, likely in settings away for the main flow of a distal alluvial fan. The Yellow sands are generally slightly finer than quartz distributions from other White sands, and point towards a possible inherited and reworked unit of pedogenized sands (or soil sediment; their color and high content in iron asserting their possible pedogenic origin in the context of the Chobe Enclave). Stratigraphically, the Yellow sands correspond to an onset transition to overlying Carbonate-rich sands or Limestone, both facies sharing

somehow similar but not identical PSD patterns. On the other hand, the Diatomite facies includes PSD with some fine sands, sometimes well sorted, and likely corresponding to dust or accidental trapped sand grains brought by wind spells or subaqueous currents of very low turbulence. Such an interpretation is also applicable to some layers of the Limestone facies. The case of carbonate layers emphasize the way quartz grains were incorporated into the sedimentary layers. As stipulated above, modes point to a finer sandy fraction and the PSD refer to more platykurtic curves compared with the other facies (Fig. 5.2). Most of the grains are subangular to subrounded and are coated by calcite (Fig. 5.3A, B). Their distribution in the thin section demonstrated that they were deposited at the same time as the carbonate mud, allowing the calcitic rim to form as an early diagenetic cement (Freytet and Plaziat, 1982). It is because calcite and quartz grains are contemporaneous that it has been possible to date the limestones using OSL (Diaz et al., 2019, Vainer et al., submitted). The examination of their microtextures must help to confirm that they were transported subaqueously by low river currents and/or by wind spells over the palustrine environment.

To conclude, modes and PSD maps point to minor variations in sand sizes and well sorted distributions. They assert reworking by subaqueous currents of probably former aeolian sediments (mainly preserved leptokurtic curves), the contribution of wind input having been constant but of varying amplitudes.

5.6.2 Interpretation of the PCA

The PCA clearly demonstrates that the distribution of samples is related to the processes at work i.e., aeolian/mechanical, subaqueous/mechanical, and weathering/chemical, but at various degrees (Fig. 5.5B). When confidence ellipsoids are plotted in the PCA plane (at 2σ), they show wide overlaps (Fig. 5.6), stressing a large share of microtextural features between the different facies. But this does not mean that there are no differences between the facies: indeed, the center of inertia of the groups and their respective ellipsoids are distributed from top to bottom of the figure, from Limestones, to Carbonate-rich sands, to White sands, and finally to Yellow sands. This geometry, including those of the ellipses, are discussed below.

The quartz grains in the Limestone facies are more influenced by the “chemical” features, and in a lower extent, by the V-shape percussion cracks (subaqueous), emphasizing the prominent role of surface weathering of quartz grains in an alkaline environment. As noted

above, the parent solutions at the origin of the calcite rims around the aureoled quartz, generated an alkaline environment in which quartz surface underwent dissolutions. This environment was also favorable to sepiolite precipitation, demonstrating the high pH reached during reactions, the sepiolite being a possible end-member of dissolved amorphous silica (Mokatse et al., 2023). In addition, in the Chobe Enclave environments, some possible rapid pH variations triggered the precipitation of secondary amorphous silica ("silica precipitation", Table 5.1 and Fig. 5.4; Suppl. Mat. Fig. 5.3A), frequently observed at the surface of quartz grains. Moreover, the vertically elongated shape of the Limestone facies' ellipsoid does not preclude the influence of the "mechanical axis", but this one probably mostly reflects a legacy imprint on quartz trapped in the carbonate layers. Nevertheless, as quartz grains in Limestones remain partly influenced by the subaqueous microfeatures, this characteristic must likely refer to an input by some low energy water flows of sandy fractions. This is not surprising in such distal and palustrine settings of an alluvial fan/floodplain environment.

Contrary to the Limestones, and as expected, most of the sandy facies are more driven by the "mechanical" axis than the "chemical" pole, although the three groups of features exert a varying influence on their distribution. The more horizontal elongated shapes of their ellipsoids contrast with the vertical one of the Limestones. Regarding the Carbonate-rich sands, they display the widest ellipsoid shape due to the influence of the carbonate environment as the overlapping ellipsoids show. Indeed, it seems reasonable to consider that the Carbonate-rich sands form a transition phase from a pure sandy to a carbonate-rich environment, a phase period during which the parent solutions changed in terms of their geochemical composition. Consequently, the Carbonate-rich sands, mostly characterized by the same microtextures as the Yellow and White sands, also include some "chemical features" as observed in the Limestones, enlarging the variability in microtextures and consequently the ellipsoid.

Yellow and White sands' ellipsoids overlap significantly. The aeolian microtextures developed extensively at the surface of the observed sand grains. These features emphasize the crucial role of wind processes in the transportation and reworking of these sands, although they also include, at a minor degree, the impact of subaqueous transportation as well as the mark of weathering processes. The smallest ellipsoid of White sands asserts the close resemblance of the various samples, which probably shared a long residence time inside dunes before their reworking by wind, low current rivers, and possibly some weathering.

Although similar to the White sands, the distribution of the Yellow sands indicates a more complex grain shaping. The color (yellow in the hue value of 10YR) obviously refers to a paleopedogenesis under the influence of iron-bearing minerals. But it is clear from field investigations and geochemical data (Mokatse et al., 2023) that the Yellow sands are not *in situ* paleosols, but reworked paleosols or “soil sediments", on which the subaqueous environment left a more visible imprint than in the White sands. Moreover, one could expect traces of a chemical weathering on these quartz grains as witnesses of the paleopedogenesis. Indeed, the paleopedogenesis altered the sand grains, explaining the slight elongation and the tilt of the ellipsoid towards the “chemical” pole, the quartz surface being covered by “etched and solution pits” (Fig. SM 5.3C); but the traces of iron oxides and oxyhydroxides could not be observed as they were removed during the preparation of the grains for SEM observation of microtextures.

It remains speculative to interpret positions of the Diatomite and Clay-rich sand facies. It can only be remarked that the two sand samples of the Clay-rich layers integrate well with the Yellow sands’ ellipsoid, whereas the microtextural signature of the Diatomite quartz do not fit in any other group of facies.

In conclusion, the PCA allowed the groups to be better differentiated and to relate them to their dominant transportation mode and depositional environment. However, it is obvious that all the facies share the imprints of the external geodynamic agents at various magnitude. But the way these imprints succeed each other, in order to reconstruct the grain history, still needs to be investigated, which is the topic of the following section.

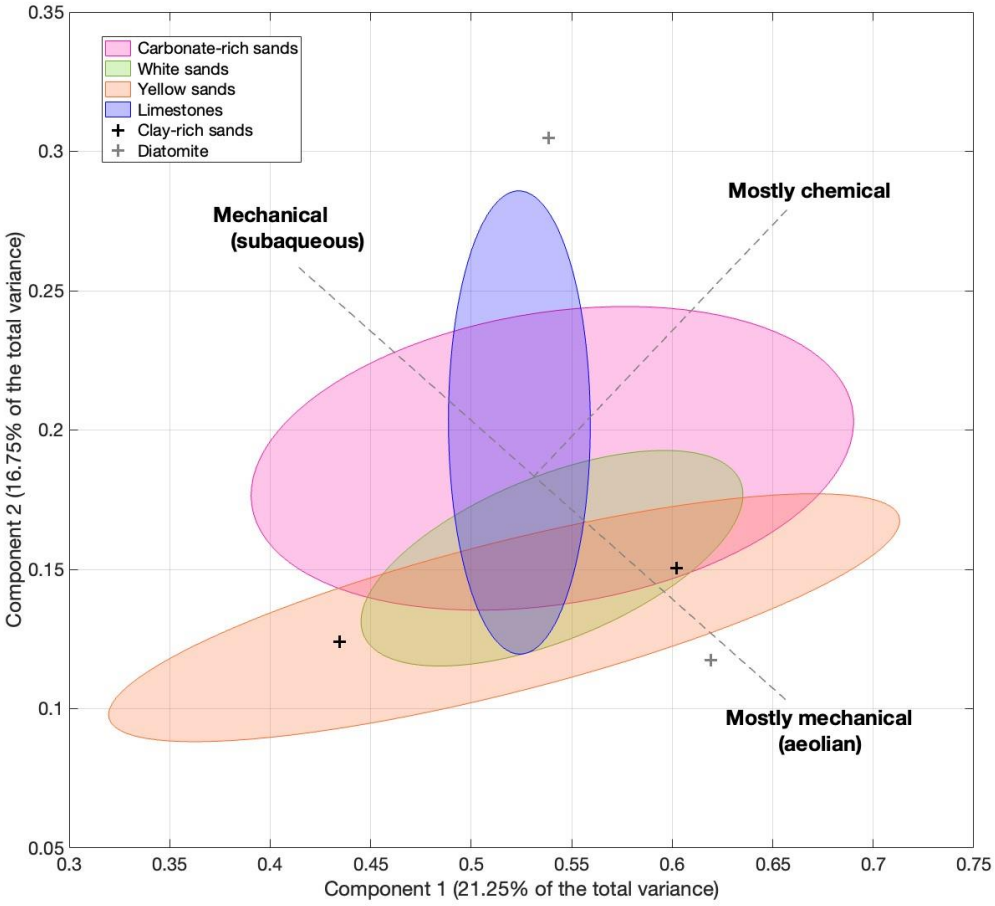

Figure 5.6: Confidence ellipsoids (at 2s) calculated from the sample groups of facies and plotted in the PCA plane. The first two principal components' space explains 38% of the total variance. The Clay-rich sands and the Diatomites are plotted with crosses as they are represented by only two samples, making the ellipsoid calculation impossible. All the ellipsoids overlap, emphasizing a share of microtextural features. Nevertheless, quartz grains in Limestones are more influenced by "chemical" features, whereas, in other sands, they seem to be more affected by the "mechanical" axis.

5.6.3 Interpretation of the floodplain evolution in the Chobe Enclave

Bond and Fernandes (1974) examined the Kalahari sand grains, concluding that the earliest texture is upturned plating of aeolian origin that later being overprinted by surface reworking from wind and water as confirmed by Thomas (1987). Abundant grains from the White sand facies show variable outlines with mostly overprinted textures. As a reminder, the observed crescentic percussion marks (Fig. 5.3F; Fig. SM 5.3D) result from grain-to-grain collisions and are characteristic of aeolian environments (Vos et al., 2014 and references therein), whereas the V-shaped percussion cracks are a result of grain-to-grain collisions in the subaqueous

environment (Krinsley and Doorkamp, 1973; Mahaney and Kalm, 2000). Moreover, quartz grains showing chemical precipitation features, like silica coatings and trapped diatoms, suggest grains derived from environments with solutions periodically close to silica saturation. On the other hand, the triangular etch pits form as a result of silica dissolution at high pH as mentioned above (Mahaney, 2002). Now, for such an environment to develop, evaporation is key to reach the right conditions. This was supported in the Chobe Enclave by the formation of fibrous clay minerals, such as sepiolite, associated with the Carbonate and Diatomite facies where alkaline conditions were prevalent (Mokatse et al., 2023).

Furthermore, the majority of Yellow sand facies exhibit aeolian surface patterns like bulbous edges and upturned plates. These quartz grains show overprinted small triangular etch pits with smoothed edges and have developed bulbous edges during wind transport (Vos et al., 2014; Fig. SM 5.3C). The grains display evidence of earlier formed marks enlarged by dissolution (Vos et al., 2014; Fig. SM 5.3C). As demonstrated above, Carbonate-rich sands, Limestones, and Diatomites exhibit relatively similar features i.e, significant adhering particles comprising of diatoms (Suppl. Mat. Figs SM 5.3A, SM 5.3B), which are relatively bigger in size compared to the lower unit facies (White and Yellow sand). Relicts of conchoidal fractures together with overprinted crescentic percussion marks are commonly observed (Figs SM 5.3A, SM 5.3B), emphasizing an aeolian imprint. Moreover, chattermarks and V-shaped percussion cracks developed during subaqueous transportation demonstrate the presence of another phase of displacement, frequently overprinting the aeolian microfeatures.

The microtextural characteristics of the sand grains in the Chobe Enclave region depict a combination of processes, hence denoting a multicycle evolution of the sediments (Fig 5.7). Surface microtextures inherited from quartz grains through aeolian transportation (crescentic percussion marks, upturned plates, bulbous edges) coexist with typical subaqueous/fluvial surface textures (V-shaped percussion mark, conchoidal fractures), in addition to chemical features imprinted on quartz grains suggesting phases of both dissolution and precipitation. These phases are related to possible weathering/pedogenic processes (Fig. 5.7). The exposure of quartz grains in conditions with higher levels of evaporation during the dry intervals increased the pH, which triggered the etching process. Based on all these remarks, Figure 5.7 proposes a succession of events for the four most important facies.

The chronology of events recorded in quartz microtextures shows a strong imprint of aeolian-produced microtextures in the White sand facies (Fig. 5.7). These microtextures are

then overprinted by subaqueous-originating microtextures, with however a minor imprint of possible other aeolian phases (reworking after sedimentation? Fig. 5.7). This phase is followed by an imprint of weathering. A significant amount of edge rounding/smoothing of earlier formed dissolution features at this stage point towards a moderate imprint of a possible subaqueous/fluvial new phase. Although some features are more frequent than others, the quartz grains from all the facies display similar pattern of events. These largely indicate an inherited aeolian origin being overprinted by a subaqueous/fluvial phase followed by a weathering and/or pedogenesis phase, a succession which is expected in alluvial fan environments. However, both White and Yellow sand facies indicate the last moderate imprint of a fluvial event. However, the close association of Limestone and Carbonate-rich facies portray a strong imprint of a weathering phase during which an alkaline environment is evidenced by strong dissolution features and adhering particles dominated by diatoms, i.e. alkaline lacustrine/palustrine environments.

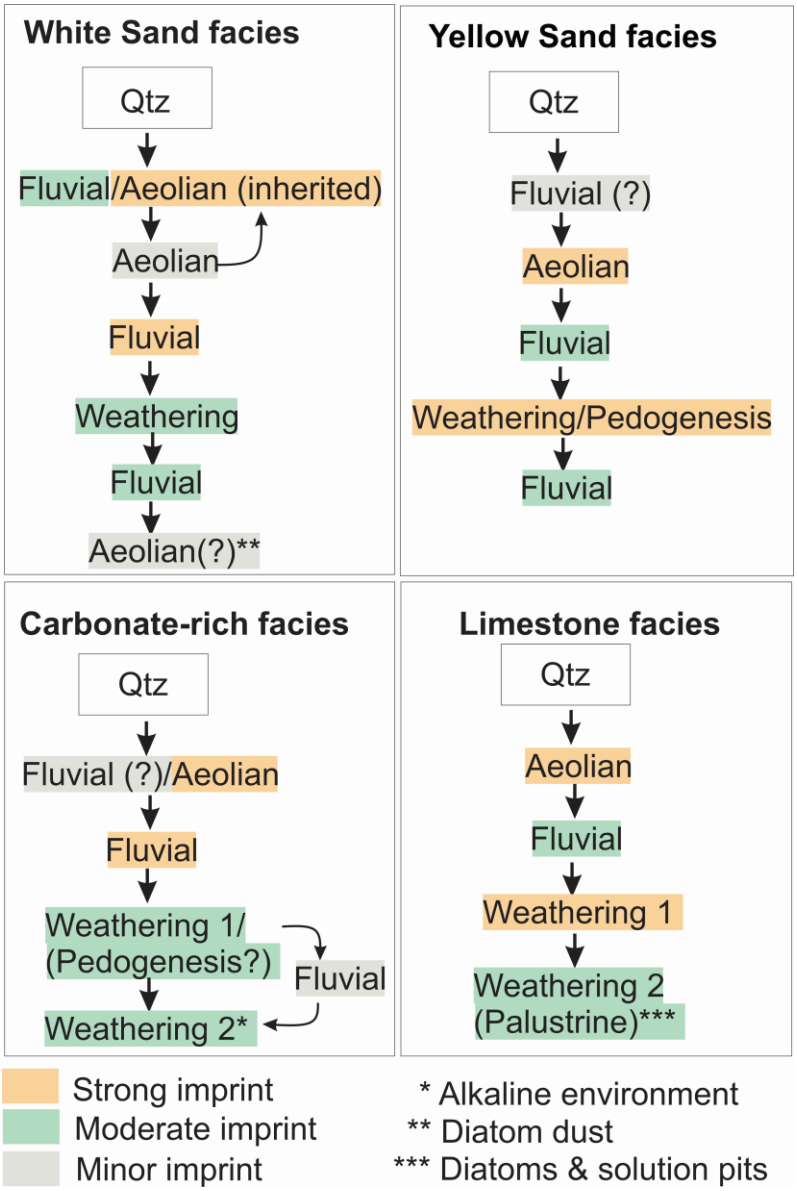

Figure 5.7: Examples of chronology of events recorded by quartz microtextures. The amplitude of the imprints (symbolized by colors) is assessed by the observed number of specific microtextures associated to a typical environment compared to the total number of microtextures. The succession of environments is based on the overprint and freshness of microtextures. Question marks report the presence of faint microfeatures. The curved arrow in the White sand facies indicate possible multiple reworking by wind; in addition, some grains incorporated at their surface a fine dust of broken diatom frustules. The curved arrows in the Carbonate-rich facies notify the possibility of some subaqueous reworking between two weathering phases. Finally, the presence of an alkaline palustrine environment during the last weathering phase in the Limestone facies is attested by the presence of diatoms and solution pits.

Referring to the dates provided in Figure 5.2, a framework of the sedimentary evolution of the Chobe Enclave can be proposed for the Late Pleistocene. The Chobe Enclave developed in an environment that was mainly resembling to a distal and very flat alluvial fan/ floodplain system, also subject to climate and tectonic disturbances. Moreover, the various microtextures detected in the Chobe Enclave floodplain are most indicative to features observed in hot-humid alluvial-fan environments and hot-arid to semiarid desert fans (Keiser et al., 2015 and references therein), suggesting a contrasted evolution of the landscape through the Late Pleistocene.

Before circa 200 Ka, the sedimentation was mainly dominated by the White sands, which deposited in an alternating fluvial/aeolian environment (with frequent alternating reworking). The presence of trapped small dust of Diatoms at the surface of the grains also attests to the existence of some large and slow current rivers and/or freshwater/pluvial ponds and small lakes. From circa 200 Ka until, possibly, between 150-120 Ka, some soils sources were eroded upstream and transported into the Chobe Enclave by low current rivers as shown by the Yellow sands. But their boundary with the White sands points to an erosion phase before the deposition of the Yellow sands, confirming a possible rhexistasic phase after a biostasic period during which soils developed in the watershed. During the time of Yellow sand deposition, formations of Diatomites as well as nodule-rich sands (paleosols?) were possible in freshwater/pluvial ponds/small lakes and in the floodplain, respectively. It is after 120 Ka that a graben extension formed in the Linyanti area (Bäumle and Himmelsbach, 2018) triggering the formation of shallow paleo-lakes, contemporaneously to highstands of the Makgadikgadi paleo-lake (Burrough et al., 2009). By the end of the MIS5, circa 80 Ka, the sedimentary system shifted to a palustrine/lacustrine environment in which limestones and diatomites formed. The hydrochemistry changed radically allowing deposition of large calcium carbonate layers, meaning that both water pH and ionic strength and composition were evolving to a more alkaline environment. It is likely that this alkalinity varied through time, mostly under the influence of evaporation intensity, which could result from the humidity fluctuations during MIS4, 3, and 2 (Chase and Meadows, 2007). It is likely that sepiolite formed in the carbonate and diatomite layers during arid spells (Mokatse et al., 2023), leaving dissolution and weathering traces on quartz surfaces. The youngest limestones deposited at the end of the LGM (Fig. 5.2). Today, they are exposed at the surface, probably due to

neotectonics, forming an inverted relief (Mokatse et al., 2022). After circa 10 Ka, the deposition of calcium carbonate ended for reasons that are still to be discovered.

5.7 Conclusions

Different facies across the Chobe Enclave floodplain were investigated using grain size distributions and microtextures of quartz grains. A combination of grain size characteristics and statistical discrimination functions helped to understand the processes and geological history of quartz grains forming most of the sedimentary record of the Chobe Enclave. A Principal Component Analysis enabled a discrimination of microtextural features by attributing them to the possible processes at work in their respective environment. Grain microtextural analyses revealed mechanical features originating from both aeolian (with a large imprint) and subaqueous transportation (fluvial – in low velocity rivers), whereas chemical features point towards the development of alkaline environments, most commonly identified in the Limestone and Carbonate-rich facies. The sedimentological system of the Chobe Enclave, as demonstrated by quartz microtextures, evolved from a primary aeolian legacy overprinted by alternating fluvial/palustrine/weathering phases, with some more recent aeolian marks. This Late Pleistocene framework is consistent with a complex history of a paleo-alluvial fan resulting from changes in paleo-hydrological conditions as well as tectonic settings.

Acknowledgements

The authors acknowledge the Ministry of Environment, Natural Resources Conservation and Tourism of the Republic of Botswana as well as the Chobe Enclave Conservation Trust for the research permits, without which this study would not have been possible, as well as the Botswana International University of Science and Technology and the University of Lausanne. Special thanks to the Van Thuyne Ridge research center team for assistance with fieldwork and logistics. This work has been supported by a Swiss National Foundation grant no 200021_172944 to EPV.

Supplementary Materials

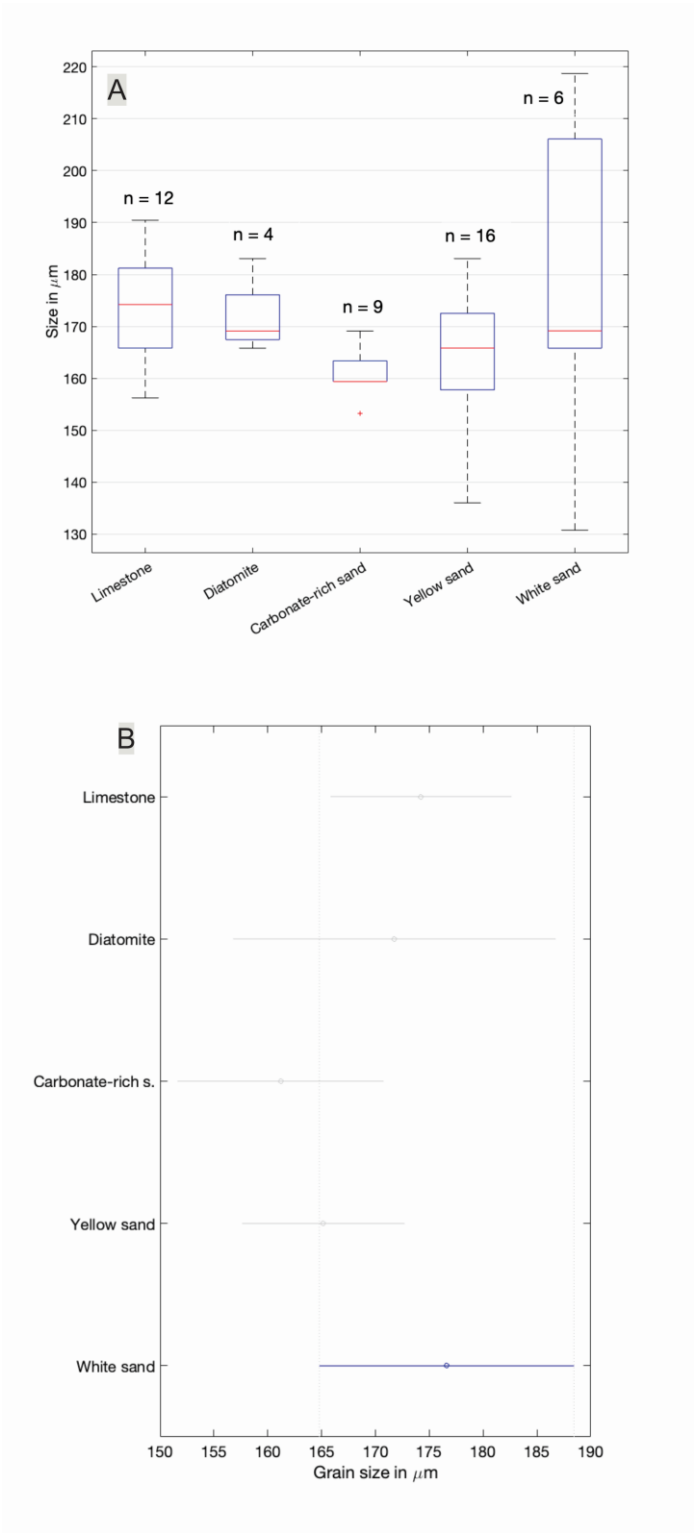

Fig. SM 5.1: (A) Boxplots showing the distribution of the modes according to the facies. All mean modes are plotted in a limited interval. The clay-rich sands are not included in the boxplot as they comprise only two samples. (B) Multiple comparison test of the various means using Tukey's honestly significant difference procedure (provided by the "multcompare" function in Matlab™).

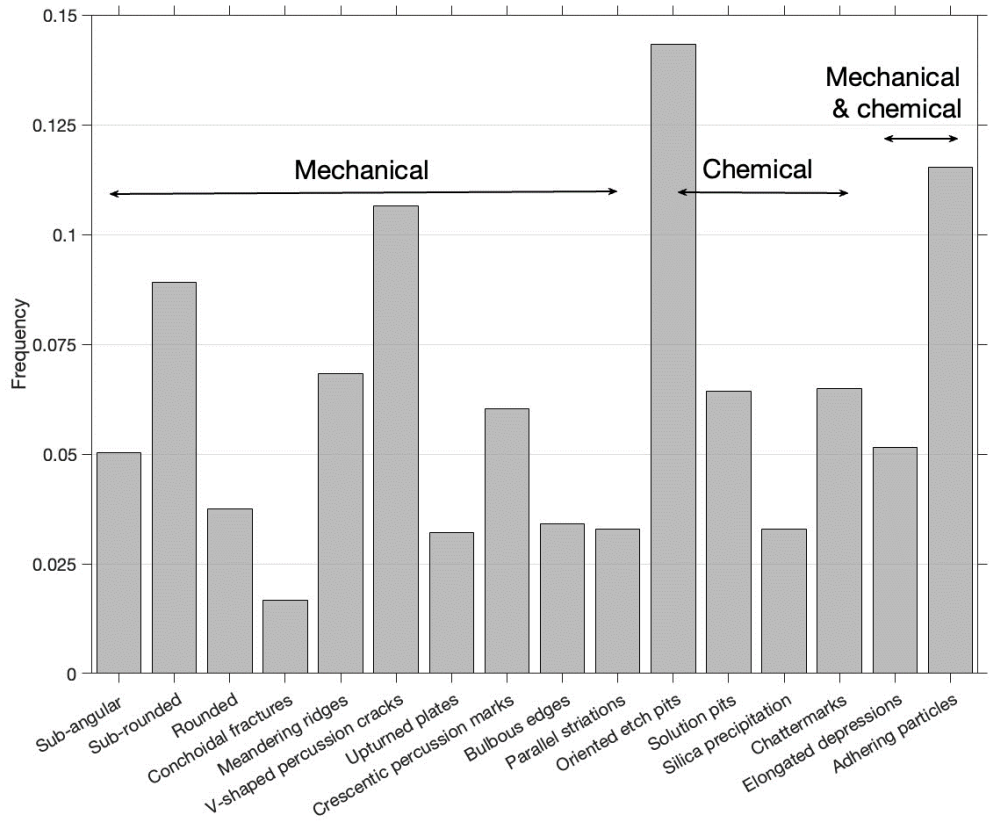

Fig. SM 5.2: Frequencies of the various quartz microtextures observed in the Chobe Enclave. The list of microtextures is given in Table 5.1. This study used sixteen different features; their recognized origin (mechanical or chemical) is given according to Vos et al. (2014).

A

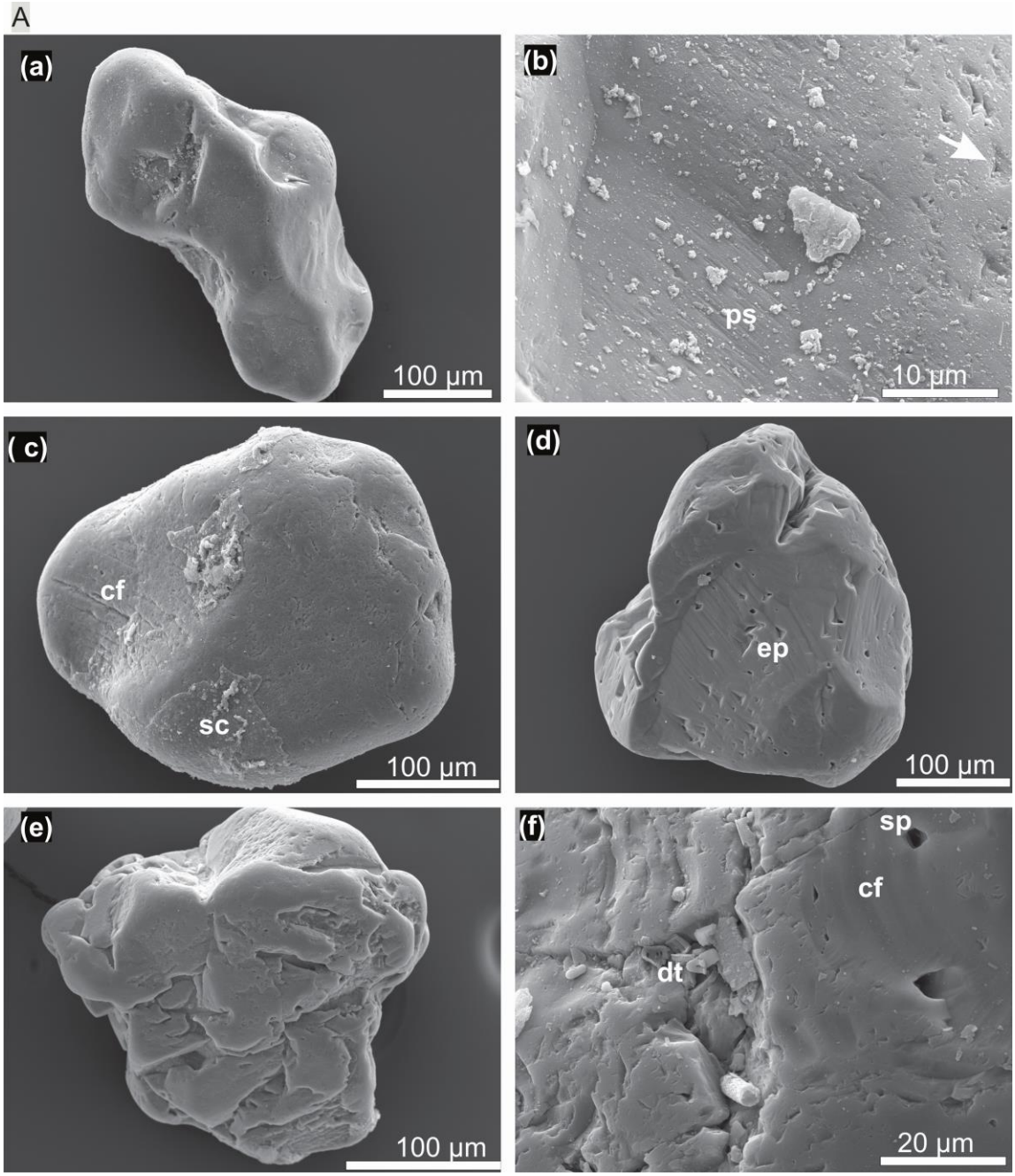

B

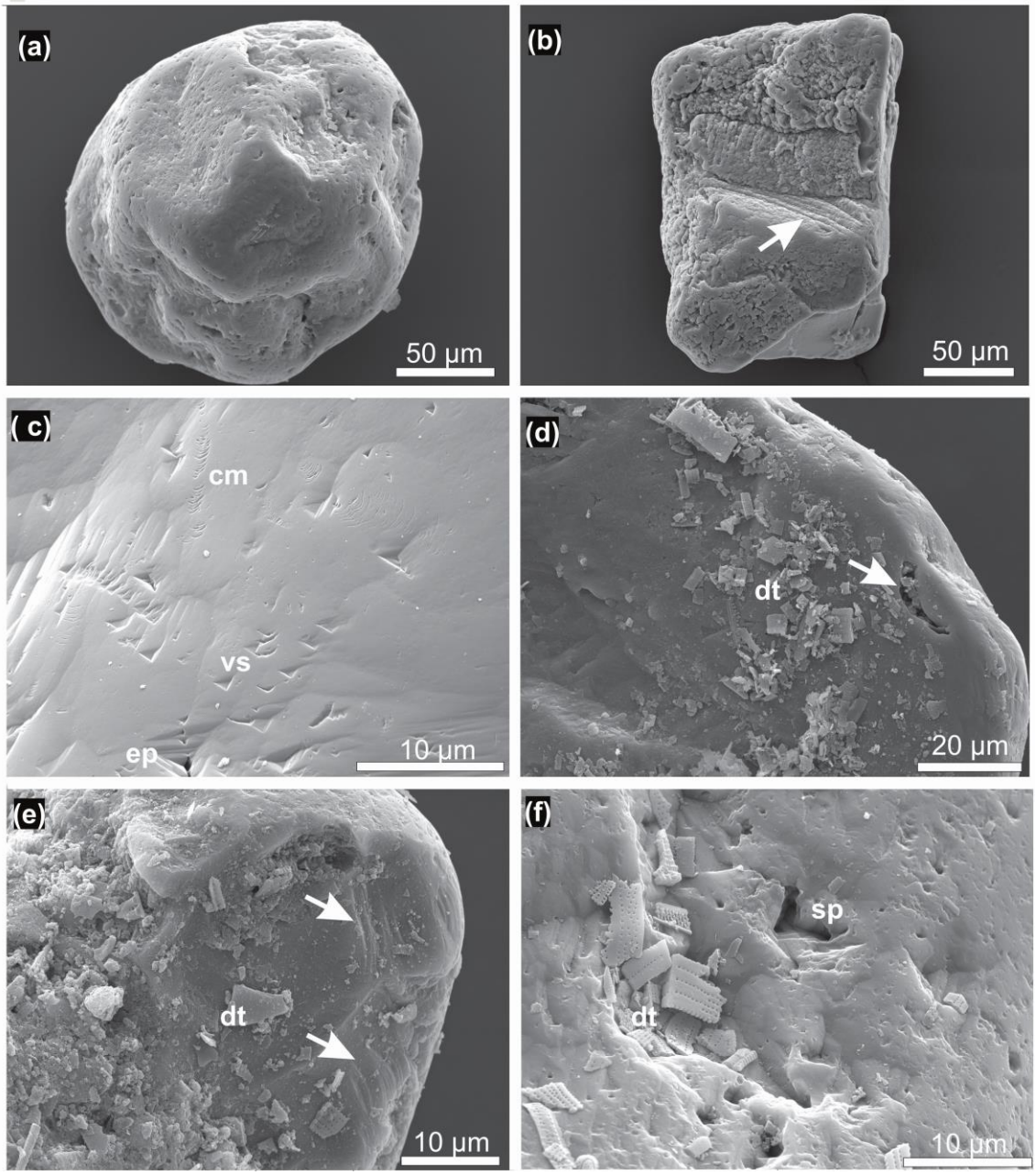

C

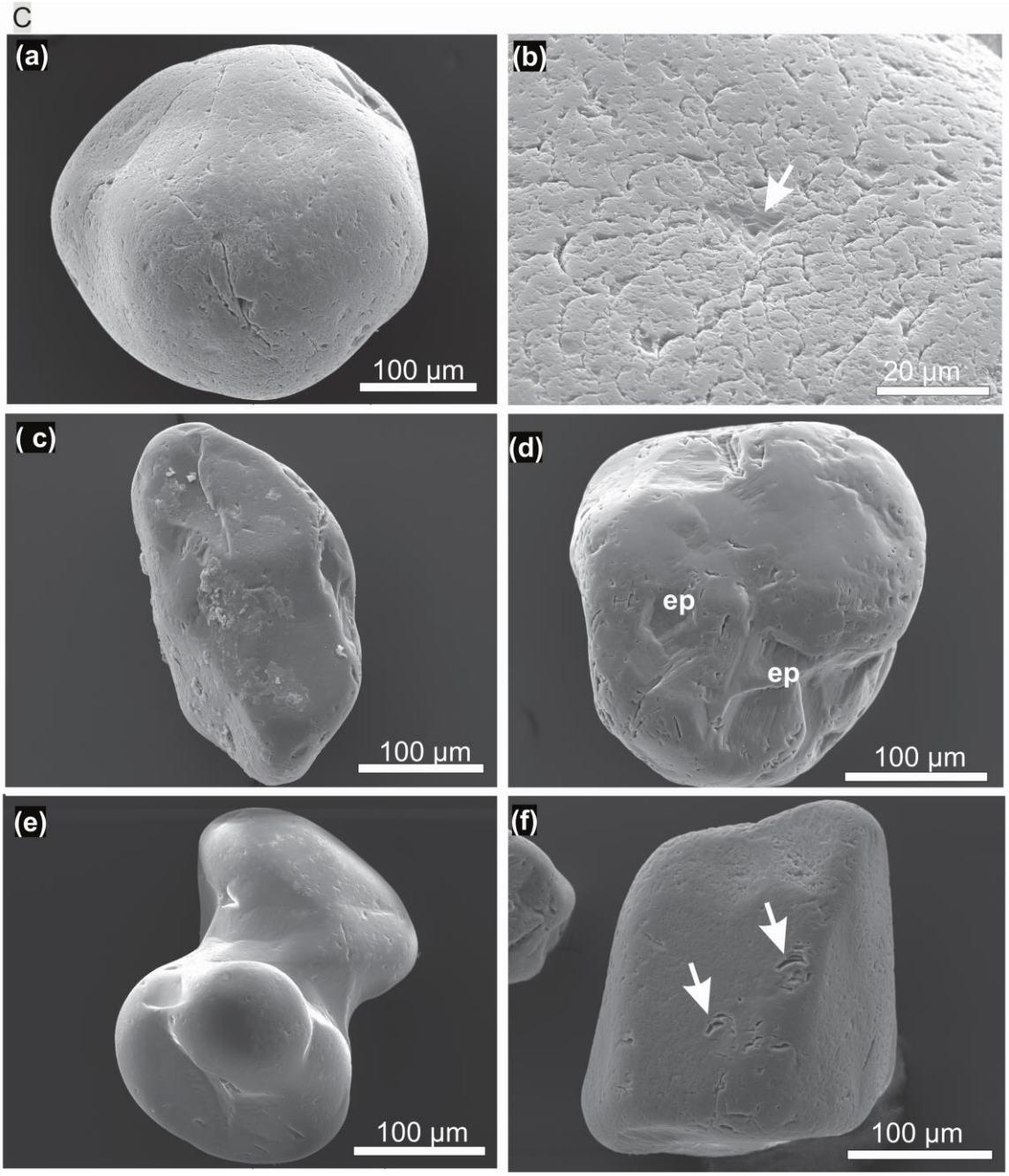

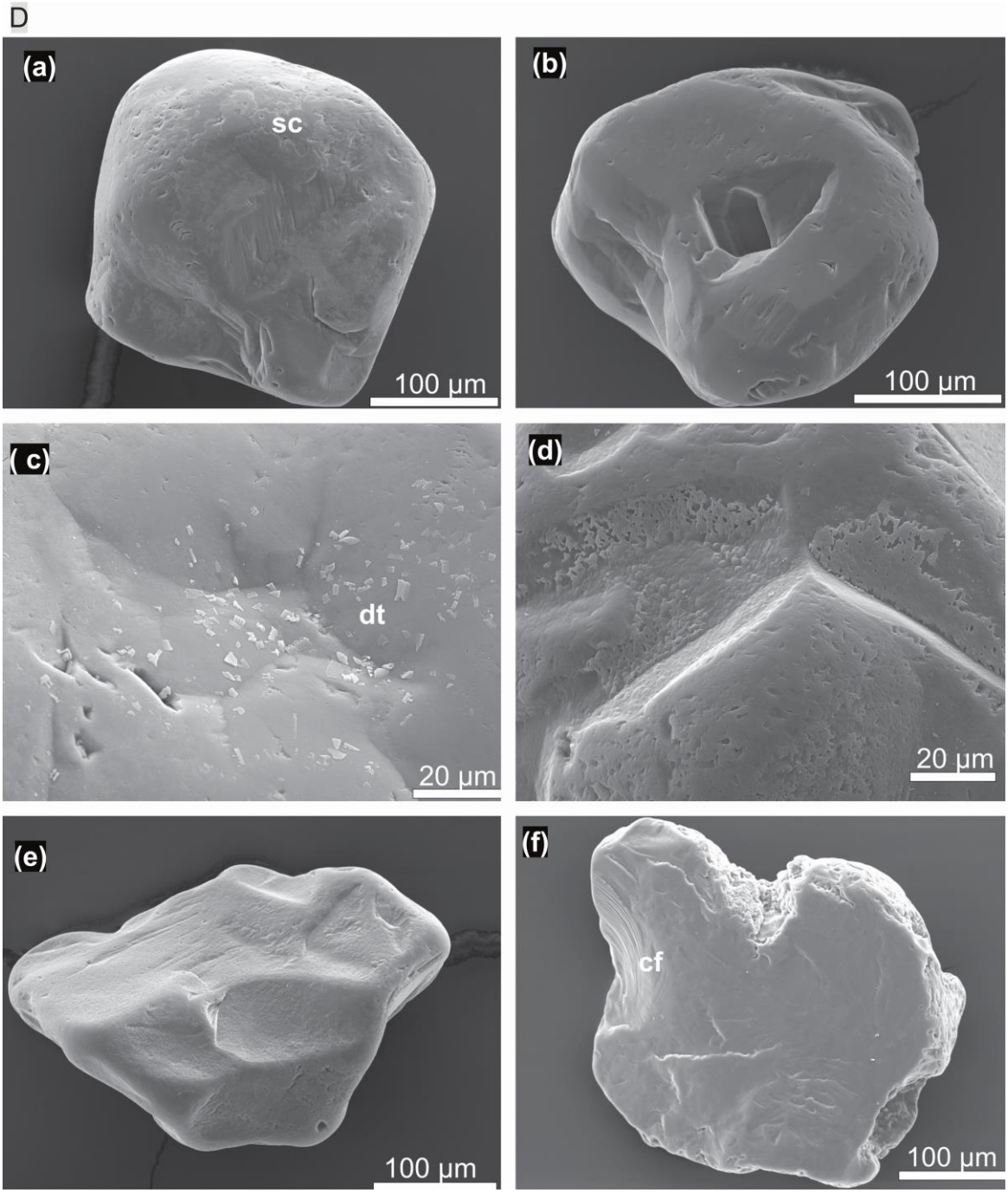

Fig. SM 5.3 A-D: Plates showing the variability of microtextures in (A) Limestones, (B) Diatomites, (C) Yellow sands, and (D) White sands. cf: conchoidal fracture; cm: chattermarks; dt: diatom; ep: etched pit; ps: parallel striation; sc: silica precipitation (coating); sp: solution pit; vs: V-shaped percussion crack.

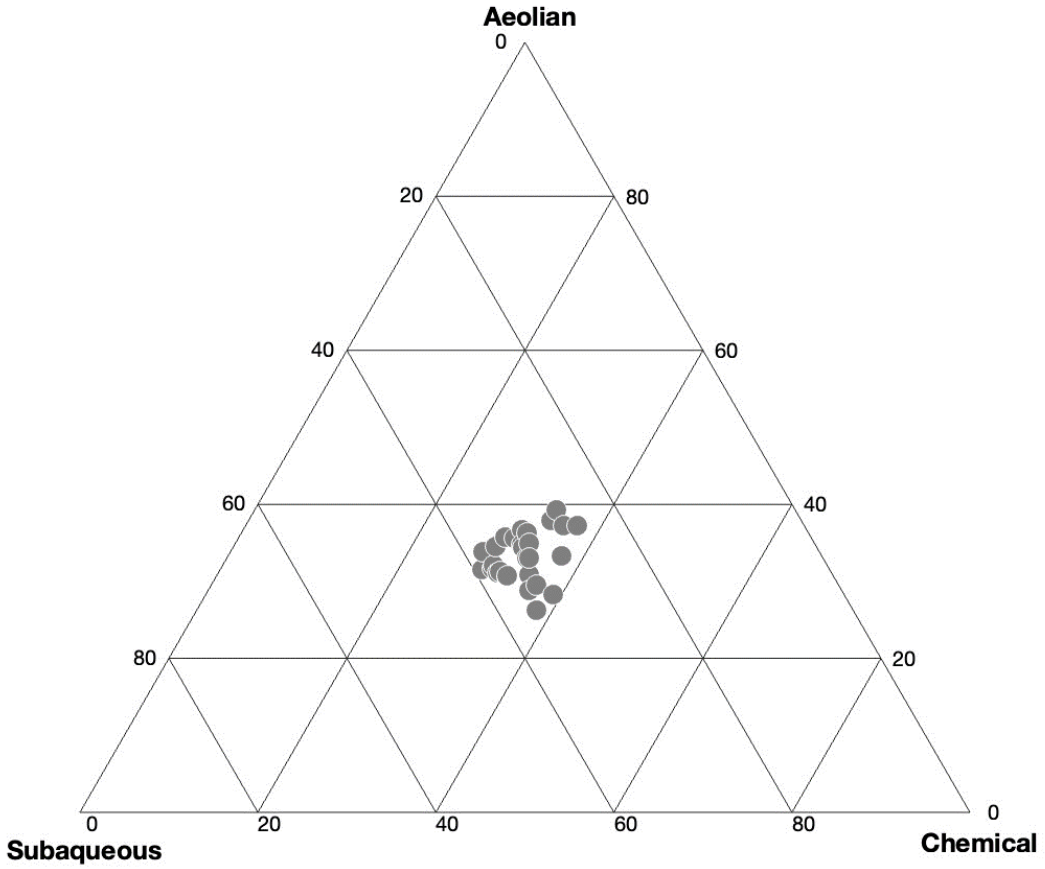

Fig. SM 5.4: Ternary diagram with all samples based on the three groups of selected features identified by the PCA (see Fig. 5.5B) according to their environmental interpretation. The samples coordinates are calculated using the sample average values in the Hellinger matrix for each group of features. All samples plot in a limited area of the ternary diagram emphasizing the presence of similar and repeated processes undergone by quartz during their evolution in the Chobe Enclave, whatever the facies type.

Table 5.1: Frequency of selected grain microtextures from SEM

Frequency on an ordinal scale as approximation of raw % (in parentheses). N = 30 grains for each calculation.

0 - not observed (0)
1 - rare (1-5)
2 - sparse (6-25)
3 - moderate (26-49)
4 - common (50-74)
5 - abundant (>75)

Facies	Site number	Angular, sub-angular	Sub-rounded	Rounded, well-rounded	Conchoidal fractures	Meandering ridges	V-shaped percussion c.	Upturned plates	Crescentic percussion m.	Bulbous edges	Parallel striations	Oriented etch pits	Solution pits	Silica precipitation	Chattermarks	Elongated depressions	Adhering particles
			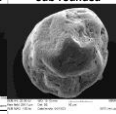	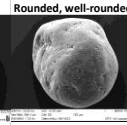	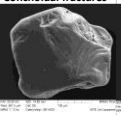			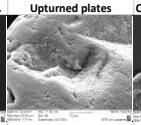			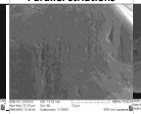	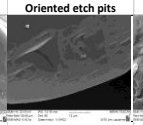	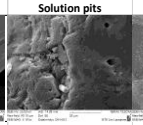	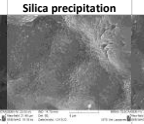		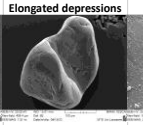	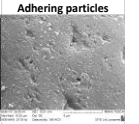
Limestone	TSC0.7	2	4	2	2	2	3	1	2	2	1	2	3	3	2	3	3
	TSC2.1	2	4	3	2	2	4	1	3	3	2	4	2	2	2	2	4
	BP1	2	4	2	2	2	3	1	3	4	1	4	2	3	2	2	4
	BP2.2	2	4	3	1	2	3	2	4	4	1	3	3	3	2	2	2
	BP3.7	2	4	3	1	2	4	2	4	3	1	3	2	3	1	2	3
	NATA1	2	4	3	2	3	4	2	3	3	2	4	3	3	1	2	3
	ACA0.3	3	3	2	2	3	3	2	2	2	1	3	4	3	1	2	5
	ACA1.6	2	3	3	2	1	4	2	4	2	2	4	3	3	1	2	3
	ACA2.4	2	3	3	2	2	3	2	3	3	2	2	2	3	4	3	1
	ACA3.2	3	2	2	2	2	3	2	2	1	2	3	3	3	2	2	3
Clay-rich layer	BP8.4	1	4	3	1	2	3	1	2	3	1	3	2	1	2	2	2
	NATA3.6	3	4	3	2	2	2	2	4	3	1	5	3	3	3	1	3
Diatomites	ACA0.6	3	3	2	1	3	4	1	2	1	2	3	4	4	3	2	5
	TSC1.8	2	4	4	2	1	2	2	4	4	2	5	3	3	4	2	3
Carbonate-rich sand	NATA0.8	2	4	2	1	2	4	1	1	4	2	5	2	3	2	3	1
	TSC0.2	4	4	2	2	2	2	2	4	4	2	5	2	4	4	2	5
	TSC1	4	4	3	2	2	3	3	3	3	1	5	5	4	3	3	4
	BP3.4	2	3	3	0	3	3	1	3	3	1	4	3	3	1	2	3
	NATA1.6	3	4	2	0	2	3	1	3	3	1	4	3	3	3	2	2
	NATA2.8	3	3	2	1	1	3	2	3	3	2	3	3	2	3	1	2
Yellow sand	TSC3.4	3	4	3	1	2	3	2	3	2	1	5	2	3	4	1	3
	ACA4.8	2	3	2	2	3	4	1	4	3	1	3	2	3	2	3	2
	BP5.5	1	3	2	1	1	3	1	2	2	0	3	2	2	2	1	2
	NATA3.2	3	3	2	1	1	2	2	4	3	2	4	3	2	3	1	2
White sand	TSC4	2	4	3	2	2	3	3	3	4	1	4	2	3	3	2	4
	BP7.2	2	4	2	2	2	3	2	2	3	1	3	2	2	2	2	1
	BP10	2	2	4	1	2	3	2	3	4	1	3	2	2	3	2	3
	NATA4.3	2	4	3	1	3	3	3	4	3	2	4	2	3	3	3	3

References

Bäumle, R., Himmelsbach, T. (2018) Exploration of deep, previously unknown semi-fossil aquifers of the Kalahari Basin (southern Africa). Grundwasser, 23, 29-45.

Beierle, B.D, Lamoureux, S.F., Cockburn, J.M.H., Spooner, I. (2002) A new method for visualizing sediment particle size distributions. J. of Paleolimnology, 27, 279–283.

Bond, G., Fernandes, T.R.C. (1974). Scanning electron microscopy applied to quartz grains from Kalahari type sands. Transactions Geological Society of South Africa, 77, 191-199.

Borcard, D., Gillet, F, Legendre, P. (2011) Numerical Ecology with R. Springer New York, 306 p.

Burrough, S.L., Thomas, D.S.G., Shaw, P.A., Bailey, R.M., 2007. Multiphase Quaternary Highstands at Lake Ngami, Kalahari, Northern Botswana. Palaeogeography, Palaeoclimatology, Palaeoecology, 253(3–4), 280–99.

Burrough, S.L., Thomas, D.S.G., and Bailey, R.M., 2009. Mega-Lake in the Kalahari: A Late Pleistocene record of the Palaeolake Makgadikgadi system. Quaternary Science Reviews 28(15–16), 1392–1411.

Chase, B.M., Meadows, M.E. (2007) Late Quaternary dynamics of southern Africa's winter rainfall zone. Earth-Science Reviews, 84, 103-138.

Davis, J.C. (1986) Statistics and data analysis in geology. John Wiley and Sons, New York, 2nd Ed., 646 p.

Diaz, N., Armitage, S.J., Verrecchia, E.P., Herman, F. (2019). OSL Dating of a carbonate island in the Chobe Enclave, NW Botswana. Quaternary Geochronology 49, 172–76.

Freytet, P. & Plaziat, J.C. (1982) Continental carbonate sedimentation and pedogenesis – Late Cretaceous and Early Tertiary of Southern France. Purser, B. (Ed.), Contributions to Sedimentology, 12, 1-213.

Haddon, I.G., McCarthy, T.S. (2005) The Mesozoic–Cenozoic interior sag basins of Central Africa: the late-cretaceous–Cenozoic Kalahari and Okavango basins. Journal of African Earth Sciences, 43(1-3), 316-333.

Itamiya, H., Sugita, R. & Sugai, T. (2019) Analysis of the surface micro- textures and morphologies of beach quartz grains in Japan and impli- cations for provenance research. Progress in Earth and Planetary Science, 6(1), 43.

Keiser, L.J., Soreghan, G. S., & Kowalewski, M. (2015). Use of quartz microtextural analysis to assess possible proglacial deposition for the Pennsylvanian–Permian Cutler Formation (Colorado, USA). Journal of Sedimentary Research, 85(11), 1310-1322.

Kinabo, B.D., Atekwana, E.A., Hogan, J.P., Modisi, M.P., Wheaton, D.D., Kampunzu, A.B. (2007) Early structural development of the Okavango rift zone, NW Botswana. J. Afr. Earth Sci. 48, 125–136.

Kinabo, B.D., Hogan, J.P., Atekwana, E.A., Abdelsalam, M.G., Modisi, M.P. (2008) Fault growth and propagation during incipient continental rifting: Insights from a combined aeromagnetic and Shuttle Radar Topography Mission digital elevation model investigation of the Okavango Rift Zone, northwest Botswana. Tectonics 27, TC3013Natu.

Krinsley, D., Doornkamp, J. (1973) Atlas of Quartz Sand Surface Textures. Cambridge: Cambridge University Press.

Li, J., Wang, X., Wu, W. (2021) Quantification of SEM quartz grain identi- fying the depositional environment. Arabian Journal of Geosciences, 14(11), 1–11.

Mahaney, W.C. (2002) Atlas of Sand Grain Surface Textures and Applica- tions. New York: Oxford University Press.

Mahaney, W.C., Kalm, V. (2000) Comparative scanning electron micros- copy study of oriented till blocks, glacial grains and Devonian sands in Estonia and Latvia. Boreas, 29(1), 35–51.

MathWorks (2022) Matlab™ version R2022a, The MathWorks Inc., MA, USA.

Matmon, A., Hidy, A.J., Vainer, S., Crouvi, O., Fink, D., Erel, Y., Arnold, M., Aumaître, G., Bourlès, D., Keddadouche, K. and Horwitz, L.K. (2015) New chronology for the southern Kalahari Group sediments with implications for sediment-cycle dynamics and early hominin occupation. Quaternary Research, 84(1), pp.118-132.

Mokatse, T., Diaz, N., Shemang, E., Van Thuyne, J., Vittoz, P., Vennemann, T., Verrecchia, E.P. (2022a) Landscapes and Landforms of the Chobe Enclave, Northern Botswana. In: Eckardt, F.D., (Ed.), Landscapes and landforms of Botswana, Springer Nature Switzerland, 91-115.

Mokatse, T., Vainer, S., Irving, J., Schmidt, C., Kgosidintsi, B., Shemang, S., Verrecchia, E.P. (2022b) Geometry of sedimentary deposits and evolution of the landforms in the Chobe Enclave, Northern Botswana. Geomorphology, 415, 108406.

Mokatse, T., Prud'Homme, C., Vainer, S., Adatte, T., Shemang, E., Verrecchia, E. P. (2023) Sepiolite as a multifactorial indicator of paleoenvironments in the Chobe Enclave (northern Botswana). Sedimentary Geology, 454, 106459.

Thomas, D.S.G. (1987). Discrimination of depositional environments, using sedimentary characteristics, in the Mega Kalahari, central southern africa. In: L.E. Frostick and I. Reid (Eds), Desert Sediments, Ancient and Modern, 293-306. Geological society of London Special Publication 35. Blackwell Scientific Publications: Oxford.

Thomas, D.S.G., Shaw, P.A., 1990. The deposition and development of the Kalahari Group sediments, Central Southern Africa. Journal of African Earth Sciences 10(1–2), 187–97.

Vainer, S., Matmon, A., Erel, Y., Hidy, A.J., Crouvi, O., De Wit, M., Geller, Y., ASTER Team, (2021) Landscape responses to intraplate deformation in the Kalahari constrained by sediment provenance and chronology in the Okavango Basin. Basin Research, 33(2), 1170-1193.

Vainer, S., Schmidt, C., Garzanti, E., Ben Dor, Y., Pastore,G., Mokatse, T., Prud'homme, C., Leanni, L., King, G., ASTER Team, Verrecchia, E. P. (2023 submitted) Chronology of sedimentation and landscape evolution in the Okavango Rift Zone, a developing young rift in southern Africa. JGR, Earth Surface, 35 pp.

Vos, K., Vandenberghe, N. & Elsen, J. (2014) Surface textural analysis of quartz grains by scanning electron microscopy (SEM): From sample preparation to environmental interpretation. Earth-Science Reviews, 128, 93–104. Available from: https://doi.org/10.1016/j.earscirev. 2013.10.013

CHAPTER 6

Conclusions

ERT survey data acquisition

6. Conclusions

This chapter presents the concluding remarks of the thesis and outlines the challenges and future research to better enhance the paleoenvironmental reconstruction.

6.1 Concluding remarks

The study conducted in the Chobe Enclave utilized a combination of geophysical, sedimentological, and mineralogical data to investigate landforms and their geological history at the region scale. The research covered the Late Pleistocene to Early Holocene periods and revealed a dynamic landscape evolution influenced by both a diversity of depositional environments (and sediments), which varied within a changing climate timeframe, and tectonic inputs.

The evolution of the Chobe landscape can be related to regional key events (Fig. 6.1):

i) A pre-rift configuration, which formed a paleosurface.

ii) The activation of Chobe graben system, which provided an accommodation space.

iii) A regional subsidence which enhanced alluvial deposition.

iv) And finally, Holocene erosion which led to relief inversions.

These major key events (Fig. 6.1) started with a paleosurface as part of an intra-cratonic basin formed during the pre-rift configuration, characterized by sedimentation in a fluvial-lake system. After continuous sedimentation in the region, the Chobe graben system formed due to reactivation of pre-existing basement structures, particularly the Ghanzi-Chobe zone where the fault lines created accommodation space that became filled with sediments in the alluvial-fluvial system (Kinabo et al., 2008). New data highlighted that the most recent major deformation event in the evolving rift probably occurred during the Middle Pleistocene transition (1.2-0.75 Ma), reflected as a striking change in the depositional environments (Vainer et al., 2023 submitted). Although the Chobe Enclave outcrops did not reach the Middle

Pleistocene sediments, it is likely that the oldest observed sands (the White sand facies) preserved in their earliest recognized features the imprint of aeolian environments, this explaining the endurance of the aeolian activity, probably even prior to the activation of the graben system (Vainer et al, 2023 submitted).

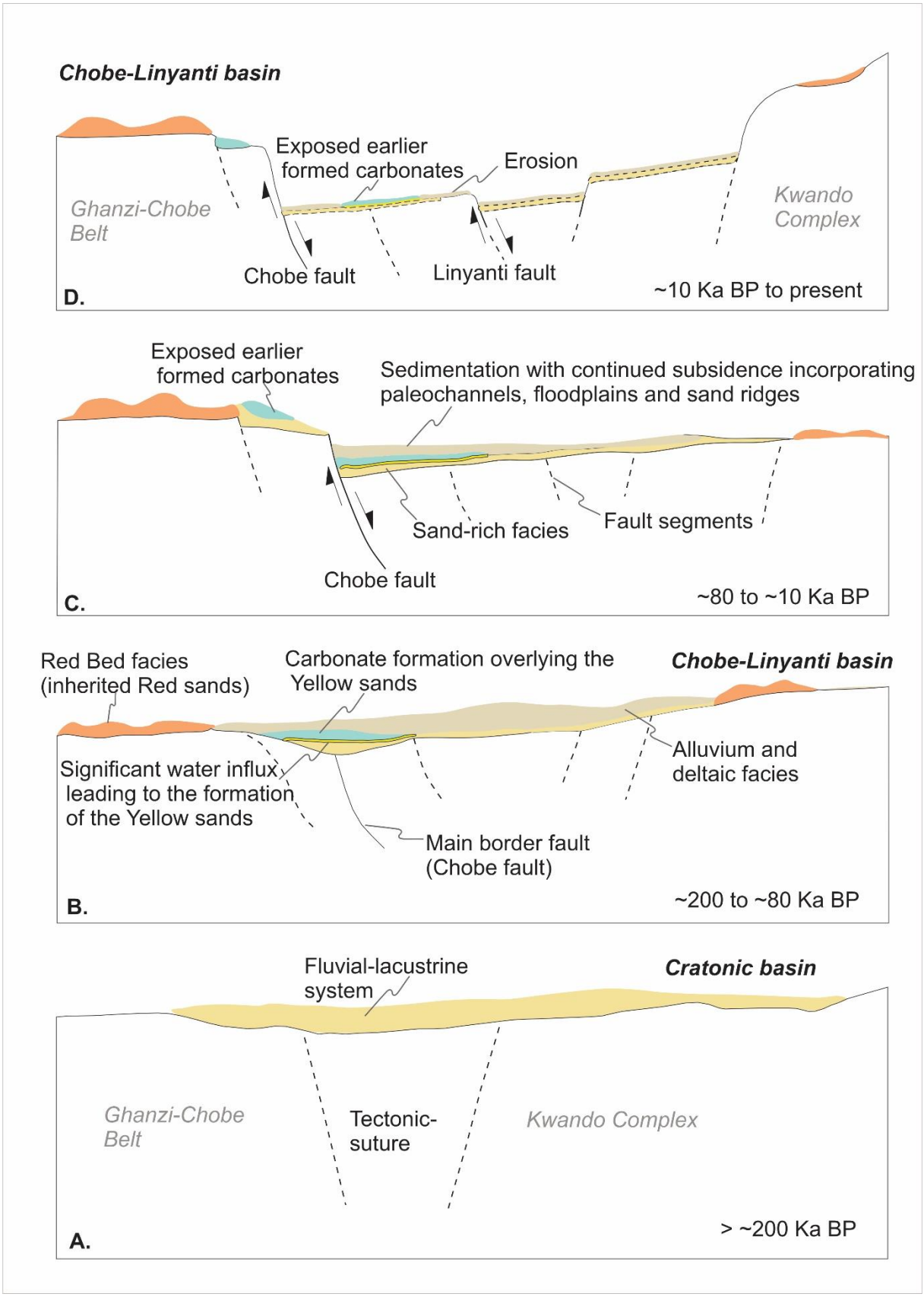

Figure 6.1: Reconstruction of Late Pleistocene basin development in the Chobe Enclave.

As the Chobe graben system evolves, the main border fault (the Chobe fault) propagated and formed a zone of high displacement (Alvarez Naranjo, 2016), generating a depocenter. With continued uplift and erosion, the footwall of the Chobe fault exposed the red sands inherited possibly from the *Red Bed facies* of the Mamuno Formation in the Ghanzi Group (Modie, 2000). These Red Bed facies correlate to the Chinamaba Hills Formation (Lehmann et al., 2015), which essentially forms the bedrock geology of the Chobe region. After their exposure and their transformation by pedogenesis, the Red sands were eroded and incorporated as soil sediments within the floodplain system, where a marked transition is observed within the Chobe Enclave lithologies as Yellow sand facies between ~200 Ka and ~150 Ka. The shift from Red to Yellow sands was likely due to the reworking by rivers of hematite-rich beds which underwent hydration, transforming hematite into more hydrated mineral, goethite, giving the yellow color to the soil sediment. The onset of the Yellow sand facies occurred as an erosional surface marking a transition to a palustrine/lacustrine environment indicating 1) sufficient water influx or tectonic subsidence and 2) a drastic change in the water chemistry. After this event, a pronounced carbonate deposition is recorded from ~100-80 Ka onwards. The formation of limestones occurred from Late Pleistocene through to Early Holocene and are observed in the present-day as large islands in the Chobe Enclave landscape.

Lastly, the continued evolution of the Chobe graben system led to the fault propagation of the Linyanti fault, inducing an uplift resulting in erosion and topographical inversion of the relief. This is depicted by the emergence of the carbonate units as reliefs in the floodplain of the Chobe Enclave, whereas limestones formed in lowlands (palustrine/lacustrine settings). Furthermore, reworked quartz grains were incorporated into the system as observed in the carbonates and diatomites. The quartz grains from these facies show imprints from eolian but also fluvial (low turbulent rivers) transportation. Notably, (neo)tectonic activity played a significant role, leading to the burial of paleochannels as well as the incision of sand ridges creating fluvial watergaps (Mokatse et al., 2022).

Moreover, the presence of authigenic sepiolite was also documented in the Chobe Enclave, with a focus on its association with carbonate and diatomite deposits in a closed lacustrine/ palustrine alkaline system, the same system as described above. Their study suggests that the formation of sepiolite was influenced by specific environmental conditions, including high [$Si(OH)_4$] and [Mg^{2+}] concentrations. Furthermore, mineralogical and

geochemical data allowed three end-members to be identified and controlling elemental contents: detrital, carbonate-sepiolite, and hydrothermalism components. The hydrothermalism component has been identified owing to the presence of barite in the sedimentary system. Finally, the distribution of the clay minerals, such as kaolinite and smectite, clearly indicated a detrital origin of the sediment, probably related to varying climatic conditions across the different sedimentary units of the Chobe Enclave.

6.2 Future perspectives

The conclusions drawn from this study provide insights into the complex geological and climatic history of the Chobe Enclave, emphasizing the need for further research to validate and explore the origin of the large palustrine carbonate deposits. Misinterpreted as “calcretes”, these carbonate layers recorded the deposition conditions and the geochemistry of the waters prevailing at the time of their formation: they are not “paleosols” but “sediments”. They also point to a new specific carbon and calcium cycle, which needs to be investigated. Additionally, tracing the source of Ca remains puzzling as the palustrine limestones deposited in a siliceous environment: what is or are the source(s) of calcium? How was it possible to shift from a pure siliceous environment to a carbonate-rich one and why? Why did calcite-rich deposits form predominantly after 80 Ka? There are still many questions pending about the presence of the palustrine limestones of the Chobe Enclave. Last, but not least, the evolution of the landscape related the timing of the tectonic influences is not properly constrained. Although a general framework has been proposed (Vainer at al., 2023 submitted), this needs a proper investigation.

References

Alvarez Naranjo, A. (2016) The role of pre-existing basement fabrics in the initiation of continental rifting: The Okavango Rift Zone, Botswana. Doctoral Dissertations. 2642. https://scholarsmine.mst.edu/doctoral_dissertations/2642.

Kinabo, B.D., Hogan, J.P., Atekwana, E.A., Abdelsalam, M.G., Modisi, M.P. (2008) Fault growth and propagation during incipient continental rifting: Insights from a combined aeromagnetic and Shuttle Radar Topography Mission digital elevation model investigation of the Okavango Rift Zone, northwest Botswana. Tectonics 27, TC3013Natu.

Lehmann, J., Master, S., Rankin, W., Milani, L., Kinnaird, J.A., Nydenov, K.A., Saalman, K. and Kumar, M. (2015) Regional aero- magnetic and stratigraphic correlations of the Kalahari Copperbelt in Namibia and Botswana. Ore Geology Reviews, 71, 169–190.

Mokatse, T., Vainer, S., Irving, J., Schmidt, C., Kgosidintsi, B., Shemang, S., Verrecchia, E.P. (2022) Geometry of sedimentary deposits and evolution of the landforms in the Chobe Enclave, Northern Botswana. Geomorphology, 415, 108406.

Vainer, S., Schmidt, C., Garzanti, E., Ben Dor, Y., Pastore,G., Mokatse, T., Prud'homme, C., Leanni, L., King, G., ASTER Team, Verrecchia, E. P. (2023 submitted) Chronology of sedimentation and landscape evolution in the Okavango Rift Zone, a developing young rift in southern Africa. JGR, Earth Surface, 35 pp.

Appendix A

Data from the PhD.

The appendix shows grain size distributions (Figure A1) and geochemical data (Tables A1 – A2) presented in the thesis.

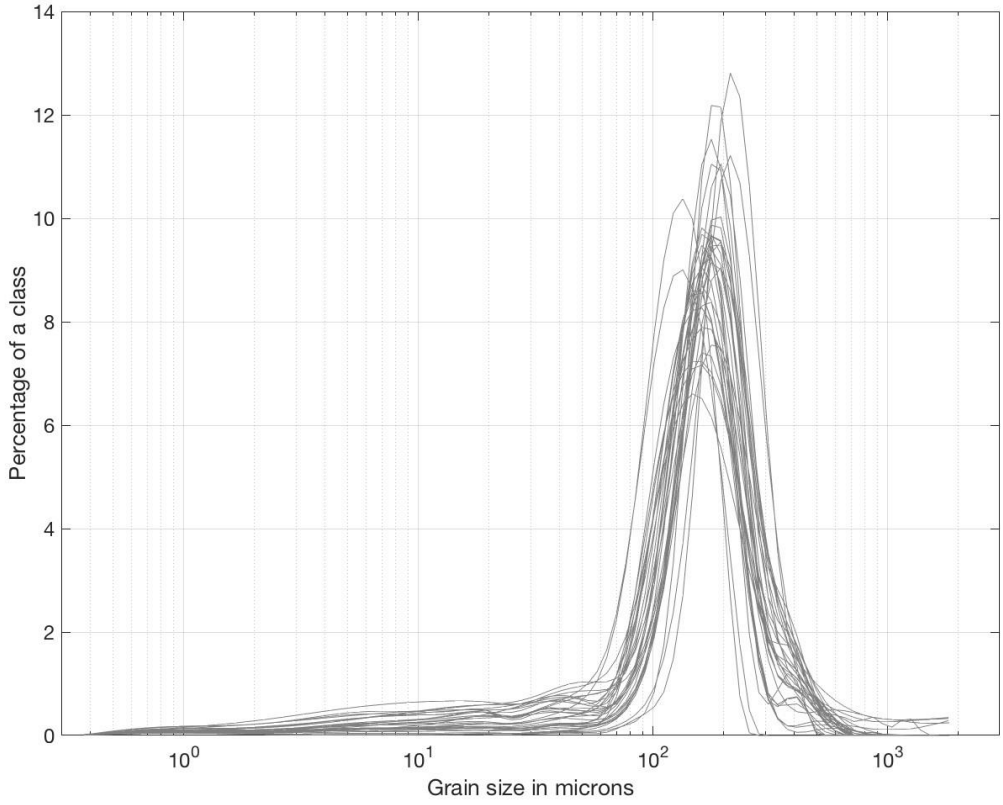

Figure A1: Grain-size distribution curves of all samples from the study sites.

Table A1: Major (wt.%) and trace (ppm) element data of samples from the study sites.

Sample No.	SiO_2	TiO_2	Al_2O_3	Fe_2O_3	MnO	MgO	CaO	Na_2O	K_2O	P_2O_5	LOI	Sum
TSC AO 0.7-0.9	24.56	0.03	0.35	0.75	0.11	1.68	36.68	0.03	0.05	0.04	33.53	97.80
TSCAO 2.1	36.25	0.03	0.42	0.98	0.16	1.31	31.45	0.03	0.07	0.05	28.83	99.58
TSC A1 0.6	67.82	0.14	2.33	2.27	0.05	1.64	9.09	0.08	0.13	0.02	16.99	99.13
TSC A1 1.0	48.55	0.08	1.30	1.83	0.13	1.48	21.56	0.08	0.09	0.02	24.38	99.87
TSC A1 1.4	38.76	0.07	0.90	1.69	0.19	1.31	26.30	0.09	0.07	0.01	27.26	99.85
TSC A1 1.8	47.27	0.08	1.14	1.76	0.16	1.28	22.91	0.09	0.10	0.01	24.99	99.72
TSC A1 2.2	48.31	0.07	0.88	1.01	0.22	0.88	24.46	0.08	0.08	0.02	22.91	99.98
TSC A1 2.6	74.04	0.11	1.18	0.92	0.07	0.57	11.10	0.08	0.12	0.02	12.11	100.03
TSC AI 3.0	83.21	0.13	1.08	4.05	0.04	0.56	2.08	0.03	0.18	0.01	9.00	99.87
TSC A1 3.4	87.58	0.20	2.14	2.06	0.02	0.34	0.37	0.08	0.16	0.01	7.06	99.15
TSC A1 3.8	92.45	0.20	1.70	0.98	0.01	0.22	0.32	0.02	0.15	0.01	4.23	99.73
TSC A1 4.0	98.86	0.09	0.62	0.15	0.01	0.06	0.03	0.06	0.02	0.00	0.25	100.01
TSC A1 0.2	84.04	0.12	1.62	1.15	0.03	0.66	1.34	0.04	0.15	0.08	11.15	99.84
BP A0 0.68-0.76	34.77	0.06	0.84	0.70	0.04	3.47	29.66	0.06	0.06	0.01	28.90	98.57
BP AI 1.0	76.42	0.13	1.77	1.50	0.06	4.29	4.91	0.10	0.16	0.01	11.16	99.89
BP AI 1.4	68.18	0.10	1.27	0.86	0.09	2.57	12.54	0.11	0.10	0.01	14.55	99.19
BP AI 1.8	55.42	0.08	0.98	0.61	0.21	2.21	20.39	0.16	0.07	0.01	19.73	99.64
BP AI 2.2	60.95	0.08	0.95	0.54	0.12	1.82	17.63	0.15	0.07	0.01	17.43	99.24
BP AI 2.6	65.93	0.08	1.06	0.64	0.19	1.63	14.41	0.14	0.11	0.01	15.38	99.75
BP AI 3.0	58.48	0.09	0.94	0.57	0.42	2.15	18.87	0.22	0.10	0.01	18.20	99.89
BP AI 3.4	61.18	0.08	0.89	0.52	0.15	1.34	18.86	0.12	0.10	0.01	17.76	99.35
BP A1 3.7	63.28	0.08	0.55	0.62	0.23	1.38	17.86	0.03	0.12	0.01	16.86	101.03
BPC 4.4	92.56	0.10	0.50	2.82	0.02	0.61	0.22	0.03	0.13	0.00	3.79	99.19
BPC 4.6	94.85	0.12	0.57	2.02	0.02	0.45	0.14	0.02	0.16	0.00	2.59	99.26
BPC 5.0	88.76	0.10	0.86	3.99	0.02	0.71	0.26	0.04	0.20	0.00	5.18	99.13
BPC 5.5	90.98	0.11	0.82	3.27	0.02	0.47	0.21	0.03	0.15	0.00	4.08	99.78
BPC 5.8	95.37	0.08	0.62	1.97	0.01	0.23	0.15	0.03	0.14	0.00	2.50	99.74
BPC 6.3	97.82	0.12	0.38	0.26	0.01	0.08	0.04	0.02	0.08	0.00	0.77	99.78
BPC 7.2	98.25	0.07	0.20	0.16	0.00	0.06	0.02	0.01	0.02	0.00	0.30	100.06

BPC 7.7	99.47	0.03	0.15	0.09	0.00	0.06	0.02	0.00	0.03	0.00	0.23	99.26
BPC 8.4-8.45	91.74	0.16	2.76	1.01	0.01	0.25	0.18	0.02	0.15	0.01	3.71	100.01
BPC 8.8-8.85	85.22	0.14	3.55	1.41	0.02	0.30	0.23	0.05	0.20	0.00	8.58	99.70
BPC 9.2-9.25	68.99	0.35	11.52	3.75	0.02	0.78	0.63	0.07	0.44	0.02	12.79	99.36
BPC 10.0	97.48	0.14	0.65	0.27	0.01	0.09	0.04	0.03	0.09	0.00	0.74	99.38
NATA 0.5	29.57	0.05	0.28	0.59	0.28	2.48	40.95	0.06	0.12	0.16	1.54	76.08
NATA 0.8-0.9	37.55	0.09	0.71	2.00	0.16	1.67	34.94	0.05	0.10	0.04	2.05	79.35
NATA 1	36.97	0.06	0.43	1.15	0.19	1.36	37.52	0.05	0.07	0.04	1.18	79.03
NATA 1.2-1.3	62.20	0.11	1.12	6.34	0.11	2.67	9.78	0.02	0.20	0.03	9.81	92.39
NATA 1.6-1.7	41.39	0.07	0.56	4.67	0.13	2.37	27.87	0.06	0.11	0.02	4.12	81.39
NATA 2.0-2.1	47.37	0.08	0.66	4.93	0.20	2.36	23.51	0.05	0.13	0.02	3.83	83.16
NATA 2.4-2.5	47.23	0.07	0.51	6.27	0.18	1.54	23.79	0.06	0.11	0.02	3.93	83.73
NATA 2.8-2.9	69.44	0.10	0.74	3.60	0.08	1.50	13.39	0.03	0.17	0.01	2.66	91.72
NATA 3.2-3.3	91.26	0.11	0.87	2.47	0.04	0.96	0.38	0.03	0.19	0.04	2.22	98.55
NATA 3.6-3.7	88.48	0.11	0.85	4.77	0.04	0.86	0.72	0.04	0.15	0.01	2.90	98.91
NATA 4.0-4.1	97.71	0.11	0.90	0.72	0.01	0.23	0.10	0.02	0.11	0.00	0.89	100.81
NATA 4.3-4.4	98.96	0.11	0.95	0.57	0.01	0.15	0.10	0.02	0.10	0.00	0.90	101.89
ACA AO 0-0.1	49.48	0.09	1.82	1.18	0.28	2.14	20.94	0.08	0.22	0.02	23.14	99.39
ACA A1 0.3-0.4	79.35	0.10	2.10	0.97	0.04	0.46	3.49	0.66	0.24	0.01	12.01	99.42
ACA A1 0.6-0.7	79.77	0.10	2.23	1.52	0.04	0.50	2.93	0.13	0.15	0.00	12.10	99.47
ACA A2 1	42.43	0.07	0.99	1.12	0.35	1.60	27.48	0.04	0.07	0.01	25.73	99.90
ACA A2 1.6-1.7	47.67	0.06	0.81	1.76	0.14	1.87	24.07	0.16	0.09	0.02	23.36	100.00
ACA A2 2.0-2.1	28.43	0.03	0.40	1.25	0.29	1.70	35.41	0.27	0.11	0.02	31.63	99.54
ACA A2 2.4-2.5	41.40	0.05	0.53	0.91	0.25	1.40	28.36	0.11	0.08	0.02	26.09	99.21
ACA A2 2.8-2.9	31.77	0.04	0.36	0.83	0.34	1.57	33.67	0.07	0.06	0.02	30.17	98.90
ACA A2 3.2-3.3	39.04	0.04	0.41	1.69	0.26	2.09	27.54	0.05	0.09	0.01	26.75	97.99
ACA A2 3.6-3.7	36.68	0.05	0.45	1.69	0.24	2.36	29.81	0.05	0.10	0.02	28.34	99.78
ACA A2 4.0-4.1	37.53	0.05	0.59	2.09	0.26	1.97	28.87	0.03	0.09	0.01	27.89	99.40
ACA A2 4.4-4.5	34.11	0.05	0.57	1.96	0.29	1.85	30.80	0.04	0.09	0.01	29.66	99.43
ACA A2 4.8-4.9	34.02	0.05	0.50	3.14	0.24	1.79	29.61	0.03	0.10	0.01	30.00	99.49
ACA A2 5.2-5.3	45.19	0.06	0.70	1.73	0.19	1.39	25.70	0.03	0.11	0.02	24.27	99.39
ACA A2 5.6-5.7	48.73	0.08	0.83	1.98	0.15	1.15	23.58	0.03	0.15	0.02	22.63	99.32
ACA A2 6.0-6.1	96.74	0.11	0.83	0.88	0.01	0.28	0.11	0.03	0.18	0.00	2.23	101.41

Sample No.	As	Ba	Ce	Co	Cr	Cu	Ga	Hf	La	Nb	Nd	Ni	Pb	Rb	Sc	Sr	Th	U	V	Y	Zn	Zr	Cs	Sm
TSC AO 0.7-0.9	8.7	1461.6	0.0	2.0	8.3	11.3	0.0	0.0	0.0	0.0	5.1	7.7	0.0	5.3	0.0	375.7	3.0	2.9	21.4	2.1	3.0	8.0	0.0	0.0
TSCAO 2.1	8.2	410.0	0.0	0.0	3.8	10.6	0.0	0.0	0.0	0.0	9.1	5.2	0.0	10.2	0.0	379.7	2.1	1.8	8.7	1.3	2.9	11.6	0.0	0.0
TSC A1 0.6	3.7	100.3	24.7	9.6	33.3	8.7	2.6	0.0	12.7	1.9	16.0	19.2	3.5	13.8	0.0	102.6	1.6	1.6	86.8	11.6	4.7	64.3	2.7	0.0
TSC A1 1.0	7.0	84.5	0.0	6.8	12.8	9.3	1.1	0.0	7.2	0.0	11.5	15.2	0.0	10.3	0.0	295.0	2.1	3.0	48.1	10.4	2.7	45.7	3.8	0.0
TSC A1 1.4	12.8	82.2	0.0	5.4	7.1	8.7	0.0	0.0	13.0	0.0	7.1	12.8	0.0	9.6	0.0	289.3	1.8	2.6	31.0	5.6	1.8	32.7	2.3	0.0
TSC A1 1.8	9.1	136.0	0.0	5.0	41.8	8.6	0.0	0.0	7.0	0.0	9.1	13.7	0.0	12.0	0.0	241.2	1.8	2.6	31.0	7.0	2.3	43.7	0.0	0.0
TSC A1 2.2	4.8	164.7	0.0	0.0	6.8	7.7	0.0	0.0	0.0	0.0	7.9	7.5	0.0	8.9	0.0	256.8	1.7	1.5	20.7	4.9	1.2	46.6	0.0	0.0
TSC A1 2.6	0.0	288.1	0.0	0.0	33.1	7.0	0.0	0.0	0.0	1.2	10.4	7.2	0.0	10.2	0.0	127.4	1.3	1.3	24.5	8.3	1.4	70.5	0.0	0.0
TSC AI 3.0	0.0	989.6	0.0	6.9	37.6	7.9	0.0	0.0	7.6	1.7	4.7	12.6	1.2	14.2	2.0	47.3	1.1	0.0	36.1	6.2	2.4	99.3	0.0	0.0
TSC A1 3.4	0.0	862.5	22.9	4.4	41.5	8.1	1.7	0.0	15.2	2.4	12.8	9.7	2.2	11.2	4.1	21.1	1.2	0.0	57.2	5.8	3.4	113.8	3.2	3.4
TSC A1 3.8	0.0	170.7	5.7	2.0	72.6	7.5	1.9	2.7	0.0	2.6	4.3	7.2	2.6	9.0	3.3	9.5	0.0	0.0	59.9	3.6	3.1	147.1	3.8	0.0
TSC A1 4.0	0.0	32.3	0.0	0.0	85.6	5.6	0.0	2.7	0.0	0.0	4.4	0.0	0.0	0.0	1.4	1.3	0.0	0.0	5.2	1.5	0.0	108.2	0.0	0.0
TSC A1 0.2	0.0	241.7	9.8	2.9	16.2	12.7	1.9	4.0	0.0	1.6	5.8	11.0	2.2	11.9	2.6	24.4	0.0	1.6	41.3	5.3	4.0	62.0	2.5	0.0
BP A0 0.68-0.76	14.0	1043.9	0.0	0.0	14.5	10.2	0.0	0.0	0.0	0.0	5.7	4.1	0.0	8.3	0.0	682.7	4.2	5.7	42.1	2.7	3.3	21.3	4.7	0.0
BP AI 1.0	3.5	299.5	7.0	2.4	13.9	9.7	1.8	0.0	7.6	1.4	6.9	8.9	1.1	15.1	0.0	98.4	1.0	0.0	29.3	2.1	5.8	57.4	0.0	0.0
BP AI 1.4	0.0	646.6	0.0	0.0	9.5	7.8	0.0	0.0	0.0	0.0	3.0	5.5	0.0	9.5	0.0	231.1	1.2	0.0	19.8	2.7	2.6	43.1	2.8	0.0
BP AI 1.8	5.0	392.5	0.0	0.0	44.7	8.0	0.0	0.0	0.0	0.0	6.5	6.8	0.0	7.4	0.0	278.5	1.1	0.0	16.1	1.7	2.4	39.6	4.5	0.0
BP AI 2.2	4.5	340.2	0.0	0.0	12.2	7.8	0.0	0.0	0.0	0.0	6.9	7.0	0.0	6.8	0.0	293.9	1.6	0.0	11.8	1.7	2.2	38.1	0.0	0.0
BP AI 2.6	5.9	514.8	0.0	0.0	15.3	7.7	0.0	0.0	0.0	0.0	0.0	6.9	0.0	6.7	0.0	206.4	0.0	0.0	24.9	1.8	1.8	39.7	0.0	4.4
BP AI 3.0	3.0	552.8	0.0	0.0	6.3	8.9	0.0	0.0	7.5	1.0	5.0	10.4	0.0	9.4	0.0	299.0	1.4	0.0	17.3	1.9	2.3	46.2	2.6	0.0
BP AI 3.4	0.0	304.9	0.0	0.0	21.1	8.1	0.0	0.0	0.0	0.0	6.6	6.8	0.0	8.6	0.0	217.5	0.0	0.0	12.9	1.8	2.0	51.0	3.1	0.0
BP A1 3.7	4.9	509.6	0.0	0.0	11.8	8.9	0.0	0.0	0.0	0.0	7.6	7.3	0.0	9.3	0.0	182.1	1.5	1.4	14.4	2.0	9.0	59.2	0.0	0.0
BPC 4.4	0.0	653.4	0.0	2.6	6.2	7.6	0.0	0.0	0.0	1.3	0.0	3.9	0.0	8.9	1.9	20.3	1.2	0.0	21.3	3.5	1.8	78.7	0.0	0.0
BPC 4.6	0.0	551.4	19.9	2.2	14.5	6.6	0.0	0.0	13.3	1.3	13.1	3.3	1.1	9.3	1.6	14.7	0.0	0.0	17.0	7.3	1.6	90.8	0.0	0.0
BPC 5.0	0.0	559.1	8.7	6.6	66.2	7.2	0.0	0.0	11.6	1.4	7.9	7.1	0.0	14.0	1.9	17.9	0.0	0.0	24.4	3.8	2.3	79.8	0.0	0.0
BPC 5.5	0.0	374.5	8.9	5.2	52.0	6.7	0.0	0.0	0.0	1.3	7.4	5.3	1.0	10.1	2.9	12.6	1.0	0.0	34.6	2.9	1.8	74.3	0.0	0.0
BPC 5.8	0.0	179.9	5.4	3.5	72.7	6.0	0.0	0.0	0.0	1.2	4.7	4.5	1.1	7.6	2.8	9.3	0.0	0.0	31.9	1.8	1.3	67.6	2.6	0.0
BPC 6.3	0.0	113.0	0.0	0.0	21.9	5.8	0.0	0.0	0.0	1.4	0.0	1.0	0.0	2.7	0.0	4.6	0.0	0.0	20.1	1.7	0.0	110.5	2.4	3.0
BPC 7.2	0.0	32.5	0.0	0.0	99.3	5.3	0.0	0.0	0.0	0.0	0.0	0.0	0.0	1.0	0.0	1.1	0.0	0.0	15.4	1.1	0.0	105.2	3.7	0.0
BPC 7.7	0.0	31.4	0.0	0.0	151.5	5.3	0.0	3.0	0.0	0.0	0.0	0.0	0.0	0.0	1.0	1.0	0.0	0.0	11.4	1.1	0.0	25.2	3.2	0.0
BPC 8.4-8.45	0.0	212.2	57.2	0.0	31.0	13.8	3.3	0.0	26.3	2.2	29.8	7.5	3.6	9.2	6.4	16.4	2.0	1.5	95.4	18.4	3.4	74.8	2.9	4.6
BPC 8.8-8.85	0.0	145.6	5.9	0.0	19.7	19.7	4.2	0.0	0.0	1.8	4.4	7.6	5.6	13.0	4.6	19.0	2.3	2.4	58.4	8.9	5.0	27.6	0.0	0.0
BPC 9.2-9.25	0.0	122.1	42.5	10.0	60.2	33.6	14.2	0.0	16.5	6.0	26.1	20.5	12.8	35.1	11.5	45.9	7.9	1.0	160.1	22.4	15.3	53.0	0.0	5.3

BPC 10.0	0.0	59.4	0.0	0.0	7.7	7.0	0.0	0.0	0.0	1.4	3.0	0.0	0.0	3.5	1.3	4.4	0.0	0.0	17.8	2.7	0.0	109.8	0.0	0.0
NATA 0.5	0.0	1227.8	0.0	0.0	2.7	13.2	0.0	0.0	0.0	0.0	7.3	4.3	0.0	6.5	0.0	518.5	3.3	3.2	11.4	1.2	7.9	14.7	0.0	0.0
NATA 0.8-0.9	0.0	149.7	0.0	3.0	9.1	10.5	0.0	0.0	0.0	0.0	10.4	10.3	0.0	8.5	0.0	271.2	1.8	1.5	30.7	7.7	2.9	35.2	0.0	10.5
NATA 1	0.0	264.7	0.0	0.0	5.6	16.5	0.0	0.0	0.0	0.0	10.9	2.9	0.0	5.6	0.0	343.8	2.7	2.2	8.0	1.7	4.3	24.4	6.3	0.0
NATA 1.2-1.3	0.0	152.6	23.9	12.2	15.4	12.7	1.4	0.0	14.2	1.2	20.2	19.7	1.3	18.6	0.0	141.1	1.7	1.7	75.9	23.1	4.5	52.2	0.0	0.0
NATA 1.6-1.7	3.0	278.0	0.0	5.8	9.2	11.2	0.0	0.0	9.3	0.0	13.9	8.5	0.0	12.2	0.0	482.8	3.7	2.9	27.2	20.9	3.0	33.1	2.5	3.8
NATA 2.0-2.1	3.5	251.9	0.0	6.4	9.4	11.7	0.0	0.0	9.8	0.0	12.6	9.2	0.0	13.1	0.0	344.2	2.5	1.9	23.0	14.3	3.4	45.5	0.0	0.0
NATA 2.4-2.5	0.0	596.6	11.7	6.1	7.4	11.3	0.0	0.0	14.1	0.0	18.2	6.6	0.0	10.3	0.0	203.9	2.6	0.0	15.5	18.2	2.6	41.3	0.0	0.0
NATA 2.8-2.9	0.0	366.6	37.1	4.2	14.7	8.9	0.0	0.0	22.8	0.0	31.0	7.9	0.0	14.6	0.0	94.5	1.7	1.3	41.5	20.2	3.7	61.9	2.5	0.0
NATA 3.2-3.3	0.0	773.6	356.6	4.4	17.5	8.7	0.0	0.0	170.4	1.2	173.4	7.6	1.5	15.2	2.2	29.9	2.1	0.0	39.1	37.9	3.8	96.4	4.8	28.9
NATA 3.6-3.7	0.0	650.7	40.3	5.8	36.2	9.5	0.0	0.0	23.2	1.2	25.4	6.8	1.3	12.3	1.7	23.8	0.0	0.0	40.3	8.4	3.7	76.6	0.0	0.0
NATA 4.0-4.1	0.0	138.4	0.0	0.0	18.7	0.0	0.0	0.0	0.0	1.4	3.9	2.6	1.5	7.8	1.9	6.6	0.0	0.0	41.4	2.5	2.3	87.0	2.9	0.0
NATA 4.3-4.4	0.0	121.8	0.0	0.0	82.6	6.0	0.0	0.0	0.0	1.3	6.0	3.1	1.0	6.8	2.4	6.1	0.0	0.0	41.0	2.4	2.4	90.0	0.0	0.0
ACA AO 0-0.1	6.0	1349.4	0.0	2.8	16.4	11.3	1.0	0.0	8.6	0.0	0.0	7.5	0.0	11.7	0.0	433.5	3.3	3.8	63.4	3.5	3.8	21.2	2.2	0.0
ACA A1 0.3-0.4	0.0	2070.4	0.0	0.0	16.5	7.4	1.0	0.0	7.7	1.3	0.0	4.8	1.1	7.0	2.0	74.3	1.3	0.0	53.3	2.0	2.6	18.0	0.0	0.0
ACA A1 0.6-0.7	0.0	1295.5	0.0	0.0	18.7	7.8	1.5	0.0	0.0	1.3	0.0	6.4	1.7	6.4	2.5	57.3	0.0	0.0	51.5	1.7	2.3	18.2	0.0	0.0
ACA A2 1	5.0	656.3	0.0	0.0	7.6	9.9	0.0	3.0	0.0	0.0	9.6	10.3	0.0	4.9	0.0	156.1	1.2	1.7	42.2	3.1	2.4	26.0	3.9	0.0
ACA A2 1.6-1.7	0.0	565.6	0.0	2.6	7.1	8.7	0.0	0.0	0.0	0.0	5.0	8.6	0.0	7.3	0.0	135.7	0.0	0.0	29.4	1.4	3.1	30.0	0.0	7.6
ACA A2 2.0-2.1	3.3	443.9	0.0	0.0	4.3	10.0	0.0	4.0	0.0	0.0	10.9	8.4	0.0	6.5	0.0	342.3	2.1	3.1	19.5	1.6	2.4	14.5	3.8	0.0
ACA A2 2.4-2.5	0.0	467.1	0.0	0.0	10.4	9.1	0.0	0.0	0.0	0.0	7.6	7.3	0.0	6.5	0.0	345.5	2.6	3.1	34.5	2.0	1.4	26.2	3.0	0.0
ACA A2 2.8-2.9	3.5	729.4	0.0	0.0	7.3	9.9	0.0	0.0	0.0	0.0	5.6	6.6	0.0	7.2	0.0	548.3	3.3	3.3	21.3	2.6	1.9	17.4	2.2	0.0
ACA A2 3.2-3.3	0.0	857.4	0.0	0.0	5.0	10.6	0.0	0.0	0.0	0.0	6.3	6.6	0.0	10.3	0.0	569.2	3.3	3.8	20.2	2.1	2.1	23.8	5.0	0.0
ACA A2 3.6-3.7	0.0	504.2	0.0	2.3	3.9	11.0	0.0	3.0	0.0	0.0	5.0	5.0	0.0	10.4	0.0	487.4	2.8	2.7	14.3	2.6	2.1	33.6	3.8	0.0
ACA A2 4.0-4.1	3.1	691.6	0.0	3.4	7.1	10.9	0.0	0.0	7.3	0.0	0.0	4.4	0.0	10.5	0.0	386.6	2.4	2.3	14.3	2.5	2.4	31.2	4.2	0.0
ACA A2 4.4-4.5	0.0	398.9	0.0	2.9	7.1	10.1	0.0	0.0	0.0	0.0	10.0	4.5	0.0	10.4	0.0	443.0	3.5	3.4	16.6	3.7	2.1	26.9	0.0	0.0
ACA A2 4.8-4.9	0.0	490.0	0.0	4.7	6.4	10.1	0.0	0.0	0.0	0.0	7.7	4.8	0.0	10.3	0.0	377.4	2.2	3.0	16.4	2.5	2.5	24.5	0.0	0.0
ACA A2 5.2-5.3	0.0	368.5	0.0	2.5	16.2	9.5	0.0	0.0	0.0	0.0	9.8	3.9	0.0	10.6	0.0	287.5	2.1	3.3	21.1	6.2	2.3	38.6	4.4	0.0
ACA A2 5.6-5.7	0.0	370.0	33.2	2.1	9.5	9.2	0.0	4.0	22.4	0.0	28.4	4.1	0.0	13.0	0.0	158.0	2.4	2.7	26.4	28.1	3.2	51.2	2.9	6.8
ACA A2 6.0-6.1	0.0	93.7	0.0	0.0	15.8	7.1	0.0	3.0	0.0	1.3	3.1	2.9	2.0	13.3	3.0	6.8	0.0	1.0	40.1	2.1	2.0	97.4	3.0	0.0

Appendix B

Published papers.

Geomorphology 415 (2022) 108406

Contents lists available at ScienceDirect

Geomorphology

journal homepage: www.journals.elsevier.com/geomorphology

Geometry of sedimentary deposits and evolution of the landforms in the Chobe Enclave, Northern Botswana

Thuto Mokatse [a,*], Shlomy Vainer [a], James Irving [b], Christoph Schmidt [a], Boniface Kgosidintsi [c], Elisha Shemang [c], Eric P. Verrecchia [a]

[a] Institute of Earth Surface Dynamics — IDYST, FGSE, University of Lausanne, 1015 Lausanne, Switzerland
[b] Institute of Earth Sciences — ISTE, FGSE, University of Lausanne, 1015 Lausanne, Switzerland
[c] Earth and Environmental Sciences, Botswana International University of Science and Technology, Botswana

ARTICLE INFO

Keywords:
Sand ridges
Neotectonics
Watergaps
Grain-size distributions
Middle Kalahari

ABSTRACT

The imprint of neotectonics is frequently obscured in low-relief environments by the sedimentary cover. This is the case in the Chobe Enclave, part of a pristine region of the Middle Kalahari Basin in northern Botswana, where numerous fossil landforms, such as sand dunes, pans, sand ridges, and carbonate islands, can be observed but whose detailed origins are unclear. In this study, a combination of near-surface geophysical surveys, sedimentological analysis, and optically-stimulated luminescence (OSL) dating were used to study the relationship between landscape development and neotectonic activity in one region of the Chobe Enclave. Specifically, electrical resistivity tomography (ERT) and ground penetrating radar (GPR) surveys were used to define the lateral and vertical distribution of sedimentary deposits associated with a prominent sand ridge and its margins. Sedimentological analysis and OSL dating of soil samples from pits taken along the survey lines were then used to calibrate the geophysical results and establish a chronostratigraphical framework. Our results lead to the following hypotheses regarding the evolution of this part of the Chobe landscape: (i) during the Late Pleistocene (>~25 ka), fluvial channels were buried due to epeirogenic movements, resulting in paleo-channels; (ii) between ~25 ka and ~6 ka, a paleo-lake shoreline formed, which resulted in the linear eastern margin observed on the considered sand ridge. Erosional bounding surfaces suggest the syndepositional uplift of the sand ridge morphologies during this time; (iii) a neotectonic influence on the evolution of the landscape is revealed by the incision of the sand ridge forming fluvial watergaps since ~6 ka ago; and (iv) due to continuous aeolian and fluvial reworking, the western-most ridge became gradually isolated from the floodplain resulting in an inherited relief. In conclusion, this investigation allowed the deformation caused by epeirogenic movements acting on a low relief landscape to be characterized in terms of landforms and sedimentary body properties.

1. Introduction

Recent and ongoing tectonics can affect landscape-shaping processes and their resultant landforms at various scales (Keller and Pinter, 1996; Holbrook and Schumm, 1999; Schumm et al., 2002). However, the imprint of neotectonics is frequently obscured in low-relief environments by the sedimentary cover, hampering identification of the origin of different landforms (Ruszkiczay-Rüdiger et al., 2009). Tectonically influenced landscapes are usually identified by a series of geomorphological indicators, such as entrenched channels, a high degree of incision along the channels flowing across active faults, or a sudden change in channel morphology (e.g., Rhea, 1993; Schumm et al., 2002; Bishop et al., 2003; Riquelme et al., 2003; Silva et al., 2003). The Chobe Enclave, situated in northern Botswana, is bounded by the Chobe and Linyanti faults and has a generally flat topography (Fig. 1a-d). It has a variety of landforms, most notable of which are sand ridges, which have been previously interpreted as relict beach ridges of a former lacustrine environment (Shaw and Thomas, 1988; Burrough and Thomas, 2008). The significance of these sand ridges for palaeoenvironmental and palaeoclimatological reconstructions was outlined in the context of OSL-derived lake stage chronologies (Burrough and Thomas, 2008). A tectonic origin for the topographic variations along the ridges in the region was also mentioned (Gumbricht et al., 2001). While all of this work has brought improved understanding of the origin of the sand ridges in the

* Corresponding author.
E-mail address: thuto.mokatse@unil.ch (T. Mokatse).

https://doi.org/10.1016/j.geomorph.2022.108406
Received 13 April 2022; Received in revised form 11 August 2022; Accepted 12 August 2022
Available online 15 August 2022

Chobe Enclave, the details regarding the influence of tectonics on their development, and on the landscape evolution in general, have been largely ignored. Further, the way that the internal architecture of these sand ridges could have been affected by neotectonics (McFarlane and Eckardt, 2007; Nash and Eckardt, 2015; Eckardt et al., 2016) remains unclear. Therefore, there is a noticeable knowledge gap concerning the occurrence and impact of neotectonic activity in the Chobe Enclave. This is addressed in this work, which represents a case study for understanding the propagation of upper crust deformation in incipient rifting settings and the resultant effect on landforms.

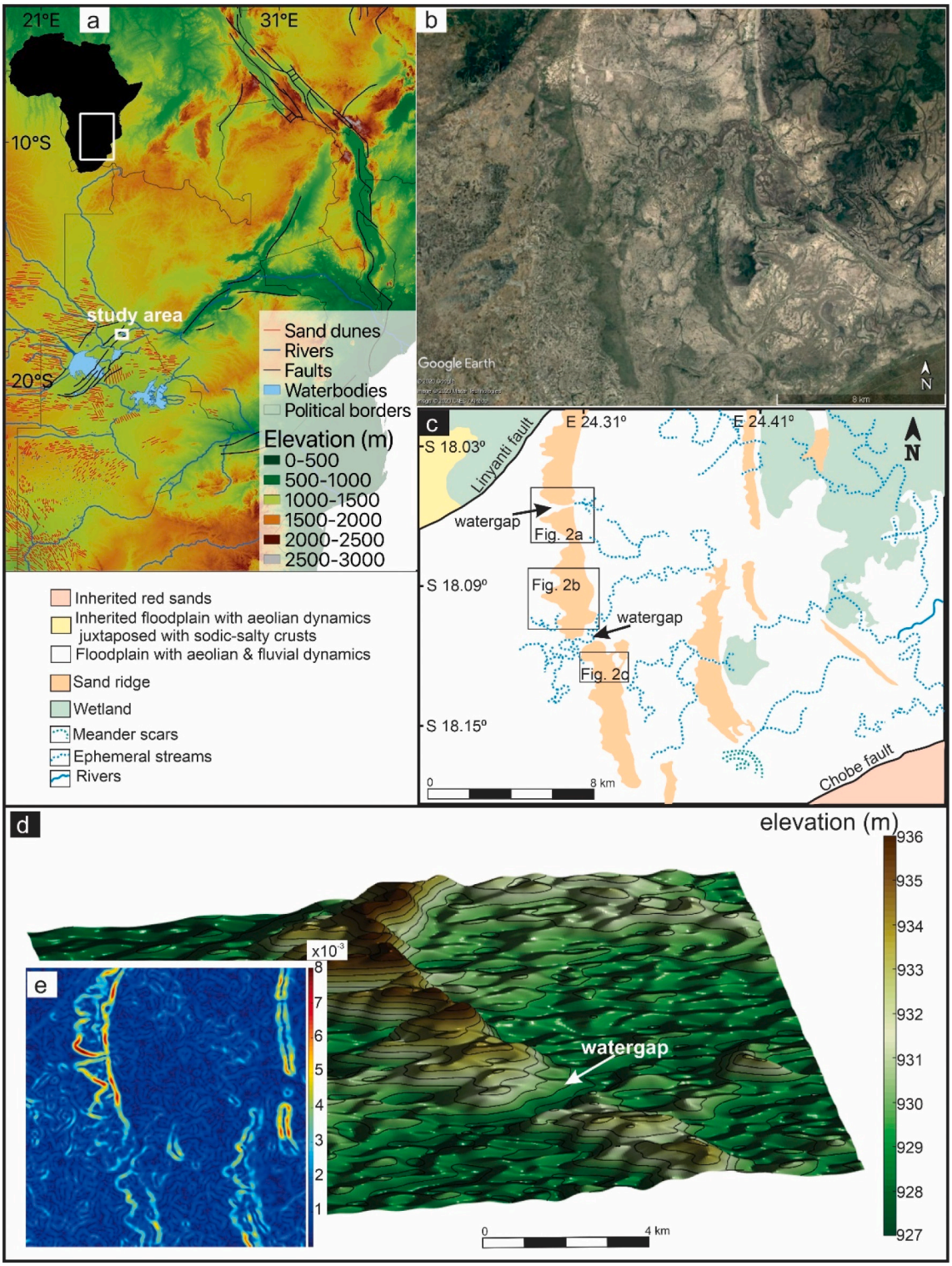

Fig. 1. (a) Main rivers, sand dune fields, and faults superimposed on the topography of southern Africa based on SRTM 30 s DEM (NASA JPL, 2013). Faults of the East African Rift System (EARS) are after Chorowicz (2005) and their possible extension to the Okavango Graben (OG) are modified from Kinabo et al. (2008). (b) Satellite image of the study area (Google Earth, 2020). (c) Geomorphological interpretation of the area depicting main landforms with localities of study sites mentioned in Fig. 2. (d) Digital elevation model of the studied sand ridge and adjacent floodplain constructed from Google Earth data. (e) Slope values of the western part of Fig. 1b and c.

In this study, we focus on the western-most sand ridge, which is the main geomorphological feature in the Chobe Enclave (Fig. 1c). We use a combination of near-surface geophysical surveys, optically-stimulated luminescence (OSL) dating, and sedimentological analyses to study the structure, lithostratigraphy, and chronology of this ridge. The main objectives of our work are: (i) to define the lateral and vertical distribution of sedimentary bodies and the boundaries of the various lithologies; (ii) to outline the possible presence of structures that could be related to neotectonic processes; and (iii) to document the influence of different deformational mechanisms. To this end, we conducted electrical resistivity tomography (ERT) and ground-penetrating radar (GPR) surveys over various parts of the ridge, where sediment samples were collected for OSL dating and sedimentological analyses. Together, these four methods provide highly complementary information for the characterization of Quaternary sediments (e.g., Aitken, 1998; Baines et al., 2002; Wisen et al., 2005; Bristow et al., 2005, 2007; Burrough and Thomas, 2008; Bristow, 2009). The establishment of a chronostratigraphical framework allows the temporal development of the inspected landforms to be drawn, ultimately gaining understanding about their evolution within the context of regional processes.

2. Geological setting

2.1. Structural context of the Chobe Enclave

On a regional scale, the Chobe Enclave is situated in the Middle Kalahari Basin, where several deformational mechanisms of different amplitude and temporal reoccurrence exist. Occupying the largest portion of the Intracratonic Kalahari Basin (Vainer et al., 2018), the Middle Kalahari is breached by the southwestward propagation of the more discretely deformed East African Rift System (EARS), and is considered to represent settings typical of incipient rifting (Fairhead and Girdler, 1969; Huntsman-Mapila et al., 2009; Kinabo et al., 2008; Fig. 1a). Based on the structures of the underlying mantle and crust, the Middle Kalahari is classified as a passive rift (Yu et al., 2015a, 2015b, 2017). The basin that overlies Proterozoic and Mesozoic rift structures (Dixey, 1956; Modisi et al., 2000; Doucouré and de Wit, 2003) is situated between elevated structural arches (Gumbricht et al., 2001). This led recent seismic tomography and magnetotelluric studies to suggest that deformation is triggered by inter-cratonic strains between the surrounding Archean cratons (Pastier et al., 2017; Yu et al., 2017). The differential deformation of the uplifted structural axes within the Kalahari Basin (Moore, 1999) resulted in the formation of several sub-basins, including the Makgadikgadi-Okavango-Zambezi basin (MOZB; McCarthy, 2013; Ringrose et al., 2005) of the Middle Kalahari, that was established in the early Pleistocene (Vainer et al., 2021a). The later segmentation of the MOZB into the current configuration that occupies the Chobe Enclave (Fig. 1b, c) is the result of Quaternary tectonics, which is assumed to be reflected in the sedimentary bodies that occupy this structural trough. Like the more developed basins in the EARS, grabens and half grabens provide space for sedimentation and the accumulation of waterbodies, whereas transfer zones link the depressed blocks and transport displacement strains between individual fault and basin segments (Gawthorpe and Hurst, 1993; McCarthy, 2013). Locally, the Chobe Enclave is bounded by the Linyanti (to the northwest) and the Chobe (to the southeast) faults (Fig. 1c), which breach the vast intracratonic Kalahari Basin to form this sub-basin within the high African plateau (Fig. 1a). Together with the Ngami and Mababe sub-basins, the Chobe Enclave comprises a syntectonic depocenter within the structural depression of the Okavango Graben (OG), which is the northern segment of the larger MOZB. This structural depression is made up of a series of NE-SW trending normal to dextral strike-slip faults (Modisi et al., 2000; Campbell et al., 2006; Bufford et al., 2012). The bounding faults of the OG on the southern part that extends into the Chobe Enclave were formed in an *en-echelon* pattern with a direction following the strike of the Precambrian basement structures (Mallick et al., 1981; Moorkamp et al., 2019). The OG has been associated with the formation of the southwestern branch of the EARS (Modisi et al., 2000; Alvarez Naranjo and Hogan, 2013). However, Pastier et al. (2017) argued that the tectonic structure of the OG better fits a transtensional basin model. Kinabo et al. (2008) coupled analysis of Shuttle Radar Topography Mission, Digital Elevation Model, and aeromagnetic data in the Chobe Enclave and revealed the development of soft linkage on segments of the Linyanti fault and evidence of a hard linkage forming between two *en-echelon* right-stepping segments of the Chobe fault.

2.2. Surficial geology and geomorphology of the Chobe Enclave

The Chobe Enclave was developed within the vast (10^6 km^2), elevated (~1000 m asl), erosional surface of the Central African Plateau, which was established by the Pliocene (Partridge, 1998; Burke and Gunnell, 2008; Daly et al., 2020) following discrete epeirogenic flexuring (Vainer et al., 2018, 2021a). Although later tectonic activity occurred, the general topography of the Chobe Enclave remains fairly flat. Even so, fluvial watergaps serve as notable geomorphological indicators in the Chobe Enclave and attribute for tectonic influence on the landscape, evidenced by incision across sand ridges (Fig. 1d). Two slopes are predominant in the area, one gently decreases from SW to NE, and the other from NW to SE, with a value of <0.02 % on average (Fig. 1e). This configuration promotes the existence of anastomosed fluvial systems, which are completely dry in the western part and become ephemeral to permanently flowing rivers to the east (Fig. 1b, c). The Chobe Enclave is mostly covered by unconsolidated sand that was introduced to the southern parts of the Kalahari approximately 2 Ma ago (Vainer et al., 2021b).

Cenozoic deposition of Kalahari Group sediments in the Chobe Enclave resulted in the accumulation of alluvial, lacustrine, fluvial, and aeolian deposits (Huntsman-Mapila et al., 2005; Podgorski et al., 2013). Sand ridges are the dominant landforms in the area (Mokatse et al., 2022), and are considered to represent late Quaternary paleolacustrine shorelines (Shaw and Thomas, 1988) formed under hydrological conditions different from the present-day (Grove, 1969; Cooke, 1980; Mallick et al., 1981; Shaw and Cooke, 1986; Shaw et al., 1988, 1997; Ringrose et al., 1999, 2005, 2009; Burrough and Thomas, 2008; Burrough et al., 2009; Moore et al., 2012). These ridges have been mostly studied in order to understand how they might relate to paleohydrological and paleoclimatological processes (Fig. 1c; Burrough et al., 2007; Burrough and Thomas, 2008).

The Chobe Enclave also includes carbonate deposits in an otherwise large siliceous-dominated basin. These deposits, which were described as palustrine limestones (Diaz et al., 2019), outcrop in the landscape as "*islands*" among the sands and are mostly observed in the central part of the Chobe Enclave, between the paleo-floodplain in the west and the large present-day floodplain in the east (Mokatse et al., 2022). These "islands" are also associated with diatomites in an unclear geometrical relationship, suggesting periods of wetter conditions and increased flows into the basin from the Chobe and Zambezi fluvial systems. Such paleo-flows likely contributed to the formation of lacustrine/palustrine deposits and were presumably developing during the surge of paleolakes witnessed in the south and the east of the Chobe Enclave by Burrough et al. (2009).

3. Methods

3.1. Site selection

This study focuses on the western-most north-south-trending sand ridge in the Chobe Enclave (Fig. 1c–e). Two key locations were targeted for data acquisition: (i) the sand ridge itself, to record morphological characteristics, which are critical to explain its origin and changes with time, and (ii) the sand ridge margins, which are pertinent to observe changes across the contact between the ridge and the floodplain.

3.2. Geophysical surveys

3.2.1. Electrical resistivity tomography (ERT)

ERT is an efficient and non-invasive geophysical technique that has been widely employed to image the spatial distribution of electrical resistivity in the shallow subsurface (e.g., Barber and Brown, 1984; Loke and Barker, 1996; Storz et al., 2000). In August 2020, a total of 6 ERT surveys were conducted in the study region (Fig. 2). Four of these surveys (ERT3, 4, 5 and 6) were at the sand ridge margins, where a transition from the fine sand of the ridge to the silt-rich sediments of the floodplain was recorded, whereas two surveys (ERT1 and 2) were acquired on the sand ridge itself. The latter two surveys represented regions where ERT imaging was possible on the sand ridge. In other locations, the highly resistive nature of the sand did not permit current flow into the ground, despite attempts to improve electrode coupling by watering with saline solution.

The ERT measurements were carried out using an IRIS Syscal Pro Switch 48-channel resistivity meter. The electrode spacing along the profiles was set to either 1 m or 2 m, and data were acquired using both the dipole-dipole and Wenner–Schlumberger electrode array configurations (Table 1). A Leica Geosystems differential GPS was used to measure the precise location and elevation of each electrode. Profiles ERT-1 and ERT-2, for which the line length exceeds the spacing times the number of available electrodes, were collected using a roll-along strategy. A pulse duration of 500 ms and a target of 50 mV for the potential readings were set as criteria for the current injection. For each resistivity quadripole, a total of four repeat measurements were performed in order to improve data quality and to help identify erroneous values.

Pre-processing of the ERT data was carried out using the Prosys II software and included deleting all resistance values where the relative standard deviation of the repeat quadripole measurements was >3 %, or where the measured electric potential had a value <5 mV. In order to prepare the data for the 2D inversion procedure, the precise x-y locations of each electrode were also projected onto a best-fitting straight line. To invert the measurements, the Boundless Electrical Resistivity Tomography (BERT) software package was employed (Günther and Rücker, 2019). The prior constraints placed on the resistivity model for the inversion were carefully evaluated and the same inversion settings were used for all of the apparent resistivity datasets. Specifically, we considered smooth (L2-norm) prior model constraints with the inversion parameter *zweight* set to 0.5 in order to reflect a balance between an isotropic (*zweight* = 1) and strongly layered (*zweight* = 0.1) resistivity distribution. Moreover, the regularization parameter *lambda,* which controls the balance between fitting the ERT measurements and respecting the prior smoothness constraints, was chosen to provide a normalized chi-squared data misfit approximately equal to one, in accordance with the assumed level of error on the potential measurements. Interpretation of the models was aided by lithological logs from pits acquired along the survey lines (Fig. 2).

3.2.2. Ground penetrating radar (GPR)

GPR allows the imaging of changes in electrical properties near the Earth's surface by recording the reflections of an emitted electromagnetic pulse from subsurface interfaces across which such properties change (Annan and Davis, 1992; Neal, 2004). Two GPR profiles were acquired at the study site (Fig. 2). Both were located on the sand ridge, where fine sand contributes to a highly electrically resistive environment which is ideally suited for GPR surveying. In contrast, at the sand ridge margins, the GPR method was not applicable because of the presence of silt-rich floodplain sediments, whose high electrical conductivity strongly attenuated the propagating GPR pulse.

The GPR data acquisition was carried out using a Mala ProEx system with 100 MHz rugged terrain antennas, which was connected to a GPS. The 100 MHz antennas allowed for a depth of penetration of approximately 12 m and were chosen because of their higher resolution compared to lower frequency antennas available for the same system (Neal, 2004). The spacing between the transmitter and receiver antennas was 2.2 m. Data were recorded using a 500 ns time window and each recorded trace was stacked 16 times in order to improve the signal-to-noise ratio (Table 2). Traces were acquired continuously while moving the antennas at an approximately constant speed, resulting in an average trace spacing along the profile of roughly 14 cm.

The GPR datasets were processed using the ReflexW software. The processing was rather standard and consisted of the following steps: (i) data binning to create an even trace spacing; (ii) "dewow" to remove the low-frequency transient upon which the GPR reflections are superimposed; (iii) time-zero adjustment to calibrate the data to the emission time of the transmitted pulse; (iv) application of a time-varying gain function to compensate for attenuation and the geometrical spreading of energy; (v) frequency-wavenumber migration (Stolt, 1978) using a constant velocity of 0.15 m/ns in order to collapse diffraction hyperbolae and to reposition reflectors to their correct positions in depth; and (vi) correction for topography along the profile.

3.3. Sample analyses

3.3.1. Pit sample analyses

Six pit sites were located along the ERT and GPR survey lines to provide a ground control of the lithology (Fig. 2). This is a pertinent way to contribute to a well-informed interpretation of the various lithologies and to the assessment of the spatial distribution of surficial sediments. The characterization of the pit sites was based on field observations and particle size distribution (PSD) analyses carried out on 35 samples. The PSD were obtained using a laser diffraction Beckmann Coulter LS 13320 on the <2 mm size fraction after leaching with 10 % hydrochloric acid. Samples were first classified under the Folk's (1954) classification scheme as general descriptors, and statistics calculated using the Folk and Ward formula (Folk and Ward, 1957). The processing of PSD data was conducted to confirm the differences between the various position of groups of samples from the sand ridge and its margins. This was done by using various modes of their PSD, which essentially aided to identify the origin of the sediments. The PSD curves were all plotted together in order to observe the overall variations of their shapes. Moreover, End-Member Mixing Analysis (EMMA) was performed based on the algorithm provided by Dietze et al. (2012) and run within the MATLAB computing environment. It was applied to all PSD curves to recognize the possible contributions of the various sedimentary sources. After identification of the end-members, each sample was described in terms of relative contribution of each end-member to its PSD. Sediments associated with a specific sedimentary process usually have a characteristic PSD referred as an end member. Essentially, the observed PSD can be considered as a result of a mixing process of a finite number of end members resulting in a complex spectrum. EMMA of sediment PSD demonstrates one way of discretizing the continuum of selective entrainment, transport, and deposition of sediments, providing deeper insights into the sedimentary environment and climatic conditions involved (Prins et al., 2002, 2007; Dietze et al., 2013a, 2013b; Schmidt et al., 2021).

3.3.2. Optically stimulated luminescence (OSL)

3.3.2.1. Sampling and preparation. One to two samples were collected from each pit to determine through OSL dating when the detrital material was last exposed to sunlight (Aitken, 1998). Sampling was completed using light-sealed tubes hammered into pit walls, at least 30 cm above the carbonate deposits, where present. Samples were then dry-sieved in subdued red-light conditions into the 180–212 μm size fraction. Quartz was isolated by dissolving carbonate and oxidizing organic matter with 10 % HCl and 30 % H_2O_2, respectively, and from other minerals by two-step heavy liquid separation using sodium polytungstate. The fraction with a density between 2.62 and 2.70 g cm^{-3} was

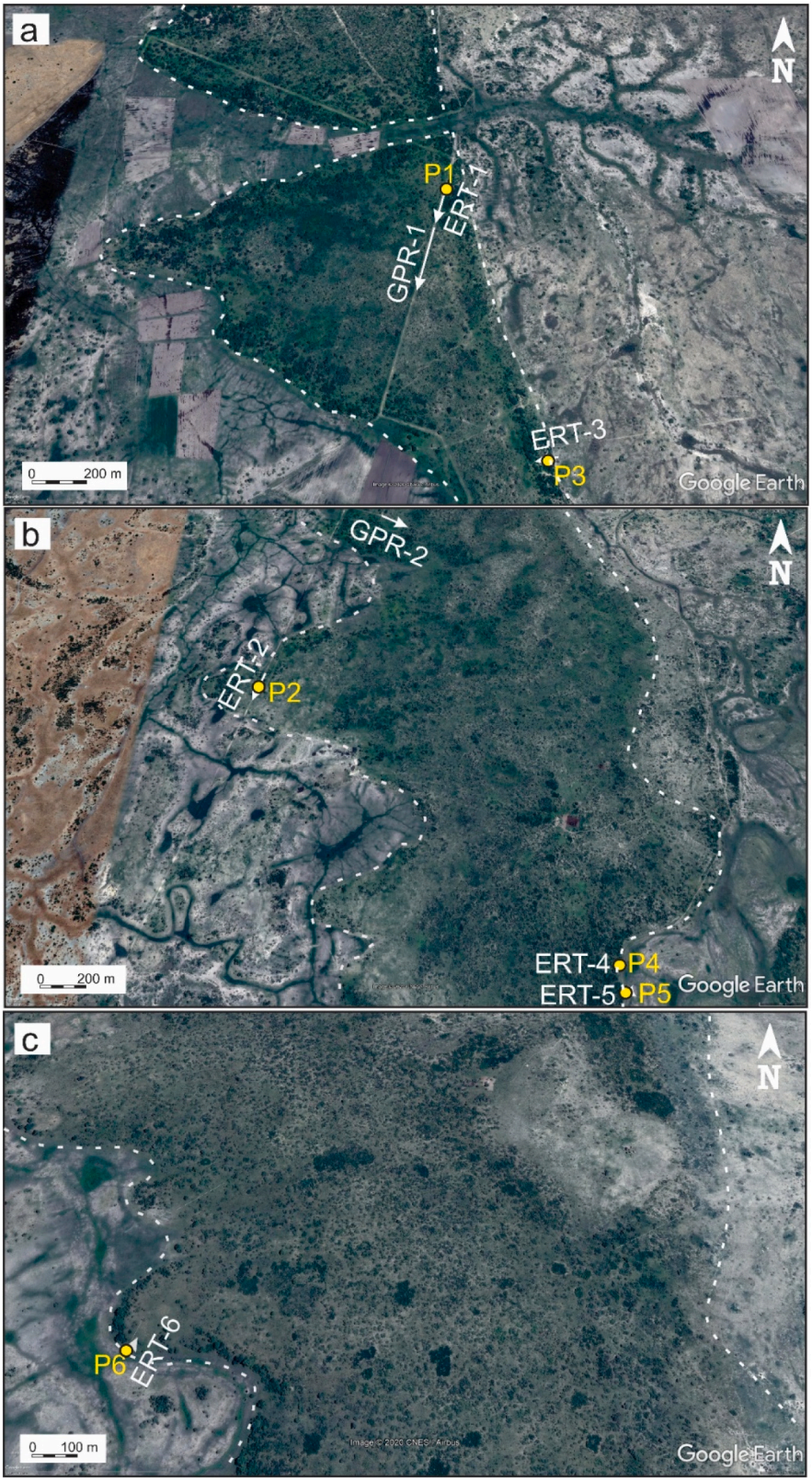

Fig. 2. Satellite images (Google Earth, 2020) showing the locations of ERT and GPR survey lines and corresponding pits (P). White arrows represent the direction and distance of geophysical surveys on the ground. White dashed lines represent the margins of the western-most sand ridge in the Chobe Enclave. The locations of images (a), (b) and (c) are shown in Fig. 1(c).

Table 1
Characteristics of the ERT profile lines considered in this study.

Profile line	Profile orientation	Profile length (m)	Number of electrodes	Electrode spacing (m)	Electrode array
ERT-1	NE–SW	214	48	2	Dipole-dipole & Wenner-Schlumberger
ERT-2	NE–SW	214	48	2	Dipole-dipole & Wenner-Schlumberger
ERT-3	E–W	94	48	2	Dipole-dipole & Wenner-Schlumberger
ERT-4	E–W	47	48	1	Dipole-dipole & Wenner-Schlumberger
ERT-5	E–W	47	48	1	Dipole-dipole & Wenner-Schlumberger
ERT-6	SW–NE	47	48	1	Dipole-dipole & Wenner-Schlumberger

etched for 40 min with 40 % HF and subsequently treated with 10 % HCl for dissolution of potential Ca-fluoride precipitates.

3.3.2.2. Equivalent dose estimation. Luminescence measurements were performed on a Risø TL/OSL-DA 20 instrument with a $^{90}Sr/^{90}Y$ β-source that delivers a dose rate of 0.144 Gy s^{-1} to quartz coarse grains on stainless steel discs (Risø calibration quartz batches 71, 90, and 113). OSL signals were stimulated by an array of blue (470 ± 5 nm) LEDs with a nominal power density of 36 mW cm^{-2} for 38 s and collected by an EMI 9235QB15 photomultiplier tube with a 7.5 mm Hoya U340 glass filter in front of it. To establish the dose response curve (DRC), signals were integrated over the first 0.7 s of the decay curve and a background averaged from the last 2 s was subtracted. The DRC was fitted with a single saturating exponential function and the equivalent dose (D_e) determined through interpolation using the Analyst software (v3.24; Duller, 2015).

Preparatory tests were performed to determine the most suitable measurement parameters for D_e determination (e.g., Kim et al., 2009). Thus, dose recovery and preheat plateau tests (DRT and PPT, respectively) were carried out on 15 aliquots from three samples collected at 1.05 m deep in Pit 1, 1.40 m deep in Pit 2, and 2.05 m deep in Pit 4 (Fig. 2), testing the temperature range between 180 and 260 °C at 20 °C increments. For the DRTs, the natural signal was bleached in a Hönle UVACube for 30 min and samples were given a β-dose in the range of the natural dose. In addition to multi-grain measurements on 1 mm aliquots, single-grain analyses of 500 grains were performed for samples collected at 1.05 m deep in Pit 1 and 2.05 m deep in Pit 4.

Equivalent doses were determined on 40 to 48 aliquots per sample by applying the single-aliquot regeneration method (SAR; Murray and Wintle, 2000). Aliquots were accepted for age calculation if the recycling ratio was in the range of 0.9–1.1, recuperation rate was <5 %, and a test dose signal error was <10 %. Furthermore, the IR-depletion ratio test (Mauz and Lang, 2004) was applied to all measurements to assure the purity of quartz. For samples that displayed a scattered D_e distribution or considerable percentage of rejected aliquots, an additional set of 24 or 48 aliquots was measured to ensure a statistically valid dose determination. The central age model (CAM; Galbraith et al., 1999) and minimum age model (MAM; Galbraith et al., 1999) were applied to all accepted D_e values via the R-package 'Luminescence' v0.9.10 (Kreutzer et al., 2012; R Core Team, 2021). The model parameter representing the overdispersion (σ_b) was estimated from the DRT.

3.3.2.3. Dose rate estimation. Present day water content was determined based on weight loss after drying samples at 40 °C and carbonate content was determined based on weight loss after dissolution in 10 % HCl. As of our understanding of the depositional environments, current moisture content does not reflect a representative value for the burial period, thus a higher water content of 10 ± 3 % was assigned to represent a former palustrine-lacustrine environment (Diaz et al., 2019).

The concentrations of U, Th and K were determined at Actlabs (Canada) via fusion inductively coupled plasma mass spectrometry (FUS-ICP-MS; Table 2). Current sample depth was considered to estimate the cosmic dose rate. The overall dose rates and luminescence ages were calculated with DRAC (v1.2; Durcan et al., 2015) using conversion factors from Guérin et al. (2011), α-attenuation factors from Brennan et al. (1991) and β-attenuation factors from Guérin et al. (2012).

4. Results

4.1. Lithological observations and particle-size distributions

Pits 1 and 2 are located on sand ridges, whereas Pits 3, 4, 5, and 6 on their margins (Fig. 2). The compilation of data from these localities is crucial for the understanding of the long-term development of the geomorphological features as well as to observe the temporal field relationships between the ridges and their surroundings (Fig. 3a, b).

The lithological logs are generalized to the dominant lithology and show a succession from silt-rich to sand-rich sediments, interbedded with sandy carbonate (Fig. 3a). Pit 1 (2.27 m deep) consists of a sandy carbonate layer of ~47 cm thickness appearing between two fine sand units, whereas Pit 2 (with a maximum depth of 1.30 m) consists of fine sands overlying a sandy carbonate layer. This pit is situated at the highest elevation, i.e., ~941 m. At Pit 3 (1.68 m deep), a sandy carbonate bed is overlain by fine sands. Sample H5P3 (Fig. 3a) contained amorphous siliceous aggregates and was not included in the end-member analysis to avoid inaccurate interpretation of the results. Pit 4 (2.2 m deep) and Pit 5 (2.18 m deep) are dominated by fine sands. Lastly, Pit 6 is positioned at the lowest elevation of ~935 m with a depth of 2 m and is dominated by fine sands in contact with silt-rich sediments at its bottom.

EMMA processing allowed four statistical sedimentary contributors (labeled EM1, 2, 3, and 4) to be identified (Fig. 4). The EM1 curve has a leptokurtic shape with a single mode in the sand fraction at 120 μm, corresponding to a very well sorted sand. In EM2, two distinct maxima are observed with a mode at 120 μm and the other at 250 μm, showing a mixing association of two sandy compartments. The EM3 curve displays a leptokurtic shape with a mode at 250 μm, emphasizing a very well sorted sand. Finally, EM4 has a leptokurtic shape with a mode at 250 μm and a minor platykurtic distribution centered in the silt fraction, around 15 μm (Fig. 4a). The weight of the distinctive EMs in each PSD allowed groups of samples to be sorted, underlying the prominent role of the sandy fractions, except when EM4 is present in a large proportion.

The sand ridge (Pits 1 and 2) is mainly characterized by EM2 in the bottom part, whereas the upper parts are comprised of EM1, EM3 and EM4 (Fig. 4b). This transition is clearly evident only on the sand ridge. On the other hand, the sand ridge margins are characterized by two

Table 2
Characteristics of the GPR profile lines considered in this study.

Profile line	Profile orientation	Profile length (m)	Time window (ns)	Number of stacks	Antennae separation (m)	Traces	Antenna frequency (MHz)
GPR-1	NE–SW	200	500	16	2.2	1697	100
GPR-2	NW–SE	220	500	16	2.2	1535	100

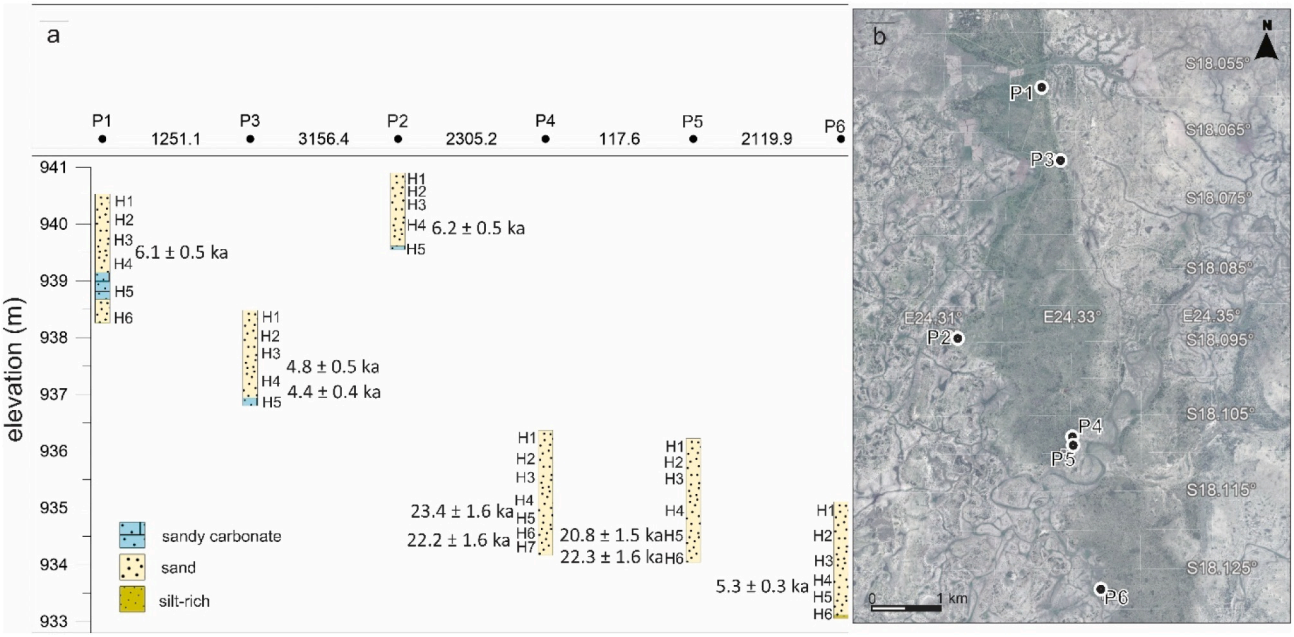

Fig. 3. (a) Lithological logs and corresponding OSL ages: classes are generalized from the particle size distribution analysis using the classification scheme by Folk (1954). Pit sites are denoted by P1 to P6. H1 to H6 refer to sample positions in each pit. Along the horizontal axis, figures between the pit numbers (P1 to P6) refer to the distance (in metres) between two successive pits from north to south. The y-axis refers to the altitude (in metres) at the top of the pit. (b) Locations of the pits referred to in (a). See also Fig. 2.

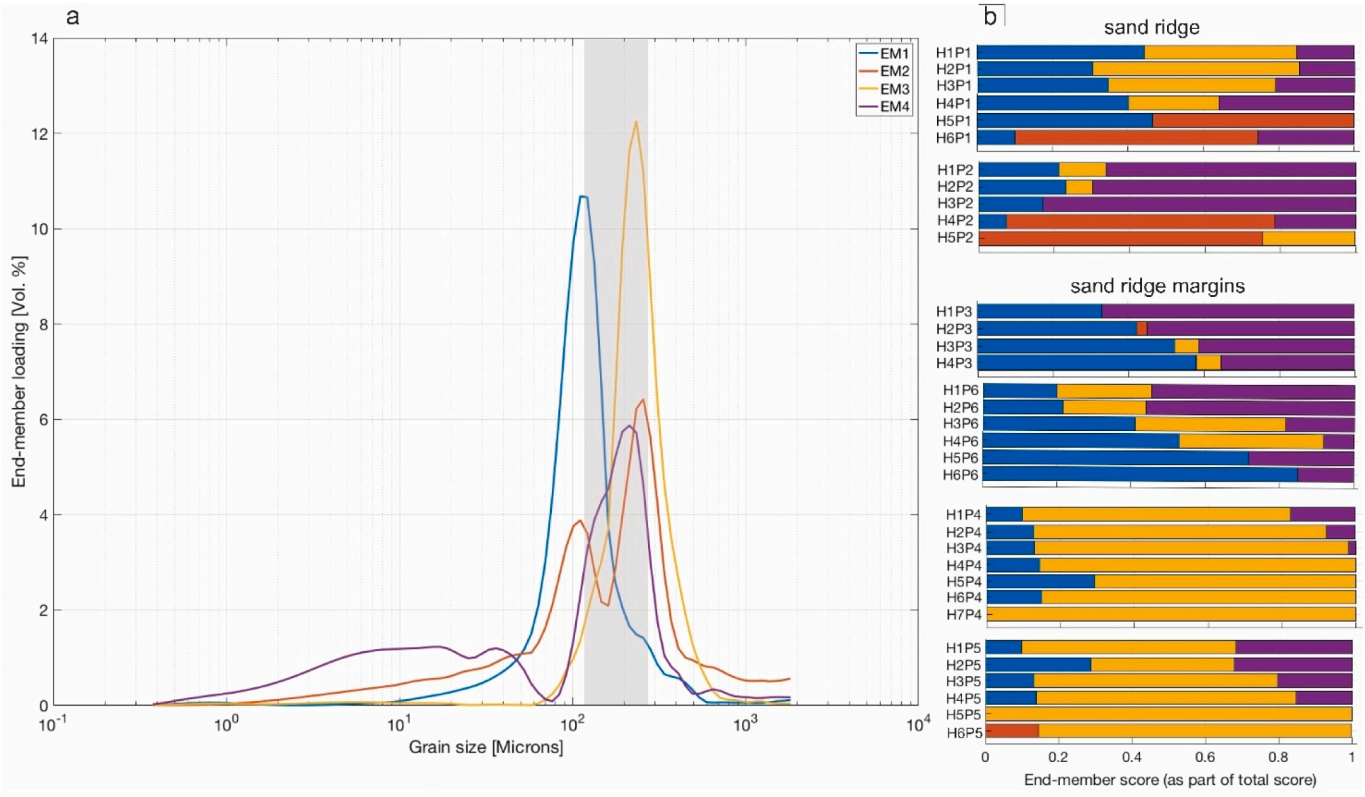

Fig. 4. (a) PSD plot of end-members determined via End-Member Mixing Analysis (EMMA). The Kalahari sand mode is displayed as a shaded area centred on 200 μm. (b) Bar chart of the end-member contributions to each sample.

distinct patterns. The first pattern, recognized in Pits 4 and 5, is dominated by EM3 and a minor contribution of EM1 and EM4 (Fig. 4b). EM3 represents very well sorted sand. The second pattern, observed in Pits 3 and 6, is mostly EM1 and EM4 with minor EM3 (Fig. 4a). Furthermore, the transition in all sites is prominent, as the EMMA results (Fig. 4b) display a clear picture of evolution of the PSD for each site, from the sand ridge to its margins. This is an equally important step in emphasizing how end-members successfully characterize the variability of the

curves (Fig. 4), ultimately giving insight into possible sedimentary sources across the region.

4.2. Electrical resistivity tomography (ERT) profiles

All the ERT inversion results presented in this work correspond to the dipole-dipole electrode array configuration, which has improved lateral resolution characteristics compared to the Wenner-Schlumberger configuration (Loke, 2004). This made it easier in our interpretations to define the lateral distribution of sedimentary bodies.

4.2.1. Sand ridge

Profile ERT-1 is 214-m long and was acquired along the sand ridge in a NE–SW direction (Fig. 2a). The ERT inversion results for this profile (Fig. 5a) show a near-surface layer having increasing thickness towards the SW, whose resistivity values range between 200 and 4000 Ωm. This layer corresponds to moderately sorted fine sands observed in Pit 1 (Fig. 3a), where variations in resistivity are likely controlled by the amount of silt present. Below these fine sands, the resistivity values along the profile are seen to decrease (<100 Ωm), which we interpret as indicating a transition from fine sand to silt-rich floodplain deposits. Within these deposits, zones of increased resistivity can be observed on the left-hand side of the profile, which may represent paleo-channels consisting of fine sand. These channels are located between approximately 8 and 20 m depth.

Profile ERT-2 was acquired across the sand ridge in a NE–SW direction (Fig. 2b). Similarly, the corresponding ERT inversion results (Fig. 5b) show a relatively resistive layer at the top overlying a dominant conductive layer of values <100 Ωm. However, the upper layer is discontinuous with the middle section showing zones we interpret as paleo-channels closer to the surface. Our interpretation of this profile (Fig. 5b) shows a fine sand layer overlying silt-rich floodplain deposits, with an eroded surface from 30 to 112 m. Paleo-channels can be identified within the floodplain at a depth of approximately 2 to 5 m.

4.2.2. Sand ridge margins

The sand ridge margins correspond to a transition between the floodplain and the sand ridge. Profile ERT-3 is situated on the eastern margin of the sand ridge in the southern part of the study area (Fig. 2a). The corresponding ERT inversion results (Fig. 6a) show a more resistive layer at the surface from approximately 30 m onwards, whose thickness increases towards the west. This layer has been identified as fine sand in Pit 3 (Fig. 3a). Below the fine sand, is a section dominated by a conductive layer of values ~20 to ~100 Ωm, corresponding to the silt-rich sediments of the floodplain. Within this conductive floodplain, a relatively resistive feature is displayed and interpreted as a paleo-channel. Profile ERT-4 crosses the sand ridge margin from N to S (Fig. 2b). Here, the ERT inversion results (Fig. 6b) again show a resistive upper layer, representing fine sand, overlying a more conductive layer corresponding to silt-rich sediments observed in Pit 4 (Fig. 3a). Likewise,

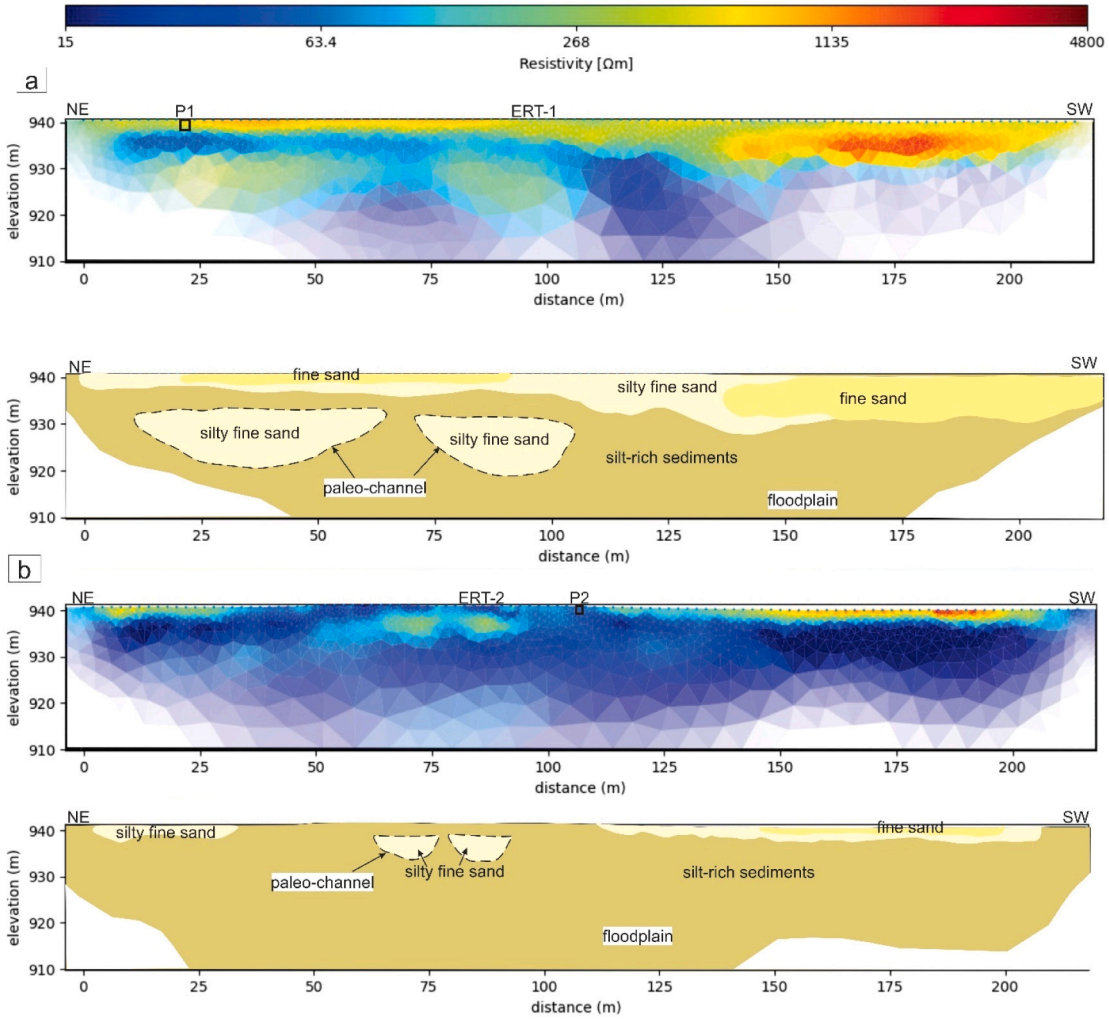

Fig. 5. Dipole-dipole ERT profiles (a) ERT-1, and (b) ERT-2, which were acquired along the sand ridge (Fig. 2). Shown are the inversion results and their interpretations based on the observed resistivity values and sedimentological data.

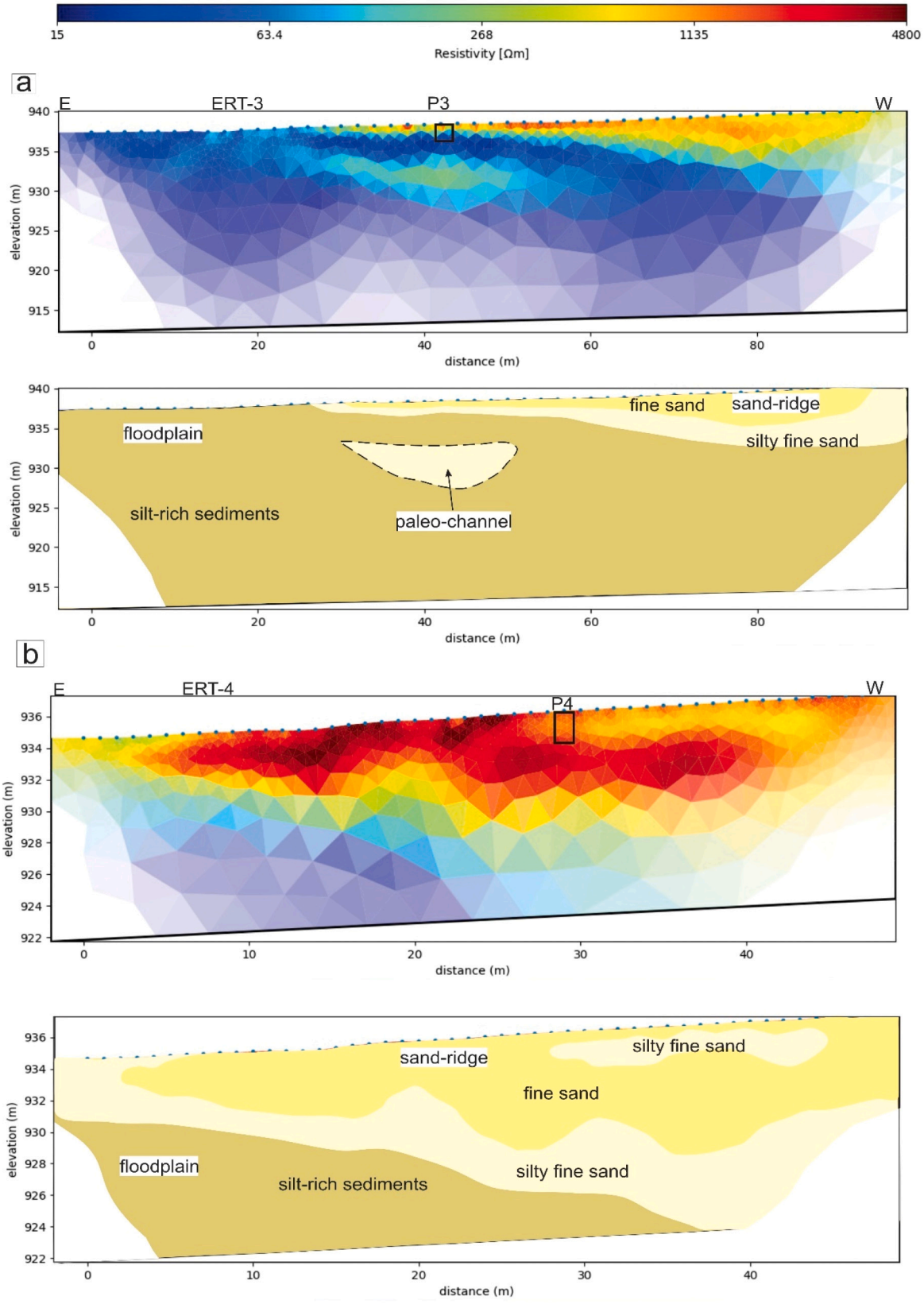

Fig. 6. Dipole-dipole ERT profiles (a) ERT-3 and (b) ERT-4 across sand ridge margins (Fig. 2). Shown are the inversion results and their interpretations based on the observed resistivity values and sedimentological data.

Profile ERT-5 runs across a sand ridge margin dominated by a resistive layer (>200 Ωm) from 20 to 47 m, which corresponds to fine sand in Pit 5 (Fig. 3a). The fine sand is underlain by a more conductive layer (<70 Ωm) representing silt-rich sediments of the floodplain. Finally, profile ERT-6 (Fig. 2c) runs along the N–S trending sand ridge margin in the southern part of the study area. The ERT inversion results (Fig. 7b) show consistency with previously presented data having a more resistive upper layer with values >600 Ωm (fine sand), and a relatively conductive lower layer (<60 Ωm) corresponding to silt-rich sediments of the floodplain below Pit 6 (Fig. 3a). It is important to note that the conductivity will vary depending on the moisture or clay content of the floodplain sediments.

4.3. Ground-penetrating radar (GPR) profiles

Profile GPR-1 is 200-m long and was acquired along the sand ridge in a NE–SW direction (Fig. 2a). The GPR results (Fig. 8a) show two continuous reflectors at approximately 2 to 4 m depth. The upper reflector terminates on the lower one, revealing the internal structure and relative chronology (Bristow and Jol, 2003) within the ridge. Profile GPR-2 is 220-m long and was acquired along the sand ridge in a NW–SE direction (Fig. 2b). Similarly, the GPR results (Fig. 8b) show two continuous reflectors running subparallel to the ground surface, each occurring between depths of ~2 to ~4 m and ~6 to ~8 m. The lower reflector occurs closer to the boundary of high signal attenuation hence appearing less continuous. Diffraction hyperbolae appearing on both profiles at an apparent depth of ~7 to 10 m are caused by trees along the survey line. The maximum GPR penetration depth along these profiles is approximately 12 m.

The Chobe Enclave sand ridges are thus characterized by prominent continuous reflectors consistent throughout the area with varying thickness, whereas the surrounding floodplains show high signal attenuation because of their increased fine sediments and/or moisture content. The interpreted models (Fig. 8a, b) emphasize some continuous bounding surfaces, characterized by continuous reflectors along the sand ridge, and a transition zone, defined by a boundary of high signal attenuation. Generally, this is consistent with the ERT inversion results showing a transition between the resistive sand ridge and the conductive silt-rich floodplain.

4.4. Optically stimulated luminescence (OSL) results

All processed samples were dry with <0.5 % water content (except for OP5-103 with <2 % water) and contained neglectable amount of carbonate and feldspar (Table 3). Preheat plateau tests (PPT) imply that a preheat temperature of 200 °C is collectively best suited for all samples (Fig. 9); this temperature along with a cut heat to 200 °C was utilized during D_e measurements. Dose recovery tests (DRT) carried out with this preheat temperature resulted in dose reproducibility within 4 %, 2 %, and 1 % for samples OP1-105, OP2-140, and OP4-205, respectively. D_e values from single-grain measurements are indistinguishable (within error) for sample OP1-105 and higher by 4 % for sample OP4-205 than the multi-grain D_e (Fig. 9). Central age model (CAM) and minimum age model (MAM) results in pits 2, 4, and 6 agree within 1σ uncertainty. In pits 1, 3, and 5, over 40 % of variance subsists between CAM and MAM, and CAM ages are presented (Table 3).

The effects of inter-grain variability in the degree of bleaching, β micro-dosimetry effects, bioturbation, and grain-to-grain differences in OSL characteristics for an analogous set of samples were discussed in Burrough et al. (2009). These authors concluded that the most suitable age model for this type of sediment is the CAM. They also estimated the internal activities of ^{238}U, ^{232}Th, and ^{40}K within the quartz grains, showing that the internal α- and β-dose would not push the age estimates outside of the assigned 1σ uncertainties and would not affect age clusters calculated subsequently. Therefore, CAM ages were calculated based on the dose rate estimated from the radioelement concentrations measured within bulk samples and the corresponding cosmic dose. The resultant ages are in stratigraphic order within 1σ uncertainties and are clustered into two age groups that range between 23.4 ka and 20.8 ka and between 6.2 ka and 4.4 ka. The older age group is found between 2.1 m and 1.7 m depths in pits 4 and 6 while in pits 1, 2, 3, and 5, where maximal sampling depth is 1.4 m, samples display a Holocene age.

5. Discussion

5.1. Geometry and internal structures of landforms

5.1.1. The sand ridge

The remnant asymmetrical and linear morphology of sand ridges in the Chobe Enclave remains sparsely vegetated with elevations reaching as high as 936 m (Fig. 1d). Secondly, the eastern margins of individual ridges show a sharp linear contact with the floodplain, whereas their western margins display typical *en-chevron* shapes (Fig. 2). This geometry is the consequence of sheetwash erosion on slopes of asymmetrical structural reliefs in arid and semiarid zones (Parsons and Abrahams, 2009), the longest slope dipping into the direction of the open *en-chevron V*-shape (Fig. 1). Nevertheless, some steep slopes enclose these geomorphological features (Fig. 1e), emphasizing some inheritance: indeed, the sand-ridge appears as a fossil relief, shaped in a different environment than at present, in order to get the *en-chevron* morphology. Today, however, erosion seems to equally affect both sides of the ridge (Fig. 1d). Moreover, the Chobe Enclave sand ridges have been formerly reported as floodplain beach ridges that were emplaced synchronously with Lake Thamalakane phases (Burrough and Thomas, 2008). Typically, beach ridges refer to stabilized, aeolian, relict wave-built shoreline features, which may consist of either siliciclastic or calcareous clastic material. Before they were stabilized, they would either have a regressive or transgressive history (Otvos, 2000). On the other hand, the internal structure of sand ridges from GPR profiles indicates the presence of bounding surfaces (Fig. 8), emphasized by continuous sub-horizontal reflectors. These internal structures suggest the past occurrence of *different depositional events within the ridges*. The processed GPR reflection data allowed the internal structure of the sand ridge to be observed to a depth of 8 m and prominent radar surfaces were identified as continuous bounding surface (*cbs*). Below these features, there is a boundary of high signal attenuation, indicating a finer conductive unit below or a zone of higher moisture content. This latter could represent the floodplain deposits or finer sediments with higher moisture content. The *cbs* correspond to possible *erosional bounding surfaces* and are characterized by continuous sub-horizontal reflectors along the sand ridge. From the above evidence, the internal structure of the sand ridge likely relates to a transition zone from the upper dry sand with erosional surfaces to lower floodplain deposits/finer sediments with high moisture content. Consequently, the erosional bounding surfaces observed in the deep parts of the sand ridge could originate either from a lacustrine (associated to shore erosion due to paleo-lakes) or an aeolian environment, or a result of both.

Furthermore, there are different sedimentary sources identified corresponding to specific origins found in the landscape of the Chobe Enclave from the interpretation of the EMMA of the PSD data. The main sedimentary sources from different bodies can be mixed in various proportions (Van Thuyne et al., 2021). Results from the *sand ridge and its margins* show similar groups of grain size contributors, but with distinct variations individually. The Kalahari sands constitute the prominent sedimentary source, characterized by the modes centered around 200 μm (Mokatse et al., 2022 and references therein) and corresponding to EM3 (Fig. 4a, b). This source has endured different phases of erosion and reworking with different proportions observed across study sites (Fig. 4b). Another depositional phase of the Kalahari sand is noted on the sand ridge margins, where two age clusters are observed (Fig. 4b). The first one shows the presence of the Kalahari sand, dominant in Pits 4 and 5 and represented by EM3, with ages ranging from 23.4 to 20.8 ka. The

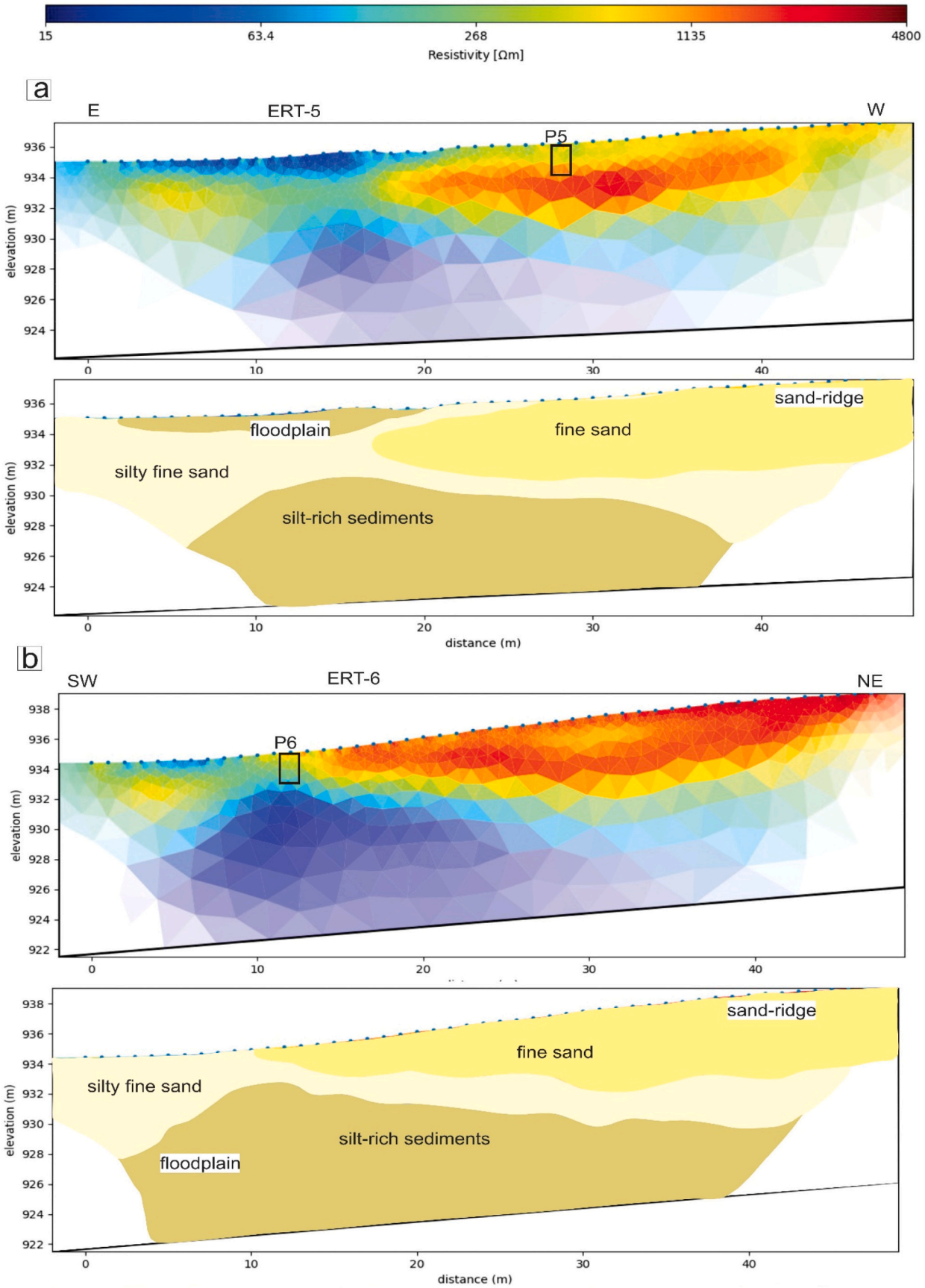

Fig. 7. Dipole-dipole ERT profiles (a) ERT-5 and (b) ERT-6 across sand ridge margins (Fig. 2). Shown are the inversion results and their interpretations based on the observed resistivity values and sedimentological data.

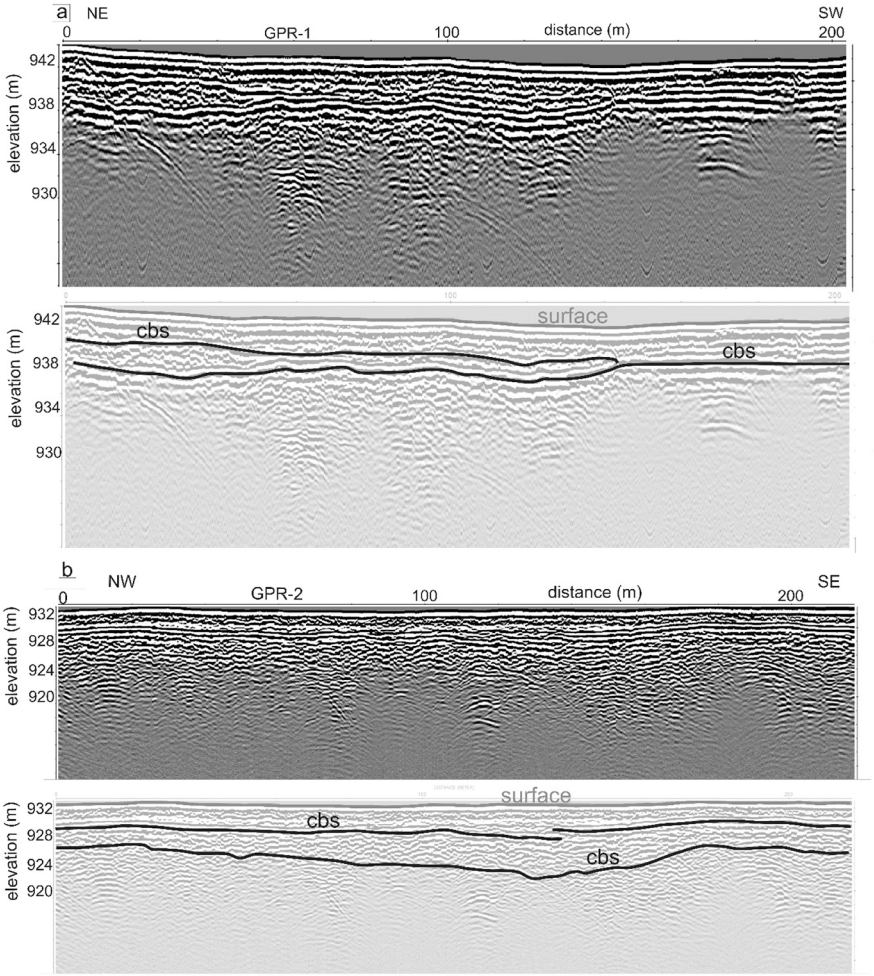

Fig. 8. GPR profiles (a) GPR-1, and (b) GPR-2, which were acquired along the sand ridge (Fig. 2). Shown are the processed 100-MHz reflection data and their interpretations. (cbs = continuous bounding surface).

second cluster shows a larger contribution of EM1 and EM4 with ages ranging from 5.3 to 4.4 ka. The sediments from these sites include a proportion of reworked Kalahari sands, desert loess, and a diatomite mud fraction (Van Thuyne et al., 2021). EM4 displays the platykurtic curve of diatomite mud with the influence of a desert loess fraction. The last depositional phase observed occurred on the sand ridge, displaying the onset of EM2 at the bottom, and contribution of EM1 and EM4 at the top (Fig. 4b). It is evident that EM2 is particularly distinct on the sand ridge with ages ranging from 6.2 to 6.1 ka. The occurrence of EM2 on the sand ridge marks the deposition of reworked material of EM3 and EM1. The sand ridge and its margins compose of a mixture of one or more grain size signatures, each corresponding to a specific source. Consequently, it is revealed that the Kalahari sands (EM3) constitute the parental material of the coarse fraction dominating on the sand ridge margins. On the other hand, the sand ridge margins show a transition to a dominant presence of fine sand (EM1) and diatomite mud (EM4). Lastly, a mixture of Kalahari sands and fine sand demonstrated by EM2 thrives on sand ridges with an increased reworking of Kalahari sand, diatomite mud, and fine sand on the upper portions of the ridges.

5.1.2. *The floodplain*

The spatial distribution of the various lithologies was assessed using ERT, which showed the presence of resistive units within floodplain deposits that we interpret as evidence of *paleo-channels* (Figs. 5 to 7). Indeed, these features likely correspond to silty fine sand bodies within the conductive silt-rich floodplain sediments. Most of the Chobe Enclave landscape is occupied by the floodplain undergoing aeolian and fluvial dynamics (Mokatse et al., 2022), and its extent limits are bounded by the Chobe and Linyanti faults. However, the sand ridge overlying the floodplain deposits displays quite astonishing features on its margins with the floodplain. These are the sharp linear contact on eastern margins and *en-chevron* patterns on the western margins. Moreover, one key feature is the antecedent drainage pattern cutting through the sand ridges (a watergap), an identification of a tectonically controlled geomorphological feature.

5.2. *The suspected role of neotectonic activity*

The present-day entrenched and anastomosed fluvial system (Fig. 1b, c) suggests that fluvial deflection in the Chobe is controlled by epeirogenic movements (Holbrook and Schumm, 1999). Indeed, the deflection of channels into the sagging basin, that is illustrated to have happened in the past by the presence of the paleo-channels revealed in this work, implies subsidence within the flanking structural highs. As it typically occurs in low-relief areas that experience a discrete topographical disturbance, deflection of a river during an uplift or into a zone of subsidence will manifest as an abrupt shift in the river course coincident with the deformed zone (Holbrook and Schumm, 1999). This is observed in the Chobe Enclave, where *fluvial watergaps* cut through sand ridges (Fig. 1b, c). Such features, observed at lower elevations are typical geomorphological indicators that usually attributes for a neotectonically influenced landscape (Clark, 1989). Furthermore, the *en-chevron* morphology displayed on the western margins and sharp linear contact on the eastern margins of the sand ridge in the Chobe Enclave are similar

Table 3
OSL ages of the studied samples, based on the central age model (CAM).

Sample	Pit no	Depth [cm]	Accepted/ measured aliquots	K [wt %]	1σ	Th [ppm]	1σ	U [ppm]	1σ	$CaCO_3$ [wt%]	Measured H_2O [wt%]	Estimated H_2O [wt%]	1σ	Dose rate [Gy ka^{-1}]	1σ	D_e [Gy]	1σ	Overdispersion [%]	1σ	Age [ka]	1σ
OP1-105	P1	105	35/35	0.06	0.01	0.6	0.08	0.4	0.02	1.6	0.1	10	3	0.372	0.022	2.26	0.13	35	4	6.1	0.5
OP2-140	P6	140	46/46	0.07	0.01	1.0	0.14	0.3	0.02	0.0	0.1	10	3	0.377	0.022	2.00	0.03	9	1	5.3	0.3
OP3-105	P3	105	78/94	0.09	0.01	0.8	0.11	0.3	0.02	1.2	0.3	10	3	0.390	0.022	1.89	0.15	66	6	4.8	0.5
OP3-120	P3	120	73/81	0.09	0.01	0.8	0.11	0.3	0.02	5.1	0.5	10	3	0.387	0.022	1.69	0.13	70	6	4.4	0.4
OP4-185	P4	185	43/47	0.06	0.01	0.6	0.08	0.2	0.01	0.0	0.0	10	3	0.314	0.020	7.35	0.18	15	2	23.4	1.6
OP4-205	P4	205	48/48	0.02	0.00	0.3	0.04	0.2	0.01	0.0	0.0	10	3	0.256	0.018	5.67	0.12	14	2	22.2	1.6
OP5-103	P2	103	43/48	0.13	0.02	0.8	0.11	0.2	0.01	1.8	1.7	10	3	0.406	0.025	2.50	0.14	35	4	6.2	0.5
OP6-170	P5	170	65/70	0.03	0.00	0.4	0.06	0.2	0.01	0.0	0.0	10	3	0.278	0.019	5.78	0.12	19	2	20.8	1.5
OP6-210	P5	210	58/72	0.03	0.00	0.4	0.06	0.2	0.01	0.0	0.0	10	3	0.270	0.019	6.02	0.15	20	2	22.3	1.6

features to those observed on the Magikwe ridge (Burrough and Thomas, 2008, their Fig. 2) in the tilted Mababe basin (Gumbricht et al., 2001), with both Magikwe ridge and the Chobe Enclave sand ridge being incised by *fluvial watergaps*. Although small-scale neotectonic activity is not easily visible, GPR imaging of the subsurface and OSL dating of the sand ridges and sand ridge margins suggest some tectonic uplift. The resultant ages showed two clusters corresponding to the sand ridges and sand ridge margins, respectively. On the sand ridges, Pits 1 and 2 display consistent ages between 6.1 ± 0.5 and 6.2 ± 0.5 ka (Fig. 3a), whereas on the sand ridge margins there are two recognizable age sub-clusters. The first cluster observed in Pits 4 and 5 provides late Pleistocene ages from 20.8 ± 1.5 to 23.4 ± 1.6 ka and the second, in Pits 3 and 6, Holocene ages from 4.4 ± 0.4 to 5.3 ± 0.3 ka (Fig. 3a). In addition, the syndepositional uplift of the ridge is further evidenced by the presence of erosional bounding surfaces. Geochronology of the sand ridge and sand ridge margins is further supported by the PSD curves using end-member contributions (Fig. 4a). Specifically, on the sand ridge, which is evidently dominated by the contribution of EM2, it is the only site with this signature. This observation possibly links the onset of EM2 on the sand ridge with the syndepositional uplift event. These observations must reflect the deformation caused by epeirogenic movements acting on the low relief landscape of the Chobe Enclave at the time. Indeed, the topographic positions of studied pits and their corresponding sedimentary signatures show evidence of variability of sediments because of erosion. The sedimentary signatures from end-member contributions in the PSD support this as well, due to the reworking of sediments. This strongly suggests that an erosional phase could have been triggered by a possible neotectonic activity, the latter providing some relief potential for sediment reworking and erosion in this otherwise very flat topography.

The development of the large-scale Chobe Enclave landscape is hypothesized to have begun with high displacement rate along the Chobe fault (Alvarez Naranjo, 2016). The Chobe fault is considered as the main border fault of the Okavango Graben; its nucleation points on the surface and its propagation direction along strike is NE–SW (Kinabo et al., 2008; Alvarez Naranjo, 2016). This configuration (zone of high displacement) resulted in a depocenter forming the Chobe-Linyanti sub-basin (Kinabo et al., 2007), where the formation of sharp linear eastern margin of the sand ridge indicative of wet (lake shoreline?) conditions likely began because of the subsidence of the Chobe fault hanging wall (Fig. 10). At this time, the subsidence of the Chobe fault hanging wall resulted in burial of a distributary channel system, observed as paleo-channels in this study. Evidence for fault segments linkage of Linyanti fault confirms its development (Kinabo et al., 2008), this resulting in uplift of the footwall and erosion. This ultimately triggers the erosion on the western margins of the sand ridge found in the Chobe Enclave and giving rise to the development of the current landscape.

5.3. Evolution of depositional environments and Chobe Enclave's landscape

The Middle Kalahari paleolake system has been a major component for understanding late Quaternary climate and hydrological dynamics. The existence of a megalake system was proposed due to a consistency in ridge altitudes within basins of this system, with major lake highstands identified from OSL dating (Burrough et al., 2009, their Fig. 4). According to Burrough et al. (2009), the paleolacustrine environment gave rise to paleolake shorelines common to the western margins of the basins. The 'wave-built' shorelines on the western margins of paleolake Makgadikgadi are considered to be constructed by an easterly wind component of the climate system. However, it is first necessary to state that the landscape formation of the Chobe Enclave occurred in an environment situated between two faults (Linyanti and Chobe), where linkages between fault segments have prevailed and proven to exert profound influence on development of neotectonics and fluvial activities. Consequently, the drainage patterns of the fluvial systems in the

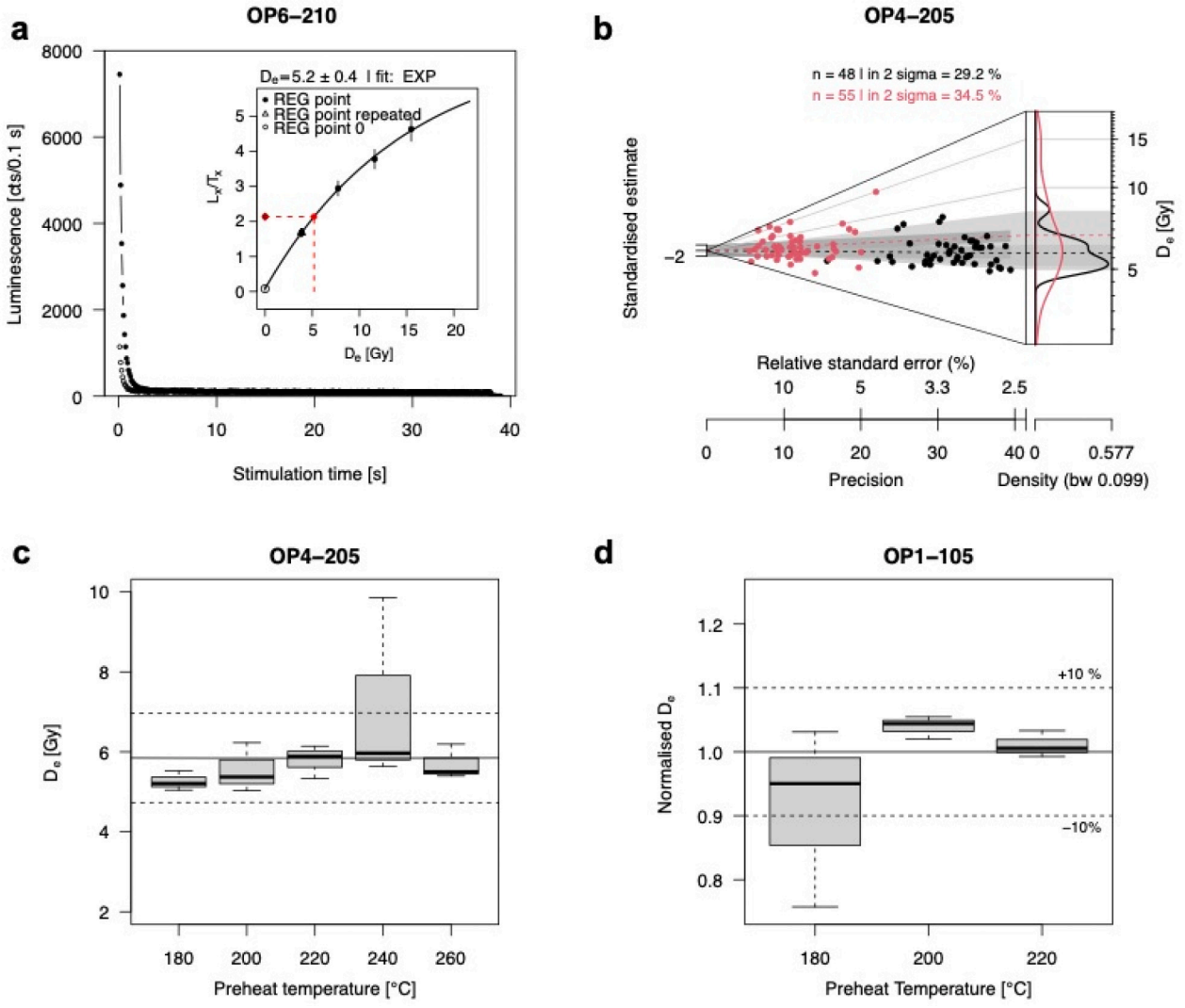

Fig. 9. Luminescence characteristics of the analysed quartz samples from the Chobe enclave. (a) OSL decay curves of one aliquot of sample OP6-210. Solid symbols denote the natural decay curve; open symbols represent the decay curve corresponding to the first test dose. The inset shows a representative dose response curve of the same sample, fitted with a single saturating exponential function. (b) Abanico plot (Dietze et al., 2016) of the multi-grain (black) and single-grain (red) D_e distributions of sample OP4-205 (weighted mean as central value). (c) Boxplot of the preheat plateau test results of sample OP4-205. Three aliquots were analysed for each preheat temperature. The solid black line marks the average dose of all shown aliquots (5.85 Gy); the dashed lines represent the standard deviation from this value. (d) Boxplot of the dose recovery test results of sample OP1-105. The recovery dose administered was 2.15 Gy. Three aliquots were analysed for each preheat temperature.

Chobe Enclave, and this part of the Middle Kalahari, were certainly influenced by these fault zones, their linkage between these zones, and the preexisting basement fabrics (Kinabo et al., 2008). This was undoubtedly a factor controlling the Late Pleistocene to Holocene landscape in the Chobe Enclave.

The evolution of the region (Fig. 10) can be summarized as follows: (1) the propagation of the NE–SW trending Chobe fault resulted in high displacement along the fault. Before ~25 ka (Fig. 10a), the fluvial systems endured burial of channels with continuous deposition across the landscape. Silty fine sand paleo-channels formed within the silt-rich floodplain deposits overlain by fine sand of the ridges. The sizes of the paleo-channels varied depending on their probable depositional patterns (Fig. 10a). These depositional patterns were the result of fluvial deflection due to epeirogenic movements (Holbrook and Schumm, 1999). (2) During a second step of neotectonic uplift events, between ~25 and ~6 ka (Fig. 10b), syntectonic deposition occurred and the continued propagation of the Chobe fault formed a depocenter making part of the Chobe-Linyanti sub-basin (Kinabo et al., 2007). During this time, some sand ridges formed. This syndepositional uplift of the sand ridge morphologies is attested by the presence of erosional bounding surfaces. This configuration triggered the formation of sharp linear eastern margin of the sand ridge, also representing a possible paleo-lake/marsh shore. Moreover, during this period, there is a prominent continued erosional phase, revealing the existence of carbonate islands emerging from the floodplain areas and creating a topographical inversion relief within the basin (Mokatse et al., 2022). Indeed, the presence of these palustrine carbonates refers to periods and/or areas of reduced clastic input and may be used as an indicator of the aggradation rate at work in the floodplain (Alonso-Zarza, 2003), as well as a change in the water chemistry. The carbonate precipitation events in the Chobe Enclave occurred irregularly, since at least ~75 ka (Diaz et al., 2019; Mokatse et al., 2022); they witness changes and some disorganization in the hydrological network, probably associated with phases triggered by neotectonics, although some climate influence cannot be totally discarded. Nevertheless, it is certainly during this phase, between ~25 and ~6 ka, that the watergaps started to form. (3) Finally, from ~6 ka to present day (Fig. 10c), continued fault growth and propagation of the Linyanti fault resulted in uplift of the footwall, which induced erosion to

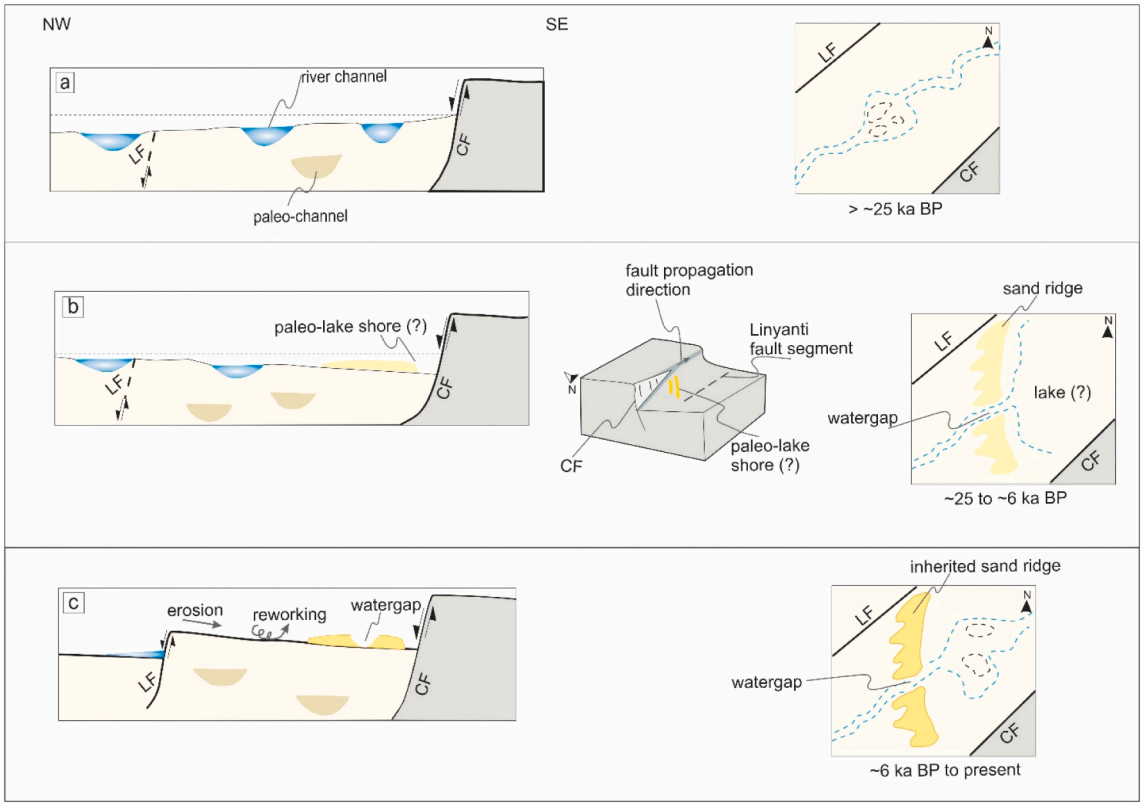

Fig. 10. Schematic diagram illustrating the landscape evolution of the Chobe Enclave during the Late Pleistocene to Holocene (for details see text). LF — Linyanti fault, CF — Chobe fault.

the NE of the Chobe Enclave. This contributed to essentially erode the western margins of the present-day sand ridge as well and deepen the fluvial watergaps. The sand ridge was progressively isolated from the floodplain level and constitutes an inherited relief, presently eroded on both of its flanks, due to aeolian and fluvial reworking as a continuous phase of the landscape shaping.

6. Conclusions

A combination of ERT, GPR, OSL, and sedimentological data was used to investigate the geometry, internal structure, and history of the Chobe Enclave's landforms. Different depositional environments were recorded during the Late Pleistocene to Holocene in the Chobe Enclave. Throughout this time, the reworking and deposition allowed the Kalahari sand to be mixed with various proportions of different sedimentary sources from desert loess to diatomite mud. The Late Pleistocene (>~25 ka) is characterized by burial of fluvial channels due to epeirogenic movements revealed as paleo-channels today. During ~25 ka to ~6 ka, a hypothetical paleo-lake shoreline formed, resulting in the linear eastern margin of the sand ridge. Furthermore, since ~6 ka, the neotectonic influence on the evolution of the landscape and drainage is attested by the incision of the sand ridge, forming fluvial watergaps. As this study gives insight on possible influence of neotectonics on the landscape, further work is needed to validate and explore the extent of neotectonics as well as development of the eastern-most sand ridges in the Chobe Enclave.

Declaration of competing interest

Eric P. Verrecchia reports financial support was provided by Swiss National Science Foundation.

Data availability

Data will be made available on request.

Acknowledgements

The authors acknowledge the Ministry of Environment, Natural Resources Conservation and Tourism of the Republic of Botswana as well as the Chobe Enclave Conservation Trust for the research permits, without which this study would not have been possible, as well as the Botswana International University of Science and Technology and the University of Lausanne. The authors also warmly thank Dr. Nathalie Diaz for her advice. This work has been supported by a Swiss National Foundation grant no. 200021_172944 to EPV.

References

Aitken, M.J., 1998. An Introduction to Optical Dating. The Dating of Quaternary Sediments by the Use of Photon-stimulated Luminescence. In: Oxford University Press, Oxford, New York, Tokyo, p. 267 pp..

Alonso-Zarza, A.M., 2003. Palaeoenvironmental significance of palustrine carbonates and calcretes in the geological record. Earth Sci. Rev. 60 (3–4), 261–298.

Alvarez Naranjo, A., 2016. The Role of Pre-existing Basement Fabrics in the Initiation of Continental Rifting: The Okavango Rift Zone, Botswana. Doctoral Dissertations, 2642. https://scholarsmine.mst.edu/doctoral_dissertations/2642.

Alvarez Naranjo, A., Hogan, J.P., 2013. The role of tectonic inheritance in the geometry and location of continental rifts-an example from the Okavango Rift Zone, Botswana. Geol. Soc. Am. Abstr. Programs 45 (7), 832.

Annan, A.P., Davis, J.L., 1992. Design and development of a digital ground penetrating radar system. In: Pilon, J. (Ed.), GroundPenetrating Radar. Geol. Surv. Can. Pap, 90-4, pp. 15–23.

Baines, D., Smith, D.G., Froese, D.G., Bauman, P., Nimeck, G., 2002. Electrical resistivity ground imaging (ERGI): a new tool for mapping the lithology and geometry of channel-belts and valley-fills. Sedimentology 49 (3), 441–449.

Barber, D.C., Brown, B.H., 1984. Applied potential tomography. J. Phys. E: Sci. Instrum. 17 (9), 723–733.

Bishop, M.P., Shroder Jr., J.F., Colby, J.D., 2003. Remote sensing and geomorphometry for studying relief production in high mountains. Geomorphology 55 (1–4), 345–361.
Brennan, B.J., Lyons, R.G., Phillips, S.W., 1991. Attenuation of alpha particle track dose for spherical grains. Int. J. Radiat. Appl. Instrum. Part D 18 (1–2), 249–253.
Bristow, C.S., 2009. Ground penetrating radar in aeolian dune sands. In: Jol, H.M. (Ed.), Ground Penetrating Radar: Theory and Applications. Elsevier Science, Amsterdam, The Netherlands, pp. 273–297.
Bristow, C.S., Duller, G.A.T., Lancaster, N., 2007. Age and dynamics of linear dunes in the Namib Desert. Geology 35 (6), 555–558.
Bristow, C.S., Jol, H.M., 2003. An introduction to ground penetrating radar (GPR) in sediments. Geol. Soc. Lond., Spec. Publ. 211 (1), 1–7.
Bristow, C.S., Lancaster, N., Duller, G.A.T., 2005. Combining ground penetrating radar surveys and optical dating to determine dune migration in Namibia. J. Geol. Soc. 162 (2), 315–321.
Bufford, K.M., Atekwana, E.A., Abdelsalam, M.G., Shemang, E., Atekwana, E.A., Mickus, K., Molwalefhe, L., 2012. Geometry and faults tectonic activity of the Okavango Rift Zone, Botswana: evidence from magnetotelluric and electrical resistivity tomography imaging. J. Afr. Earth Sci. 65, 61–71.
Burke, K., Gunnell, Y., 2008. The african erosion surface: a continental-scale synthesis of geomorphology, tectonics, and environmental change over the past 180 million years (Vol. 201). Mem. Geol. Soc. Am. 201, 1–66.
Burrough, S.L., Thomas, D.S., Shaw, P.A., Bailey, R.M., 2007. Multiphase quaternary highstands at lake Ngami, Kalahari, northern Botswana. Palaeogeogr. Palaeoclimatol. Palaeoecol. 253 (3–4), 280–299.
Burrough, S.L., Thomas, D.S.G., 2008. Late Quaternary lake-level fluctuations in the Mababe Depression: Middle Kalahari palaeolakes and the role of Zambezi inflows. Quat. Res. 69 (3), 388–403.
Burrough, S.L., Thomas, D.S., Singarayer, J.S., 2009. Late Quaternary hydrological dynamics in the Middle Kalahari: forcing and feedbacks. Earth Sci. Rev. 96 (4), 313–326.
Campbell, G., Johnson, S., Bakaya, T., Kumar, H., Nsatsi, J., 2006. Airborne geophysical mapping of aquifer water quality and structural controls in the lower Okavango DeltaBotswana. South African Journal of Geology 109 (4), 475–494.
Chorowicz, J., 2005. The East African rift system. J. Afr. Earth Sci. 43 (1–3), 379–410.
Clark, G.M., 1989. Central and southern Appalachian water and wind gap origins: review and new data. Geomorphology 2 (1–3), 209–232.
Cooke, H.J., 1980. Landform evolution in the context of climatic change and neo-tectonism in the Middle Kalahari of north-Central Botswana. Trans. Inst. Br. Geogr. 5 (1), 80–99.
Daly, M.C., Green, P., Watts, A.B., Davies, O., Chibesakunda, F., Walker, R., 2020. Tectonics and landscape of the Central African Plateau and their implications for a propagating Southwestern Rift in Africa. Geochem. Geophys. Geosyst. 21 (6), e2019GC008746.
Diaz, N., Armitage, S.J., Verrecchia, E.P., Herman, F., 2019. OSL dating of a carbonate island in the Chobe Enclave, NW Botswana. Quat. Geochronol. 49, 172–176.
Dietze, E., Hartmann, K., Diekmann, B., IJmker, J., Lehmkuhl, F., Opitz, S., Borchers, A., 2012. An end-member algorithm for deciphering modern detrital processes from lake sediments of Lake Donggi Cona, NE Tibetan Plateau, China. Sedimentary Geology 243, 169–180.
Dietze, M., Kreutzer, S., Burow, C., Fuchs, M.C., Fischer, M., Schmidt, C., 2016. The abanico plot: visualising chronometric data with individual standard errors. Quat. Geochronol. 31, 12–18.
Dietze, E., Maussion, F., Ahlborn, M., Diekmann, B., Hartmann, K., Henkel, K., Kasper, T., Lockot, G., Opitz, S., Haberzettl, T., 2013a. Sediment transport processes across the Tibetan Plateau inferred from robust grain size end-members in lake sediments. Clim. Past 9, 4855–4892.
Dietze, E., Wünnemann, B., Hartmann, K., Diekmann, B., Jin, H., Stauch, G., Yang, S., Lehmkuhl, F., 2013b. Early to mid-Holocene Lake high-stand sediments at Lake Donggi Cona, northeastern Tibetan Plateau, China. Quat. Res. 79, 325–336.
Dixey, F., 1956. The east African rift system. HM Stationery Office.
Doucouré, C.M., de Wit, M.J., 2003. Old inherited origin for the present near-bimodal topography of Africa. J. Afr. Earth Sci. 36 (4), 371–388.
Duller, G.A.T., 2015. The analyst software package for luminescence data: overview and recent improvements. Ancient TL 33, 35–42.
Durcan, J.A., King, G.E., Duller, G.A.T., 2015. DRAC: dose rate and age calculator for trapped charge dating. Quat. Geochronol. 28, 54–61.
Eckardt, F.E., Flügel, T., Cotterill, F., Rowe, C., McFarlane, M., 2016. Kalahari tectonic landforms and processes beyond the Okavango Graben. Quat. Int. 404, 194.
Fairhead, J.D., Girdler, R.W., 1969. How far does the rift system extend through Africa? Nature 221 (5185), 1018–1020.
Folk, R.L., 1954. The distinction between grain size and mineral composition in sedimentary-rock nomenclature. J. Geol. 62, 344–359.
Folk, R.L., Ward, W.C., 1957. Brazos River bar: a study in the significance of grain size parameters. J. Sediment. Petrol. 27 (1), 3–26.
Galbraith, R.F., Roberts, R.G., Laslett, G.M., Yoshida, H., Olley, J.M., 1999. Optical dating of single and multiple grains of quartz from jinmium rock shelter, northern Australia: part I, experimental design and statistical models. Archaeometry 41, 339–364.
Gawthorpe, R.L., Hurst, J.M., 1993. Transfer zones in extensional basins: their structural style and influence on drainage development and stratigraphy. J. Geol. Soc. Lond. 150, 1137–1152.
Google Earth, 2020. Chobe region, Botswana. Pro V 7.3.4.8573, CNES/Airbus 2020. http://www.earth.google.com.
Grove, A.T., 1969. Landforms and climatic change in the Kalahari and Ngamiland. Geogr. J. 135 (2), 191–212.
Guérin, G., Mercier, N., Adamiec, G., 2011. Dose-rate conversion factors: update. Ancient TL 29 (1), 5–8.
Guérin, G., Mercier, N., Nathan, R., Adamiec, G., Lefrais, Y., 2012. On the use of the infinite matrix assumption and associated concepts: a critical review. Radiat. Meas. 47 (9), 778–785.
Gumbricht, T., McCarthy, T.S., Merry, C.L., 2001. The topography of the Okavango Delta, Botswana, and its tectonic and sedimentological implications. S. Afr. J. Geol. 104 (3), 243–264.
Günther, T., Rücker, C., 2019. Boundless Electrical Resistivity Tomography BERT v2. 2–The User Tutorial. LIAG Hannover, TU Berlin, 338 pp. http://www.resistivity.net/download/bert-tutorial.pdf.
Holbrook, J., Schumm, S.A., 1999. Geomorphic and sedimentary response of rivers to tectonic deformation: a brief review and critique of a tool for recognizing subtle epeirogenic deformation in modern and ancient settings. Tectonophysics 305 (1–3), 287–306.
Huntsman-Mapila, P., Kampunzu, A.B., Vink, B., Ringrose, S., 2005. Cryptic indicators of provenance from the geochemistry of the Okavango Delta sedimentsBotswana. Sedimentary Geology 174 (1–2), 123–148.
Huntsman-Mapila, P., Tiercelin, J.J., Benoit, M., Ringrose, S., Diskin, S., Cotten, J., Hémond, C., 2009. Sediment geochemistry and tectonic setting: Application of discrimination diagrams to early stages of intracontinental rift evolution, with examples from the Okavango and Southern Tanganyika rift basins. J. Afr. Earth Sci. 53 (1–2), 33–44.
Keller, E.A., Pinter, N., 1996. Active Tectonics. Prentice-Hall, Upper Saddle River, 338 pp.
Kim, J.C., Duller, G.A.T., Roberts, H.M., Wintle, A.G., Lee, Y.I., Yi, S.B., 2009. Dose dependence of thermally transferred optically stimulated luminescence signals in quartz. Radiat. Meas. 44 (2), 132–143.
Kinabo, B.D., Atekwana, E.A., Hogan, J.P., Modisi, M.P., Wheaton, D.D., Kampunzu, A. B., 2007. Early structural development of the Okavango rift zoneNW Botswana. J. Afr. Earth Sci. 48, 125–136.
Kinabo, B.D., Hogan, J.P., Atekwana, E.A., Abdelsalam, M.G., Modisi, M.P., 2008. Fault growth and propagation during incipient continental rifting: Insights from a combined aeromagnetic and shuttle Radar Topography Mission digital elevation model investigation of the Okavango Rift Zone, Northwest Botswana. Tectonics 27, TC3013Natu.
Kreutzer, S., Schmidt, C., Fuchs, M.C., Dietze, M., Fischer, M., Fuchs, M., 2012. Introducing an R package for luminescence dating analysis. Ancient TL 30 (1), 1–8.
Loke, M.H., 2004. Rapid 2-D Resistivity & IP inversion using the least-squares method. Wenner (a,b,g), dipole-dipole, inline pole-pole, pole-dipole, equatorial dipole-dipole, Wenner-Schlumberger and non-conventional arrays on land, underwater and cross-borehole surveys. In: RES2DINV ver. 3.54 Manual. Geotomo Software.
Loke, M.H., Barker, R.D., 1996. Rapid least-squares inversion of apparent resistivity pseudosections by a quasi-Newton method1. Geophys. Prospect. 44 (1), 131–152.
Mallick, D.I.J., Habgood, F., Skinner, A.C., 1981. A geological interpretation of Landsat imagery and air photography of Botswana. In: Overseas Geology and Mineral Resources, 56. Institute of Geological Sciences, London, 36 pp.
Mauz, B., Lang, A., 2004. Removal of the feldspar-derived luminescence component from polymineral fine silt samples for optical dating applications: evaluation of chemical treatment protocols and quality control procedures. Ancient TL 22 (1), 1–8.
McCarthy, T.S., 2013. The Okavango Delta and its place in the geomorphological evolution of southern Africa. S. Afr. J. Geol. 116 (1), 1–54.
McFarlane, M.J., Eckardt, F.D., 2007. Palaeodune morphology associated with the Gumare fault of the Okavango graben in the Botswana/Namibia borderland: a new model of tectonic influence. S. Afr. J. Geol. 110 (4), 535–542.
Modisi, M.P., Atekwana, E.A., Kampunzu, A.B., Ngwisanyi, T.H., 2000. Rift kinematics during the incipient stages of continental extension: evidence from the nascent Okavango rift basin, Northwest Botswana. Geology 28 (10), 939–942.
Mokatse, T., Diaz, N., Shemang, E., Van Thuyne, J., Vittoz, P., Vennemann, T., Verrecchia, E.P., 2022. Landscapes and landforms of the Chobe Enclave, Northern Botswana. In: Eckardt, F. (Ed.), Landscapes and Landforms of Botswana. Springer-Nature, Dordrecht, pp. 91–116. https://doi.org/10.1007/978-3-030-86102-5_6.
Moore, A.E., 1999. A reappraisal of epeirogenic flexure axes in southern Africa. S. Afr. J. Geol. 102, 363–376.
Moore, A.E., Cotterill, F.P.D., Eckardt, F.D., 2012. The evolution and ages of Makgadikgadi palaeo-lakes: consilient evidence from Kalahari drainage evolution south-central Africa. S. Afr. J. Geol. 115 (3), 385–413.
Moorkamp, M., Fishwick, S., Walker, R.J., Jones, A.G., 2019. Geophysical evidence for crustal and mantle weak zones controlling intra-plate seismicity–the 2017 Botswana earthquake sequence. Earth Planet. Sci. Lett. 506, 175–183.
Murray, A.S., Wintle, A.G., 2000. Luminescence dating of quartz using an improved single-aliquot regenerative-dose protocol. Radiat. Meas. 32, 57–73.
NASA JPL, 2013. NASA shuttle radar topography mission global 1 arc second. In: Nasa Lp Daac, p. 15.
Nash, D.J., Eckardt, F.D., 2015. Drainage development, neotectonics and base-level change in the Kalahari Desert, southern Africa. S. Afr. Geogr. J. 98 (2), 308–320.
Neal, A., 2004. Ground-penetrating radar and its use in sedimentology: principles, problems and progress. Earth Sci. Rev. 66 (3–4), 261–330.
Otvos, E.G., 2000. Beach ridges—definitions and significance. Geomorphology 32 (1–2), 83–108.
Parsons, A.J., Abrahams, A.D., 2009. Geomorphology of desert environments. In: Parsons, A.J., Abrahams, A.D. (Eds.), Geomorphology of Desert Environments. Springer Nature, Dordrecht, pp. 3–7.
Partridge, T.C., 1998. Of diamonds, dinosaurs and diastrophism: 150 million years of landscape evolution in southern Africa. S. Afr. J. Geol. 101 (3), 167–184.

Pastier, A.-M., Dauteuil, O., Murray-Hudson, M., Moreau, F., Walpersdorf, A., Makati, K., 2017. Is the Okavango Delta the terminus of the East African Rift System? Towards a new geodynamic model: geodetic study and geophysical review. Tectonophysics 712–713, 469–481.

Podgorski, J.E., Green, A.G., Kgotlhang, L., Kinzelbach, W.K., Kalscheuer, T., Auken, E., Ngwisanyi, T., 2013. Paleo-megalake and paleo-megafan in southern Africa. Geology 41 (11), 1155–1158.

Prins, M.A., Bouwer, L.M., Beets, C.J., Troelstra, S.R., Weltje, G.J., Kruk, R.W., Vroon, P. Z., 2002. Ocean circulation and iceberg discharge in the glacial North Atlantic: Inferences from unmixing of sediment size distributions. Geology 30 (6), 555–558.

Prins, M.A., Vriend, M., Nugteren, G., Vandenberghe, J., Lu, H., Zheng, H., Weltje, G.J., 2007. Late Quaternary aeolian dust input variability on the Chinese Loess Plateau: inferences from unmixing of loess grain-size records. Quat. Sci. Rev. 26 (1–2), 230–242.

R Core Team, 2021. R: A Language and Environment for Statistical Computing. R Foundation for Statistical Computing, Vienna, Austria. https://www.R-project.org/.

Rhea, S., 1993. Geomorphic observations of rivers in the Oregon Coast Range from a regional reconnaissance perspective. Geomorphology 6 (2), 135–150.

Ringrose, S., Downey, B., Genecke, D., Sefe, F., Vink, B., 1999. Nature of sedimentary deposits in the western Makgadikgadi basinBotswana. J. Arid Environ. 43 (4), 375–397.

Ringrose, S., Huntsman-Mapila, P., Kampunzu, H., Downey, W.D., Coetzee, S., Vink, B., Vanderpost, C., 2005. Geomorphological and geochemical evidence for palaeo feature formation in the northern Makgadikgadi sub-basin, Botswana. Palaeogeogr. Palaeoclimatol. Palaeoecol. 217, 265–287.

Ringrose, S., Harris, C., Huntsman-Mapila, P., Vink, B.W., Diskins, S., Vanderpost, C., Matheson, W., 2009. Origins of strandline duricrusts around the Makgadikgadi Pans (Botswana Kalahari) as deduced from their chemical and isotope composition. Sediment. Geol. 219 (1–4), 262–279.

Riquelme, R., Martinod, J., Hérail, G., Darrozes, J., Charrier, R., 2003. A geomorphological approach to determining the Neogene to recent tectonic deformation in the Coastal Cordillera of northern Chile (Atacama). Tectonophysics 361 (3–4), 255–275.

Ruszkiczay-Rüdiger, Z., Fodor, L., Horváth, E., Telbisz, T., 2009. Discrimination of fluvial, eolian and neotectonic features in a low hilly landscape: a DEM-based morphotectonic analysis in the Central Pannonian BasinHungary. Geomorphology 104 (3–4), 203–217.

Schmidt, C., Zeeden, C., Krauß, L., Lehmkuhl, F., Zöller, L., 2021. A chronological and palaeoenvironmental re-evaluation of two loess-palaeosol records in the northern Harz foreland, Germany, based on innovative modelling tools. Boreas 50, 746–763.

Schumm, S.A., Dumont, J.F., Holbrook, M.J., 2002. Active Tectonics and Alluvial Rivers. In: Cambridge University Press, Cambridge, p. 276.

Silva, P.G., Goy, J.L., Zazo, C., Bardaj, T., 2003. Fault-generated mountain fronts in Southeast Spain: geomorphologic assessment of tectonic and seismic activity. Geomorphology 50 (1–3), 203–225.

Shaw, P.A., Cooke, H.J., 1986. Geomorphic evidence for the late Quaternary palaeoclimates of the middle Kalahari of northern Botswana. Catena 13 (4), 349–359.

Shaw, P.A., Thomas, D.S.G., 1988. Lake Caprivi: a late Quaternary link between the Zambezi and middle Kalahari drainage systems. Z. Geomorphol. 32 (3), 329–337.

Shaw, P.A., Cooke, H.J., Thomas, D.S.G., 1988. Recent advances in the study of Quaternary landforms in Botswana. In: Collection Palaeoecology of Africa, 19, pp. 15–26.

Shaw, P.A., Stokes, S., Thomas, D.S.G., Davies, F.B.M., Holmgren, K., 1997. Palaeoecology and age of a Quaternary high lake level in the Makgadikgadi Basin of the Middle KalahariBotswana. South African Journal of Science 93 (6), 273–276.

Stolt, R.H., 1978. Migration by Fourier transform. Geophysics 43, 23–48.

Storz, H., Storz, W., Jacobs, F., 2000. Electrical resistivity tomography to investigate geological structures of the earth's upper crust. Geophys. Prospect. 48 (3), 455–472.

Vainer, S., Erel, Y., Matmon, A., 2018. Provenance and depositional environments of Quaternary sediments in the southern Kalahari Basin. Chem. Geol. 476, 352–369.

Vainer, S., Matmon, A., Erel, Y., Hidy, A.J., Crouvi, O., De Wit, M., Geller, Y., Team, A.S. T.E.R., 2021. Landscape responses to intraplate deformation in the Kalahari constrained by sediment provenance and chronology in the Okavango Basin. Basin Research 33 (2), 1170–1193.

Vainer, S., Matmon, A., Dor, Y.B., Verrecchia, E., Eckardt, F.D, Team, A.S.T.E.R, 2021. Eolian chronology reveals causal links between tectonics, climate, and erg generation. In: Royal, S. (Ed.), PRE_PRINT-Researchsquare. https://doi.org/10.21203/rs.3.rs-801542/v1.

Van Thuyne, J., Darini, I., Mainga, A., Verrecchia, E.P., 2021. Are fungus-growing termites super sediment-sorting insects of subtropical environments? J. Arid Environ. 193, 104566.

Wisen, R., Auken, E., Dahlin, T., 2005. Combination of 1D laterally constrained inversion and 2D smooth inversion of resistivity data with a priori data from boreholes. In: Near Surface Geophysics, 3. European Association of Geoscientists & Engineers, pp. 71–79.

Yu, Y., Gao, S.S., Moidaki, M., Reed, C.A., Liu, K.H., 2015a. Seismic anisotropy beneath the incipient Okavango rift: implications for rifting initiation. Earth Planet. Sci. Lett. 430, 1–8.

Yu, Y., Liu, K.H., Moidaki, M., Reed, C.A., Gao, S.S., 2015b. No thermal anomalies in the mantle transition zone beneath an incipient continental rift: evidence from the first receiver function study across the Okavango rift zoneBotswana. Geophys. J. Int. 202 (2), 1407–1418.

Yu, Y., Liu, K.H., Huang, Z., Zhao, D., Reed, C.A., Moidaki, M., Lei, J., Gao, S.S., 2017. Mantle structure beneath the incipient Okavango rift zone in southern Africa. Geosphere 13 (1), 102–111.

Sedimentary Geology 454 (2023) 106459

Contents lists available at ScienceDirect

Sedimentary Geology

journal homepage: www.elsevier.com/locate/sedgeo

Sepiolite as a multifactorial indicator of paleoenvironments in the Chobe Enclave (northern Botswana)

Thuto Mokatse [a,*], Charlotte Prud'Homme [a], Shlomy Vainer [a], Thierry Adatte [b], Elisha Shemang [c], Eric P. Verrecchia [a]

[a] Institute of Earth Surface Dynamics – IDYST, FGSE, University of Lausanne, 1015 Lausanne, Switzerland
[b] Institute of Earth Sciences – ISTE, FGSE, University of Lausanne, 1015 Lausanne, Switzerland
[c] Earth and Environmental Sciences, Botswana International University of Science and Technology, Botswana

ARTICLE INFO

Article history:
Received 22 February 2023
Received in revised form 19 June 2023
Accepted 21 June 2023
Available online 28 June 2023

Editor: Dr. Massimo Moretti

Keywords:
Sepiolite
Amorphous silica
Terrestrial carbonates
Lacustrine/palustrine environments
Quaternary

ABSTRACT

The origin and evolution of clay minerals in sedimentary basins are usually influenced by changes in depositional hydrochemistry. The formation and preservation of rare fibrous magnesium-rich clay minerals, like sepiolite, are of interest in the Chobe Enclave, northern Botswana, as it occurred in a siliceous-rich intra-cratonic basin. New X-ray diffraction (XRD) data, scanning electron (SEM) and transmission electron (TEM) microscopy analyses, as well as geochemical data, are used to study the origin of authigenic sepiolite and the sub-environments related to its formation in the Chobe Enclave. The paleoenvironment record during the Late Pleistocene to Holocene demonstrates that the deposition in the region was preceded by an aluvial fan/fluvial deposits in humid conditions. The upper-basin catchment yielded a clay assemblage, including kaolinite and minor smectite amounts, now preserved in the Chobe as a detrital phase. The alluvial fan deposits were later overlain by deposits from lacustrine/palustrine environments where significant hydrochemical changes took place: during these changes, a fibrous clay mineral (authigenic sepiolite) formed in shallow lake/marshes in a closed system with low energy, under the influence of magnesium-rich and alkaline waters. The mineralogical and geometrical (diagenetic) relationships between the palustrine deposits (carbonate facies) and sepiolite point to a sequence of precipitation from an evaporitic system in which calcite, sepiolite, and finally amorphous silica follow one another. In addition, although the sepiolite parent solution was enriched from a water source concentrated in Mg^{2+}, the presence of Ba^{2+} ions also emphasizes some spells of hydrothermal activity.

1. Introduction

Clay minerals form under different geological environments and their depositional and diagenetic assemblages in sedimentary basins constitute a potential record of morphological, tectonic, and climatic conditions that prevailed during their formation (Webster and Jones, 1994; Lopez and Gonzalez, 1995; Akbulut and Kadir, 2003; Cuevas et al., 2003; Hong et al., 2007). Because the origin of the clay minerals can be either authigenic or detrital (Chamley, 1989), changes in depositional hydrochemistry that can be caused by tectonics and drainage evolution affecting source area lithology, influence the characteristics of clay mineral assemblages. The changing depositional hydrochemistry involves varying parameters, such as pH, ion species and concentrations in both surface and pore waters. In sedimentary environments, neoformation (or authigenesis) can take place in both syngenetic and diagenetic settings, whereas transformation is mainly related to diagenesis with formation of specific clay minerals depending on physico-chemical conditions (Chamley, 1989). Sepiolite, a relatively rare clay mineral in nature, is a fibrous clay mineral of the following average structural formula: $Mg_4Si_6O_{15}(OH)_2 \cdot 6H_2O$ (Galán and Singer, 2011). The sepiolite structure is composed of a 2:1 type ribbon with four octahedral positions occupied by Mg^{2+} and sometimes by Al^{3+} or Fe^{3+} (Fersmann, 1913; Shannon, 1929; Kauffman Jr., 1943; Galán and Singer, 2011). Its origin commonly lies on authigenic processes, i.e., its precipitation takes place directly from a solution in which the main sepiolite components, namely magnesium and silicon, are present in high concentrations (Mizutani et al., 1991; Galán and Carretero, 1999; Akbulut and Kadir, 2003; Wang et al., 2009). The first step necessary to precipitate sepiolite consists of an increase in Mg^{2+} and Si^{4+} ion activities in the solution, as well as the persistence of low Al^{3+} activity (Birsoy, 2002). So far, these conditions were observed in two different environments: (1) the most documented is related to the alteration and weathering of volcanic rocks (Yalçin and Bozkaya, 2011) as well

* Corresponding author.
E-mail address: thuto.mokatse@unil.ch (T. Mokatse).

https://doi.org/10.1016/j.sedgeo.2023.106459

as low temperature hydrothermalism (Irkec and Ünlü, 1993; Galán and Pozo, 2011), and (2) the transformation of previous sedimentary minerals, such as dolomite or smectite (Jones and Conko, 2011). Once the required ions are in the solution, sepiolite precipitation can be triggered by progressive and increasing concentrations of Mg^{2+} and Si^{4+} ions in the parent solution, frequently obtained during evaporation (Helgeson et al., 1969). Furthermore, a high pH (usually >8–9) and a low concentration of impurities within a low energy waterbody, constitute ideal conditions to form the fibrous crystals of sepiolite (Pozo and Calvo, 2018).

Sepiolite is principally observed in lacustrine to palustrine environments with high evaporation rates, due to prevalent semiarid to arid climate conditions (Stoessell and Hay, 1978; Tateo et al., 2000; García-Romero et al., 2007; Pozo and Calvo, 2015; Draidia et al., 2016). However, its occurrence in a large sandy silica-rich basin has only been scarcely documented (Pardo et al., 2009; Miller et al., 2010). Moreover, critical questions arise relating to the source of Ca being able to form carbonate beds associated with sepiolite in a highly siliceous environment. Some decimeter-thick deposits, with the presence of various amounts of sepiolite, have been investigated to characterize these clay minerals and to provide clues about the major processes at play. Therefore, this study aims at assessing the sub-environments and their relation to the formation of sepiolite in the Chobe Enclave, located in Northern Botswana.

The following questions are investigated: (1) What lithofacies are associated with the fibrous clay minerals? (2) What could be the origin of the input of Mg^{2+}, river transportation or hydrothermal input? (3) Was the increase of the pH solution obtained through evaporation and/or degassing? (4) And finally, what does sepiolite precipitation mean in terms of paleoenvironmental reconstruction?

2. Geological settings

Northern Botswana (Fig. 1) is characterized by large Quaternary sandy deposits of several hundred meters thick laying on a crustal basement constituted by Neoproterozoic formations, which are part of the Kwando complex (Key and Ayres, 2000; Lehmann et al., 2015). These formations belong to the Ghanzi Chobe Belt, an igneous and metamorphic region set up during the Neoproterozoic and observed from West Botswana to the Chobe Enclave (Schwartz et al., 1996; Modie, 2000). Moreover, a "Karoo basalt formation" spreads out in the northern Botswana and is part of the Large Igneous Province (LIP), which formed between 179 and 181 Ma ago, as the last volcanic formation described in this area, with some dolerite dykes (Le Gall et al., 2002; Jourdan et al., 2004).

The Chobe Enclave is an extensional basin bounded by two major faults, the Chobe Fault (southeast) and the Linyanti Fault (northwest; Fig. 1). The tectonic nature of the basin can have multiple origins and is located between the East African Rift System at the northeastern part of the Chobe Enclave and the structural depression of the Okavango Basin at its southwestern part (Vainer et al., 2021). These large tectonic structures possess a different extensional scheme, but both develop a succession of horst/graben systems affected by normal faulting (Gumbricht et al., 2001; Chorowicz, 2005). However, in this area of southern Africa, the topography is characterized by large plateaus with a flat relief (Mokatse et al., 2022a).

The Chobe Enclave forms part of the Chobe–Linyanti sub-basin, infilled with Quaternary sediments largely dominated by sands deposited in semiarid conditions (Burrough et al., 2007, 2009). This basin is situated inside the intracratonic Kalahari Basin, where Plio-Pleistocene eolian and fluvial sands, as well as sandstones, represent the most common sediments (Thomas and Shaw, 1990; Haddon and McCarthy, 2005; Matmon et al., 2015; Vainer et al., 2021, 2022). In the Chobe Enclave, the Quaternary deposits, probably between 50 and 100 m thick (Thomas and Shaw, 1991), overlay a Proterozoic metamorphic and magmatic basement. In terms of drainage, two main rivers flow into the Chobe Enclave, the Kwando/Linyanti in the southwest, and the Chobe in the northeast (Fig. 1). Finally, it must be noted that hydrothermalism is locally evidenced at the present-day by the presence of hot springs in the northern part of the Chobe Enclave (Mukwati et al., 2018). These hot springs undoubtedly point to the influence of active neotectonics in the region.

3. Material and methods

3.1. Study sites

The study sites in the Chobe Enclave, i.e. (i) TSC site, (ii) Baobab quarry, (iii) Nata site and (iv) Acacia quarry (Fig. 1) are located on a paleo-floodplain and in a fossil carbonate-rich palustrine environment with a variety of closely associated carbonates, diatomites, and sandy deposits. Descriptions and interpretations of the facies associations were conducted at these four main sites (Fig. 2) across the landscape, where preferential erosion of sands around the carbonate-rich formations is observed today as elevated carbonate islands (inverted relief; Diaz et al., 2019).

3.2. X-ray diffraction analysis (XRD)

XRD analyses of the whole-rock and clay mineral <2 μm fraction (Adatte et al., 1996; Godet et al., 2008) were carried out using an ARL Thermo X'tra X-ray diffractometer at the University of Lausanne on fifty-four (54) samples. The samples were prepared following the procedure of Kübler (1987) and Adatte et al. (1996). Whole-rock mineralogy characterization was performed on randomly oriented powder of the bulk sample. Whole-rock composition was determined by XRD based on methods described by Klug and Alexander (1974), Kübler (1987) and Rolli (1990). This method for semi-quantitative analysis of the whole-rock mineralogy used external standards. Clay crystals were separated from the whole rock by removing carbonate in a 10 % HCl solution for 20 min, by controlling and adjusting the pH, and stirred using air injection. An ultrasonic bath tank was used to break aggregates, followed by centrifugation and repeated washing of the insoluble residue until the solution reached pH = 7. The <2 μm grain size fraction was obtained by sedimentation based on Stokes Law. The obtained solution was placed on a watch glass to evaporate prior to analysis. XRD analyses of oriented clay samples were made after air drying at room temperature and ethylene-glycol solvated conditions. The intensities of selected XRD peaks characterizing each clay mineral present in the size fraction (e.g., kaolinite, sepiolite, smectite, chlorite) were measured for a semi-quantitative estimate of the proportion of clay minerals present in the <2 μm fraction. Therefore, clay minerals are given in relative percent abundance without correction factors. Content in swelling (% smectite) is estimated by using the method of Moore and Reynolds (1989). In addition to clay minerals, a semi-quantitative calculation of other mineral proportions in the bulk fraction was applied to identify their assemblages associated with sepiolite.

3.3. Optical and electron microscopy

Samples were observed using optical and electronic microscopy i.e., a scanning electron microscope (SEM) as well as a transmission electron microscope (TEM). The observation of thin sections was performed using an Olympus BX61 optical microscope to identify the various minerals and amorphous phases. Analyses were carried out on selected fragments of fresh samples on stubs. In addition, a SEM was used to observe at high magnification the relationship between quartz, calcite, amorphous silica, and sepiolite on freshly fractured samples. Observations were conducted at the University of Lausanne with a Tescan Mira II LMU coupled to an EDX Penta-FET 3x detector after gold coating of fresh samples and examined by secondary electron images for textural analysis. The working conditions were 20.00 kV and a working distance of ~15.0 mm. Finally, a TEM (Philips CM-200) with a high-resolution camera

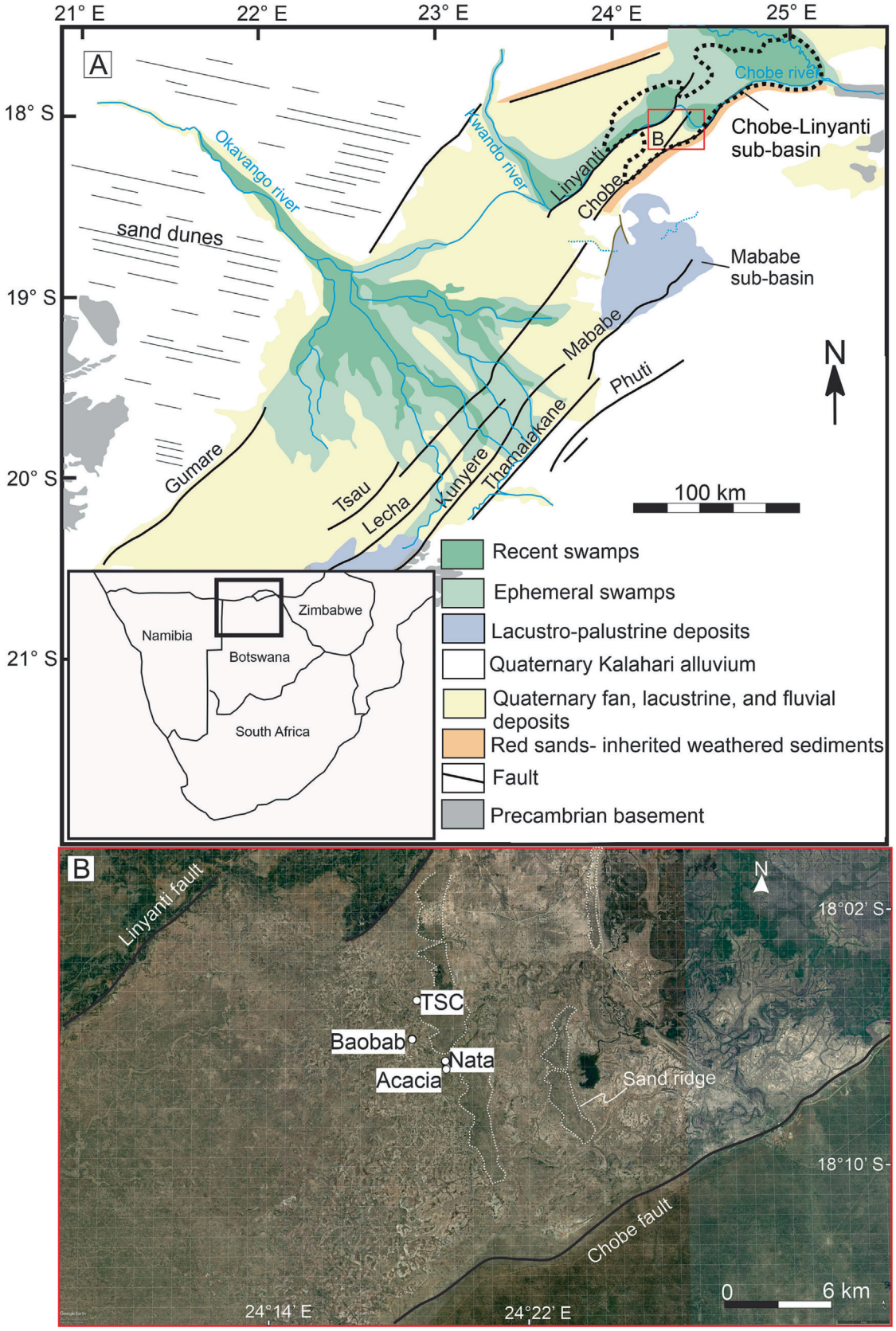

Fig. 1. (A) Lower-left corner, map of Southern Africa with a black frame referring to the regional map in A; regional and surficial geological map of the Okavango–Linyanti graben showing the study area within the Chobe–Linyanti sub-basin (dotted line). The red rectangle refers to the area in B. (B) Satellite image showing the location of the study sites (Google Earth, 2022). The Chobe and Linyanti faults are emphasized by a bold black line and sand ridges by fine dotted white lines.

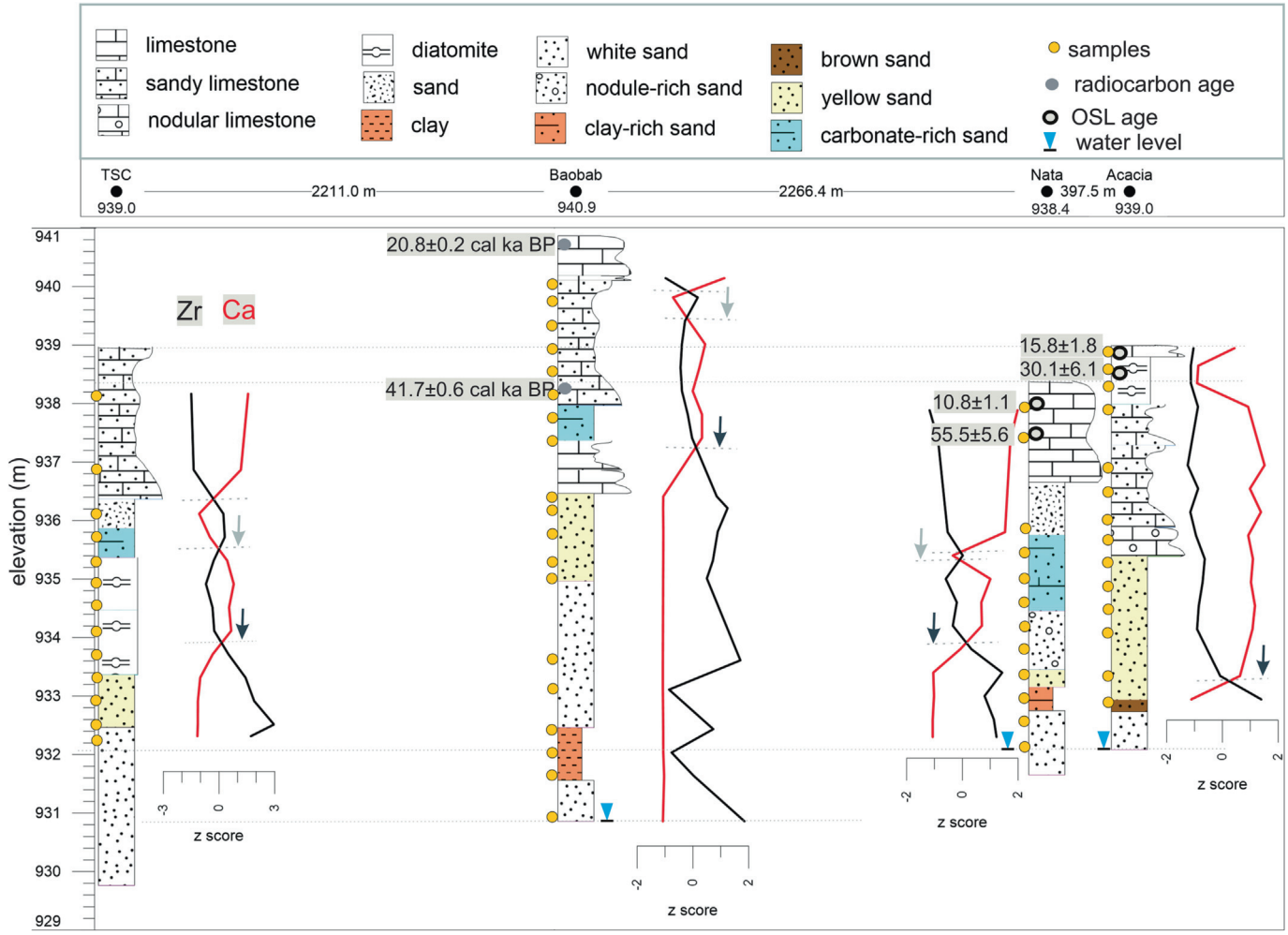

Fig. 2. Lithological logs showing variations in Ca and Zr contents expressed in standardized units, OSL and radiocarbon ages (Diaz et al., 2019; Mokatse et al., 2022a), and altitudinal relationships across study sites. The selection of these variables is based on the PCA results as they are strongly anti-correlated along the first principal component (see Fig. 8). The black arrows indicate sediment input during wet periods, and the gray arrows indicate reworking/detrital input (see discussion in the text).

device was used at the CSEM (Centre Suisse d'Electronique et de Microtechnique, Neuchâtel, Switzerland) to observe the structure of the clay minerals at high resolution. The settings were the following: the beam was accelerated at 200 kV and the working distance was 360 mm; the fraction <2 μm was dispersed in distilled water and deposited as a drop, and then evaporated on copper grids used for observations under TEM.

3.4. Geochemical analyses and data processing

An approximation of the geochemical compositions of the fibrous clays was obtained with an EDAX microprobe (Oxford Instrument) coupled with the TEM used for observations of the clay structure: EDAX analyses were performed on the same samples. EDAX results were expressed in weight %. Relative contributions of Si, Mg, and Al + Fe have been standardized, plotted in a ternary diagram, and compared to contents in sepiolite and palygorskite from the literature (based on Suárez and García-Romero, 2011).

The bulk elemental chemistry of the samples was obtained using a PANalytical Axiosm AX X-ray fluorescence device at the University of Lausanne. All samples were analyzed for major and trace elements according to two different methods. For major elements, the bulk rock powder was heated to 1050 °C (fusion temperature) with $B_4Li_2O_7$, and for trace elements, crushed samples were mixed with wax and pressed.

The relationships between the different variables (mineralogical as well as geochemical) were assessed using principal component analyses (PCA). Data were standardized before processing with Matlab™ 2022a version. Moreover, proportions of clay minerals form a simplex i.e., the sum of the variables in each item (proportions) is a constant common to all items (100 %), destroying the potential independence of variances and covariances and leading to Pearson's spurious correlations. To avoid such unwanted correlations, only two standardized clay variables were used, sepiolite and kaolinite (authigenic and detrital respectively) in order to break the simplex for PCA, and each of the minerals is used as a proxy for contrasting environments.

4. Results

4.1. Macroscale distribution and facies associations

4.1.1. TSC site

The section is approximately 6.6 m deep (Fig. 3A), located in the Chobe Enclave floodplain west of the N–S sand ridge (Fig. 1). The top of the section is composed of a 2.6 m-thick sandy limestone with a heterogeneous karstic surface; this layer consists of a mixture of 0.3 m-maximum diameter clasts within a microcrystalline matrix. Below this carbonate layer, a <1 m-thick carbonate-rich sand bed makes the transition to a ~2 m-thick diatomite earth formed by a fine, white material with a very low density and easily crushed to powder in the field. These diatomite beds include some carbonate-rich material. The diatomite bed is underlain by white sands, typical

of the Kalahari Sand (Mokatse et al., 2022a). This white sand includes some siliceous nodules. Between the diatomite and the white sands, a brown/yellow sand (~1 m thick) layer is enriched in $CaCO_3$ nodules, with bioturbations.

4.1.2. Baobab quarry

The section refers to a ~10 m high quarry wall (Fig. 3B) made up with varying lithologies from palustrine carbonate (Diaz et al., 2019) to sand. The palustrine carbonate displays different facies: a sandy limestone overlain by a brecciated carbonate layer with carbonate nodules. Below the sandy carbonate, there is a layer of soft laminated carbonate of ~0.4 m thick. Generally, the boundary between the carbonate beds and the below sands is pronounced. In some places, the contact is characterized by carbonate-rich sands. Moreover, there is a sharp contact of brown/yellow sands between the white sand and the carbonate units. This observation is similar to the aforementioned *TSC island* site. Lastly, one key feature is the occurrence of a clay-rich layer (~0.9 m thick) between two white sand units (in orange in Fig. 3B). These white sand units have occasional siliceous concretions, and groundwater intersected at ~10 m in depth.

4.1.3. Nata site

The site outcrops in a fluvial water gap cutting across the N–S sand ridge (Fig. 1). It is made up of a ~1.7 m-thick limestone unit overlying a carbonate-rich material (Fig. 3C). This material consists of $CaCO_3$ nodules of various sizes (pluri-centimeters) and has a sharp contact with the white sand below. The sharp contact is composed of yellow sand with a clayey–sandy layer.

4.1.4. Acacia quarry

The quarry section is ~6 m deep with a 0.2-m thick top part consisting of a thin limestone layer overlying a 0.8-m thick diatomite bed (Fig. 3D). The diatomite is made of a white material with a low density with some siliceous centimetric nodules. Below is a sandy limestone with a lower contact enriched in $CaCO_3$ nodules. As observed at *TSC site* and *Baobab quarry*, the contact between the sandy limestone and the

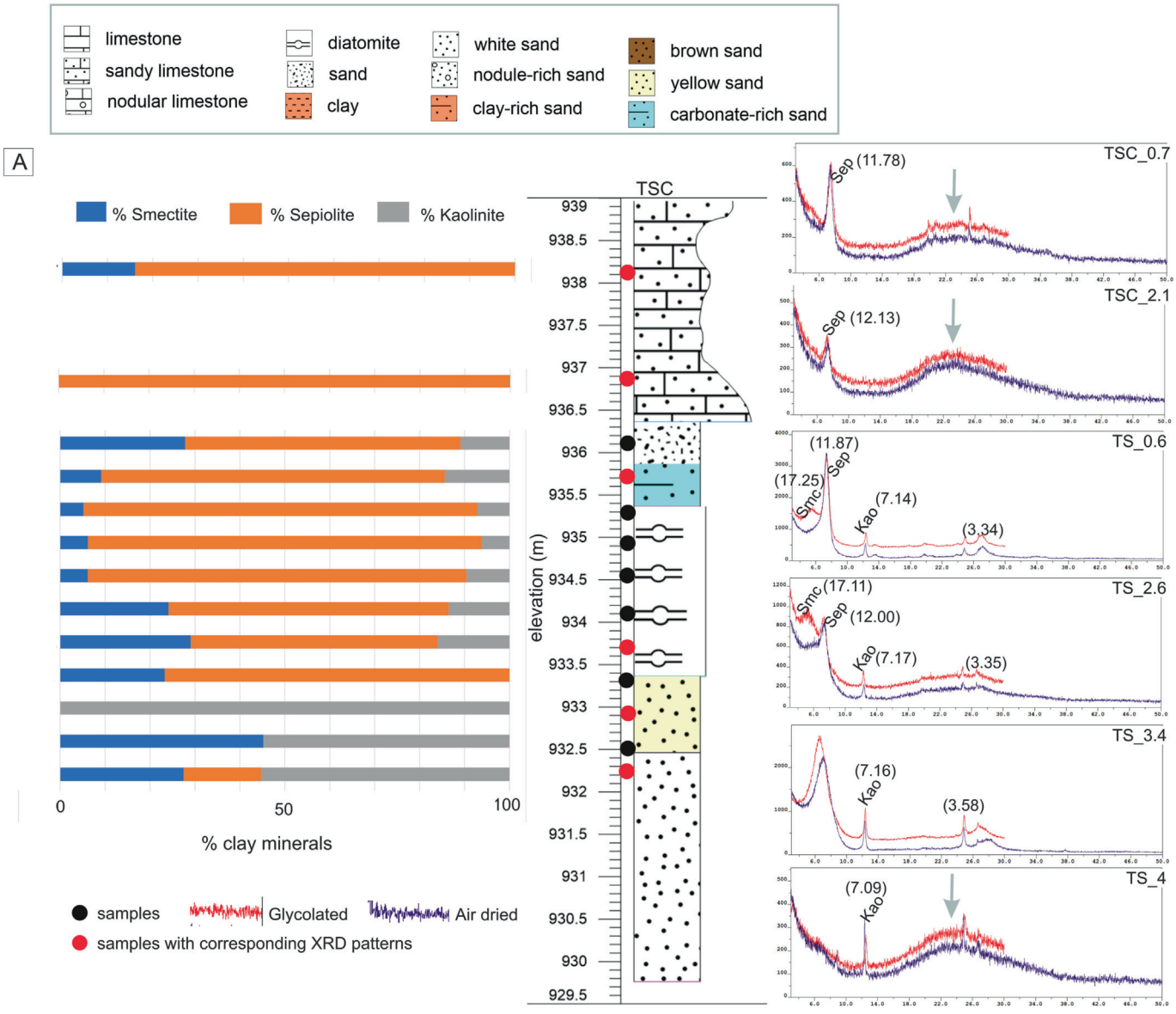

Fig. 3. Lithological log of the four study sites with corresponding clay mineral abundances and XRD patterns of the clay size fraction (<2 μm). Sep = sepiolite, Smc = smectite and Kao = kaolinite. (A) TSC site. (B) Baobab quarry. (C) Nata site (D) Acacia quarry. The gray arrow shows the diffuse peak over the angular range 14° to 36° indicating the presence of amorphous silica. The d-spacing is given in angstrom (Å).

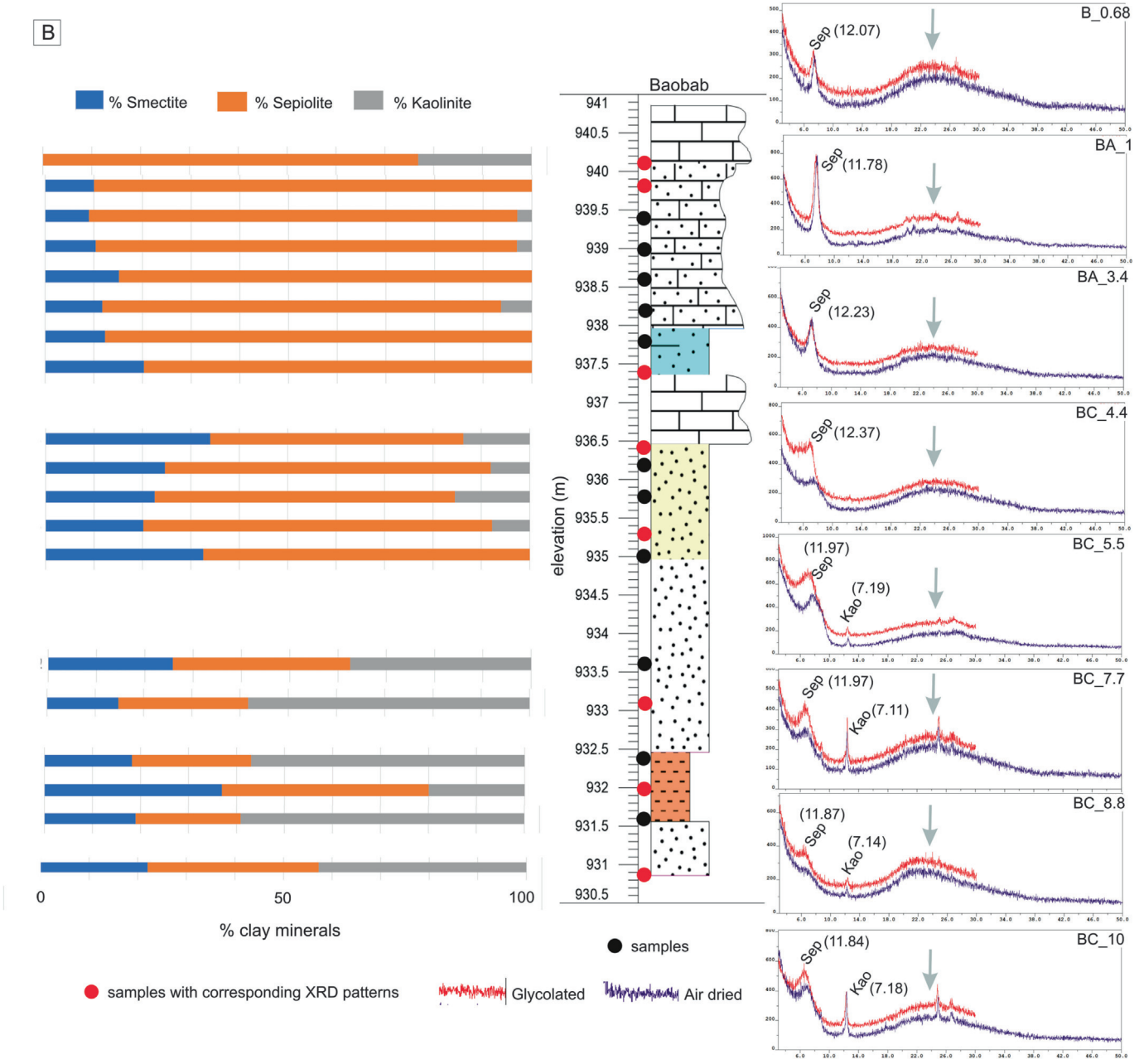

Fig. 3 (*continued*).

white sand below is made up of a yellow/brown sand. This is a significant feature, and the brown/yellow sands can be considered as a transition between two different paleoenvironments.

To summarize, all the outcrops include Kalahari Sands at their base. The transitions toward the top sandy limestones are made of some yellow sands with carbonate and occasionally, the presence of diatomitic layers.

4.2. Microscale distribution and fabric of the Chobe Enclave sepiolite

The proportions of phyllosilicates in the minerals present in the outcrops vary from 0 to 72 % (see Table in Suppl. mat.) with an average value of 23 % and a standard deviation of 14 %. When present, the proportions of sepiolite can reach 100 % among the phyllosilicates. Only two samples are totally devoid of this clay mineral. Within the phyllosilicates, sepiolite proportions in the Chobe Enclave sites have an average value of 69 % with a standard deviation of 26 %, making sepiolite the most prominent clay mineral of the area.

The distribution of sepiolite at the microscale allowed its relationship with other minerals to be assessed and to shed light on the sedimentological and chemical conditions that prevailed during its formation. The crystal morphology was first described using TEM as it is a pertinent approach to investigate, through the crystal shape, the potential in situ or reworked (detrital) origin of the mineral. Soil micromorphology descriptions have been used on multiple thin sections from sepiolite-rich layers. The following section describes their main characteristics observed in carbonate-rich and diatomite samples (*carbonate and diatomite facies*) containing sepiolite.

Carbonate facies are composed of microcrystalline, sandy, and nodular limestone with occasional *diatomite facies* intercalations (Fig. 2). These samples display a random distribution pattern with a single spaced porphyric c/f-related distribution (Fig. 4A, B). The coarse fraction is

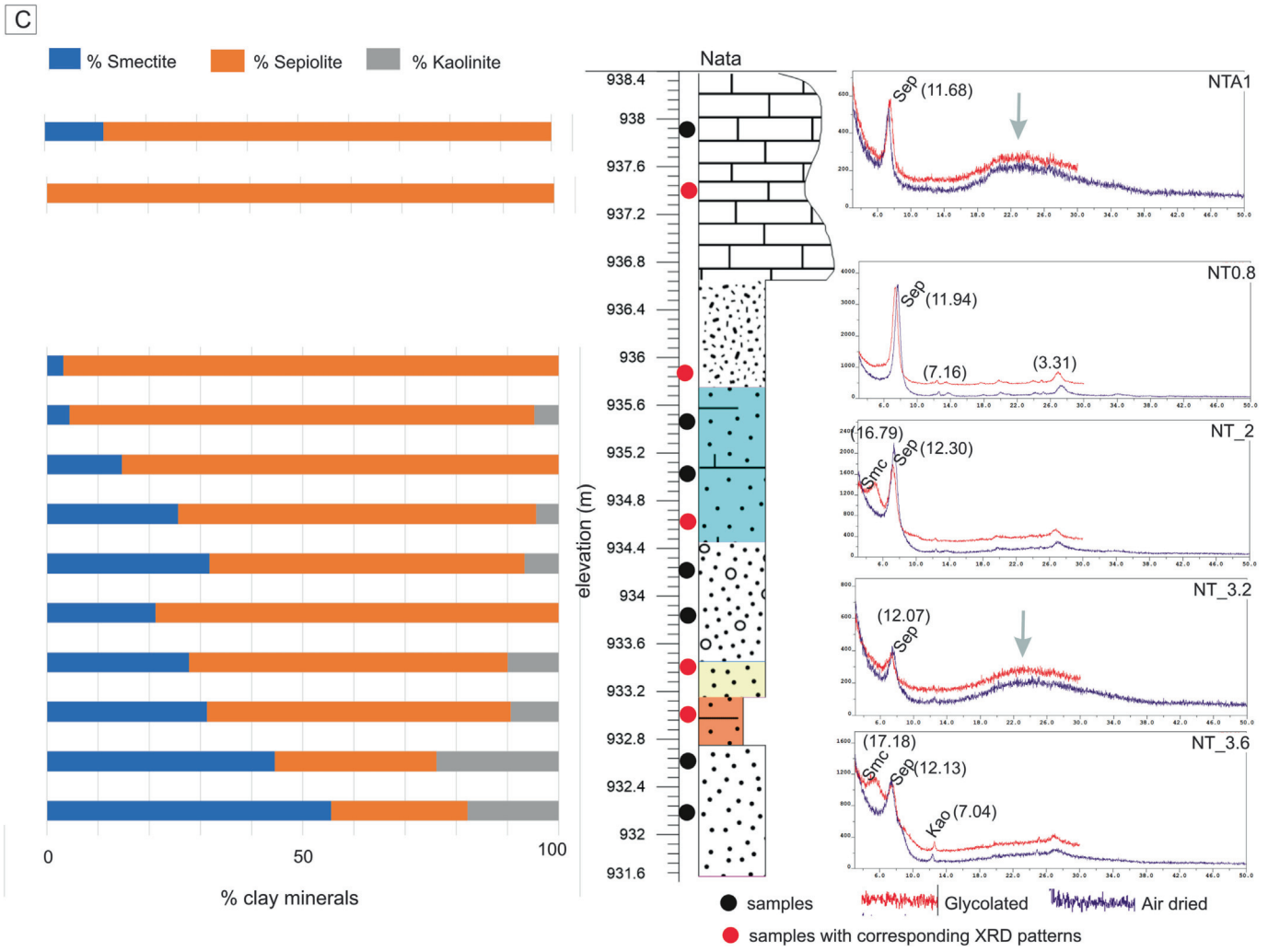

Fig. 3 (*continued*).

formed by quartz grains whose proportions are constant in the samples (around 30 %). Quartz grains are usually smooth, with a high to moderate sphericity and roundness, and well sorted. Their grain-size mode is around 200 μm and their leptokurtic distribution has been attested using conventional measurement of their grain-size distributions: these sands are mineralogically, as well as in terms of grain-size, like those forming the eolian Kalahari Sand (Thomas and Shaw, 1991; Vainer et al., 2018, 2022; Mokatse et al., 2022a). In addition to quartz grains, pedofeatures such as nodules, are frequently observed. They can be made of calcium carbonate (micritic disorthic nodules) or of amorphous to cryptocrystalline silica, attested using a first order retardation plate shifting the birefringence colors to the second order (Fig. 4C). The presence of amorphous silica associated with sedimentary deposits of the Kalahari Basin has already been documented (McCarthy and Ellery, 1995; Ringrose et al., 2008; Diaz et al., 2019). Regarding the micromass, which constitutes 65 % of the thin section area, its mineralogy is complex: it is a mixed phase of abundant sepiolite, with traces of carbonate and a clay size diatomitic mud. In addition to the micromass, other intrusive pedofeatures are present (forming around 5 % of the thin section) i.e., coatings around quartz grains, which can vary from calcite to sepiolite.

SEM investigations on sepiolite-rich samples of each location studied allowed the geometry between the various mineral phases to be clarified. As expected, crystals of homogenous fibrous sepiolite form mineral grain coatings (Fig. 5A) but also impregnate the groundmass (Fig. 5B), forming a dense mesh in the micromass, confirming the fabric observed under the optical microscope. Coatings are commonly observed on quartz grains and diatoms, but also on and next to rhombohedral calcite crystals (Fig. 5C). In samples with high contents of sepiolite, large cements of amorphous silica precipitate in a botryoidal pattern associated with individual spheres (Fig. 5D). Such facies could attest supersaturation spans, regarding the silicon ion, affecting the parent solution, and therefore some variability in pH toward alkalinity (Arbey, 1980). The differentiation between quartz grains, amorphous silica, or diatoms on one side, and sepiolite crystals on the other side, remains somehow challenging at some places, as the surface of the former minerals often shows dissolution features associated with visibly authigenic sepiolite. The thickness of sepiolite coatings varies but can reach about 10 μm for the thickest ones. Finally, TEM images confirmed the perfectly fibrous aspect of sepiolite, sometimes forming sheets, as documented in the literature (Wang et al., 2009). Individual fiber crystals have variable sizes but are 10 nm-large on average (Fig. 5E, F). The sheet-like arrangements of sepiolite crystals can form thin layers on large areas (Fig. 5E, F), which may coalesce (hundreds of μm^2) and finally coat quartz grains (Fig. 5A).

In conclusion, microscopical investigations allow a succession of sediments and phases to be assigned: quartz grains from the Kalahari Sands constitute the coarse fraction of the beds. A diatomite mud is frequently associated with this sand, forming the initial groundmass. This groundmass is then enriched in calcium carbonate as either traces of micrite in the micromass or as disorthic to anorthic micritic nodules. Impregnative sepiolite invades the micromass and coats large grains (quartz sand), the diatomite micromass, and pore walls. Finally, an

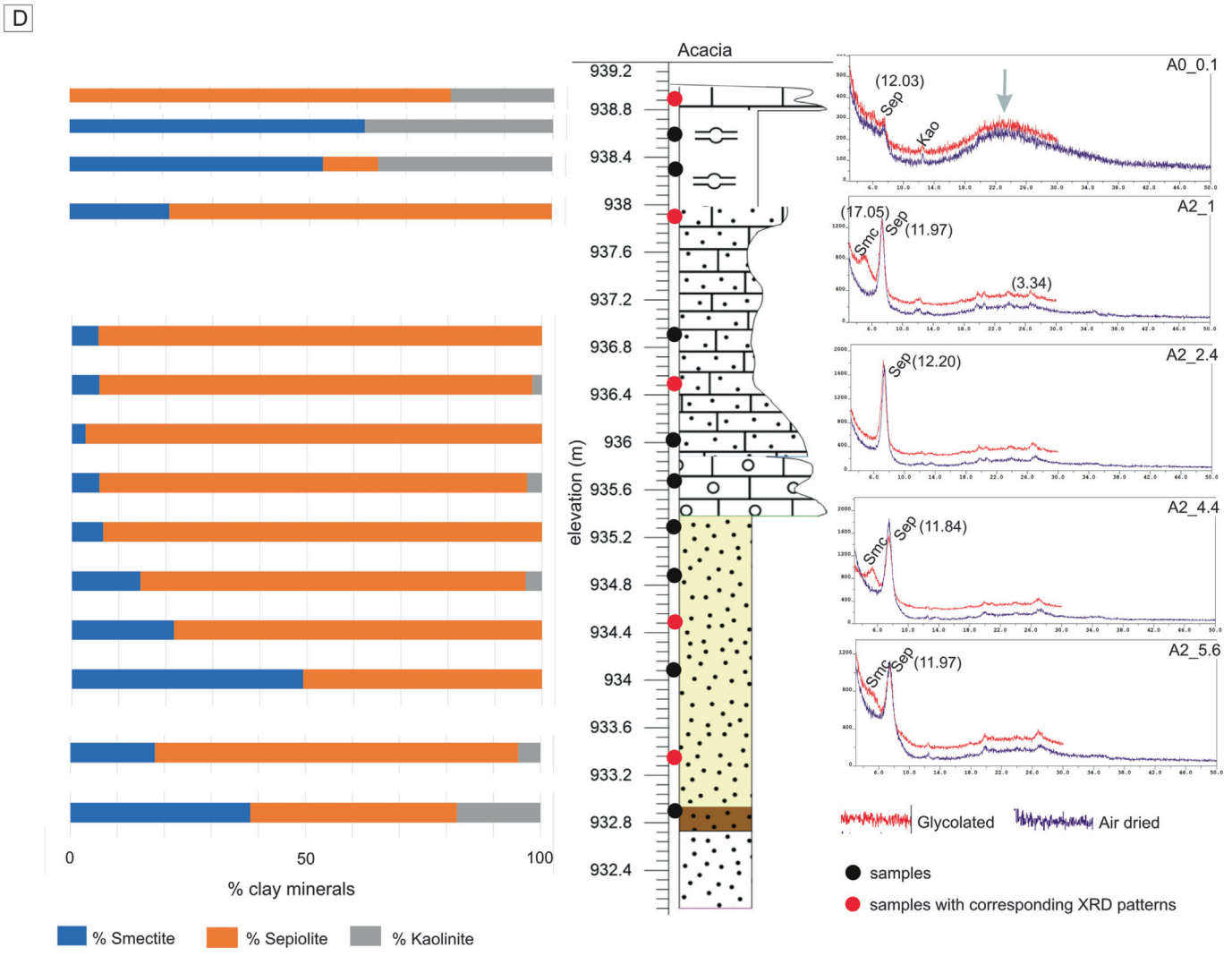

Fig. 3 (*continued*).

amorphous siliceous phase, in a botryoidal pattern associated with individual spheres, ends this mineralogical sequence. This sequence must reflect the evolving composition of the solution in the environment. Regarding sepiolite, its silicon part can easily be provided by the environment, rich in siliceous components, whereas the origin of the Mg^{2+} remains unsolved.

4.3. Minerals associated with sepiolite

Analyses of bulk-XRD samples are dominated by three main types of minerals: quartz (and amorphous silica), calcite, and phyllosilicates, which were identified using a semi-quantitative method (see Table in Suppl. mat.). Quartz is always present in the samples and constitutes almost 100 % of the mineral fraction in the deepest deposits found at each location. These layers correspond to the Kalahari Sands. The composition of sediments changes along the outcrops with varying proportions of calcite, with a content reaching sometimes ~80 % in the carbonate-rich layers, e.g., in TSC and Nata sites. The clay mineral XRD analyses display sepiolite dominated sections, mostly occurring in carbonates associated with some smectite and kaolinite. The presence of kaolinite and smectite would indicate a greater contribution from the detrital material, probably originating from the weathering of the Karoo basalts (Garzanti et al., 2014). Barite ($BaSO_4$) has also been detected in some samples but (i) it cannot be quantified due to the low intensity of their respective peaks, and (ii) occurs mostly as an accessory mineral and represents <5 %. However, the presence of barite associated with palustrine limestone is of interest (Fig. 6), as occurrence of both sepiolite and barite raises more questions regarding the sources of Mg and Ba, respectively. There are also some traces of gypsum, which appear only on XRD diffractograms of a few samples, mainly located in the Acacia Quarry and associated with diatoms (amorphous silica phase).

Moreover, in the literature, sepiolite deposits are generally associated with potential sources of magnesium, such as dolomite (Watts, 1980; Galán and Pozo, 2011). Surprisingly, there is no trace of dolomite in the study samples. Consequently, the magnesium ion must originate from another host rock or source to support the precipitation of sepiolite.

Finally, X-ray diffraction (XRD) patterns clearly point to a clay fraction almost exclusively composed of sepiolite, with minor proportions of smectite and kaolinite, although an amorphous silica phase is also present (likely as a diatomite fine earth; Fig. 3A–D). XRD patterns noticeably record all the expected peaks of sepiolite, according to Galán and Singer (2011), when the clay mineral is present in large amounts; its identification is still easy in diffractograms with peaks of less amplitude.

4.4. The chemical composition of sepiolite

Semi-quantitative chemical compositions of sepiolite carried out by TEM-EDAX are plotted on a ternary diagram (Fig. 7): the three variables refer to the respective contents in silicon (Si expressed as SiO_2 wt%), magnesium (as MgO wt%), and iron plus aluminum (expressed as

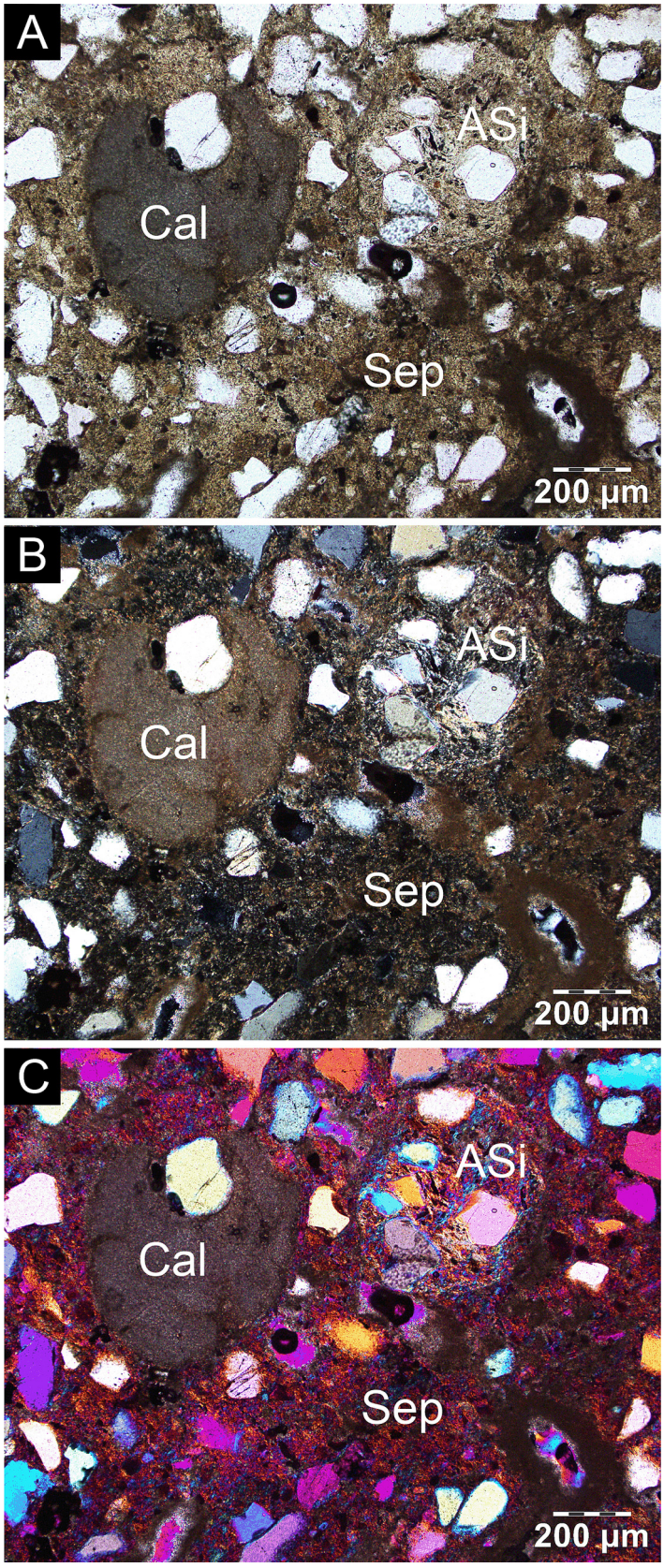

Fig. 4. Optical microscope images of a sample with a high sepiolite content. The groundmass includes pure sepiolite (Sep) in the micromass, which is also coating some quartz grains (in white in A; in white to dark gray in B). The presence of calcite is attested by a nodule of micrite (Cal) and there is only scarce micrite in the micromass. Moreover, another nodule, this time of amorphous silica (ASi) emphasizes the presence in the thin section of other siliceous phases than clay minerals. (A) Natural light (PPL). (B) Crossed-polarized light (XPL). (C) Cross-polarized transmitted light with the first order retardation plate (gypsum plate) inserted into the light path; the use of the gypsum plate facilitates the identification of silica-rich phases by shifting the color of quartz, sepiolite, and amorphous silica to a higher order i.e., bright blue, yellow, and pink; calcite remains the same as in XPL.

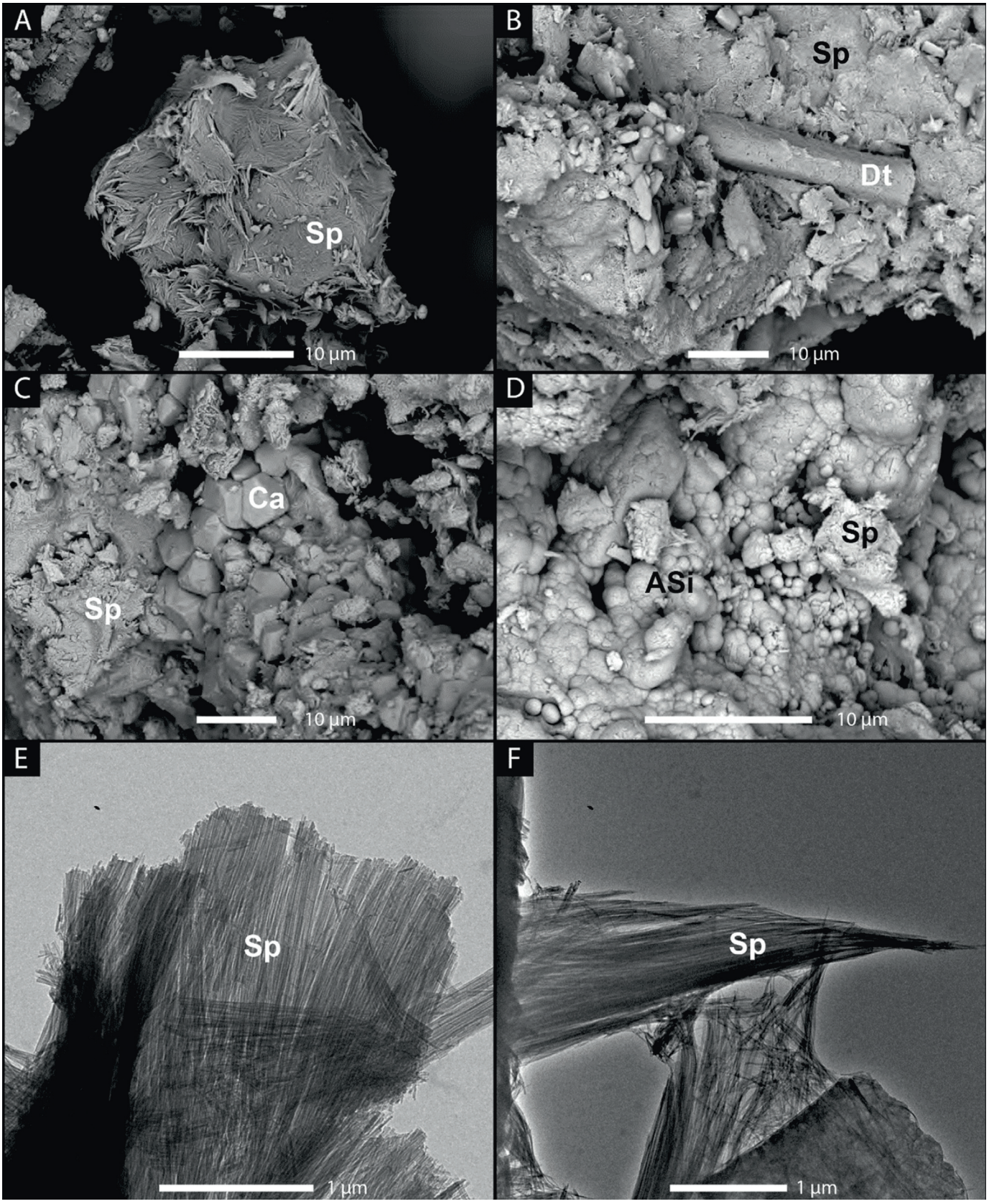

Fig. 5. Scanning electron microscope (SEM) and transmission electron microscope (TEM) images of sepiolite. A) SEM micrograph of a sepiolite (Sp) coating on a quartz grain showing a random orientation of crystals with fusiform shape tips. B) SEM view of a preserved diatom (Dt) in a sepiolite (Sp) matrix with some fine silt-size quartz. Sepiolite crystals are thinner and smaller than in A). C) SEM view of a rhombohedral calcite cement (Ca) associated and partly covered by sepiolite crystals (Sp). D) SEM image showing amorphous silica spheres (ASi) arranged in a botryoidal texture and precipitated inside a pore in a sepiolite (Sp) matrix. The C) and D) SEM views emphasize the following succession of minerals: calcite precipitated first, then sepiolite, and finally amorphous silica. E) TEM image showing the fibrous structure of the sepiolite (Sp) and particularly a large sheet of sepiolite fibers. F) TEM view of fusiform sepiolite (Sp) arrangements.

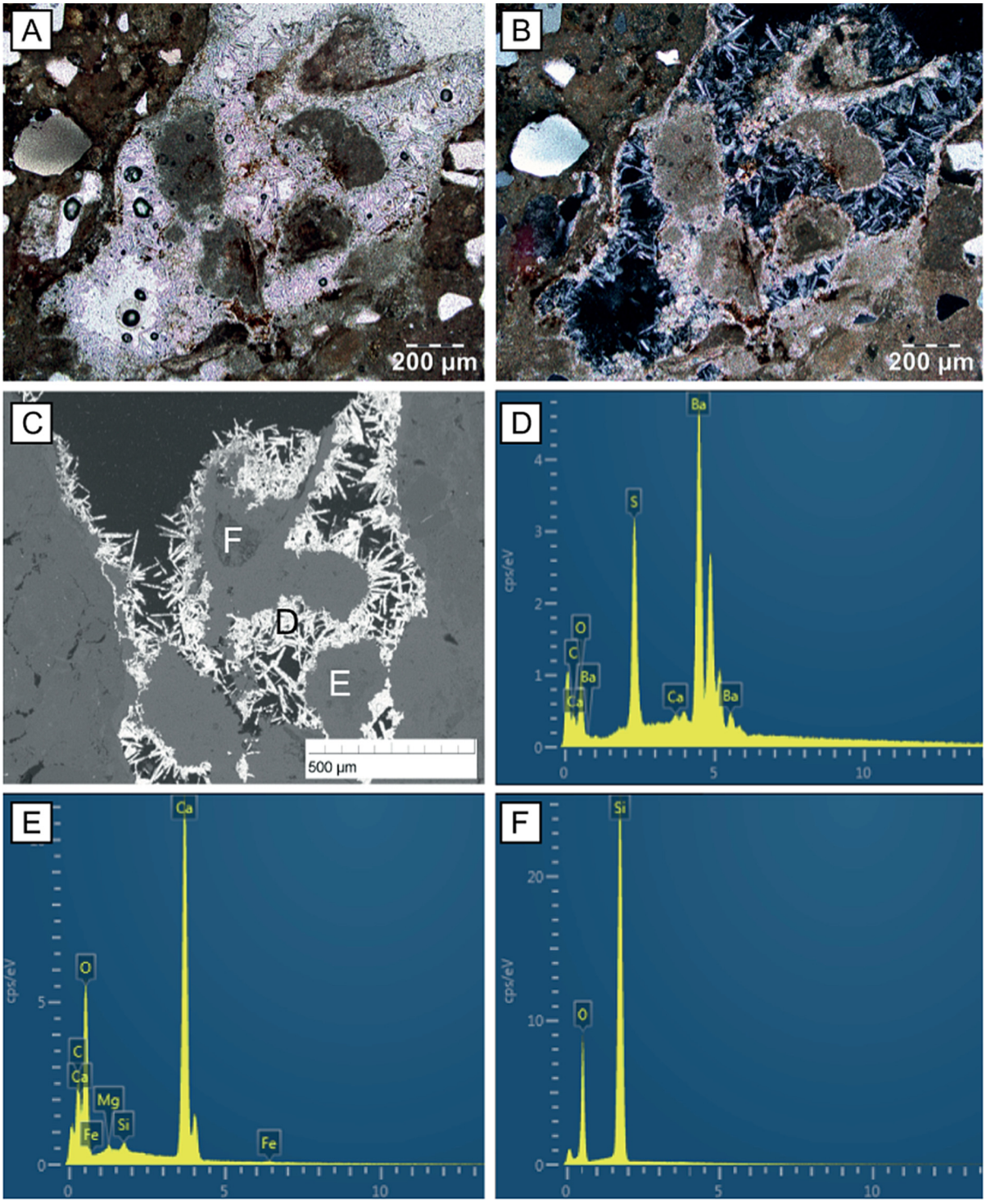

Fig. 6. A) Thin section of a palustrine limestone in which styloidic crystals of barite formed, attached to micritic clasts of reworked mud. View in plane-polarized light. B) Same view in crossed-polarized light. Bright needles of barite contrast with the extinct background. The large white minerals different from barite are quartz grains. C) Same thin section observed with a scanning electron microscope in backscattered electron mode: barite appears in white (greater atomic number than the compounds of the background). D, E, and F letters refer to the areas analyzed by EDAX. EDAX spectra are the following: D) spectrum of barite crystals; presence of Ba and S, as barite is a barium sulfate; E) spectrum of the calcium carbonate micromass forming the palustrine limestone (presence of Ca); F) quartz grain with essentially silicon (Si).

$[Fe_2O_3 + Al_2O_3]$ wt%). The selection of these elements is justified by the theoretical composition of sepiolite, which is:

$$\left(Mg_{8-y-z}R^{3+}_{y}\square_{z}\right)\left(Si_{12-x}R^{3+}_{x}\right)O_{30}(OH)_4(OH_2)_4R^{2+}_{(x-y+2z)/2}(H_2O)_8$$

according to the review by Suárez and García-Romero (2011) and based on Brauner and Preisinger's (1956) formula, where cation occupancies (R) are mainly Al^{3+}, Fe^{3+}, Fe^{2+}, Ti^{2+}, rarely Cr^{3+} and Ni^{2+} (with the range of octahedral cations varying between 6.87 and 8.11). Moreover, a similar ternary diagram by Suárez and García-Romero (2011), compiling a large set of data from the literature, is used to compare the amounts of elements found in the Chobe Enclave sepiolite with sepiolite compositions from other sites worldwide (Fig. 7). Indeed, the sepiolite compositions from Suárez and

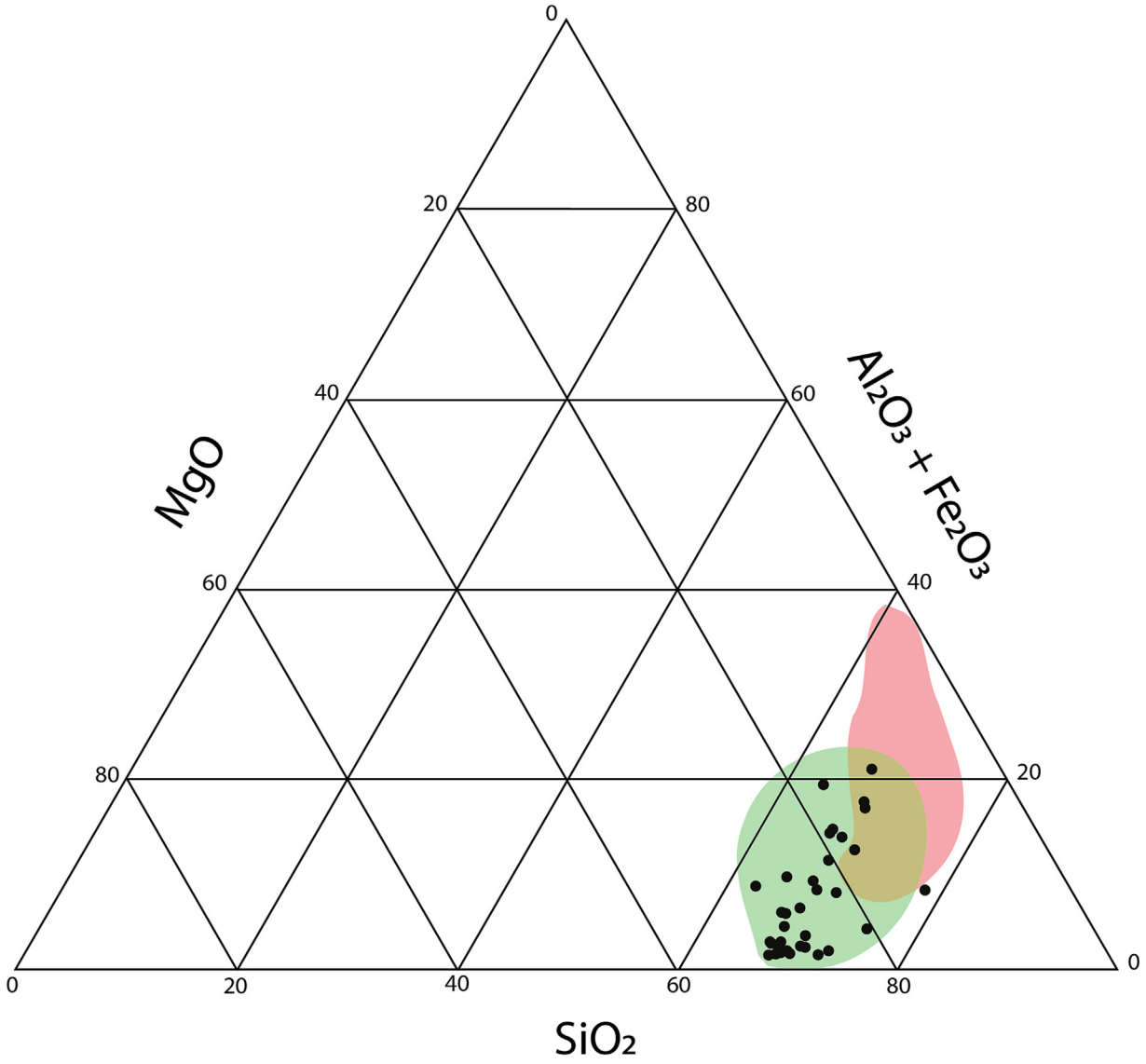

Fig. 7. Relative contents of Si, Mg, and Al + Fe (expressed as oxides, SiO_2-MgO-Al_2O_3 + Fe_2O_3) in sepiolite crystals from study sites and literature plotted in a ternary diagram. Measurements have been performed with an EDAX microprobe coupled to a TEM. Black dots refer to the results from this study, whereas the diversity of sepiolite and palygorskite compositions given in the literature review from Suárez and García-Romero (2011) is symbolized as two clouds in green and red, respectively.

García-Romero's (2011) data set are all included in the green area drawn in Fig. 5 (for comparison, palygorskite data are clustered in the red area; Fig. 7). As expected, the observed samples from the Chobe Enclave (n = 36) are all included in the sepiolite area from Suárez and García-Romero (2011), emphasizing their clear and expected sepiolite composition. Nevertheless, there is a slight dispersion of sepiolite chemical compositions, varying from values situated in the bottom part of the green cluster (Fig. 7) to its top where slightly enriched Al-sepiolites are plotted. Although there is a minor superimposition of the respective chemical domains of the two fibrous clays in the reference ternary plot (Suárez and García-Romero, 2011), Al-sepiolite is more likely than palygorskite as this mineral is hardly detected in XRD patterns. In conclusion, XRD and TEM-EDAX analyses of clay fractions highlight the particular enrichment in sepiolite associated with specific deposits of the Chobe Enclave.

4.5. Major and trace elements in sepiolite beds

Contents of major elements in sediments reflect the composition of the three main minerals detected by XRD analyses i.e., quartz, calcite, and sepiolite. Silicon and calcium are the dominant elements, and their respective proportions vary with the rock type, from calcite cemented sandstones to limestones. Samples with sepiolite are enriched in magnesium compared to limestones due to the composition of the fibrous clay. Soil samples of Acacia quarry contain significant proportions of iron. Fe_2O_3 contents can reach almost 6 % in sandy sediments (with 80 % SiO_2), whereas limestones contain <2.5 % of Fe_2O_3.

Contents of barium in the different quarries vary from <100 ppm to almost 2400 ppm. Unexpectedly, these values are high compared to the mean Ba content observed in Karoo basalts and dolerite (<500 ppm), which are the nearest and most potential sources of Ba easily transportable by rivers. This large difference has been also observed in the Makgadikgadi paleo-lake located in the south of the Chobe Enclave. This paleo-lake deposit contains, at its minimum, 190 ppm of Ba in silcretes but can reach 4820 ppm in deposits composed by a mixed silcrete and calcrete layer (Ringrose et al., 2009). Surprisingly, the Sr content in the Chobe Enclave does not seem to be related to Ba, contrarily to Ringrose et al. (2009).

Finally, in Acacia quarry, sample contents in aluminum are correlated to silica contents. This relationship must be explained by the

presence of diatom frustules, which can enhance aluminum enrichment, as suggested by Koning et al. (2007), Michalopoulos et al. (2000), and Ren et al. (2013). Nevertheless, the presence of some Al sources from sepiolite cannot be totally precluded because, as emphasized above in the section about the chemical composition of sepiolite, the presence of some Al-sepiolite remains possible.

To conclude, the results emphasize a mineralogical system with four mineralogical end-members i.e., quartz, calcite, sepiolite, and amorphous silica (in the shape of diatoms or as a secondary amorphous cement). The presence of sepiolite is somehow difficult to explain if it is referred to the conventional environments described in the literature (Galán and Pozo, 2011). Although strong evaporation and the presence of dissolved silica in the water seem likely in this region, the necessary contribution of a magnesium source remains challenging. Indeed, in the literature, sepiolite precipitation is often associated with dissolution of dolomite or alteration of magnesium-rich metamorphic rocks (Galán and Pozo, 2011). In the Chobe Enclave, there is no trace of dolomite and the nearest volcanic rocks (the Karoo Complex) seem unlikely to provide the necessary amount of magnesium to provide surface water with a suitable concentration of Mg^{2+}. Another important discrepancy with literature lies in the fact that the evaporitic mineralogical series, usually associated with sepiolite, is absent in the Chobe Enclave. Only carbonate is formed, whereas gypsum, found in some samples, represents only a minor part of the mineral phase, and is probably related to the activity of termites (Van Thuyne et al., 2021) or to some eolian contributions (McCarthy, 2013). Finally, the discovery of a large quantity of Ba in the form of barite adds one more question to the sedimentary settings of the Chobe Enclave. This mineral, seldom associated with sepiolite, could point to a hypothesis not yet discussed, i.e., hydrothermalism.

Consequently, the relationships between the various mineralogical and geochemical variables were assessed using a principal component analysis (PCA). The PCA clearly differentiates between three clusters: a carbonate–sepiolite one, a detrital pole, and a last one related to a likely hydrothermal influence (Fig. 8). Planes plotted using PC4 vs. PC1 (Fig. 8A) and PC2 vs. PC1 (Fig. 8B) account for 54.9 % and 65.0 % of the total data variance, respectively. The first principal component (PC1) shows a positive correlation with Si, Zr, and kaolinite components (Fig. 8A, B), and correlates negatively with sepiolite, Mg, Mn, and Ca. The second principal component (PC2) correlates negatively with Fe and K (Fig. 8B). Moreover, the fourth principal component (PC4) correlates negatively with only Ba (Fig. 8A). A high positive PC1 score indicates detrital material, whereas the carbonate facies have a negative PC1 score. On the other hand, the hydrothermalism pole plots in the negative field of the PC4 coordinate. Consequently, on one hand, most variations accounted for by PC1 are a function of lithological variation i.e., from the detrital component to the carbonate–sepiolite reactor. On the other hand, variations accounted for by PC4 point to chemical changes due to potential hydrothermal input (Ba variable). In addition, the approaching right angles between Ba and PC1, and Fe–K and PC1, emphasize an absence of linear relationships between these variables and PC1: in other words, these elements are not controlled by the two end-members given above, but are likely to be part of an assemblage associated with either hydrothermalism, for Ba, or with weathering of some mineral phases that host Fe and K. All these relationships will be discussed in the following section.

5. Discussion

The sepiolite precipitation in the Chobe Enclave must reflect a specific type of depositional environment. The geochemical composition of sepiolite, which includes Si and Mg, reflects the enrichment in these elements of the parent solution from which the sepiolite precipitated. In the literature, two main factors contribute to increase the concentration of these elements in a hydro-sedimentary environment: (i) a significant input of ions from rivers or from hydrothermalism (Irkec and Ünlü, 1993; Galán and Pozo, 2011), and (ii) an evaporative system (Helgeson et al., 1969). Tectonic activity has been obviously operating in the study area, changing the watershed and basin geometry forming and re-shaping various waterbodies in the Kalahari Basin (Shaw and Thomas, 1988; Burrough and Thomas, 2008; Vainer et al., 2021) that are clearly attributed to the result of such tectonic effects (Moore, 1999; Ringrose et al., 2005; McCarthy, 2013). Alongside the influence

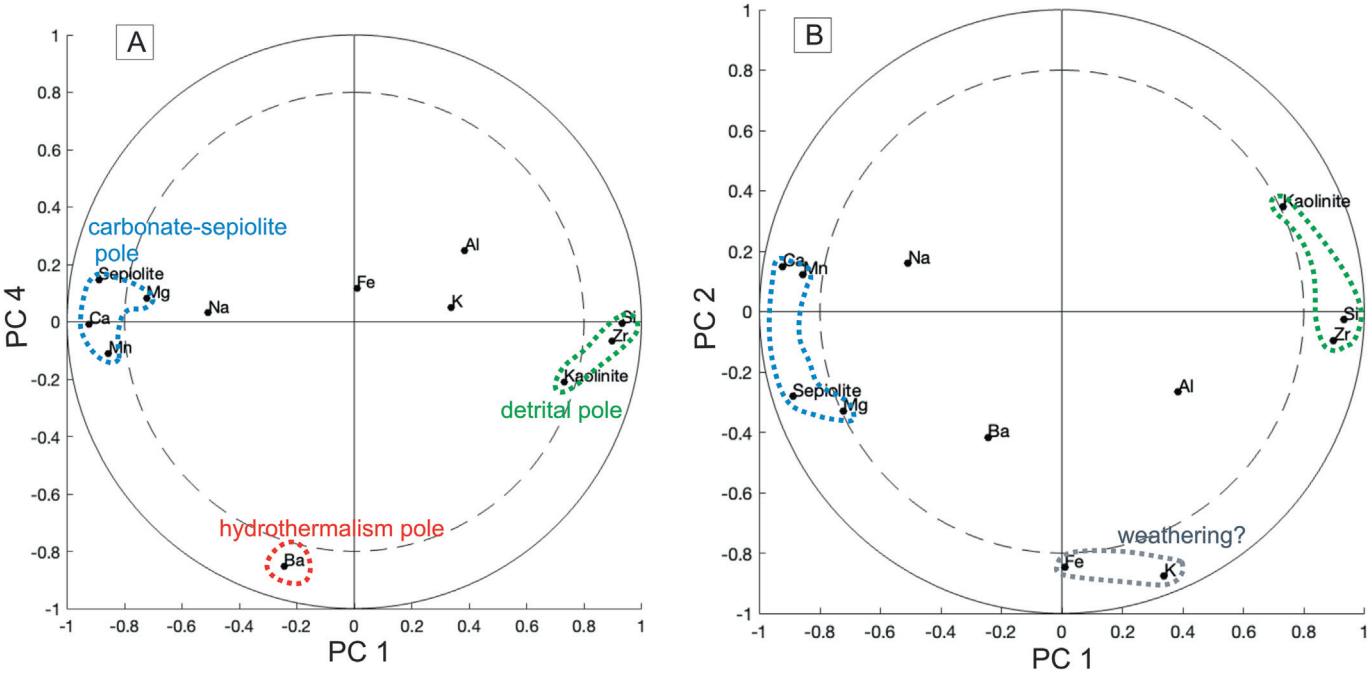

Fig. 8. Circle of correlations between variables and principal components obtained during PCA of Chobe Enclave samples showing the two planes, (A) PC4 vs. PC1 and (B) PC2 vs. PC1. Three groups of variables are identified; they refer to three main poles: a carbonate–sepiolite, a detrital, and a hydrothermalism one according to their color. A fourth cluster centered on Fe and K variables could eventually refer to a weathering pole, although still questionable. The plane in A explains 54.9 % of the total variance whereas it is 65.03 % in plane in B. See also Table 1.

of neotectonics on the landscape evolution in the Chobe Enclave (Mokatse et al., 2022b), hydrothermal springs of low temperature have been reported in northern Botswana (Niles, 2012; Mukwati et al., 2018). However, the potential influence of hydrothermal springs on the sedimentology of the Chobe–Linyanti sub-basin was never mentioned. Furthermore, the hydrological system of northern Botswana and its history through the Quaternary are complex (Nugent, 1990; Moore et al., 2012). In this context, the settings that governed the precipitation of sepiolite might provide interesting evidence on the paleoenvironmental system of the Chobe Enclave during the Quaternary (Fig. 2). The following discussion explores the potential origin of parent solutions and the establishment of sub-environments related to sepiolite formation (Tosca and Masterson, 2014). This approach will also be based on a precipitation model for sepiolite in the Chobe Enclave. Finally, potential hydrological and sedimentological properties of the Chobe Enclave area will be introduced with the aim of proposing a reconstruction of the environment in which sepiolite has been precipitated during the Quaternary.

5.1. The origin of sepiolite

5.1.1. Source area contributions

One aspect to understand the origin of sepiolite is to decipher the sources of Mg and Si ions. One of the primary concerns about fibrous clay minerals is whether their origin is a transformation of precursor clay minerals or a precipitation directly from solutions (Singer, 1979; Pozo and Galán, 2015). In the Chobe, SEM and TEM analyses reveal the sepiolite to be authigenic (Fig. 5), indicating that the parent solution must be concentrated enough in magnesium and dissolved silica to trigger the precipitation of the mineral. In this case, possible water sources constitute relevant concerns to explore in the region. In the present day, the main origin of water flowing to the Chobe Enclave is sourced from the watersheds located in the equatorial Angolan highlands and Zambia. Water is provided to the south by three main rivers: 1) the Kwando–Linyanti, 2) the Cuito spilling in the Okavango from the Angola watershed, and 3) the Zambezi from the Zambia watershed (Moore et al., 2012; Fig. 1). Surface water in the region can be classified as calcium–magnesium–(sodium)-bicarbonate type waters from the aforementioned major rivers. Even so, the geology of the catchments slightly varies as the Zambezi River waters have a higher Ca/Mg compared to the Okavango River waters. In addition, the Zambezi River waters have a pH of around 7.5 compared to about 6.9 of the Okavango, suggesting the presence of carbonate-bearing rocks in the Zambezi basin (Mokatse et al., 2022a). However, the extremely evaporated terminal swamp waters of the Chobe/Linyanti are sodium–(potassium)-chloride type with local sulfate concentrations (Atekwana et al., 2016; Dyer, 2017). Still, there are less recognized mineral phases of evaporites in the studied samples of the Chobe Enclave than would be expected from these different sources.

The deposits in the Chobe Enclave largely show a lower unit dominated by sand-rich material (white sands). This unit contains detrital clays and reworked detrital sediments. Kaolinite and minor smectite are dominant in the white sands (Fig. 3A, B). Moreover, this lower unit shows Zr enrichment (Fig. 2) that is consistent across all sites, emphasizing a detrital origin (Fig. 8). The detrital origin of the clay minerals is also attested by the PCA (Fig. 8), hence, suggesting the deposition by fluvial systems which drained relatively wetter climate areas than in the present time (Garzanti et al., 2014, 2022). However, it is worth noting the minor contents of sepiolite observed in this unit, which could have likely not formed in situ. Above the lower unit, there is a transition zone denoted by yellow/brown sands. This zone shows significantly lower contents of detrital clays (Fig. 3), with a notable enrichment of Ca (Fig. 2). This would emphasize the input from wet periods/spells: indeed, deposition of carbonate in a palustrine environment and diatomite facies occurred preferentially in humid conditions. Following this period, the enrichment of Zr and depletion of Ca (Fig. 2) indicate a period of reworking/detrital input. Presently, both the carbonate and diatomite facies host sepiolite (Fig. 4) with relatively lower content in diatomites (Fig. 3A, D) and higher content in carbonate. This consequently underlines the adequate input of Mg and Si ions in the system able to precipitate sepiolite during the deposition of these beds.

5.1.2. Sepiolite precipitation: was the Chobe Enclave an evaporitic environment?

The conditions in which the sepiolite is stable provide clues about the paleoenvironment they form in. A thermodynamic stability diagram, adapted from Helgeson et al. (1969), shows what a precipitation sequence of minerals must be expected from a water body in a $CaO–MgO–SiO_2–CO_2–H_2O$ evaporitic system of a lake in the Sierra Nevada (Fig. 9). Fig. 9 clearly displays the succession of the mineral phases during the evaporation process i.e., when the solution concentrates with time. The various species in the parent solution ($Si(OH)_4$, Ca^{2+} and Mg^{2+}) exhaust during the sequential precipitation of minerals i.e., calcite first, then sepiolite, and finally amorphous silica. The solution concentration due to the evaporation also triggers an increase in pH, leading to the precipitation of Ca-carbonate from the aqueous solution at pH around 8.4, and amorphous silica at a pH around 8.7. Obviously, as long as there are carbonate and calcium ions in the solution, calcite will precipitate until the Ca^{2+} reservoir is exhausted. The sepiolite precipitation occurs after calcite nucleation at a pH slightly more alkaline (Fig. 9). The stability of sepiolite is a function of pH (Galán and Singer, 2011). At this moment, the Mg^{2+} concentration starts to decrease in the aqueous solution as it is integrated into the sepiolite. Regarding the dissolved silica concentration, it continues to increase even if some silicon is incorporated into the fibrous clay. Finally, when Mg^{2+} is exhausted from the parent solution, $Si(OH)_4$ amorphous silica precipitates as the final mineral component. Consequently, the mineralogical assemblage (calcite, sepiolite, and amorphous silica) observed in the Chobe Enclave (Figs. 4 and 5C, D) results from a succession that is identical to the one provided by the model. Indeed, the geometrical relationships between the mineral phases (Fig. 5C, D) clearly show the presence of a rhombohedral calcitic cement associated with and partly covered by sepiolite crystals, as the clay minerals precipitated after the Ca-carbonate. On top of the sepiolite and calcite association, spherical amorphous silica precipitated inside a pore coated with sepiolite. This succession highlights the sequence of precipitation i.e., calcite precipitated first, then sepiolite, and finally amorphous silica. Moreover, the presence of sepiolite in palustrine carbonate facies is often considered to be closely related to semiarid evaporitic environments (Singer, 1984; Jones and Galán, 1988; Chamley, 1989 and references therein). However, the absence (or lack) of evaporites in the Chobe Enclave possibly indicates that the sepiolite was not generated under conventional extreme evaporitic conditions, especially since the regional waters are presently enriched in sulfates (see section above). Consequently, another potential and contributing source for ions must be proposed: it is likely that some parent solution was also locally enriched from a water source also concentrated in ions such as Mg^{2+} and Ba^{2+}, a hydrothermal source, a hypothesis discussed in the next section.

5.1.3. Is hydrothermalism a common feature of the Chobe Enclave?

Barite is often observed associated with carbonates in the Chobe Enclave (Fig. 7), raising the same question about the origin of the barium ion. Barite is usually documented in environments under the influence of hydrothermal or evaporation processes (Hanor, 2000) but was also recognized in soils and surficial sediments (Stoops and Zavaleta, 1978). It is frequently associated with sepiolite, calcite, and amorphous silica (Brock-Hon et al., 2012; Robins et al., 2012; Brock-Hon and Elliot, 2013), as it is in the Chobe Enclave (Figs. 5 and 6). In the Chobe samples, barite clearly postdates the silicification process and calcite formation (Fig. 6), as also observed by Clarke et al. (2016). Although its formation can be attributed to soil dynamics, it remains difficult to explain the source and presence of barium in the Kalahari Sands prior its

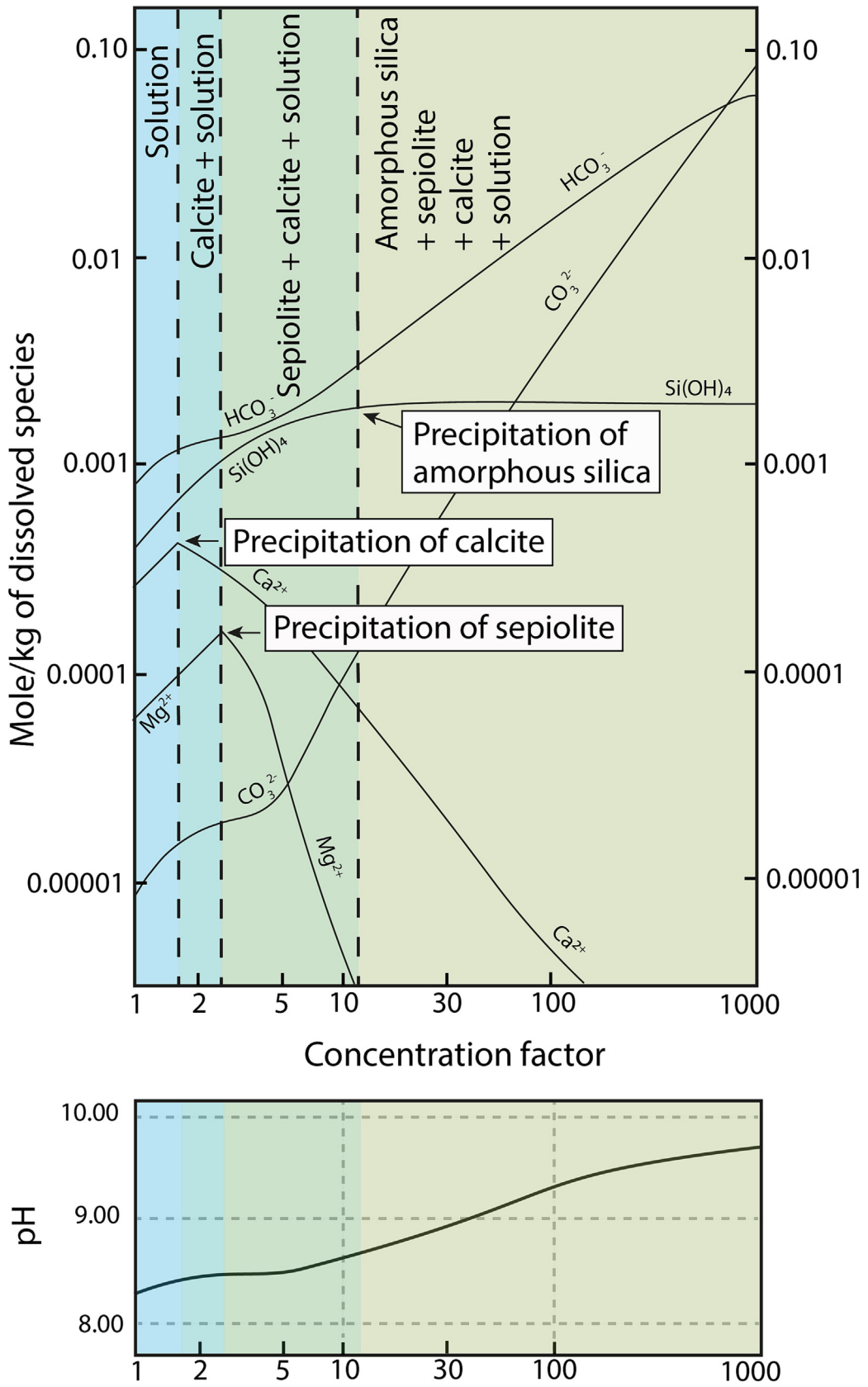

Fig. 9. Plots of concentrations in various element species and pH values in a water solution during an evaporation process based on Helgeson et al. (1969). The x-axis refers to the concentration factor of the solution, whereas the y-axis refers either to the content in mol·kg^{-1} of dissolved species (top) or to pH (bottom). Calculations have been made by Helgeson et al. (1969) for a system composed by CaO–MgO–CO_2–SiO_2–H_2O at 25 °C. Activity coefficients and equilibrium constants used for their diagram come from both their field and computed data (see their paper).
Redrawn and adapted from Helgeson et al.'s (1969) Fig. 8.

remobilization through pedogenic processes. However, the PCA suggests that barium does not show any correlation with the detrital and carbonate–sepiolite end-members (a π/2 rad angle between the variable poles; Fig. 8 and Table 1), although accounting for 7.5 % of the total variance, which is not negligible. This absence of significant correlation can easily be interpreted as a random process, which is superimposed and associated neither with detrital phases nor with some conventional evaporitic process, as documented by the two poles along PC1 (Fig. 8). As in such environments, the barium leached by hydrothermal waters from the basement rock can combine with sulfur, forming barite after silicifications and calcite formation (Su et al., 2020). Even though barite has been clearly identified as a secondary mineral in the Chobe Enclave (Fig. 8), its origin and significance still need further investigations. In conclusion, a possible lacustrine hydrothermal contribution seems to be likely in some specific layers (Fig. 8), strengthening fortuitously conditions for, eventually, local sepiolite formation.

5.2. Sepiolite and the Chobe Enclave evolution during the Quaternary

From the mineralogical and PCA results, clay minerals, such as kaolinite and smectite (although with minor contents), were identified as witnesses of detrital phases. On the other hand, the absence of palygorskite in the Chobe Enclave is pointing to a closed palustrine/lacustrine system, in which the water body was depleted in aluminum and iron (Galán and Singer, 2011; Fig. 7). The detrital clays, particularly kaolinite and likely smectite, are relatively abundant on the lower white sands (alluvial fan/fluvial) of the Chobe Enclave (Fig. 3A, B). These detrital phases suggest that kaolinite was produced possibly in humid upper-catchment regions of sub-equatorial Angola and Zambia (Garzanti et al., 2014). Hence, this assemblage associated with the sandy-rich lithology (Fig. 2) depicts conditions prior to the palustrine carbonate formation in the Chobe Enclave. This humid event was followed by a dryer episode, which increased the salinity of shallow lakes/marshes in a closed lacustrine/palustrine system with low energy. With favorable depositional conditions i.e., increased pH and requested ionic concentrations, it was possible to precipitate authigenic sepiolite, associated with the palustrine carbonate facies. The environmental conditions, documented from past and present-day systems and favorable for precipitation of fibrous magnesium-rich clays, probably also occurred during the Late Pleistocene to Holocene when palustrine carbonate deposited in the Chobe Enclave. Indeed, the carbonate precipitation events occurred irregularly, since ~75 ka (Diaz et al., 2019; Mokatse et al., 2022a; Fig. 2). These palustrine carbonate facies, with the highest authigenic sepiolite content, suggest the presence of a favorable reactor for sepiolite precipitation in semiarid or arid conditions (Helgeson et al., 1969). The presence of amorphous silica, also points to relatively higher alkalinity in the system (Galán and Singer, 2011; Fig. 9).

Sediment association found in the Chobe Enclave is closely like the Okavango alluvial fan deposits described by Ringrose et al. (2008). There, the lower part of the deposits, characterized by carbonate as a dense groundmass (McCarthy et al., 2012), directly lies on thick quartz sand layers: this suggests a shallow lake episode in the Chobe Enclave, with a lower water table depth compared to the present level, and provided by a hydrological or climate change (Cordova et al., 2017). Such deposits have been documented in the Madrid Basin where "the sepiolite deposits formed mainly associated with alluvial fan facies, palustrine conditions in marginal lake environments, and associated with other Mg-clays in mud-flat facies" (Pozo and Calvo, 2018). In addition, Ringrose et al. (2008) interpreted the presence of sepiolite as resulting from desiccation events. All these conditions fit with a large alluvial fan/palustrine paleoenvironment, making sepiolite unsurprising as a clay mineral in the Chobe Enclave. Finally, similar sedimentological assemblage and geochemical characteristics are found in a desiccated waterbody in the southern Kalahari Basin (Vainer et al., 2018). In this semiarid environment, Mg-rich clays of sepiolite (Bateman et al., 2003), palygorskite, and montmorillonite dominate the fine fraction. There, Sr isotopic ratios suggest the incorporation of Mg from the dissolution of adjacent dolomites. Analogously to the Chobe Enclave, Ba is enriched in these southern Kalahari sediments that also contain amorphous phases. These proxies alongside ratios between iron phases and regional field observations led Vainer et al. (2018) to propose an oxygen-poor, brackish, and alkaline waterbody, with an average depth column of 6 m during its ~450 ka of existence (Matmon et al., 2015). The similarity in the sedimentology and structural settings could imply on the Chobe Enclave as one of several waterbodies filling the Kalahari Basin throughout the Quaternary, such as the current alluvial fan of the Okavango.

As documented above, sepiolite precipitation needs an efficient evaporitic system to concentrate Mg^{2+}, as well as an alkaline pH for keeping $Si(OH)_4$ in solution until both ions reach the needed value of the solubility product for saturation state (Fig. 9). A closed lake system provides some necessary but not sufficient conditions to directly precipitate sepiolite from the water: evaporation and hydrology parameters (origin and nature of the fluids) also play a prominent role in the sedimentary process of sepiolite authigenesis.

6. Conclusions

The present study documents the occurrence and origin of authigenic sepiolite and demonstrates the possible conditions that were suitable for the formation of fibrous, magnesium-rich clay minerals in the Chobe Enclave. Authigenic sepiolite is reported with fibrous structure associated with carbonate and diatomite deposits. A closed lacustrine/palustrine alkaline system gave rise to high $Si(OH)_4$ and Mg^{2+} concentrations, enabling direct precipitation of sepiolite. A specific sequence of events is observed along pore walls and reflects the evolution of the parent solution and its ionic composition through time in an evaporitic system: firstly, calcite precipitates, secondly, sepiolite formation, followed by precipitation of amorphous silica. While the precipitation of sepiolite can be triggered from river waters transporting Mg^{2+} ions, some other sources of Mg-rich waters could have been provided during spells of hydrothermal activity. Principal component analysis demonstrates that the variability of element contents is controlled by three end-members i.e., detrital, carbonate–sepiolite, and hydrothermalism components, with the latter being asserted by the presence of barium. On one hand, kaolinite and minor smectite occurrences refer to a detrital clay assemblage in the lower units (sand-rich) of the Chobe Enclave, indicating the imprint of humid conditions (input via large rivers and reworking) prior to carbonate formation. On the other hand, sepiolite is mostly associated with carbonate–diatomite facies in the upper units, indicating its likely formation

Table 1
Results of principal component analysis. PC: principal components from 1 to 4. Expl. var.: percentage (%) of explained variance by each PC. Cum. var.: cumulative percentage (%) of explained variance with the first four PC. Numbers under the variables refer to the correlation coefficients between each variable and the PC. This coefficient is calculated as $r_i = \sqrt{\lambda_i} \cdot u_i$ where r_i is the correlation coefficients between the variables and the i^{th} PC and λ_i and u_i the eigenvalue and the eigenvector of the i^{th} PC, respectively. $r_i \geq 0.85$ is in bold.

PC	Expl. var.	Cum. var.	Al	Ca	Fe	K	Mg	Mn	Na	Si	Ba	Zr	Sepiolite	Kaolinite
PC1	47.44	47.44	0.38	**−0.92**	0.01	0.34	−0.72	**−0.86**	−0.51	**0.93**	−0.24	**0.90**	**−0.89**	0.73
PC2	17.59	65.03	−0.27	0.15	**−0.85**	**−0.87**	−0.33	0.12	0.16	−0.03	−0.42	−0.10	−0.28	0.35
PC3	10.52	75.55	0.76	−0.02	−0.30	0.15	0.26	0.12	0.63	−0.04	0.14	0.06	−0.09	0.26
PC4	7.45	83.00	0.25	0.12	−0.12	0.05	0.08	−0.11	0.03	−0.01	**−0.85**	−0.07	0.15	−0.21

by direct precipitation from solution (neoformation/authigenesis). Moreover, the formation and preservation of this sepiolite in palustrine carbonate dominated deposits reflect compatibility with the dominance of semiarid climate conditions during the Late Pleistocene to Holocene periods in the region where favorable conditions prevailed.

Data availability

Data will be made available on request.

Declaration of competing interest

The authors declare that they have no known competing financial interests or personal relationships that could have appeared to influence the work reported in this paper.

Acknowledgements

The authors acknowledge the Ministry of Environment, Natural Resources Conservation and Tourism of the Republic of Botswana as well as the Chobe Enclave Conservation Trust for the research permits, without which this study would not have been possible, as well as the Botswana International University of Science and Technology and the University of Lausanne. Special thanks to the Van Thuyne Ridge research center team for assistance with fieldwork and logistics. The authors also thank Mr. Dimitri Rigoussen for his discussions, and the reviewers, who greatly improved the first draft of this manuscript. This work has been supported by a Swiss National Science Foundation grant no 200021_172944 to EPV.

Appendix A. Supplementary data

Supplementary data to this article can be found online at https://doi.org/10.1016/j.sedgeo.2023.106459.

References

Adatte, T., Stinnesbeck, W., Keller, G., 1996. Lithostratigraphic and mineralogic correlations of near K/T boundary sediments in northeastern Mexico: implications for origin and nature of deposition. In: Ryder, G., Fastovsky, D., Gartner, S. (Eds.), The Cretaceous–Tertiary Event and Other Catastrophes in Earth History Geological Society of America Special Papervol. 307, pp. 211–226.

Akbulut, A., Kadir, S., 2003. The geology and origin of sepiolite, palygorskite and saponite in Neogene lacustrine sediments of the Serinhisar-Acipayam basin, Denizli, SW Turkey. Clays and Clay Minerals 51 (3), 279–292.

Arbey, F., 1980. Les formes de la silice et l'identification des évaporites dans les formations silicifiées. Bulletin des Centres de Recherches Exploration-Production Elf-Aquitaine 4 (1), 309–365.

Atekwana, E.A., Molwalefhe, L., Kgaodi, O., Cruse, A.M., 2016. Effect of evapotranspiration on dissolved inorganic carbon and stable carbon isotopic evolution in rivers in semiarid climates: the Okavango Delta in Northwest Botswana. Journal of Hydrology: Regional Studies 7, 1–13.

Bateman, M.D., Thomas, D.S., Singhvi, A.K., 2003. Extending the aridity record of the Southwest Kalahari: current problems and future perspectives. Quaternary International 111 (1), 37–49.

Birsoy, R., 2002. Formation of sepiolite–palygorskite and related minerals from solution. Clays and Clay Minerals 50 (6), 736–745.

Brauner, K., Preisinger, A., 1956. Struktur und Entstehung des Sepioliths. Tschermaks Mineralogische Und Petrographische Mitteilungen 6 (1–2), 120–140.

Brock-Hon, A.L., Elliot, T.R., 2013. Three-dimensional investigation of petrocalcic materials: insight into pedogenic processes and future applications. Soil Science Society of America Journal 77 (4), 1436–1441.

Brock-Hon, A.L., Robins, C.R., Buck, B.J., 2012. Micromorphological investigation of pedogenic barite in Mormon Mesa petrocalcic horizons, Nevada USA: implication for genesis. Geoderma 179, 1–8.

Burrough, S.L., Thomas, D.S.G., 2008. Late Quaternary lake-level fluctuations in the Mababe Depression: Middle Kalahari palaeolakes and the role of Zambezi inflows. Quaternary Research 69, 388–403.

Burrough, S.L., Thomas, D.S.G., Shaw, P.A., Bailey, R.M., 2007. Multiphase Quaternary highstands at Lake Ngami, Kalahari, Northern Botswana. Palaeogeography, Palaeoclimatology, Palaeoecology 253 (3–4), 280–299.

Burrough, S.L., Thomas, D.S.G., Bailey, R.M., 2009. Mega-lake in the Kalahari: a Late Pleistocene record of the palaeolake Makgadikgadi system. Quaternary Science Reviews 28 (15–16), 1392–1411.

Chamley, H., 1989. Clay Sedimentology. Springer-Verlag, Berlin.

Chorowicz, J., 2005. The east African rift system. Journal of African Earth Sciences 43 (1–3), 379–410.

Clarke, C.E., Majodina, T.O., Du Plessis, A., Andreoli, M.A.G., 2016. The use of X-ray tomography in defining the spatial distribution of barite in the fluvially derived palaeosols of Vaalputs, Northern Cape Province, South Africa. Geoderma 267, 48–57.

Cordova, C.E., Scott, L., Chase, B.M., Chevalier, M., 2017. Late Pleistocene–Holocene vegetation and climate change in the Middle Kalahari, Lake Ngami, Botswana. Quaternary Science Reviews 171, 199–215.

Cuevas, J., De La Villa, R.V., Ramirez, S., Petit, S., Meunier, A., Leguey, S., 2003. Chemistry of Mg smectites in lacustrine sediments from the Vicalvatro sepiolite deposit, Madrid Neogene Basin (Spain). Clays and Clay Minerals 51, 457–472.

Diaz, N., Armitage, S.J., Verrecchia, E.P., Herman, F., 2019. OSL dating of a carbonate island in the Chobe Enclave, NW Botswana. Quaternary Geochronology 49, 172–176.

Draidia, S., El Ouahabi, M., Daoudi, L., Havenith, H.B., Fagel, N., 2016. Occurrences and genesis of palygorskite/sepiolite and associated minerals in the Barzaman Formation, United Arab Emirates. Clay Minerals 51 (05), 763–779.

Dyer, S., 2017. Water Cycle in the Northern Kalahari. Univ. of Lausanne (Unpubl. Master of Science in Biogeosciences).

Fersmann, A., 1913. Research on magnesian silicates. Mémoires de l'Académie des sciences de St. Petersburgvol. 32, pp. 321–430.

Galán, E., Carretero, M.I., 1999. A new approach to compositional limits for sepiolite and palygorskite. Clays and Clay Minerals 47 (4), 399–409.

Galán, E., Pozo, M., 2011. Palygorskite and sepiolite deposits in continental environments. Description, genetic patterns and sedimentary settings. Developments in Clay Sciencevol. 3, pp. 125–173.

Galán, E., Singer, A. (Eds.), 2011. Developments in palygorskite-sepiolite research. Development in Clay Sciencevol. 3, p. 501.

García-Romero, E., Suárez, M., Santarén, J., Alvarez, A., 2007. Crystallochemical Characterization of the palygorskite and sepiolite from the Allou Kagne deposit, Senegal. Clays and Clay Minerals 55 (6), 606–617.

Garzanti, E., Padoan, M., Setti, M., López-Galindo, A., Villa, I.M., 2014. Provenance versus weathering control on the composition of tropical river mud (southern Africa). Chemical Geology 366, 61–74.

Garzanti, E., Pastore, G., Stone, A., Vainer, S., Vermeesch, P., Resentini, A., 2022. Provenance of Kalahari Sand: paleoweathering and recycling in a linked fluvial–aeolian system. Earth-Science Reviews 224, 103867.

Godet, A., Bodin, S., Adatte, T., Föllmi, K.B., 2008. Platform-induced clay-mineral fractionation along a northern Tethyan basin-platform transect: implications for the interpretation of Early Cretaceous climate change (Late Hauterivian–Early Aptian). Cretaceous Research 29 (5–6), 830–847.

Google Earth, 2022. Chobe region, Botswana. Pro V 7.3.6.9345, CNES/Airbus 2022. http://www.earth.google.com.

Gumbricht, T., McCarthy, T.S., Merry, C.L., 2001. The topography of the Okavango Delta, Botswana, and its tectonic and sedimentological implications. South African Journal of Geology 104 (3), 243–264.

Haddon, I.G., McCarthy, T.S., 2005. The Mesozoic–Cenozoic interior sag basins of Central Africa: the Late-Cretaceous–Cenozoic Kalahari and Okavango basins. Journal of African Earth Sciences 43 (1–3), 316–333.

Hanor, J.S., 2000. Barite–celestine geochemistry and environments of formation. Reviews in Mineralogy and Geochemistry 40 (1), 193–275.

Helgeson, H.C., Garrels, R.M., Mackenzie, F.T., 1969. Evaluation of irreversible reactions in geochemical processes involving minerals and aqueous solutions—II. Applications. Geochimica et Cosmochimica Acta 33 (8), 451–483.

Hong, H., Yu, N., Xiao, P., Zhu, Y.H., Zhang, K.X., Xiang, S.Y., 2007. Authigenic palygorskite in Miocene sediments in Linxia basin, Gansu, northwestern China. Clay Minerals 42, 45–58.

Irkec, T., Ünlü, T., 1993. An example to sepiolite formation in volcanic belts by hydrothermal alteration: Kibriscik (Bolu) sepiolite occurrence. Mineral Research and Exploration Bulletin 115, 49–68.

Jones, B.F., Conko, K.M., 2011. Environmental influences on the occurrences of sepiolite and palygorskite: a brief review. Developments in Clay Sciencevol. 3, pp. 69–83.

Jones, B.F., Galán, E., 1988. Sepiolite and palygorskite. In: Bailey, S.W. (Ed.), Hydrous Phyllosilicates. Reviews in Mineralogyvol. 19. Mineralogical Society of America, Washington, pp. 631–674.

Jourdan, F., Féraud, G., Bertrand, H., Kampunzu, A.B., Tshoso, G., Le Gall, B., Tiercelin, J.J., Capiez, P., 2004. The Karoo triple junction questioned: evidence from Jurassic and Proterozoic $^{40}Ar/^{39}Ar$ ages and geochemistry of giant Okavango dyke swarm (Botswana). Earth and Planetary Science Letters 222, 989–1006.

Kauffman Jr., A.J., 1943. Fibrous sepiolite from Yavapai County, Arizona. American Mineralogist 28, 512–520.

Key, R.M., Ayres, N., 2000. The 1998 edition of the national geological map of Botswana. Journal of African Earth Sciences 30 (3), 427–451.

Klug, H.P., Alexander, L.E., 1974. X-ray Diffraction Procedures: for Polycrystalline and Amorphous Materials. p. 992.

Koning, E., Gehlen, M., Flank, A.-M., Calas, G., Epping, E., 2007. Rapid post-mortem incorporation of aluminum in diatom frustules: evidence from chemical and structural analyses. Marine Chemistry 106 (1–2), 208–222.

Kübler, B., 1987. Cristallinité de l'illite: méthodes normalisées de préparation, méthode normalisée de mesure, méthode automatique normalisée de mesure. Cahiers de l'Institut de Géologie, Université de Neuchâtel, Suisse Série ADX n° 2.

Le Gall, B., Tshoso, G., Jourdan, F., Féraud, G., Bertrand, H., Tiercelin, J.J., Kampunzu, A.B., Modisi, M.P., Dyment, J., Maia, M., 2002. $^{40}Ar/^{39}Ar$ geochronology and structural data from the giant Okavango and related mafic dyke swarms, Karoo igneous province, northern Botswana. Earth and Planetary Science Letters 202, 595–606.

Lehmann, J., Master, S., Rankin, W., Milani, L., Kinnaird, J.A., Naydenov, K.V., Saalmann, K., Kumar, M., 2015. Regional aeromagnetic and stratigraphic correlations of the Kalahari Copperbelt in Namibia and Botswana. Ore Geology Reviews 71, 169–190.
Lopez, F., Gonzalez, J.M.G., 1995. Fibrous clays in the Almazan Basin (Iberian range, Spain): genetic pattern in a calcareous lacustrine environment. Clay Minerals 30 (4), 395–406.
Matmon, A., Hidy, A.J., Vainer, S., Crouvi, O., Fink, D., Erel, Y., Arnold, M., Aumaître, G., Bourlès, D., Keddadouche, K., Horwitz, L.K., 2015. New chronology for the southern Kalahari Group sediments with implications for sediment-cycle dynamics and early hominin occupation. Quaternary Research 84 (1), 118–132.
McCarthy, T.S., 2013. The Okavango Delta and its place in the geomorphological evolution of southern Africa. South African Journal of Geology 116 (1), 1–54.
McCarthy, T.S., Ellery, W.N., 1995. Sedimentation on the distal reaches of the Okavango Fan, Botswana, and its bearing on calcrete and silcrete (ganister) formation. Journal of Sedimentary Research 65 (1a), 77–90.
McCarthy, T.S., Humphries, M.S., Mahomed, I., Le Roux, P., Verhagen, B.T., 2012. Island forming processes in the Okavango Delta, Botswana. Geomorphology 179, 249–257.
Michalopoulos, P., Aller, R.C., Reeder, R.J., 2000. Conversion of diatoms to clays during early diagenesis in tropical, continental shelf muds. Geology 28 (12), 1095–1098.
Miller, R.M., Pickford, M., Senut, B., 2010. The geology, paleontology and evolution of the Etosha pan, Namibia: implications for terminal Kalahari deposition. South African Journal of Geology 113 (3), 307–334.
Mizutani, T., Fukushima, Y., Okada, A., Kamigaito, O., 1991. Hydrothermal synthesis of sepiolite. Clay Minerals 26 (03), 441–445.
Modie, B.N., 2000. Geology and mineralisation in the Meso- to Neoproterozoic Ghanzi–Chobe belt of northwest Botswana. Journal of African Earth Sciences 30 (3), 467–474.
Mokatse, T., Diaz, N., Shemang, E., Van Thuyne, J., Vittoz, P., Vennemann, T., Verrecchia, E. P., 2022a. Landscapes and landforms of the Chobe Enclave, Northern Botswana. In: Eckardt, F.D. (Ed.), Landscapes and Landforms of Botswana. Springer Nature Switzerland, pp. 91–115.
Mokatse, T., Vainer, S., Irving, J., Schmidt, C., Kgosidintsi, B., Shemang, E., Verrecchia, E.P., 2022. Geometry of sedimentary deposits and evolution of the landforms in the Chobe Enclave, Northern Botswana. Geomorphology 415, 108406. https://doi.org/10.1016/j.geomorph.2022.108406.
Moore, A.E., 1999. A reappraisal of epeirogenic flexure axes in southern Africa. South African Journal of Geology 102 (4), 363–376.
Moore, D., Reynolds, R., 1989. X-ray Diffraction and the Identification and Analysis of Clay-minerals. Oxford University Press, Oxford (332 pp.).
Moore, A.E., Cotterill, F.P.D., Eckardt, F.D., 2012. The evolution and ages of Makgadikgadi palaeo-lakes: consilient evidence from Kalahari drainage evolution south-central Africa. South African Journal of Geology 115 (3), 385–413.
Mukwati, B.T., Tadesse, N., Bagai, Z.B., Laletsang, K., 2018. Hydrogeochemistry of the Kasane Hot Spring, Botswana. Universal Journal of Geoscience 6, 130–145.
Niles, M.C., 2012. Chemical and Isotopic Analysis of Hot Springs in Zambia; No Evidence for Near Surface Rift-related Magmatic Body. Oklahoma State University, Stillwater (BSc. Thesis).
Nugent, C., 1990. The Zambezi River: tectonism, climatic change and drainage evolution. Palaeogeography Palaeoclimatology Palaeoecology 78, 55–69.
Pardo, P., Bastida, J., Serrano, F.J., Ibáñez, R., Kojdecki, M.A., 2009. X-ray diffraction line-broadening study on two vibrating, dry-milling procedures in kaolinites. Clays and Clay Minerals 57 (1), 25–34.
Pozo, M., Calvo, J.P., 2015. Madrid Basin (Spain): a natural lab for the formation and evolution of magnesian clay minerals. In: Pozo, M., Galán, E. (Eds.), Magnesian Clays: Characterization, Origin and Applications. AIPEA Educational Series, Pub. No. 2. Digilabs, Bari, Italy, pp. 229–281.
Pozo, M., Calvo, J.P., 2018. An overview of authigenic magnesian clays. Minerals 8 (11), 520.
Pozo, M., Galán, E., 2015. Magnesian clay deposits: mineralogy and origin. In: Pozo, M., Galán, E. (Eds.), Magnesian Clays: Characterization, Origin and Applications. AIPEA Educational Series, Pub. No. 2. Digilabs, Bari, Italy, pp. 175–227.
Ren, H., Brunelle, B.G., Sigman, D.M., Robinson, R.S., 2013. Diagenetic aluminum uptake into diatom frustules and the preservation of diatom-bound organic nitrogen. Marine Chemistry 155, 92–101.
Ringrose, S., Huntsman-Mapila, P., Kampunzu, A.B., Downey, W., Coetzee, S., Vink, B., Matheson, W., Vanderpost, C., 2005. Sedimentological and geochemical evidence for palaeo-environmental change in the Makgadikgadi subbasin, in relation to the MOZ rift depression, Botswana. Palaeogeography, Palaeoclimatology, Palaeoecology 217 (3–4), 265–287.
Ringrose, S., Huntsman-Mapila, P., Downey, W., Coetzee, S., Fey, M., Vanderpost, C., Vink, B., Kemosidile, T., Kolokose, D., 2008. Diagenesis in Okavango fan and adjacent dune deposits with implications for the record of paleo-environmental change in Makgadikgadi–Okavango–Zambezi basin, northern Botswana. Geomorphology 101 (4), 544–557.
Ringrose, S., Harris, C., Huntsman-Mapila, P., Vink, B.W., Diskins, S., Vanderpost, C., Matheson, W., 2009. Origins of strandline duricrusts around the Makgadikgadi Pans (Botswana Kalahari) as deduced from their chemical and isotope composition. Sedimentary Geology 219, 262–279.
Robins, C.R., Brock-Hon, A.L., Buck, B.J., 2012. Conceptual mineral genesis models for calcic pendants and petrocalcic horizons, Nevada. Soil Science Society of America Journal 76 (5), 1887–1903.
Rolli, M., 1990. Dosage semi-quantitatif RX sur Scintag. Cahiers de l'Institut de Géologie de Neuchâtel, Suisse, v. Série ADXvol. 1, p. 49.
Schwartz, M.O., Kwok, Y.Y., Davis, D.W., Akanyang, P., 1996. Geology, geochronology and regional correlation of the Ghanzi Ridge, Botswana. South African Journal of Geology 99, 245–250.
Shannon, E.V., 1929. Tschermigite, ammoniojarosite, epsomite, celestite and palygorskite from Southern Utah. Proceedings of the United States National Museum 74 (13), 12.
Shaw, P.A., Thomas, D.S.G., 1988. Lake Caprivi: a late Quaternary link between the Zambezi and middle Kalahari drainage systems. Zeitschrift für Geomorphologie 32, 329–337.
Singer, A., 1979. Palygorskite in sediments: detrital, diagenetic or neoformed—a critical review. Geologische Rundschau 68, 996–1008.
Singer, A., 1984. Pedogenic palygorskite in the arid environment. In: Singer, A., Gala'n, E. (Eds.), Palygorskite–Sepiolite. Occurrences, Genesis and Uses. Developments in Sedimentologyvol. 37. Elsevier, Amsterdam, pp. 169–177.
Stoessell, R.K., Hay, R.L., 1978. The geochemical origin of sepiolite and kerolite at Amboseli, Kenya. Contributions to Mineralogy and Petrology 65, 255–267.
Stoops, G.J., Zavaleta, A., 1978. Micromorphological evidence of barite neoformation in soils. Geoderma 20 (1), 63–70.
Su, C., Zhong, D., Qin, P., Wang, A., 2020. Mineral precipitation sequence and formation of the lacustrine hydrothermal sediments in the Lower Cretaceous Tenggeer Formation in the Baiyinchagan Sag, China. Sedimentary Geology 398, 105586.
Suárez, M., García-Romero, E., 2011. Advances in the crystal chemistry of sepiolite and palygorskite. In: Galàn, E., Singer, E. (Eds.), Developments in Clay Science. Elsevier, pp. 33–65.
Tateo, F., Sabbadini, R., Morandi, N., 2000. Palygorskite and sepiolite occurrence in Pliocene lake deposits along the river Nile: evidence of an arid climate. Journal of African Earth Sciences 31 (3–4), 633–645.
Thomas, D.S.G., Shaw, P.A., 1990. The deposition and development of the Kalahari Group sediments, Central Southern Africa. Journal of African Earth Sciences 10 (1–2), 187–197.
Thomas, D.S.G., Shaw, P.A., 1991. The Kalahari Environment. Cambridge University Press, p. 284.
Tosca, N.J., Masterson, A.L., 2014. Chemical controls on incipient Mg-silicate crystallization at 25 C: implications for early and late diagenesis. Clay Minerals 49 (2), 165–194.
Vainer, S., Erel, Y., Matmon, A., 2018. Provenance and depositional environments of Quaternary sediments in the southern Kalahari Basin. Chemical Geology 476, 352–369.
Vainer, S., Matmon, A., Erel, Y., Hidy, A.J., Crouvi, O., De Wit, M., Geller, Y., ASTER Team, 2021. Landscape responses to intraplate deformation in the Kalahari constrained by sediment provenance and chronology in the Okavango Basin. Basin Research 33 (2), 1170–1193.
Vainer, S., Matmon, A., Ben Dor, Y., Verrecchia, E.P., Eckardt, F., 2022. Eolian chronology reveals causal links between tectonics, climate, and erg generation. Nature Communications 13 (1), 1–9.
Van Thuyne, J., Darini, I., Mainga, A., Verrecchia, E.P., 2021. Are fungus-growing termites super sediment-sorting insects of subtropical environments? Journal of Arid Environments 193, 104556.
Wang, M.K., Tseng, P.C., Chang, S.S., Ray, D.T., Shau, Y.H., Shen, Y.W., Chen, R.C., Chiang, P. N., 2009. Origin and mineralogy of sepiolite and palygorskite from the Tuluanshan Formation, Eastern Taiwan. Clays and Clay Minerals 57 (5), 521–530.
Watts, N.L., 1980. Quaternary pedogenic calcretes from the Kalahari (southern Africa): mineralogy, genesis and diagenesis. Sedimentology 27 (6), 661–686.
Webster, D.M., Jones, B.F., 1994. Paleoenvironmental implications of lacustrine clay minerals from the double lakes formation, southern high plains, Texas. In: Renaut, R.W., Last, W.M. (Eds.), Sedimentology and Geochemistry of Modern and Ancient Saline Lakes. SEPM Spec. Publvol. 50, pp. 159–172.
Yalçin, H., Bozkaya, Ö., 2011. Sepiolite–palygorskite occurrences in Turkey. Developments in Clay Science. vol. 3. Elsevier, pp. 175–200.